Preparation, Chemistry and Applications of Novel Carbon Nanomaterials

Martin Rosillo-Lopez

Thesis submitted in partial fulfilment of the requirements for the degree of Doctor of Philosophy

Department of Chemistry

University College London (UCL)

April 2018

Declaration

I, Martin Rosillo-Lopez, confirm that the work presented in this thesis is my own. Where information has been derived from other sources, I confirm that this has been indicated in the thesis.

Signature: ……

Date: ……

To my parents,

for everything.

Abstract

The isolation of graphene in 2004, and subsequent Nobel Prize for Physics being awarded to Andre Geim and Konstantin Novoselov in 2010, has sparked a renewed interest in graphene around the world due to graphene's remarkable physical properties such as mechanical stability, optical transparency, impermeability and electrical and thermal conductivity. Graphene Oxide (GO), the oxidised analogue of graphene, has also received much attention owing to its hydrophilic nature. This has made GO a very promising material for aqueous processing, giving it a significant advantage over graphene. In this way, GO has been used in many composite materials, involving biological molecules, metal-organic-frameworks (MOFs) and other hybrid systems. Unfortunately, much uncertainty surrounds the chemical nature of GO, and therefore its chemistry, thus creating a lot of controversy in the literature. Similarly, the preparation of GO also results in lengthy procedures and toxic by-products. To address these issues, this thesis describes the preparation of alternative carbon nanomaterials, as a potential substitute to GO, which have well-defined structures and chemistry and/or reduce the toxic waste produced. The chemistry and applications of these new materials are explored and benchmarked against conventional GO, which is prepared *via* permanganate oxidation (PM-GO).

The preparation of three novel carbon materials, carboxylated graphene nanoflakes (cx-GNFs), nano-graphene oxide (nGO) and GO prepared via dichromate oxidation (DC-GO) are initially reported, along with extensive characterisations. The cx-GNFs are a highly soluble (~100 mg mL^{-1}) and well-defined material consisting of carboxyl groups and unoxidised sp^2 carbon only. nGO is prepared *via* an eco-friendly procedure producing nano-sized GO and DC-GO was prepared in order to elucidate its chemical structure which remains uncertain in the literature.

The thermal annealing behaviour of the materials are reported next and the cx-GNFs and the nGO are shown to form carboxylic anhydrides in yields up to 81%, which is the first experimental evidence for this functional group at the graphene edge. The existence of carboxylic anhydrides in dynamic equilibrium with carboxylic acids in water was demonstrated at room temperature for the cx-GNFs, and was consequently exploited for room temperature chemical functionalisations with well-known amines such as ethylenediamine and cysteamine. These functionalised materials were then explored in the context of tagging gold nanoparticles and changing the zeta potential of the native cx-GNFs. The application of these novel materials in heavy-metal extraction is also presented and found to greatly exceed the capacity of PM-GO - by up to six times. Collaborations with other research groups in the field of nano-sensors, ice-nucleation and electrochemistry, revealed the cx-GNFs to be a particularly promising material.

Impact Statement

This thesis describes the preparation, characterisation, chemistry and applications of novel carbon nanomaterials. The materials presented constitute significant advances over other carbon materials in the literature. In this regard, well-defined materials in terms of structure and chemistry have been presented, allowing for easier interpretation of the reaction products. From an academic and industrial perspective, this allows for easier structural comparisons between materials before and after chemical processing. Some of the chemistry taking place occurs *via* carboxylic anhydrides, which are native to the materials, allowing for click-chemistry reactions to occur under environmentally-friendly conditions. In general, the existence of carboxylic anhydrides on the graphene edge was experimentally proven for the first time using these materials.

Detailed discussions on the structural nature of the various materials produced under different oxidation regimes will be beneficial to ascertain the mechanisms by which carbon materials undergo oxidation, which remains largely unknown.

The materials reported here have been utilised in various applications with a number of other research groups in collaboration. For instance, the first experimental evidence demonstrating that carbon nanomaterials can nucleate ice was reported, which can have profound implications in atmospheric chemistry. The use of these materials in the extraction of heavy-metals from water was also presented and shown to exceed the capacities of conventional carbon materials by up to six times. The potential impact of this is significant in the context of wastewater management and the purification of drinking water.

It is expected that these materials will find their uses in a wide range of applications, both academic and industrial.

Acknowledgements

First and foremost, I would like to thank my supervisor Dr. Christoph G. Salzmann for all the support and guidance he has given me over the last five years (yes, five years!). I would also like to acknowledge Dr. Katherine Holt, Dr. Matthew Blunt and Dr. Simon Banks who supervised me as the UCL physical chemistry teaching assistant during my PhD. I would also like to thank all the wonderful people I have met here at UCL over the years, of which there are so many. Special thanks go to everyone in the office in room 460 for making my day bright and pleasant every single day. Additional thanks go to Dr. Katherine Holt and Dr. Steve Firth for useful discussions throughout my PhD-thank you Steve for all the help with the TEM, SEM and Raman instruments!

Specific acknowledgements go to Ms. Tai Jung Lee for recording and analysing the AFM data in Fig. 3.7 as well as the optical absorbance spectra in Fig. 3.14, Mr. Martin Hart for recording the TEM image in Fig. 3.8 and Dr. Abil Aliev and Dr. Srinivas Gadipelli for recording solid state NMR spectra and TGA data respectively. A final thanks go to all the collaborators: Mailis Lounasvuori (UCL), Katherine Holt (UCL), Tom Whale (Leeds), Ben Murray (Leeds), Colin Crick (ICL), Jasmine Sze (ICL) and Joshua Edel (ICL).

Lastly, I dedicate this thesis to my parents who have supported me through everything. I love you both so very much.

Table of Contents

Appendix

List of Symbols

c	speed of light	$m\ s^{-1}$
e	elementary charge	C
E_B	binding energy	eV
E_K	kinetic energy	eV
h	Planck constant	J s
I	intensity of transmitted light	n/a
I_0	intensity of incident light	n/a
k	force constant	$kg\ s^{-2}$
K	kelvin	K
k_B	Boltzmann constant	$m^2\ kg^{-2}\ K^{-1}$
n_0	bulk ion concentration	$mol\ dm^{-3}$
z	ion charge	n/a
ε	molar extinction coefficient	$dm^3\ mol^{-1}\ cm^{-1}$
ε_0	permittivity of the vacuum	$F\ m^{-1}$
ε_r	relative dielectric constant	$F\ m^{-1}$
ζ	zeta potential	mV
η	viscosity	$kg\ m^{-1}$
θ	angle	°
κ	Debye-Huckel parameter	m^{-1}
λ	wavelength	m
μ	reduced mass	kg
v	wavenumber	m^{-1}
ν	frequency	s^{-1}
υ	electrophoretic mobility	$m^2s^{-1}V^{-1}$
π	pi	n/a
$\Phi_{spectrometer}$	spectrometer work function	eV
°	degrees (angle)	
°C	degrees celsius	

List of Abbreviations

0D	0 dimensional
1D	1 dimensional
2D	2 dimensional
3D	3 dimensional
A	absorbance
AC	armchair (graphene edge)
AFM	atomic force microscopy
at%	atomic percentage
B.E.	binding energy
BET	Brunauer-Emmett-Teller
BSE	backscattered electrons
CNTs	carbon nanotubes
CVD	chemical vapour deposition
Cys-GNFs	cysteamine functionalised graphene nanoflakes
cx-GNFs	carboxylated graphene nanoflakes
DC-GO	dichromate oxidised graphene oxide
DC-GO (Chandra)	dichromate oxidised graphene oxide using Chandra's protocol
DC-GO (optimised)	dichromate oxidised graphene oxide using the optimised protocol
DMF	dimethylformamide
DMTD-K^+	2,5-dimercapto-1,3,4-thiadiazole dipotassium salt
EDTA	ethylenediaminetetraacetic acid
EDX	energy-dispersive X-ray spectroscopy
Equiv.	equivalents by mass
Eth-GNF	ethylenediamine functionalised graphene nanoflakes
Eth-GNF (DMF)	ethylenediamine functionalised graphene nanoflakes in dimethylformamide solvent
FT-IR	fourier-transform infrared spectroscopy
GL	Gaussian-Lorentzian ratio
GNRs	graphene nanoribbons
GO	graphene oxide
HOMO	highest occupied molecular orbital

HOPG	highly oriented pyrolytic graphite
HPDEC	high-power proton decoupling
H_2SO_4-GIC	sulfuric acid-graphite intercalation compound
HRTEM	high-resolution transmission electron microscopy
IMFP	inelastic mean free path
IR	infrared spectroscopy
l	path length
LK	Lerf-Klinowski
L_D	average distance between two defects
LUMO	lowest unoccupied molecular orbital
MAS	magic angle spinning
MOFs	metal organic frameworks
MS	mass spectrometry
MWCNTs	multi-walled carbon nanotubes
nGO	nano-graphene oxide
nm	nanometers
OD	oxidative debris
Oxo-group	functional groups containing oxygen
PM-GO	permanganate oxidised graphene oxide
PM-GO (Chandra)	permanganate oxidised graphene oxide using Chandra's protocol
PM-GO (Chen)	permanganate oxidised graphene oxide using Chen's protocol
PM-GO (optimised)	permanganate oxidised graphene oxide using the optimised protocol
PXRD	powder X-ray diffraction
RBM	radial breathing modes
rGO	reduced graphene oxide
SD	Szabo-Dekany
SEM	scanning electron microscopy
SiO_2-NH_2	silica gel capped and terminated with amine
SiO_2-GNF	silica gel functionalised with graphene nanoflakes
SSNMR	solid-state nuclear magnetic resonance
SWCNTs	single-walled carbon nanotubes
TEM	transmission electron microscopy
TGA	thermogravimetric analysis

TGA-MS	thermogravimetric analysis coupled with mass spectrometry
U.V.-Vis	ultraviolet-visible spectroscopy
VOC	volatile organic compounds
ν_{as}	asymmetric stretch
ν_{s}	symmetric stretch
XPS	X-ray photoelectron spectroscopy
ZZ	zig-zag (graphene edge)

List of Figures

List of Tables

List of Appendix Figures

List of Publications

I would like to declare that part of this thesis has been adapted from the first two publications listed below.

1. Rosillo-Lopez M, Lee TJ, Bella M, Hart M, Salzmann CG. 2015. Formation and chemistry of carboxylic anhydrides at the graphene edge. *RSC Adv.* 5:104198-202

2. Rosillo-Lopez M, Salzmann CG. 2016. A simple and mild chemical oxidation route to high-purity nano-graphene oxide. *Carbon* 106:56-63

3. Whale TF, Rosillo-Lopez M, Murray BJ, Salzmann CG. 2015. Ice Nucleation Properties of Oxidized Carbon Nanomaterials. *J. Phys. Chem. Lett.* 6:3012-6

4. Crick CR, Sze JYY, Rosillo-Lopez M, Salzmann CG, Edel JB. 2015. Selectively Sized Graphene-Based Nanopores for in Situ Single Molecule Sensing. *ACS Appl. Mater. Interfaces* 7:18188-94

5. Lounasvuori MM, Rosillo-Lopez M, Salzmann CG, Caruana DJ, Holt KB. 2015. The influence of acidic edge groups on the electrochemical performance of graphene nanoflakes. *J. Electroanal. Chem.* 753:28-34

6. Lounasvuori MM, Rosillo-Lopez M, Salzmann CG, Caruana DJ, Holt KB. 2014. Electrochemical characterisation of graphene nanoflakes with functionalised edges. *Faraday Discuss.* 172:293-310

Chapter: 1 Introduction

1.1 Carbon materials

All elements have their own unique properties, but carbon stands out as being particularly special. It constitutes the backbone of all of organic chemistry, and life itself is dependent on its unique ability to form multiple strong bonds with itself and many other elements. It is because of this that all life on Earth is carbon based. Carbon also exhibits a wide variety of stable allotropes, including cubic and stacking-disordered diamond, carbon nanotubes- which may be single or multiwalled, fullerenes, graphite and of course graphene. With the exception of diamond, all of these carbon allotropes have at least some degree of sp^2 hybridised character (if not entirely) and therefore have highly delocalised electrons, giving the materials unique properties such as very high electrical conductivity (1-4). Fig. 1.1 illustrates how graphene, which is a single sheet of hexagonally arranged sp^2 hybridised carbon, can be hypothetically used as a template for the synthesis of the other sp^2 carbon allotropes.

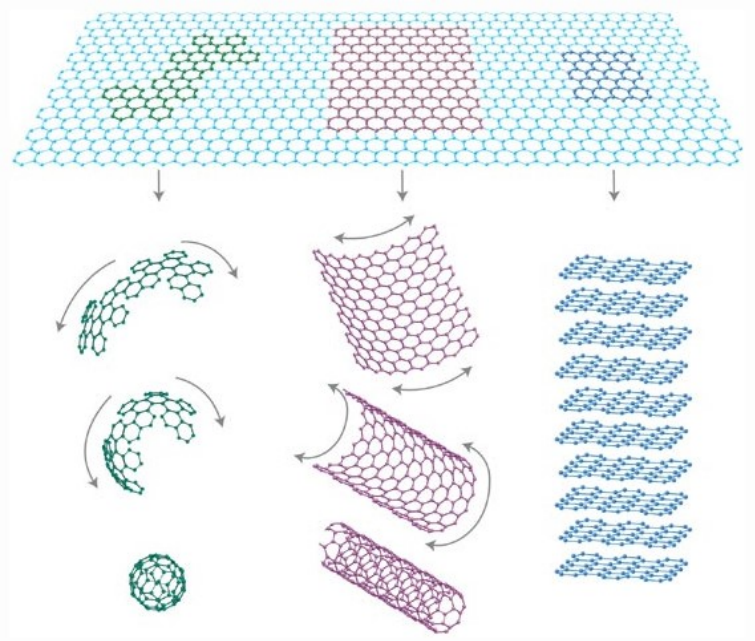

Fig. 1.1 Graphene is a 2D building material for carbon materials of all other dimensionalities. It can be wrapped up into 0D buckyballs, rolled into 1D nanotubes or stacked into 3D graphite. Reproduced from ref. (5) by permission from Macmillan Publishers Ltd (5).

Fullerenes, shown in green in Fig. 1.1, are often referred to as 0 dimensional (0D) materials. They can be schematically 'wrapped' up from graphene to form a ball consisting of five and six membered carbon rings. In the case of C_{60} (a fullerene containing 60 carbon atoms), each 5- membered ring is surrounded by only 6- membered carbon rings. Interestingly, C_{60} itself is not super-aromatic like other planar sp^2 structures (6). Similarly, carbon nanotubes (CNTs, referred to as 1D materials) shown in purple in Fig. 1.1, can be rolled up from a single sheet of graphene (to form single walled carbon nanotubes, SWCNTs) or from multiple sheets to form multiwalled carbon nanotubes, MWCNTs. The properties of carbon nanotubes can vary drastically depending on how they have been 'rolled' up. Typically, two categories of CNT arise, those with semi-conducting properties and those with metallic behaviour (7). Finally, graphite (shown in dark blue in Fig. 1.1), is denoted as '3D' and is simply the stacking of two dimensional graphene into a regular lattice; although stacking disordered graphite has been observed as well (8; 9). The layers of graphite (i.e. graphene) are held together by relatively weak van der Waals dispersion forces, but the delocalisation of electrons remains within the layers.

1.2 The rise of Graphene

For many years graphene was considered a thermodynamically unstable allotrope of carbon and its isolation was thought to be impossible (10). However in 2004 a research group at the University of Manchester, UK, successfully isolated the material by the simple mechanical exfoliation of graphite using scotch tape (11). Not only was the graphene found to be stable, but it also exhibited the remarkable physical properties it was predicted to have, such as high electron mobility (1) and thermal conductivity (12), elasticity, high impermeability (13) as well as being incredibly strong (14). The potential of graphene was immediately realised and in 2010 the Nobel Prize for Physics was awarded to Andre Geim and Konstantin Novoselov. Since then there has been a huge surge in graphene related research across the globe.

1.2.1 Structure of Graphene

In its idealised form, graphene is a single sheet of sp^2 hybridised carbon atoms arranged into hexagons; is defect free, and the carbon atoms at the edges of the sheet all have an unpaired electron, which is stabilised by the electron delocalisation that occurs throughout the sheet. In reality however, the structure of graphene is far more

complicated (15-21). The graphene sheet will contain defects, including holes (22), carbon rings of various sizes (23)-most notably Stone-Wales defects (5- and 7-membered rings formed from two 6- membered rings) (23; 24), triple bonds (25), dangling bonds (26), C-H bonds (27) and more (28). The high resolution transmission electron microscopy image (HRTEM) in Fig. 1.2 illustrates the various defects which can be found on the graphene sheet (23).

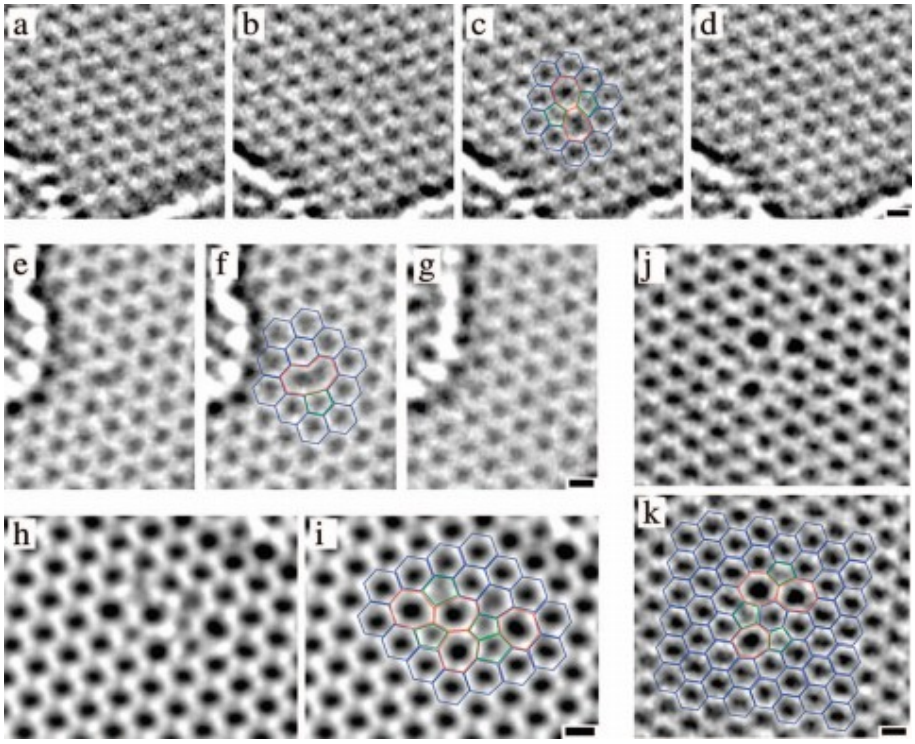

Fig. 1.2 Metastable defects found in HRTEM image sequences. (a-d) Stone-Wales (SW) defect: (a) unperturbed lattice before appearance of the defect, (b) SW defect (c) same image with atomic configuration superimposed, (d) relaxation to unperturbed lattice (after ca. 4 s). (e-g) Reconstructed vacancy: (e) original image and (f) with atomic configuration; a pentagon is indicated in green. (g) Unperturbed lattice, 4 s later. (h and i) Defect image and configuration consisting of four pentagons (green) and heptagons (red). Note the two adjacent pentagons. (j and k) Defect image and configuration consisting of three pentagons (green) and three heptagons (red). This defect returned to the unperturbed lattice after 8 s. In spite of the odd number of 5-7 pairs, this is not a dislocation core (it is compensated by the rotated hexagon near the center of the structure). All scale bars are 2 Å. Adapted with permission from ref. (23).

It is not just the basal plane of the graphene sheet which suffers from defects but also the edge sites. Classically, the edges of graphene are thought to consist of ‘zig-zag’ (ZZ) or ‘armchair’ (29) (AC) type configurations as depicted in Fig. 1.3.

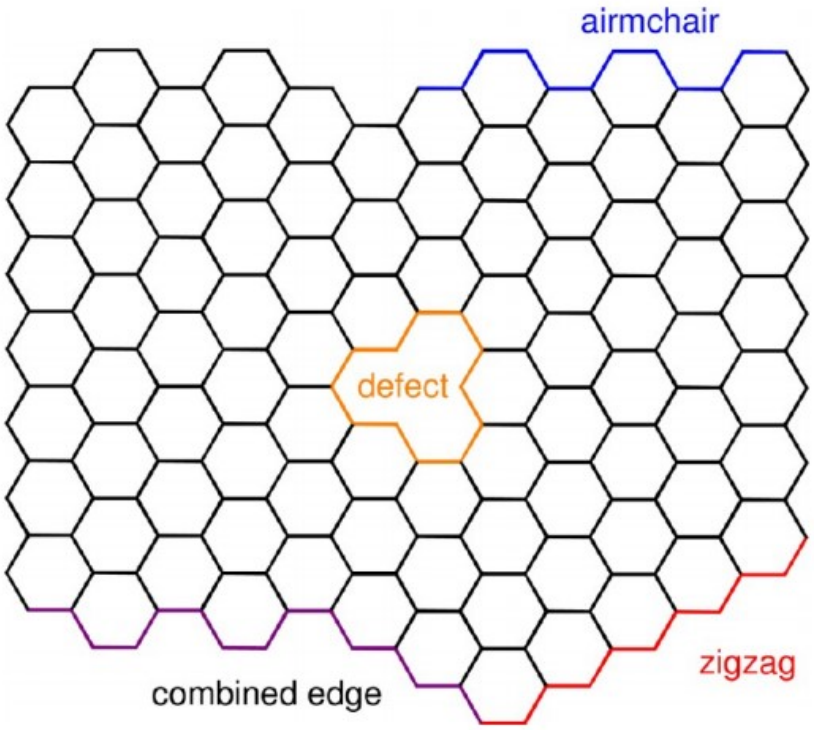

Fig. 1.3 Schematic Representation of Reactive Sites in Graphene Sheets: Surface Faces, Edges and Defects.(30) Adapted with permission from ref. (30).

Zig-zag edges are thought to be polycarbenes (19; 31), whilst in the armchair configuration it is considered that a triple bond exists between the two open edge carbon atoms (32). In reality, this is just a common generalisation and many stable (or metastable) edge configurations may exist (33). Indeed, it has been shown in real-time HRTEM that edge carbon atoms can literally move freely across the edge sites reversibly forming 5- and 7- membered carbon rings from 6-membered rings, as can be seen in Fig. 1.4 (26).

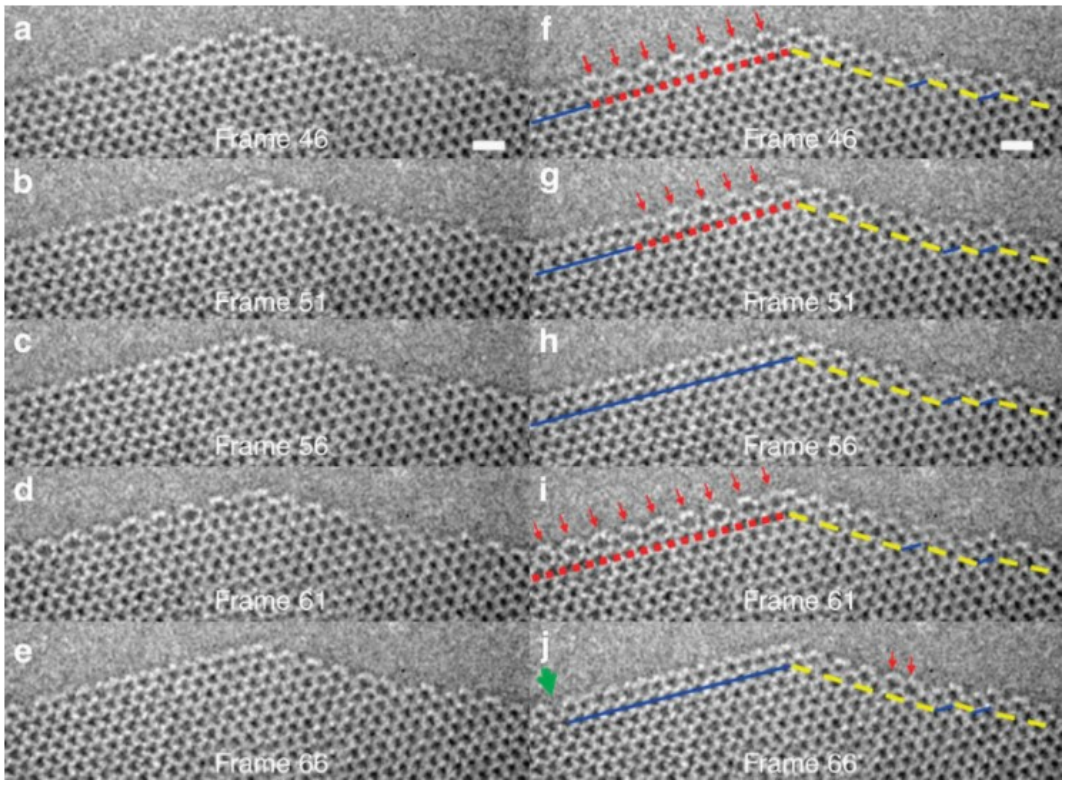

Fig. 1.4 (a–e) A time series of TEM images of graphene edge. Each image is apart from each other by five frames. The left (right) segments have the ZZ (AC) edge configuration. Scale bar, 0.5 nm. (f–j) The same sequential TEM images with edge representations. The red arrow indicates a heptagon ring. The blue solid and red dotted lines represent 6–6 ZZ and 5–7 reconstructed ZZ edges, respectively. The yellow dashed lines show AC edge configuration. The green arrow in **j** shows a vacancy defect. Adapted from ref. (26) with permission.

The structure of graphene, particularly at the edge, is clearly dynamic in nature (assuming no influence from the electron beam), and therefore a lot more research will be required to fully appreciate the complexity of this material. Interestingly, however, the defective nature of graphene provides for richer chemistry and catalysis, particularly in the field of electrochemistry (34; 35).

1.2.2 Production of Graphene

The large scale preparation of high purity graphene remains challenging (36), and currently only small scale approaches to the production of high quality graphene exist. Nonetheless, graphene can be produced in a number of ways, including mechanical exfoliation (11), chemical vapour deposition (CVD) (37-45), reduction of graphene oxide *via* chemical/electrochemical (46; 47) means or disproportionation through heat

treatment (48), liquid phase exfoliation (49-55), epitaxial growth (56), ion intercalation (57; 58) and bottom-up organic synthesis (59; 60).

The CVD synthesis of graphene is becoming the preferred method for electronic related applications which require defect-free graphene (61; 62). In this process, graphene is formed on the surface of a substrate-typically a transition metal (Cu, Pt, Pd, Ni or Ir) from a carbon source such as methane under high temperatures, light or electrical discharge (38-42; 63; 64). Copper is emerging as the most favourable substrate owing to its low cost and tendency to produce larger sheets of graphene (41; 65). One of the main drawbacks of using CVD approaches is the lack of control over the growth mechanism, which remains poorly understood (66). Furthermore, removal of graphene from the substrate is also an inconvenience.

1.3 Graphene and Graphite Oxide

As the name suggests, graphene oxide (GO) is the oxidised analogue of graphene; if multiple layers of graphene oxide are stacked then 3D graphite oxide is produced.

1.3.1 History

The very first reported preparation of graphite oxide dates back to 1859 with Brodie (67), who oxidised flake graphite using potassium chlorate ($KClO_3$) in fuming nitric acid (HNO_3). The preparation was later modified by Staudenmaier in 1898 who increased the equivalents of $KClO_3$ and used a mixture of fuming HNO_3 and sulfuric acid (H_2SO_4) to increase the acidity of the mixture (68). The procedure was significantly improved on later by Hummers and Offeman by replacing $KClO_3$ and fuming HNO_3 with potassium permanganate ($KMnO_4$) and potassium nitrate (KNO_3) in concentrated H_2SO_4 (69). The 'Hummers method', as this procedure is now known, is the most commonly employed method for preparing GO owing to its safer (*i.e.* the almost complete removal of NO_x fumes and explosive $KClO_3$), and overall more efficient approach. For the sake of transparency, it is noteworthy that the original use of a $KMnO_4/H_2SO_4$ mixture to oxidise graphite was first reported by Charpy (70), some fifty years before Hummers. Unfortunately, this fact has not been fully realised in the literature.

Nowadays, there are many 'spin-off' approaches to the preparation of GO including modified Hummers methods which remove KNO_3 entirely from the synthesis (71-73) and

the ‘Tour’ method (74); as well as more unique approaches such as potassium dichromate ($K_2Cr_2O_7$) and $NaNO_3$ in H_2SO_4 (75), potassium ferrate (K_2FeO_4) in H_2SO_4 (76) and more (77; 78).

In the ‘Tour’ method, $KMnO_4$ is combined with a mixture of 9:1 H_2SO_4/H_3PO_4 in the absence of KNO_3.The use of H_3PO_4 was based on the group’s previous work with graphene nanoribbon (GNR) synthesis, which showed that the use of H_3PO_4 resulted in GNR with more intact basal planes (79). Consequently, it was believed that H_3PO_4 will reduce the number of defects on the GO sheets. The use of H_3PO_4 is also less exothermic compared with conventional Hummers methods (74). It is also noteworthy that twice the amount of $KMnO_4$ is used in the ‘Tour’ method than the original Hummers method, in order to obtain a higher degree of oxidation (74).

The use of $K_2Cr_2O_7$ as an alternative to $KMnO_4$ has also been reported but the nature of the final GO product obtained remains unclear. There has been some speculation that the resulting GO is over-oxidised resulting in its decomposition (80). However, in chapter 3 of this thesis, the chemical nature of this material is elucidated.

The recently reported use of K_2FeO_4 in H_2SO_4 as an alternative to Hummers has gained some interest. This is because it is the first potentially viable option to industrial scale GO synthesis, since reactions rates are fast and there is no need to dispose of Mn waste. The reaction media has also been shown to be recyclable many times over (>10 times).(76) Unfortunately, K_2FeO_4 is not currently produced on an industrial scale, is moisture sensitive and readily decomposes in water (81).

1.3.2 Mechanism of GO formation

There still remains a lot of uncertainty surrounding the oxidation mechanism of GO (82; 83). however it is generally regarded that the mechanism can be sub-divided into three main intermediate steps (83). In the first step, sulfuric acid initiates the reaction by intercalating within the graphite layers forming a sulfuric acid-graphite intercalation compound (H_2SO_4-GIC) (84-86). The initial formation of a GIC is always the first step regardless of the oxidation protocol used, only the identity of the intercalant will be different (83). The resulting intercalation increases the interlayer spacing between the graphite sheets allowing access to the active oxidising species (see step 2). It is noteworthy that this first step in the oxidation mechanism is the fastest step, taking only a few minutes-but will be dependent on the flake size (83).

In stage 2 of the mechanism, the active oxidising species inserts in between the graphite sheets and subsequently oxidises the graphite (83). In all cases, the identity of the active oxidising species remains elusive, however it has been suggested for the Hummers procedure that the permanganyl cation (MnO_3^+) (83; 87; 88) and/or dimanganese heptoxide (Mn_2O_7) (89) are the active species in the oxidation of graphite (90). The reaction scheme below shows how the formation of these species might occur:

$$MnO_4^- + 3\ H_2SO_4 \rightarrow \mathbf{MnO_3^+} + H_3O^+ + 3\ HSO_4^- \qquad [1]$$

$$MnO_3^+ + MnO_4^- \rightarrow \mathbf{Mn_2O_7} \qquad [2]$$

Since this second step involves the diffusion of the active oxidising species in between the graphite layers, it is the rate limiting step in the reaction.

In the third and final stage, water is added to the reaction mixture which reacts with the various manganese species, effectively quenching the reaction. Subsequent washing with water results in the exfoliation of graphite oxide to GO. There is also evidence to suggest that water also reacts with the graphite oxide-initially it is believed that cyclic sulphate groups exist on graphite oxide which then hydrolyse to form tertiary alcohols which are observed in the final GO product (72; 91; 92).

1.3.3 Structure of GO

The proposed structural models of GO date back to the 1930s (93; 94), with the most notable models being those of Lerf-Klinowski (LK) in 1998 (95) and Szabo-Dekany (SD) in 2006 (96). In the LK model, GO is defined as a sheet of randomly distributed intact sp^2 domains mixed with oxidised sp^3 regions. The functional groups constituting the oxidised sp^3 regions are epoxides and hydroxyls (tertiary alcohols) which are found on the basal plane; carboxylic acids and hydroxyls are suspected of decorating the edges (95). The SD model by contrast, consists of a periodic array of aromatic and cyclohexane rings, with the cyclohexane rings functionalised with hydroxyls and 4-membered ring ethers. The model also suggests that at the points of C-C bond cleavage, ketones and quinones exist (96). Fig. 1.5 shows the differing structures of the two models. It is noteworthy that the models proposed by LK and SD are adaptations of the first models devised by Reuss, Clauss, Hofmann, Scholz and Boehm (97; 98).

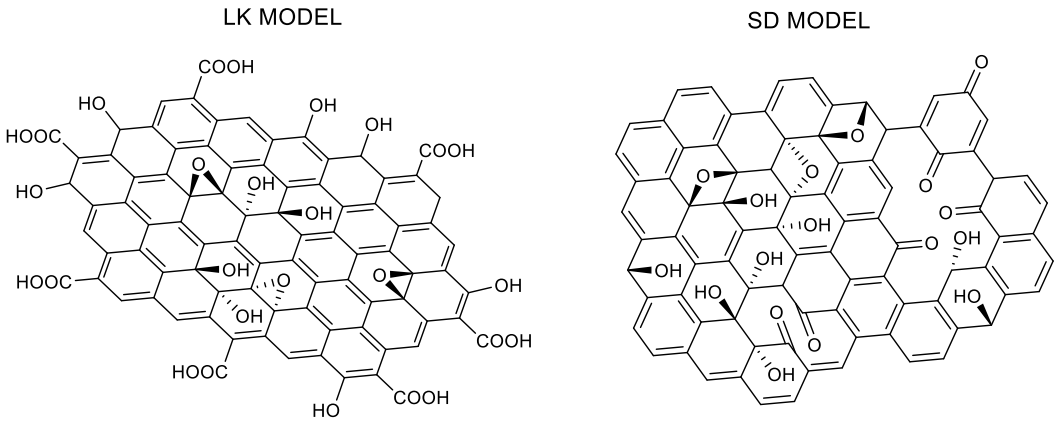

Fig. 1.5 The LK and SD proposed structural models of GO

Nowadays, the LK model is the most widely accepted model for the structure of GO. Indeed, the randomly distributed domains of sp^2 and sp^3 hybridised carbon have been confirmed by HRTEM by Erickson *et al* (99).

One of the major controversies surrounding the LK model is that it is unable to account for the acidity of GO in aqueous media (100). The only (significantly) acidic functional groups predicted by the LK model are carboxylic acids which are only present in small quantities at the graphene edges. Recently, Dimiev *et*. *al.* suggested that the origin of this acidity could be accounted for by considering the structure of GO in solution as dynamic, readily reacting with water to generate acidic species (100). In this model, C-C bond cleavage occurs between adjacent hydroxyl groups after water deprotonates one of the hydroxyls. The deprotonation results in the formation of acidic functional groups such as enols and vinylogous carboxylic acids (see Fig. 1.6) (100). The acidity is further enhanced under basic conditions since hydroxide is a much stronger base than water and able to initiate the process more effectively. Dimiev *et*. *al*. also propose that highly acidic organosulfate groups exist on GO in significant enough quantities to also contribute to the acidity of GO (100).

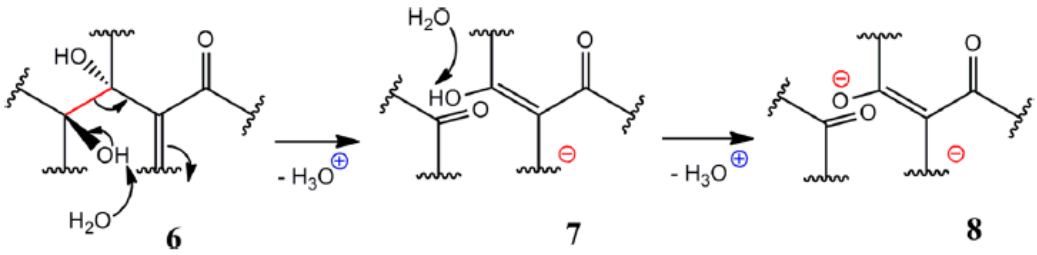

Fig. 1.6 Formation of a vinylogous carboxylic acid by ionization of a tertiary alcohol and C-C bond cleavage. In 6 the C-C bond to be cleaved is represented in red. Structure 7 contains a ketone and a vinylogous carboxylic acid formed as result of C-C bond cleavage. Structure 8 is an ionized form of 7, showing the vinylogous carboxylate. Reprinted with permission from ref (100).

A drastically different model was proposed by Rourke *et. al*. in 2011 in which GO is treated as a two-component model, in stark contrast to all the previously reported one-component models (101; 102). In this model, GO is actually comprised of a relatively unoxidised graphenic backbone (first component) upon which highly oxidised organic fragments, which they term oxidative debris, OD, (second component), is adsorbed onto (101), see Fig. 1.7. It is suggested that a lot of the spectroscopic features observed for GO are actually due to OD, such as the absorption bands in UV-Vis and IR as well as the photoluminescence properties (103). A number of recent research articles have also analysed their findings on the 'factual' basis of the two-component model to explain the luminescence (104), chemistry (105), electroactivity (106) and adsorption (107) behaviour of GO. It should be noted that the notion of OD is not new in the carbon literature, and it has been demonstrated that OD is present on CNTs after acidic oxidation (108; 109). However, in these cases the OD can be justified since CNTs often contain amorphous carbon or defective CNTs which can be easily broken down into small fragments (108-110). Graphite on the other hand, is by definition pristine and therefore does not contain any amorphous carbon from which OD could be formed.

Although the two-component model of GO cannot be completely proven nor disproven, it has probably created the greatest degree of controversy in the GO literature to date (110-116). Indeed, all of the alleged findings of the two-component model can be explained in terms of a one-component model (110).

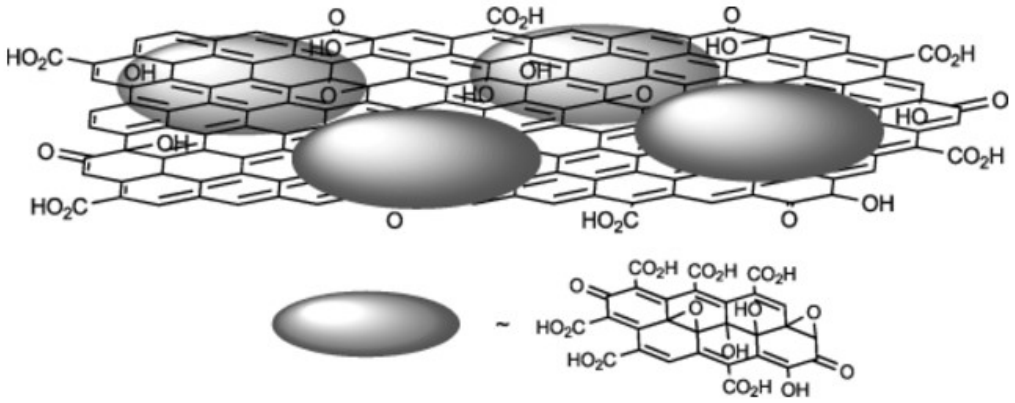

Fig. 1.7 Large oxidatively functionalized graphene-like sheets with surface-bound debris. Note that the graphene-like sheets extend further than depicted. Reprinted with permission from ref (102).

1.3.4 Applications of GO

The applications of GO are extensive, including energy storage (117), electronic (118) and biomedical (119) applications, desalination (120), gas sorption (121), extraction of heavy metals (122), a precursor to graphene (48; 123) and more (124). In fact, a recent review article hinted that the potential of GO may even exceed that of graphene (21).

1.4 Objectives

The primary aims of this thesis are three-fold: (1) to prepare novel (graphenic) carbon nanomaterials as an alternative to conventional GO prepared *via* permanganate oxidation (PM-GO); (2) to understand their structure and chemistry and (3) to explore their potential applications. Overall, it is expected that the investigation into the preparation, characterisation and chemistry of these materials will provide further insight into the structure of carbon materials in general, and even contribute towards the current knowledge on the structure of PM-GO.

The breakdown of this thesis is as follows: In chapter 2, the various characterisation techniques used to characterise the carbon materials are outlined. Chapters 3 to 6 constitute the work undertaken in this thesis; and for each of these chapters, a short

literature review sets the work in context. Chapter 3 is dedicated to the preparation and characterisation of these nanomaterials, whilst chapter 4 examines the thermal annealing behaviour of the materials, which is becoming increasingly relevant in the context of graphene synthesis. Chapter 5 will explore the chemistry of the most promising of these materials, in particular towards nucleophiles such as amines; and likewise chapter 6 will look into the potential applications of the material, such as heavy-metal extraction, which is a hot topic in the literature. Lastly, chapter 7 summarises the work conducted in this thesis and chapter 8 describes the experimental procedures.

1.5 Chapter 1 References

1. Meric I, Han MY, Young AF, Ozyilmaz B, Kim P, Shepard KL. 2008. Current saturation in zero-bandgap, topgated graphene field-effect transistors. *Nat. Nanotechnol.* 3:654-9

2. Jonsson D, Norman P, Ruud K, Agren H, Helgaker T. 1998. Electric and magnetic properties of fullerenes. *J. Chem. Phys.* 109:572-7

3. Ebbesen TW, Lezec HJ, Hiura H, Bennett JW, Ghaemi HF, Thio T. 1996. Electrical conductivity of individual carbon nanotubes. *Nature* 382:54-6

4. Marinho B, Ghislandi M, Tkalya E, Koning CE, de With G. 2012. Electrical conductivity of compacts of graphene, multi-wall carbon nanotubes, carbon black, and graphite powder. *Powder Technol.* 221:351-8

5. Geim AK, Novoselov KS. 2007. The rise of graphene. *Nat. Mater.* 6:183-91

6. Chen ZF, Wu JI, Corminboeuf C, Bohmann J, Lu X, et al. 2012. Is C-60 buckminsterfullerene aromatic? *Phys. Chem. Chem. Phys.* 14:14886-91

7. Wildoer JWG, Venema LC, Rinzler AG, Smalley RE, Dekker C. 1998. Electronic structure of atomically resolved carbon nanotubes. *Nature* 391:59-62

8. Wagoner G. 1964. TURBOSTRATIC GRAPHITE. *Carbon* 1:404-5

9. Li ZQ, Lu CJ, Xia ZP, Zhou Y, Luo Z. 2007. X-ray diffraction patterns of graphite and turbostratic carbon. *Carbon* 45:1686-95

10. Fradkin E. 1986. CRITICAL-BEHAVIOR OF DISORDERED DEGENERATE SEMICONDUCTORS .2. SPECTRUM AND TRANSPORT-PROPERTIES IN MEAN-FIELD THEORY. *Phys. Rev. B* 33:3263-8

11. Novoselov KS, Geim AK, Morozov SV, Jiang D, Zhang Y, et al. 2004. Electric field effect in atomically thin carbon films. *Science* 306:666-9

12. Balandin AA, Ghosh S, Bao W, Calizo I, Teweldebrhan D, et al. 2008. Superior thermal conductivity of single-layer graphene. *Nano. Lett.* 8:902-7

13. Bunch JS, Verbridge SS, Alden JS, van der Zande AM, Parpia JM, et al. 2008. Impermeable atomic membranes from graphene sheets. *Nano. Lett.* 8:2458-62

14. Lee C, Wei X, Kysar JW, Hone J. 2008. Measurement of the elastic properties and intrinsic strength of monolayer graphene. *Science* 321:385-8

15. Koskinen P, Malola S, Hakkinen H. 2009. Evidence for graphene edges beyond zigzag and armchair. *Phys. Rev. B* 80

16. Girit CO, Meyer JC, Erni R, Rossell MD, Kisielowski C, et al. 2009. Graphene at the Edge: Stability and Dynamics. *Science* 323:1705-8

17. Dubois SMM, Lopez-Bezanilla A, Cresti A, Triozon F, Biel B, et al. 2010. Quantum Transport in Graphene Nanoribbons: Effects of Edge Reconstruction and Chemical Reactivity. *ACS Nano* 4:1971-6

18. Koskinen P, Malola S, Hakkinen H. 2008. Self-passivating edge reconstructions of graphene. *Phys. Rev. Lett.* 101

19. Radovic LR, Bockrath B. 2005. On the chemical nature of graphene edges: Origin of stability and potential for magnetism in carbon materials. *J. Am. Chem. Soc.* 127:5917-27

20. Huang B, Liu M, Su NH, Wu J, Duan WH, et al. 2009. Quantum Manifestations of Graphene Edge Stress and Edge Instability: A First-Principles Study. *Phys. Rev. Lett.* 102

21. Eftekhari A, Garcia H. 2017. The necessity of structural irregularities for the chemical applications of graphene. *Today Chem.* 4:1-16

22. Navalon S, Dhakshinamoorthy A, Alvaro M, Garcia H. 2014. Carbocatalysis by Graphene-Based Materials. *Chem. Rev.* 114:6179-212

23. Meyer JC, Kisielowski C, Erni R, Rossell MD, Crommie MF, Zettl A. 2008. Direct Imaging of Lattice Atoms and Topological Defects in Graphene Membranes. *Nano. Lett.* 8:3582-6

24. Stone AJ, Wales DJ. 1986. THEORETICAL-STUDIES OF ICOSAHEDRAL C60 AND SOME RELATED SPECIES. *Chem. Phys. Lett.* 128:501-3

25. Kawai T, Miyamoto Y, Sugino O, Koga Y. 2000. Graphitic ribbons without hydrogen-termination: Electronic structures and stabilities. *Phys. Rev. B* 62:R16349-R52

26. Kim K, Coh S, Kisielowski C, Crommie MF, Louie SG, et al. 2013. Atomically perfect torn graphene edges and their reversible reconstruction. *Nat. Commun.* 4

27. Kobayashi Y, Fukui K, Enoki T, Kusakabe K. 2006. Edge state on hydrogen-terminated graphite edges investigated by scanning tunneling microscopy. *Phys. Rev. B* 73

28. A E, H G. 2017. The necessity of structural irregularities for the chemical applications of graphene In *Today Chem.*, pp. 1-16

29. Jia XT, Campos-Delgado J, Terrones M, Meunier V, Dresselhaus MS. 2011. Graphene edges: a review of their fabrication and characterization. *Nanoscale* 3:86-95

30. Quintana M, Vazquez E, Prato M. 2013. Organic Functionalization of Graphene in Dispersions. *Acc. Chem. Res.* 46:138-48

31. Matsuda K, Nakamura N, Takahashi K, Inoue K, Koga N, Iwamura H. 1995. DESIGN, SYNTHESIS, AND CHARACTERIZATION OF 3 KINDS OF PI-CROSS-CONJUGATED HEXACARBENES WITH HIGH-SPIN (S=6) GROUND-STATES. *J. Am. Chem. Soc.* 117:5550-60

32. He K, Lee GD, Robertson AW, Yoon E, Warner JH. 2014. Hydrogen-free graphene edges. *Nat. Commun.* 5

33. Cruz-Silva E, Jia XT, Terrones H, Sumpter BG, Terrones M, et al. 2013. Edge-Edge Interactions in Stacked Graphene Nanoplatelets. *ACS Nano* 7:2834-41

34. Lee W, Suzuki S, Miyayama M. 2014. Electrode properties of defect-introduced graphene sheets for electrochemical capacitors using aqueous electrolyte. *Electrochim. Acta* 142:240-6

35. Davies TJ, Hyde ME, Compton RG. 2005. Nanotrench arrays reveal insight into graphite electrochemistry. *Angew. Chem. Int. Ed.* 44:5121-6

36. Liu XR, Zheng MT, Xiao K, Xiao Y, He CL, et al. 2014. Simple, green and high-yield production of single- or few-layer graphene by hydrothermal exfoliation of graphite. *Nanoscale* 6:4598-603

37. Kibena E, Mooste M, Kozlova J, Marandi M, Sammelselg V, Tammeveski K. 2013. Surface and electrochemical characterisation of CVD grown graphene sheets. *Electrochem. Commun.* 35:26-9

38. Nam J, Kim DC, Yun H, Shin DH, Nam S, et al. 2017. Chemical vapor deposition of graphene on platinum: Growth and substrate interaction. *Carbon* 111:733-40

39. Cho JH, Gorman JJ, Na SR, Cullinan M. 2017. Growth of monolayer graphene on nanoscale copper-nickel alloy thin films. *Carbon* 115:441-8

40. Wu TR, Zhang XF, Yuan QH, Xue JC, Lu GY, et al. 2016. Fast growth of inch-sized single-crystalline graphene from a controlled single nucleus on Cu-Ni alloys. *Nat. Mater.* 15:43-+

41. Ta HQ, Perello DJ, Duong DL, Han GH, Gorantla S, et al. 2016. Stranski-Krastanov and Volmer-Weber CVD Growth Regimes To Control the Stacking Order in Bilayer Graphene. *Nano Lett.* 16:6403-10

42. Li XS, Colombo L, Ruoff RS. 2016. Synthesis of Graphene Films on Copper Foils by Chemical Vapor Deposition. *Adv. Mater.* 28:6247-52

43. Cabrero-Vilatela A, Weatherup RS, Braeuninger-Weimer P, Caneva S, Hofmann S. 2016. Towards a general growth model for graphene CVD on transition metal catalysts. *Nanoscale* 8:2149-58

44. Deokar G, Avila J, Razado-Colambo I, Codron JL, Boyaval C, et al. 2015. Towards high quality CVD graphene growth and transfer. *Carbon* 89:82-92

45. Ruan GD, Sun ZZ, Peng ZW, Tour JM. 2011. Growth of Graphene from Food, Insects, and Waste. *ACS Nano* 5:7601-7

46. Toh SY, Loh KS, Kamarudin SK, Daud WRW. 2014. Graphene production via electrochemical reduction of graphene oxide: Synthesis and characterisation. *Chem. Eng. J.* 251:422-34

47. De Silva KKH, Huang HH, Joshi RK, Yoshimura M. 2017. Chemical reduction of graphene oxide using green reductants. *Carbon* 119:190-9

48. Zhang HB, Wang JW, Yan Q, Zheng WG, Chen C, Yu ZZ. 2011. Vacuum-assisted synthesis of graphene from thermal exfoliation and reduction of graphite oxide. *J. Mater. Chem.* 21:5392-7

49. Smith RJ, Lotya M, Coleman JN. 2010. The importance of repulsive potential barriers for the dispersion of graphene using surfactants. *New J. Phys* 12

50. Zhou KQ, Shi YQ, Jiang SH, Song L, Hu Y, Gui Z. 2013. A facile liquid phase exfoliation method to prepare graphene sheets with different sizes expandable graphite. *Mater. Res. Bull.* 48:2985-92

51. Xu LX, McGraw JW, Gao F, Grundy M, Ye ZB, et al. 2013. Production of High-Concentration Graphene Dispersions in Low-Boiling-Point Organic Solvents by Liquid-Phase Noncovalent Exfoliation of Graphite with a Hyperbranched Polyethylene and Formation of Graphene/Ethylene Copolymer Composites. *J. Phys. Chem. C* 117:10730-42

52. Schlierf A, Yang HF, Gebremedhn E, Treossi E, Ortolani L, et al. 2013. Nanoscale insight into the exfoliation mechanism of graphene with organic dyes: effect of charge, dipole and molecular structure. *Nanoscale* 5:4205-16

53. Kovtyukhova NI, Wang YX, Berkdemir A, Cruz-Silva R, Terrones M, et al. 2014. Non-oxidative intercalation and exfoliation of graphite by Bronsted acids. *Nat. Chem.* 6:957-63

54. Paton KR, Varrla E, Backes C, Smith RJ, Khan U, et al. 2014. Scalable production of large quantities of defect-free few-layer graphene by shear exfoliation in liquids. *Nat. Mater.* 13:624-30

55. Del Rio-Castillo AE, Merino C, Diez-Barra E, Vazquez E. 2014. Selective suspension of single layer graphene mechanochemically exfoliated from carbon nanofibres. *Nano Research* 7:963-72

56. Berger C, Song ZM, Li XB, Wu XS, Brown N, et al. 2006. Electronic confinement and coherence in patterned epitaxial graphene. *Science* 312:1191-6

57. Abdelkader AM, Kinloch IA, Dryfe RAW. 2014. Continuous Electrochemical Exfoliation of Micrometer-Sized Graphene Using Synergistic Ion Intercalations and Organic Solvents. *ACS Appl. Mater. Interfaces* 6:1632-9

58. Viculis LM, Mack JJ, Kaner RB. 2003. A chemical route to carbon nanoscrolls. *Science* 299:1361-

59. Cai JM, Ruffieux P, Jaafar R, Bieri M, Braun T, et al. 2010. Atomically precise bottom-up fabrication of graphene nanoribbons. *Nature* 466:470-3

60. Jiang L, Niu TC, Lu XQ, Dong HL, Chen W, et al. 2013. Low-Temperature, Bottom-Up Synthesis of Graphene via a Radical-Coupling Reaction. *J. Am. Chem. Soc.* 135:9050-4

61. Munoz R, Gomez-Aleixandre C. 2013. Review of CVD Synthesis of Graphene. *Chem. Vap. Deposition* 19:297-322

62. Geng DC, Wang HP, Yu G. 2015. Graphene Single Crystals: Size and Morphology Engineering. *Adv. Mater.* 27:2821-37

63. Ma T, Ren WC, Liu ZB, Huang L, Ma LP, et al. 2014. Repeated Growth-Etching-Regrowth for Large-Area Defect-Free Single-Crystal Graphene by Chemical Vapor Deposition. *ACS Nano* 8:12806-13

64. Lin L, Liu ZF. 2016. GRAPHENE SYNTHESIS On-the-spot growth. *Nat. Mater.* 15:9-10

65. Li XS, Cai WW, An JH, Kim S, Nah J, et al. 2009. Large-Area Synthesis of High-Quality and Uniform Graphene Films on Copper Foils. *Science* 324:1312-4

66. Yan Z, Peng ZW, Tour JM. 2014. Chemical Vapor Deposition of Graphene Single Crystals. *Acc. Chem. Res.* 47:1327-37

67. Brodie B. 1859. On the Atomic Weight of Graphite. *Philos. Trans. R. Soc. London* 149:249-59

68. Staudenmaier L. 1898. Verfahren Zur Darstellung Der Graphitsaure. *Ber. Dtsch. Chem. Ges.* 21:1481-7

69. Hummers WS, Offeman RE. 1958. PREPARATION OF GRAPHITIC OXIDE. *J. Am. Chem. Soc.* 80:1339-

70. Charpy G. 1909. Sur la formation de l'oxyde graphitique et la définition du graphite C. R. . *Hebd. Séances Acad. Sci* 148:920-3

71. Chen J, Yao BW, Li C, Shi GQ. 2013. An improved Hummers method for eco-friendly synthesis of graphene oxide. *Carbon* 64:225-9

72. Dimiev A, Kosynkin DV, Alemany LB, Chaguine P, Tour JM. 2012. Pristine Graphite Oxide. *J. Am. Chem. Soc.* 134:2815-22

73. Chen J, Zhang Y, Zhang M, Yao BW, Li YR, et al. 2016. Water-enhanced oxidation of graphite to graphene oxide with controlled species of oxygenated groups. *Chem. Sci.* 7:1874-81

74. Marcano DC, Kosynkin DV, Berlin JM, Sinitskii A, Sun Z, et al. 2010. Improved Synthesis of Graphene Oxide. *ACS Nano* 4:4806-14

75. Chandra S, Sahu S, Pramanik P. 2010. A novel synthesis of graphene by dichromate oxidation. *Mater. Sci. Eng., B* 167:133-6

76. Peng L, Xu Z, Liu Z, Wei YY, Sun HY, et al. 2015. An iron-based green approach to 1-h production of single-layer graphene oxide. *Nat. Commun.* 6

77. Wojtoniszak M, Mijowska E. 2012. Controlled oxidation of graphite to graphene oxide with novel oxidants in a bulk scale. *J. Nanopart. Res.* 14

78. Chattopadhyay J, Mukherjee A, Hamilton CE, Kang J, Chakraborty S, et al. 2008. Graphite epoxide. *J. Am. Chem. Soc.* 130:5414-+

79. Higginbotham AL, Kosynkin DV, Sinitskii A, Sun ZZ, Tour JM. 2010. Lower-Defect Graphene Oxide Nanoribbons from Multiwalled Carbon Nanotubes. *ACS Nano* 4:2059-69

80. Eigler S, Dimiev A. 2017. Functionalization and Reduction of Graphene Oxide. In *Graphene Oxide. Fundamental and Applications*. London: Wiley and Sons

81. Lowe SE, Zhong YL. 2017. Challenges of Industrial-Scale Graphne Oxide Production. In *Graphene Oxide: Fundamentals and Applications*, ed. A Dimiev, S Eigler. London: Wiley and Sons. Number of.

82. Yuan R, Yuan J, Wu YP, Chen L, Zhou HD, Chen JM. 2017. Efficient synthesis of graphene oxide and the mechanisms of oxidation and exfoliation. *Appl. Surf. Sci.* 416:868-77

83. Dimiev AM, Tour JM. 2014. Mechanism of Graphene Oxide Formation. *ACS Nano* 8:3060-8

84. Dimiev AM, Bachilo SM, Saito R, Tour JM. 2012. Reversible Formation of Ammonium Persulfate/Sulfuric Acid Graphite Intercalation Compounds and Their Peculiar Raman Spectra. *ACS Nano* 6:7842-9

85. Eklund PC, Olk CH, Holler FJ, Spolar JG, Arakawa ET. 1986. Raman scattering study of the staging kinetics in the c-face skin of pyrolytic graphite- H2SO4. *J. Mater. Res.* 1:361-7

86. Yosida Y, Tanuma S, Okabe K. 1990. INSITU OBSERVATION OF X-RAY-DIFFRACTION IN A SYNTHESIS OF H2SO4-GICS. *Synth. Met.* 34:341-6

87. Royer DJ. 1961. EVIDENCE FOR THE EXISTENCE OF THE PERMANGANYL ION IN SULPHURIC ACID SOLUTIONS OF POTASSIUM PERMANGANATE. *J. Inorg. Nucl. Chem.* 17:159-67

88. Dzhabiev TS, Denisov NN, Moiseev DN, Shilov AE. 2005. Formation of ozone during the reduction of potassium permanganate in sulfuric acid solutions. *Russ. J. Phys. Chem.* 79:1755-60

89. Dreyer DR, Park S, Bielawski CW, Ruoff RS. 2010. The chemistry of graphene oxide. *Chem. Soc. Rev.* 39:228-40

90. Dimiev A. 2017. Mechanism of Formation and Chemical Structure of Graphene Oxide. In *Graphene Oxide: Fundamentals and Applications*. London: Wiley and Sons. Number of.

91. Brimacombe JS, Foster AB, Hancock EB, Overend WG, Stacey M. 1960. ASPECTS OF STEREOCHEMISTRY .3. ACIDIC AND BASIC HYDROLYSIS OF SOME DIOL CYCLIC SULPHATES AND RELATED COMPOUNDS. *J. Am. Chem. Soc.*:201-11

92. Eigler S, Dotzer C, Hof F, Bauer W, Hirsch A. 2013. Sulfur Species in Graphene Oxide. *Chem. A. Eur. J.* 19:9490-6

93. Hofmann U, Holst R. 1939. Über die Säurenatur und die Methylierung von Graphitoxyd. *Ber. Dtsch. Chem. Ges.* 72:754-71

94. Hofmann VU, König E. 1937. Untersuchungen über Graphitoxyd. *Zeitsch. Anorg. Allg. Chem.* 234:311-36

95. Lerf A, He HY, Forster M, Klinowski J. 1998. Structure of graphite oxide revisited. *J. Phys. Chem. B* 102:4477-82

96. Szabo T, Berkesi O, Forgo P, Josepovits K, Sanakis Y, et al. 2006. Evolution of surface functional groups in a series of progressively oxidized graphite oxides. *Chem. Mater.* 18:2740-9

97. Clause A, Plass R, Boehm HP, Hofmann U. 1957. Untersuchungen zur Struktur des Graphitoxyds. *Z. Anorg. Allg. Chem.* 291:205-20

98. Scholz W, Boehm HP. 1969. Betrachtungen zur Struktur des Graphitoxids. *Z. Anorg. Allg. Chem.* 369:327-40

99. Erickson K, Erni R, Lee Z, Alem N, Gannett W, Zettl A. 2010. Determination of the Local Chemical Structure of Graphene Oxide and Reduced Graphene Oxide. *Adv. Mater.* 22:4467-72

100. Dimiev AM, Alemany LB, Tour JM. 2013. Graphene Oxide. Origin of Acidity, Its Instability in Water, and a New Dynamic Structural Model. *ACS Nano* 7:576-88

101. Rourke JP, Pandey PA, Moore JJ, Bates M, Kinloch IA, et al. 2011. The Real Graphene Oxide Revealed: Stripping the Oxidative Debris from the Graphene-like Sheets. *Angew. Chem. Int. Ed.* 50:3173-7

102. Thomas HR, Day SP, Woodruff WE, Valles C, Young RJ, et al. 2013. Deoxygenation of Graphene Oxide: Reduction or Cleaning? *Chem. Mater.* 25:3580-8

103. Thomas HR, Valles C, Young RJ, Kinloch IA, Wilson NR, Rourke JP. 2013. Identifying the fluorescence of graphene oxide. *J. Mater. Chem. C* 1:338-42

104. Hu CF, Liu YL, Yang YH, Cui JH, Huang ZR, et al. 2013. One-step preparation of nitrogen-doped graphene quantum dots from oxidized debris of graphene oxide. *J. Mater. Chem. B* 1:39-42

105. Faria AF, Martinez DST, Moraes ACM, da Costa M, Barros EB, et al. 2012. Unveiling the Role of Oxidation Debris on the Surface Chemistry of Graphene through the Anchoring of Ag Nanoparticles. *Chem. Mater.* 24:4080-7

106. Bonanni A, Ambrosi A, Chua CK, Pumera M. 2014. Oxidation Debris in Graphene Oxide Is Responsible for Its Inherent Electroactivity. *ACS Nano* 8:4197-204

107. Coluci VR, Martinez DST, Honorio JG, de Faria AF, Morales DA, et al. 2014. Noncovalent Interaction with Graphene Oxide: The Crucial Role of Oxidative Debris. *J. Phys. Chem. C* 118:2187-93

108. Salzmann CG, Llewellyn SA, Tobias G, Ward MAH, Huh Y, Green MLH. 2007. The role of carboxylated carbonaceous fragments in the functionalization and spectroscopy of a single-walled carbon-nanotube material. *Adv. Mater.* 19:883-+

109. Verdejo R, Lamoriniere S, Cottam B, Bismarck A, Shaffer M. 2007. Removal of oxidation debris from multi-walled carbon nanotubes. *Chem. Commun.*:513-5

110. Dimiev AM, Polson TA. 2015. Contesting the two-component structural model of graphene oxide and reexamining the chemistry of graphene oxide in basic media. *Carbon* 93:544-54

111. Dave SH, Gong CC, Robertson AW, Warner JH, Grossman JC. 2016. Chemistry and Structure of Graphene Oxide via Direct Imaging. *ACS Nano* 10:7515-22

112. Chen XX, Chen BL. 2016. Direct Observation, Molecular Structure, and Location of Oxidation Debris on Graphene Oxide Nanosheets. *Environ. Sci. Technol.* 50:8568-77

113. Naumov A, Grote F, Overgaard M, Roth A, Halbig CE, et al. 2016. Graphene Oxide: A One- versus Two-Component Material. *J. Am. Chem. Soc.* 138:11445-8

114. Guo Z, Wang S, Wang G, Niu Z, Yang J, Wu W. 2014. Effect of oxidation debris on spectroscopic and macroscopic properties of graphene oxide. *Carbon* 76:203-11

115. Rourke JP, Wilson NR. 2016. Letter to the Editor: A defence of the two-component model of graphene oxide. *Carbon* 96:339-41

116. Rodriguez-Pastor I, Ramos-Fernandez G, Varela-Rizo H, Terrones M, Martin-Gullon I. 2015. Towards the understanding of the graphene oxide structure: How to control the formation of humic- and fulvic-like oxidized debris. *Carbon* 84:299-309

117. Wu ZS, Zhou GM, Yin LC, Ren W, Li F, Cheng HM. 2012. Graphene/metal oxide composite electrode materials for energy storage. *Nano Energy* 1:107-31

118. Eda G, Fanchini G, Chhowalla M. 2008. Large-area ultrathin films of reduced graphene oxide as a transparent and flexible electronic material. *Nat. Nanotechnol.* 3:270-4

119. Chung C, Kim YK, Shin D, Ryoo SR, Hong BH, Min DH. 2013. Biomedical Applications of Graphene and Graphene Oxide. *Acc. Chem. Res.* 46:2211-24

120. You Y, Sahajwalla V, Yoshimura M, Joshi RK. 2016. Graphene and graphene oxide for desalination. *Nanoscale* 8:117-9

121. Srinivas G, Burress JW, Ford J, Yildirim T. 2011. Porous graphene oxide frameworks: Synthesis and gas sorption properties. *J. Mater. Chem.* 21:11323-9

122. Zhao GX, Li JX, Ren XM, Chen CL, Wang XK. 2011. Few-Layered Graphene Oxide Nanosheets As Superior Sorbents for Heavy Metal Ion Pollution Management. *Environ. Sci. Technol.* 45:10454-62

123. Stankovich S, Dikin DA, Piner RD, Kohlhaas KA, Kleinhammes A, et al. 2007. Synthesis of graphene-based nanosheets via chemical reduction of exfoliated graphite oxide. *Carbon* 45:1558-65

124. Zhu YW, Murali S, Cai WW, Li XS, Suk JW, et al. 2010. Graphene and Graphene Oxide: Synthesis, Properties, and Applications. *Adv. Mater.* 22:3906-24

Chapter 2: Characterisation Techniques

In this chapter a brief description of the techniques used to characterise carbon nanomaterials is reported. These include spectroscopic and non-spectroscopic techniques as well as imaging methods, and are mentioned in the order in which they appear in the upcoming results chapters of this thesis.

2.1 X-ray Photoelectron Spectroscopy (XPS)

XPS is an ionisation, surface-sensitive technique in which monochromatic X-rays, typically from an AlK_{α} source (λ = 1486.6 eV), are directed at a sample resulting in the emission of its electrons (photoelectrons) which are then detected *c.f.* Fig. 2.1(a)). From this, the elemental composition (excluding hydrogen and helium) and oxidation states of those elements can be determined.

If an X-ray photon interacts with one of the sample's electrons, exceeding its ionisation energy, the electron will be ejected and the difference in energy between the energy of the photon and the binding energy (B.E.) of the electron will be the kinetic energy (K.E.) which is conferred to the electron. This is described by equation 2.1. Note that a small correction ($\phi_{spectrometer}$) needs to be made to correct for the slight loss in K.E. that occurs when the photoelectron interacts with the detector (1).

$$E_{K.E.} = h\nu - E_{B.E.} - \phi_{spectrometer} \qquad [2.1]$$

Electrons which are situated closer to the nucleus will have higher B.E. (and therefore lower K.E.), hence the exact orbital from which electrons have emanated from will be known. Likewise, the B.E. of electrons in the same orbital will be different for different elements as a consequence of the effective nuclear charge. By consideration of the relative sensitivity of the photoelectrons (which will be dependent on factors such as the element's cross section and orbital type), elemental quantification is made possible. Furthermore, given that the B.E. of an electron is influenced by the oxidation state of the element it resides in, the oxidation state of the element can also be determined by analysing the high resolution spectrum of the element in question (2).

Although the XPS spectrum is mainly built up from incident electrons (which can be either elastically or inelastically scattered, *c.f.* Fig. 2.1), secondary electrons emitted during a photoelectron event are also very common. The most notable of which are Auger electrons (Fig. 2.1(b)) which occur when a vacancy left behind by an exiting photoelectron is filled by a higher energy electron, resulting in the simultaneous transfer of this energy difference to a third electron (Auger electron), resulting in its emission. The K.E. of this Auger electron is hence independent of the X-ray photon, and is equal to the difference between the energy transferred to it and its own B.E (1).

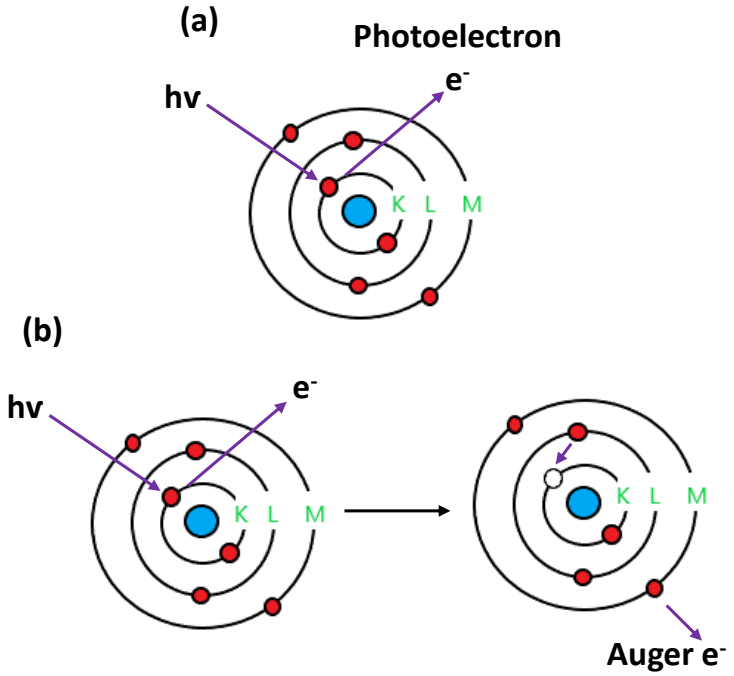

Fig. 2.1(a) ejection of a photoelectron whose K.E. is dependent on the energy of the photon and (b) emission of an Auger electron whose K.E. is independent on the energy of the photon

It was mentioned earlier that XPS is a surface sensitive technique. Whilst X-rays are well known to penetrate deeply into a sample, the inelastic mean free path (IMFP) of an electron is much shorter < 10 nm. Hence there will be a significantly stronger contribution from electrons exiting from the surface than in the bulk. The consequence of this is that surface contaminants are strongly enhanced in XPS. This is typically overcome by etching away the surfaces of samples (*i.e.* with Ar^+ ions) to reveal the true identity of the sample beneath.

In this thesis, XPS measurements were carried out on a Thermo Scientific K-Alpha XPS machine with a monochromated Al K_α source (E=1486.6 eV), a double focusing 180

degree hemisphere analyser of ~125 mm radius and detected with a 18 channel position-sensitive detector. A dual-beam flood gun (electrons and argon ions) was used to compensate for charge accumulation on the measured surfaces. All carbon samples were pressed onto an indium substrate before analysis to ensure no other background contributions from other carbon sources. Survey scans (which refers to the full scan range, encompassing all the potential elements present), were collected 3 times and coadded with a resolution of 1 eV and pass energy of 200 eV. High-resolution elemental regions were scanned 10 times with a resolution of 0.1 eV and pass energy of 50 eV. Both the survey and elemental scans were recorded with a 50 ms dwell time and 400 µm spot size. To ensure the spectrometer was calibrated, graphite flakes and elemental gold were measured and the C1s and $Au4f_{7/2}$ peaks were centered at 284.5 and 84.0 eV respectively.

Survey spectra were utilised for the relative elemental quantification of the samples. An example XPS survey spectrum of carboxylated graphene nanoflakes (cx-GNFs) treated with Pb^{2+} cations resulting in the precipitation of Pb^{2+}@GNFs can be shown in Fig. 2.2.

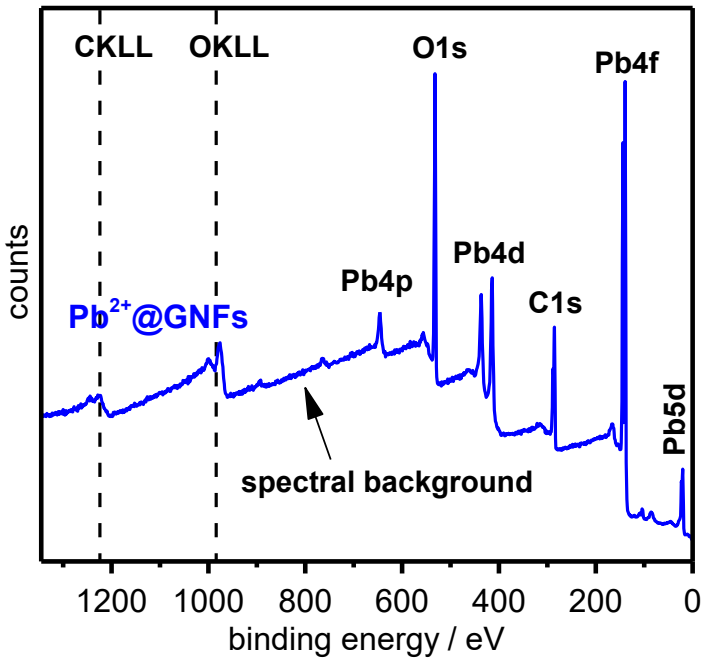

Fig. 2.2 XPS survey spectrum of Pb^{2+}@GNFs

In the case of Pb^{2+}@GNFs in Fig. 2.2, peaks corresponding to photoelectrons emitted from their respective element and orbital can be clearly seen and readily assigned. Auger peaks from carbon (CKLL) and oxygen (OKLL) can also be observed at higher binding energies. For clarity, the spectral background constituting the inelastic processes is also assigned. The intensities of the peaks are related to the relative sensitivities of the

elements/orbitals and hence the Pb4f peaks is the most sensitive to XPS (22.7 times more sensitive than C1s!). Using CASAXPS software (3), the ratios of the elements present can be determined by consideration of these sensitivities. In this way, the Pb/C elemental ratio from the survey spectrum in Fig. 2.2 was found to be 0.16.

XPS high-resolution spectra of the elemental regions are also analysed to gain information on the oxidation states of these elements. In particular, the C1s region is routinely deconvoluted in order to deduce the functional groups present on the material (which correspond to a particular oxidation state). In this work, the elemental regions were initially calibrated against the C-C/C=C peak position at 285.0 eV from the C1s high-resolution spectrum before being deconvoluted using XPSPEAK version 4.1 software (4), using Shirley background functions and Voigt functions for the peak fitting, respectively. Typically, the Voight functions were initially constrained by fixing the Gaussian-Lorentzian (GL) ratio (70% Gaussian) and fixing the peak positions (binding energies) of the peaks. Once the number of peaks has been decided, an iterative process is used to minimise the difference between the sum of the theoretically fitted peaks and experimental area sum respectively (*i.e*. reduce the chi-squared value, to as close to zero as possible). This iteration firstly considers the fitted peak areas and full width at half maximum (FWHM) only. Next, the GL ratio constraint of the fitted peaks is removed and the iterative process is repeated once again to obtain the lowest chi-squared value. This is repeated one last time but now the binding energy constraint has been removed. This order was chosen because the peak positions of the functional groups are the least subjective out of all the other parameters. Hence, fitting should always be considered from most to least known. Once a good fit has been obtained, the parameters are kept for future fits of a similar nature, in order to reduce error.

In the case of Pb^{2+}@GNFs, the XPS high-resolution C1s region can be seen in Fig. 2.3 and has been deconvoluted into three peaks, which can be assigned to the unoxidised sp^2 carbon of the cx-GNFs (285.0 eV) and the Pb-π interaction (286.7 eV) and the Pb-carboxylate interaction (288.2 eV) between the Pb^{2+} cations and the cx-GNFs respectively. Integration of the peaks can be made to quantify the relative amounts of each species, however there will always be some degree of error due to the subjective nature of peak-fitting. In this case, a qualitative description will suffice.

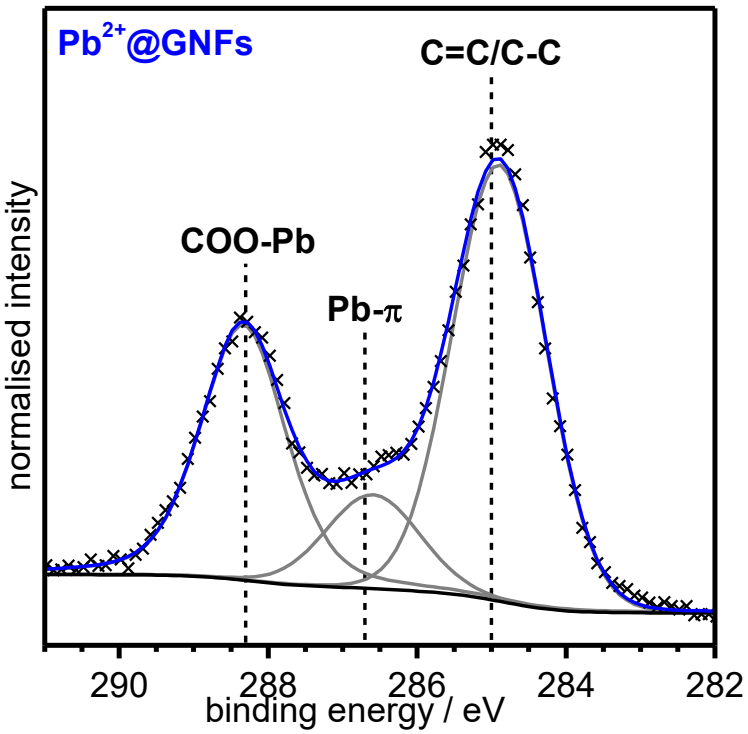

Fig. 2.3 High-resolution XPS C1s spectrum of Pb^{2+}@GNFs. The crosses are the experimental data, grey lines are the fitted peaks, black line is the Shirley background function and the blue line is the peak sum respectively.

2.2 ^{13}C solid-state Nuclear Magnetic Resonance (ssNMR) Spectroscopy

In NMR spectroscopy, a sample is subjected to an external magnetic field causing its NMR active nuclei to align either with (low energy) or against (high energy) the magnetic field, resulting in an energy difference. Consequently, an induced magnetic field is created which can shield or de-shield the nucleus from the applied magnetic field, the extent to which is dependent on the chemical bonding environment (5). For instance, in a C-O bond the more electronegative oxygen atom polarises the electrons in the covalent bond towards itself, resulting in an electron deshielded carbon nucleus and a more shielded oxygen nucleus. These differences in nuclear shielding are detected by NMR, thus providing information on the binding environment of the nucleus and thus the element to which it corresponds to. Furthermore, NMR active nuclei which are near other active nuclei, either through chemical bonds or through space, can interact with each other providing characteristic peak splitting patterns which can be used to elucidate the immediate environment around the nucleus.

NMR relies on the isotropic averaging of spin interactions (6). Whilst this is not an issue for small molecules in solution (due to their rapid tumbling), larger molecules (> 10 kDa) suffer from slow tumbling rates and therefore spin anisotropy results. To perform NMR on these larger molecules, such as the carbon nanomaterials utilised in this thesis, solid state NMR is required. The spin interactions in ssNMR are of course orientation dependent, however the anisotropy can be removed by spinning the sample at a specific angle (known as the magic angle) which is 54.7°. So long as the spinning frequency exceeds the magnitude of anisotropy, the anisotropic effects can be negated (7).

Since carbon materials such as graphene oxide exhibit broad peaks in the ^{13}C ssNMR spectra (due to their amorphous nature), proton decoupling is often employed to remove any ^{13}C-^{1}H interactions which can further complicate the spectra. In this thesis, magic angle spinning (MAS) and high power proton decoupling (HPDEC) were used to acquire ^{13}C ssNMR spectra.

A major advantage of ^{13}C-ssNMR over XPS is that NMR allows the type of functional groups to be more readily determined than in XPS, which only gives information regarding the oxidation states of the elements. For instance, NMR can readily differentiate between sp^2 and sp^3 unoxidised carbon, as can be seen in the NMR spectrum of the cx-GNFs in Fig. 2.4. The ^{13}C-ssNMR spectra of the cx-GNFs exhibits two peaks, one for unoxidised sp^2 carbon at ~130 ppm and the other for carboxylic acids at ~170 ppm. If there had been sp^3 unoxidised carbon present, peaks would appear <50 ppm in the spectrum, which in the case of the cx-GNFs is not observed. XPS on the other hand, cannot differentiate between the two, since the unoxidised carbon atoms in each case are in the C(0) oxidation state.

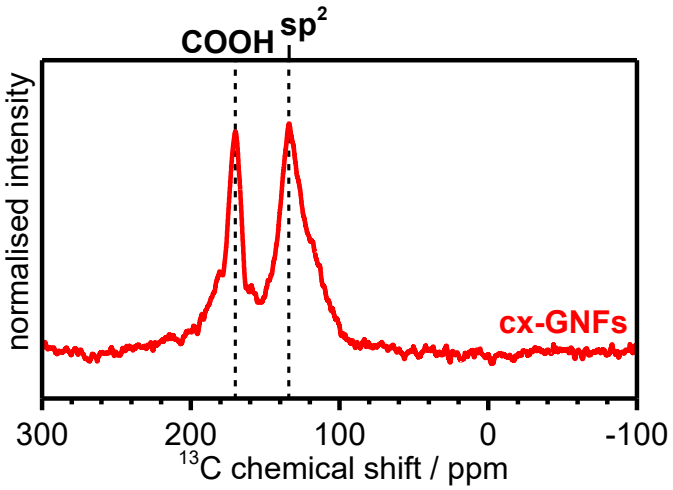

Fig. 2.4 ^{13}C-ssNMR spectra of cx-GNFs

Although ssNMR is incredibly powerful at functional group elucidation, typically ~100 mg of carbon material is required to record a spectrum which can take between 1-3 days to acquire. Furthermore, specialist knowledge of the instrument is necessary to carry out the measurements, making ssNMR a relatively challenging technique. For instance, a typical ^{13}C-ssNMR experiment used in this thesis can be described as follows:

A Bruker Avance 300 spectrometer with 7.05 T wide-bore magnet at ambient probe temperature was used to perform all ^{13}C-solid-state measurements. High-resolution ^{13}C solid-state NMR spectra were recorded at 75.5 MHz with a Bruker 4 mm double-resonance magic-angle spinning (MAS) probe using high-power proton decoupling (HPDEC). Typical operating conditions were a ^{13}C 90°C pulse with a 3.7 μs delay; recycle delay of 120 s with 908 transients. The samples were packed into zirconia rotors of 4 mm external diameter and spun at 12 kHz MAS frequency with a stability greater than ±3 Hz. The ^{13}C chemical shifts are reported with respect to tetramethylsilane (TMS) which was calibrated against an aqueous solution of 4,4-dimethyl-4-silapentane-1-sulfonic acid (DSS, 0 ppm), and glycine (176.46 ppm) respectively.

2.3 Fourier-Transform Infrared (FT-IR) Spectroscopy

FT-IR spectroscopy relies on the interaction of infrared radiation in the region of 4000 to 400 cm^{-1} with matter. The absorption of infrared radiation at these wavelengths results in the excitation of fundamental vibrations which can be attributed to specific functional groups. Quantification of a particular functional group is possible by consideration of the number of photons that is absorbed, analogous to the Beer-Lambert law.

In order for a functional group to be IR-active, there must be a change in dipole-moment (8). In its simplest form, bond vibrations can be described using a simple harmonic oscillator and the fundamental vibrational frequency can be defined by equation 2.2:

$$\nu = \frac{1}{2\pi c}\sqrt{\frac{k}{\mu}} \qquad [2.2]$$

where k is the force constant and μ is the reduced mass of the bond between two atoms of mass m_1 and m_2 respectively:

$$\mu = \frac{m_1 . m_2}{m_1 + m_2} \qquad [2.3]$$

From equations 2.2 and 2.3 it can be seen that the vibrational frequency of a fundamental vibration increases with *k* (which is directly proportional to the bond strength) and decreases with *μ*. Hence strong bonds (double and triple bonds) and bonds between lighter elements will be observed at higher frequencies than single bonds/bonds between heavier elements.

For oxidised carbon nanomaterials, the polar functional groups, notably carbon-oxygen functionality, can be readily probed by IR spectroscopy. Although there is a lot of overlap between functional groups in IR spectra, particularly in the fingerprint region (1500 to 500 cm^{-1}), outside of this region some functional groups can be unequivocally assigned. An example of this are the carboxylic anhydrides which are formed when cx-GNFs are annealed under high-vacuum conditions, *c.f.* Fig. 2.5. The dashed lines represent the carboxylic anhydride functional group (~1780 and 1840 cm^{-1}) which is characteristic at these frequencies (9). This functional group cannot be readily assigned using XPS or NMR techniques.

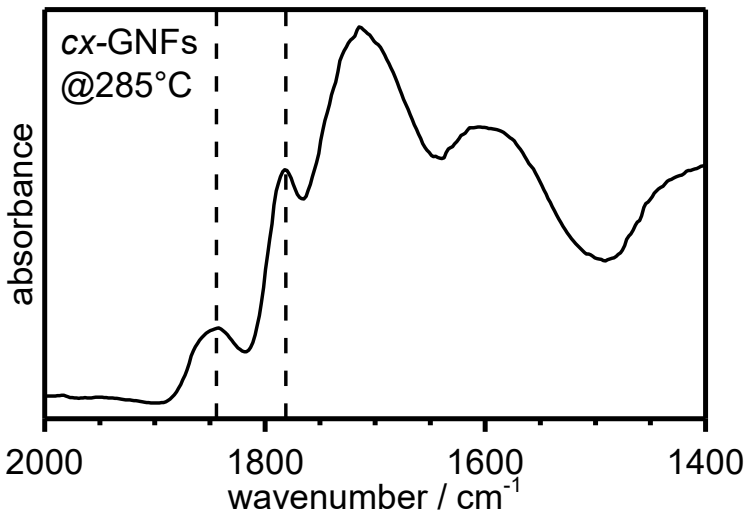

Fig. 2.5 FT-IR spectra of cx-GNFs annealed to 285°C under high-vacuum conditions. Dashed lines illustrate the peak positions of the carboxylic anhydride functional group.

In the work conducted in this thesis, all FT-IR spectra were collected on a Bruker Tensor 27 FTIR spectrometer using the attenuated total reflectance infrared spectroscopy mode (ATR-IR) fitted with a room temperature DLaTGS detector at 4 cm^{-1} resolution and a diamond crystal as the internal reflection element. A background spectrum was allowed to run for 256 scans before recording each sample measurement which were then recorded for the same length of time.

2.4 Raman Spectroscopy

Raman spectroscopy is a light scattering technique which complements FT-IR spectroscopy. Whilst FT-IR relies on a change in dipole-moment, the selection rules for Raman spectroscopy require a change in the polarisability of the molecule (10).

Typically, monochromatic light from the visible region of the electromagnetic spectrum is used in Raman lasers. This results in the excitation of vibrational modes (amongst other processes) to a virtual or non-virtual energy state, which then relaxes back down with the emission of a photon (11). In the vast majority of cases (99.9999%), the emitted photon will be of the same energy as the incident photon (*i.e*. the Raman laser). Hence, mainly elastic processes occur, which are known as Rayleigh scattering. However, in the remainder of cases (0.0001%), inelastic scattering occurs and this is what Raman spectroscopy is concerned with. At room temperature, nearly all molecules are in the ground (v=0) vibrational state, with a minority populating the v=1 vibrational state. This means when inelastic scattering takes place, the molecule will almost always be vibrationally excited from the v=0 level to a virtual (or real) energy state, and relax back down to an excited vibrational level (typically the v=1 state). Thus, the photon emitted will be of lower energy (lower frequency). This is demonstrated in Fig. 2.6, and is referred to as Stokes Raman scattering. The small minority of molecules occupying excited vibrational energy states such as the v=1 level will relax back to the ground state, emitting a photon of higher frequency than was absorbed (known as anti-Stokes Raman scattering) –Fig. 2.6. Note that if the molecule relaxed back down to the v=1 level, the photon would be of the same frequency as the one absorbed, and would also be considered Rayleigh scattering.

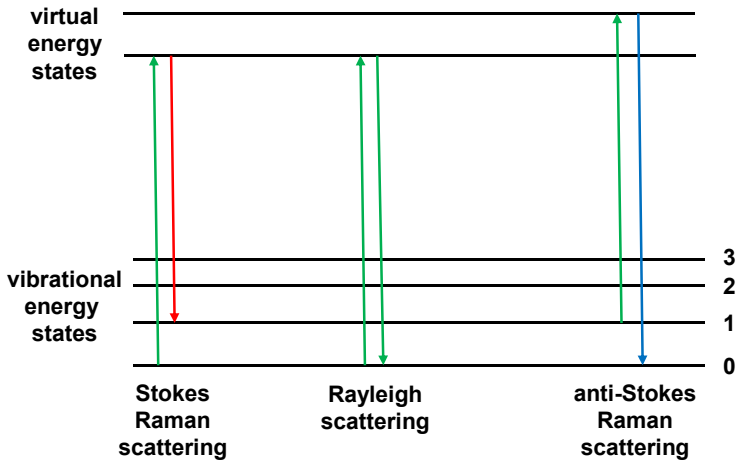

Fig. 2.6 Energy level diagram showing the various transitions that occur during elastic and inelastic light scattering.

Raman spectroscopy measures the change in wavelength between the incident photon and the emitted photon which is known as the Raman shift. Since most of these processes will involve Stokes Raman scattering, Raman spectroscopy essentially probes the Stokes Raman shift. These shifts are very characteristic of specific vibrations (due to the specific energies of vibrational quantum states), and can be assigned to particular functional groups. Hence, Raman spectroscopy can be used to elucidate the functional groups present in a molecule. The true potential in Raman spectroscopy is its ability to compliment FT-IR. Some functional groups are Raman active but not FT-IR active, and *vice versa*; therefore with a combination of both techniques a more accurate description of the sample can be made. It is noteworthy that Raman spectroscopy only works well with non-fluorescent samples. When a sample undergoes fluorescence, the radiative pathway changes and hence the emitting photon will be of a different energy, and although a peak will be observed in the Raman spectrum, it will not correspond to a Raman shift.

In the context of carbon materials, graphene oxides exhibit at least two Raman active bands at ~1350 and 1600 cm^{-1} known as the D and G bands respectively (12). For the Raman spectrum of the cx-GNFs in Fig. 2.7, these can be clearly seen. Moreover, fluorescence, contributing to the relatively high spectral background, can also be identified. The other Raman active bands such as the 2D peak, which is the overtone of the D band, are usually too weak to be observed.

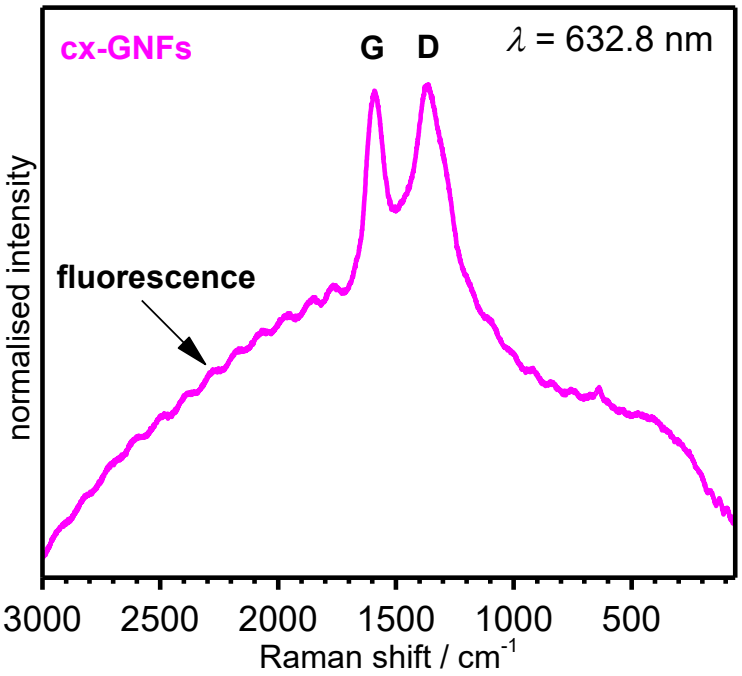

Fig. 2.7 Raman spectrum of cx-GNFs.

In this thesis, all Raman measurements were carried out on a Renishaw Ramascope using a 632.8 nm laser using 50-fold magnification objectives. Each spectrum was scanned for 20 seconds and collected 4 times. The acquired spectra were then calibrated against a Ne discharge lamp.

2.5 Atomic Force Microscopy (AFM)

AFM is a very high resolution imaging technique which provides topographical information of the sample, including its dimensions (vertical and horizontal) and surface roughness.

AFM is typically employed in either contact or tapping mode. In contact mode, a cantilever with a sharp tip (2-12 nm) at the end is brought into contact with the sample surface. A laser is reflected of the back of the cantilever and a feedback loop ensures that the optical path remains constant. The cantilever then scans along the sample surface and the optical path is maintained constant by displacing the sample w.r.t the cantilever. The extent of displacement of the sample allows a topographical image to develop.

An issue with contact mode is that the tip is always in contact with the sample which can cause tip and sample damage, resulting in lower quality images. The alternative, tapping

mode, minimises the contact time between the tip and the sample (by simply tapping the sample), thus minimising damage. In tapping mode, the cantilever is instead oscillated near to its resonant frequency and the sample is brought into contact with the cantilever. At the point of contact the frequency of oscillation will be dampened as a result of interatomic forces (van der Waals, dipole-dipole, electrostatic *etc*.). This change in oscillation is fed back into a feedback loop which controls the height of the cantilever above the sample to ensure a constant oscillation amplitude.

Given the strong adhesive forces between carbon materials and cantilever tips (13), which is in part due to adsorbed layers of water (as a consequence of recording AFM under ambient conditions), tapping mode was utilised in all AFM measurements in this thesis. This was performed using a digital instruments multimode 8 nanoscope scanning probe microscope with a Bruker nanoscope IV controller using an 'E' scanner. Sample preparation typically involved one drop of a ~0.2 mg/mL aqueous dispersion of the carbon nanomaterial being spin coated onto freshly cleaved 'highly oriented pyrolytic graphite' (HOPG) using a Laurell Technologies WS-650 spin-coater (5000 rpm).

An example AFM image of the cx-GNFs deposited onto a HOPG substrate can be seen in Fig. 2.8(a). The height and size distribution of the flakes shown in Figs. 2.8(b)-(c) respectively can be determined from line profiles such as the one in Fig. 2.8(d), which measures a small section of the AFM image in Fig. 2.8(a). AFM line profiles are used throughout this thesis to obtain height and size distributions. Similarly, all AFM analysis in this work was carried out using NanoScope analysis version 1.7 software, and all the recorded raw AFM images were initially 'flattened' with either a first or second order polynomial before performing any analysis on the images. In some cases, the roughness of the AFM image was considered by calculating the image Ra, image Rq and image Rmax, which represent the average, root mean square (RMS) and maximum depth roughness of the entire image respectively.

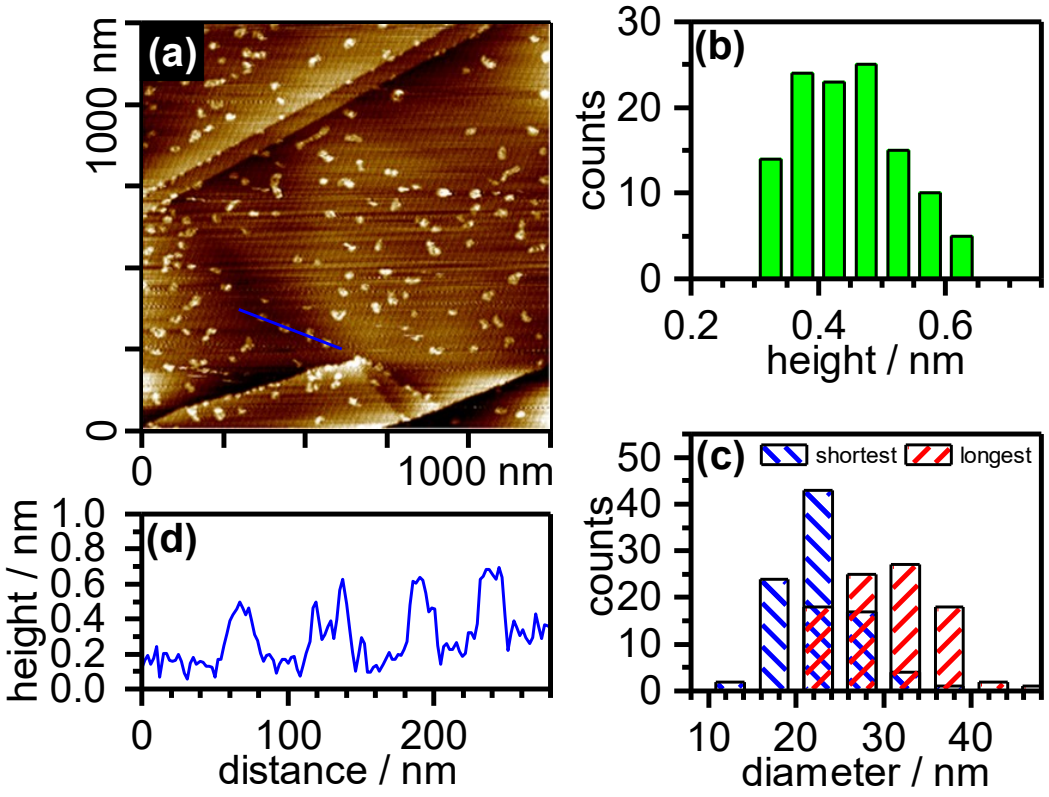

Fig. 2.7 (a) AFM image of cx-GNFs spin coated onto HOPG, (b) height and (c) diameter distribution and (d) line profile of the cx-GNFs taken from the blue line in (a).

2.6 Transmission Electron Microscopy (TEM)

TEM works in a similar way to an optical microscope, using various lenses to focus a beam of electrons (as opposed to light) through a sample. The main advantage of TEM, and electron microscopes in general, over optical microscopes is the shorter de Broglie wavelength of electrons compared with most wavelengths of light. This means that significantly higher resolutions can be achieved with TEM, with the most powerful TEM microscopes able to image individual atoms (14).

However, in order to obtain such high resolution images, TEM is conducted under ultra-high vacuum (UHV) conditions, and must be regularly maintained. Indeed, TEM is amongst the most expensive characterisation methods available to the materials scientist. Furthermore, due to the very high resolution, only small sample sizes can be measured at a time, requiring for a lot of images to be taken to ensure a representative depiction of the sample. Another issue with TEM is that the interaction of electrons with a sample can cause sample damage, which is well known to occur with carbon materials (15).

TEM relies on electrons being absorbed (scattered, diffracted or otherwise) by a sample in order to generate an image (16). The denser the sample, the fewer the electrons which are transmitted through the sample and detected. Hence, these dense samples appear as dark objects in the TEM image, whilst less dense structures appear lighter. In other words, the quality of the image (in terms of contrast) relies on strongly electron absorbing samples. This is of concern where monolayer graphene is concerned since only a relatively small number of electrons will be absorbed by the sample-almost all the electrons transmit through the sample. Hence, good quality images of 2D carbon materials is challenging with TEM alone which is why other imaging techniques such as AFM and SEM are used to back up the images collected by TEM.

For TEM imaging in this thesis, one drop of a ~0.2 mg/mL aqueous dispersion of the carbon nanomaterial was drop coated onto a lacy carbon TEM grid. The TEM measurements were then performed on a Jeol CX100 TEM at 100 kV with a tungsten filament and a Gatan Erlanshen ES500W camera. An example TEM image showing a couple of cx-GNFs can be seen in Fig. 2.9(a). Just like with AFM, line profiles can be used to determine size distributions, *c.f.* Fig. 2.9(b). In this case, Gatan digital micrograph software was used for the data analysis.

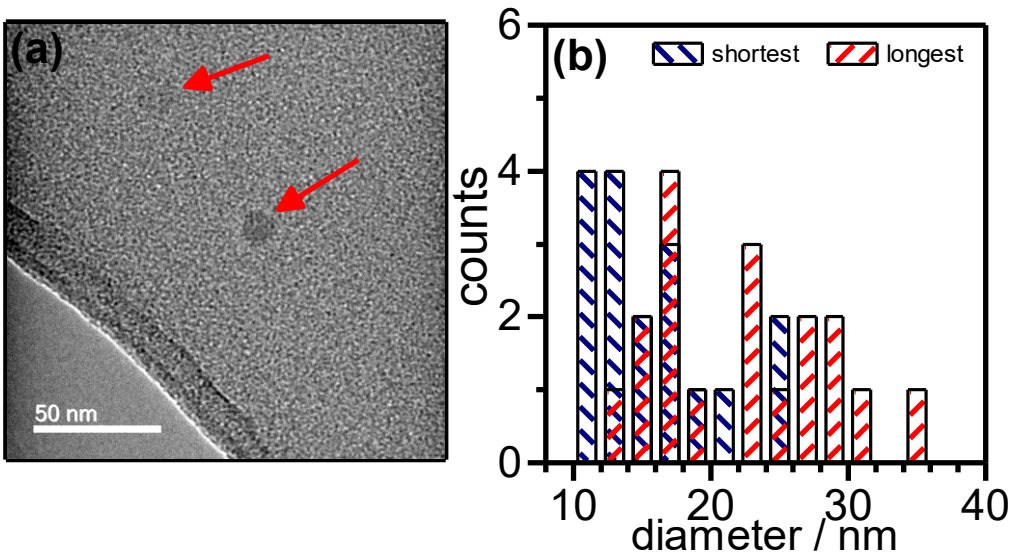

Fig. 2.9 (a) TEM image of two cx-GNFs highlighted by red arrows and (b) diameter distribution of the cx-GNFs as seen in TEM.

2.7 Optical absorbance spectroscopy

Optical absorbance spectroscopy, also commonly referred to as ultraviolet-visible (U.V.-Vis) spectroscopy is the interaction of light in the visible and ultraviolet region with matter. Electromagnetic radiation at these wavelengths has sufficient enough energy to excite the electrons in a sample from the highest occupied molecular orbital (HOMO) to the lowest unoccupied molecular orbital (LUMO) (17). Since electronic states are highly quantised, transitions of this nature occur at very well defined energies, allowing for specific assignments to be made. Under ideal conditions, the absorption of a particular wavelength of light by a sample is directly proportional to the concentration of the sample as described by the Beer-Lambert law, in equation 2.4:

$$A = \log\frac{I_0}{I} = \varepsilon c l \qquad [2.4]$$

where A is the absorbance, I_0 and I are the intensity of the incident and transmitted light respectively (of a particular wavelength), ε is the molar extinction coefficient, c the concentration and l the path length.

Optical absorbance spectroscopy is therefore commonly employed in the quantification of samples of unknown concentration, where the absorbance at a specific frequency of light is known. Graphenic materials absorb strongly in the visible, and particularly the U.V. region of light due to the highly conjugated electrons (and thus overlapping orbitals) which create a multitude of electronic quantum states. Therefore, quantification of graphenic concentrations could (in theory) be calculated readily from any frequency of light.

In this thesis, for example, optical absorbance spectra were used to quantitatively determine the concentration of lead ions extracted by carbon materials. Fig. 2.10 shows the optical absorbance spectrum of the remaining (excess) lead ions after extraction with the cx-GNFs. Given that the concentration of lead ions initially added to the cx-GNFs is known, then the differences in absorbances and thus concentrations, can be related back to a calibration curve which obeys the Beer-Lambert law, and thus the extraction capability of the cx-GNFs can be determined.

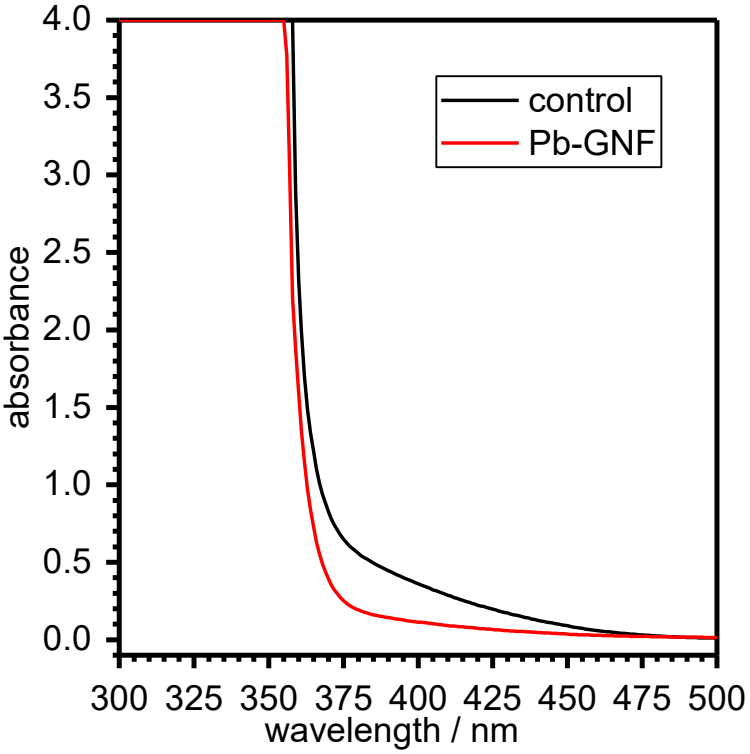

Fig. 2.10 Optical absorbance spectra of lead ions before (black) and after (red) extraction with cx-GNFs. A chelating agent was used to colour the lead solutions before absorbance measurements and the pH was kept constant with dilute HCl. Absorbance values at λ = 400 nm were found to obey the Beer-Lambert equation.

For all optical absorbance spectra undertaken in this thesis, the spectra were recorded in quartz cuvettes (path length = 10 mm) on a PerkinElmer Lambda 365 UV/VIS spectrophotometer at data intervals of 1.0 nm and scan rate of 100 nm min^{-1}.

2.8 Scanning Electron Microscopy (SEM)

SEM, like TEM, is an electron microscopic technique but differs from TEM in that the electron beam is focussed to a tiny point which is then raster scanned across the sample surface. When the electrons interact with the sample, many scattering processes may occur, the detection of which will be dependent on the penetration depth. Secondary electrons, for instance, have short IMFP and therefore only those within a few nm of the surface will be detected (18). These electrons will provide topographical information, as well as surface atomic composition since some these electrons will be Auger electrons. Deeper within the sample, tens of nanometers deep, secondary electrons are no longer

detected and backscattered electrons (BSE) predominate. These provide information regarding the different elements present-heavier elements appearing brighter than lighter elements (19). At depths > 100 nm to several μm, X-rays will still be detected and can provide details on the bulk atomic composition of the sample (*i.e*. EDX), as well as (in some cases) cathodoluminescence (19). For this reason, most SEM instruments have EDX mapping built into them.

SEM has advantages over TEM in that its overall handling and mechanics are much simpler and convenient to use. Samples are also less susceptible to beam damage since the beam is not focussed continuously at one point in the sample. However, SEM samples need to be electrically conducting, otherwise scanning faults may arise as well as artifacts. To overcome this issue with non-conducting samples (such as graphene oxide), gold sputters are used to coat the samples with gold nanoparticles, which serve to increase the conductive properties.

An example SEM image of both amorphous (a-GNFs) and turbostratic GNFs (t-GNFs) can be seen in Fig. 2.11(a) and (b) respectively. Just from a qualitative perspective, it is clear that the morphology of each material is completely different, despite the chemical composition of both materials being identical.

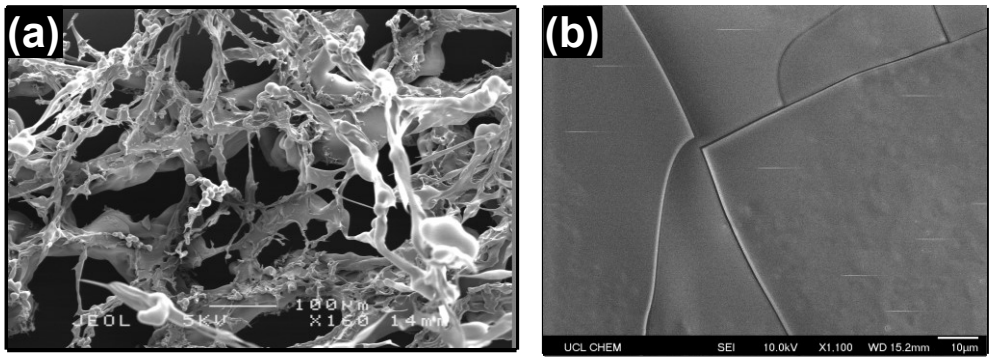

Fig. 2.11 SEM images of (a) a-GNFs and (b) t-GNFs.

It is noteworthy that in this thesis, SEM measurements were carried out on a Jeol JSM-6700F Field emission scanning electron microscope using secondary electron ionisation (SEI). Secondary electrons, backscattered electrons and X-rays are all detected.

2.9 Powder X-ray diffraction (PXRD)

X-ray diffraction is typically employed to elucidate the crystal structure of crystalline materials. The technique relies on utilising monochromatic X-rays of a wavelength similar to the interatomic spacing of lattice planes. As the X-rays interact with the sample, various diffraction processes can occur, but since atoms are regularly arranged in a crystal, specific reflections can take place which can be detected and assigned to a specific lattice plane (20). In order for the reflections to take place, constructive interference between the adjacent lattice planes needs to occur. Given that the spacing between particular planes in a crystal is constant (since crystals are by definition regular in structure), then constructive interference can be defined by equation 2.5, known as Bragg's law.

$$n\lambda = 2dsin\theta \qquad [2.5]$$

where n is an integral multiple of the wavelength λ, d is the interatomic spacing and θ is the angle of the incoming X-ray.

Fig. 2.12 illustrates how equation 2.5 is derived. In order for both X-rays (shown in blue) reflecting of adjacent planes to interfere constructively, the X-ray penetrating deeper into the sample must travel an additional distance equal to 2dsinθ. Where dsinθ (indicated by the red bars) is the additional distance the X-ray have travelled to reach the plane below, and hence the same extra distance again is required to leave the plane.

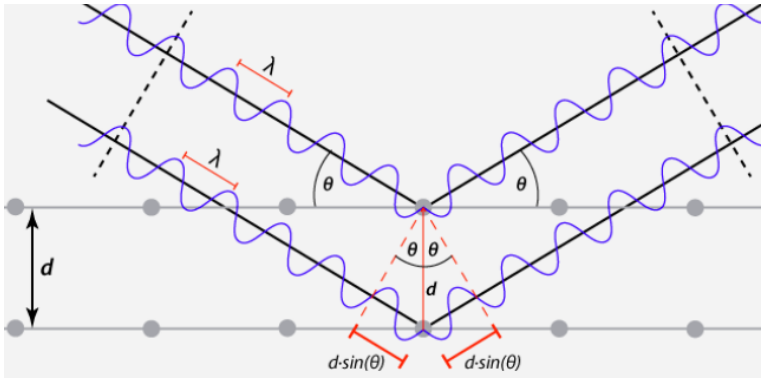

Fig. 2.12 In order for both X-Rays to interfere constructively the X-ray penetrating deeper into the sample must traverse the extra distance equal to 2dsinθ (21). Figure reprinted with permission from reference 19.

It should be noted that in oxidised carbon materials, the disorder produced within the graphenic framework as a direct result of the oxidation, often results in only the peak

associated with the interplanar distance being observed. In this thesis, X-ray diffraction is employed to differentiate between amorphous and turbostratic materials. Turbostratic materials have a permanent rotational and translational misalignment between adjacent layers, yet there exists enough order for broad peaks to be observed in the XRD pattern (22). Fig. 2.13 illustrates the difference between amorphous (a-GNFs) and turbostratic (t-GNFs) cx-GNFs. In the case of t-GNFs, two broad peaks are clearly observed which are absent in the pattern of the a-GNFs. Hence the t-GNFs have some degree of long range order (or pseudo-crystallinity) unlike the a-GNFs.

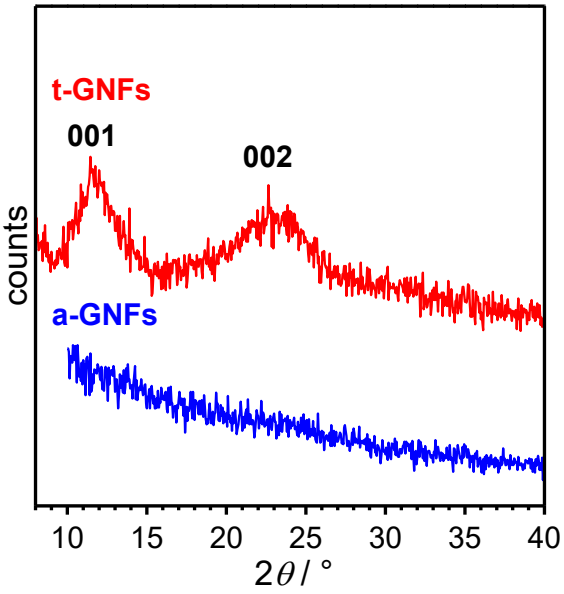

Fig. 2.13 X-ray diffraction patterns of a-GNFs and t-GNFs.

In this work, all XRD measurements were carried out on powder samples using a Bruker D4 Endeavor instrument.

2.10 Brunauer-Emmett-Teller (BET)

BET is widely employed to determine the surface areas of materials. This is done by first degassing the sample (usually above room temperature) and then passing molecular nitrogen gas through the sample at the boiling temperature of liquid nitrogen (77 K). The principle of the technique relies on the nitrogen gas adsorbing and filling all the surface sites (including cavities) within the material (23). The concept itself, is an extension of Langmuir theory, extended to include multilayer adsorption. In this way, $1 / v[(p_0/p) -1]$

can be plotted against (p/p_0), where v is the volume of gas adsorbed, and p_0 and p are the equilibrium and saturation pressures of the adsorbates at the temperature of adsorption (24). The gradient and intercept can then be utilised to calculate the specific surface area (or BET area) of the material. Fig. 2.14 shows an example BET surface area plot of low surface area carbonised cx-GNFs.

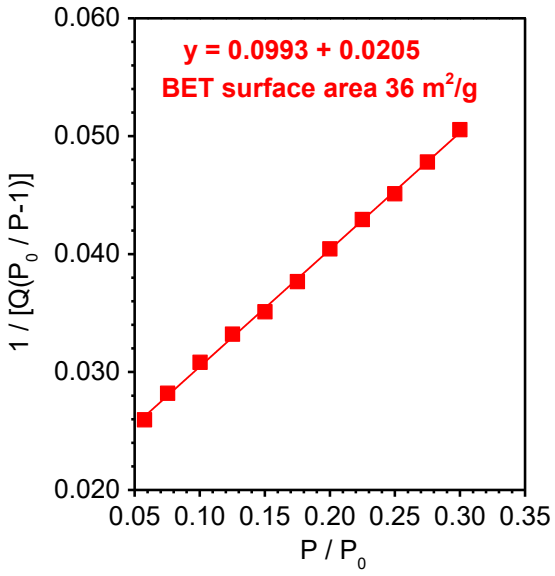

Fig. 2.14 BET surface area of carbonised cx-GNFs.

The BET measurements carried out in this thesis were performed using N_2 in a Micrometrics ASAP 2020 Automatic High Resolution Micropore Physisorption Analyser. The samples were degassed at 80°C (12 h) under vacuum before measurements. The data collected automatically plotted $1 / v[(p_0/p) -1]$ against (p/p_0), where the P/P_0 values between 0.05 and 0.35 are representative of the linear regime.

2.11 Thermogravimetric Analysis (TGA)

TGA involves the precise measurement of the change in a sample's mass as a function of temperature (25). These measurements are usually performed at a constant heating rate (< 10°C.min^{-1}), and can be under inert or reactive conditions. TGA is often employed in carbon composite materials to calculate the degree of chemical functionalisation from the mass loss in the TGA data; and this is what this thesis is concerned with. Other information on physical properties such as phase transitions and sorption processes can also be deduced from TGA. An example TGA plot of the cx-GNFs is shown in Fig. 2.15.

Mass loss over the temperature range initially corresponds to the removal of physisorbed water, followed by the decomposition of the functional groups on the cx-GNFs.

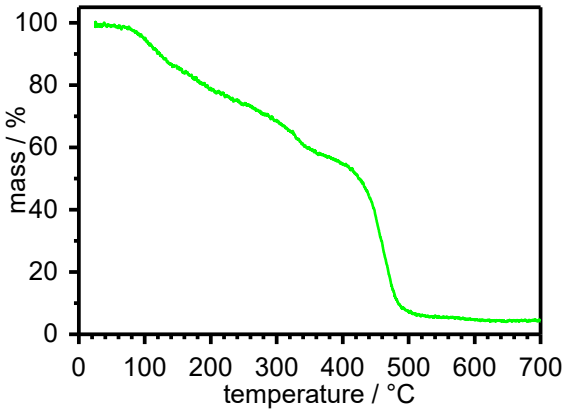

Fig. 2.15 TGA plot of cx-GNFs.

TGA in this thesis was performed in air or oxygen at a heating rate of 3°C or 10°C min^{-1} at a flow rate of 100 $mL.min^{-1}$ on a SETARAM SETSYS 16/18 instrument.

2.12 Mass spectrometry (MS)

MS involves bombarding a chemical species with electrons resulting in its ionisation *via* the stripping of its electrons, typically resulting in monovalent cations. These cations are then accelerated through an electric field and then deflected using a magnetic field (26). Given that the extent of deflection depends on the mass and charge of the species, a pattern of mass / charge or *m*/*z* can be produced. MS is particularly useful in sorting out isotopes of atoms which differ only by mass. Similarly, high-resolution MS can differentiate between molecules of very similar molecular weight, *i.e*. CO and N_2. MS also has its uses in organic chemistry. Complex molecules will give characteristic fingerprint MS patterns as a result of specific fragmentation processes.

In functionalised carbon materials, MS can be used to elucidate the nature of the desorbing gaseous species when the materials are annealed. This will provide insight into the mechanisms which are at play along with the nature and relative stoichiometry of the functional groups present. Fig. 2.16 shows the MS pattern of the gaseous desorbing species when the cx-GNFs are annealed under high-vacuum conditions. The

m/*z* values at 18, 28 and 44 are characteristic of desorbing H_2O, CO and CO_2 respectively.

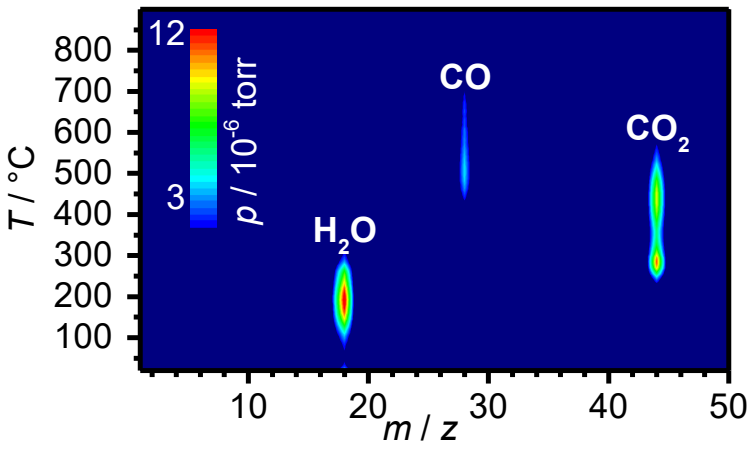

Fig. 2.16 *In-situ* MS pattern of the desorbing gaseous species when the cx-GNFs are annealed under high-vacuum conditions.

In this work, all MS measurements were carried out on a HAL RC 201 mass spectrometer from Hiden Analytical using a Faraday Cup as the detector. Samples were placed inside a quartz tube under high vacuum conditions (<1.5 x 10^{-5} mbar) using a molecular turbo and a double stage rotary vane pump as the backing pump. The sample under vacuum is then placed inside a Carbolite MTF 1200 horizontal tube furnace and heated at 10°C.min^{-1} from ambient temperature to 900°C. The total pressure increases resulting from desorbing gas were monitored *in-situ* as a function of temperature using a PTR225 cold cathode pressure gauge from Leybold. The nature of the gaseous species were analysed with a HAL RC 201 mass spectrometer from Hiden Analytical using a Faraday Cup as the detector by scanning along the 1 to 200 a.m.u mass range every 5°C from room temperature to 900°C. If *ex-situ* IR spectra were also collected then the samples were heated from room temperature to the desired temperature and then immediately cooled back down to room temperature under ambient conditions. IR was then recorded on the sample immediately afterwards.

2.13 Zeta potential

Charged particles in solution exhibit an electrochemical potential which is significantly different from the bulk. The zeta potential, also known as the electrokinetic potential,

quantifies this difference and is defined as the potential difference of the slipping plane of a particle (see Fig. 2.17) relative to the bulk solution (which is considered electrochemically neutral). Typically the zeta potential is measured by applying an electric field across a dispersion, resulting in the migration of the charged particles towards the electrode of opposite charge (27). The velocity at which the particles migrate towards the electrode is proportional to its charge (*i.e*. zeta potential) (27), and since the measured velocity is directly proportional to the particle's (electrophoretic) mobility as described by equation 2.6, then the zeta potential can be calculated from the electrophoretic mobility by rearranging equation 2.7 (27).

$$v = \upsilon . E \qquad [2.6]$$

where v is the velocity, υ is the electrophoretic mobility and E is the electric field strength.

$$\upsilon = \frac{4\pi\varepsilon_0\varepsilon_r\zeta(1+\kappa r)}{6\pi\eta} \qquad [2.7]$$

where ε_0 and ε_r are the permittivity of the vacuum and the relative dielectric constant respectively, ζ is the zeta potential, η is the viscosity of the medium, r is the particle radius and κ is the Debye-Huckel parameter which is defined in equation 2.8:

$$\kappa = \left(\frac{2n_0 z^2 e^2}{\varepsilon_0\varepsilon_r k_B T}\right)^{\frac{1}{2}} \qquad [2.8]$$

where n_0 is the bulk ionic concentration, z is the charge on the ion, e is the charge of the electron, k_B is the Boltzmann constant and T is the temperature.

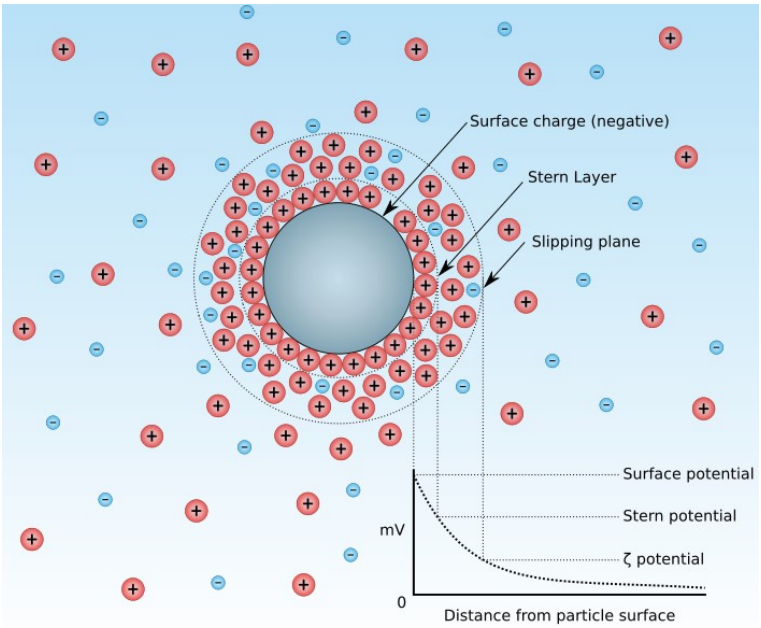

Fig. 2.17 Zeta potential of a particle in dispersion.(28) Figure reprinted with permission from reference 26.

Zeta potential is often employed to determine the stability of a colloidal dispersion. Typically, values exceeding ± 40 mV indicate the colloid is well dispersed, whilst values lower than this suggest the dispersion is less stable and could be prone to aggregation and precipitation (29; 30). Since dispersed carbon materials are colloids, zeta potential can hence be used as a measure of the dispersion's stability. The zeta potential of an aqueous dispersion of 0.1 mg/mL cx-GNFs, shown in Fig. 2.18, was found to be ~-45 mV, illustrating their excellent dispersibility in water. The negative zeta potential is expected due to the many negatively charged carboxylate groups present on the cx-GNFs.

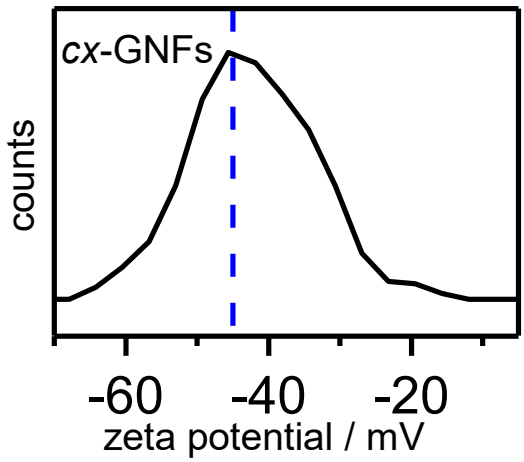

Fig.2.18 Zeta potential distribution of a 0.1 mg/mL aqueous dispersion of cx-GNFs.

In this thesis, zeta potential measurements were carried out on a Malvern Zetasizer Nano (ZEN3600) machine using disposable DTS 1060C plastic cuvettes. All dispersions were diluted to 0.1 $mg.mL^{-1}$ for measuring.

2.14 Chapter 2 References

1. Hufner S. 1995. *Photoelectron Spectroscopy: Principles and Applications*. Springer Verlag

2. Sydlik SA, Swager TM. 2013. Functional Graphenic Materials Via a JohnsonClaisen Rearrangement. *Adv. Funct. Mater.* 23:1873-82

3. http://www.casaxps.com/.

4. http://xpspeak.software.informer.com/4.1/.

5. Pranitha D, Parthiban N, Kumar D, Ghosh S, Banji D, Jana S. 2011. SOLID STATE NUCLEAR MAGNETIC RESONANCE SPECTROSCOPY – A REVIEW. *Asian J. Pharm. Clin. Res.* 4:9-14

6. Schmidt-Rohr K, Wolfgang H. 1994. *Multidimensional Solid-State NMR and Polymers.*: Elsevier

7. Hennel J, Klinowski J. 2005. *New Techniques in solid-state NMR*. Springer-Verlag

8. Paula J, Atkins P. 2009. *Elements of physical chemistry*. pp 459. Oxford: Oxford U.P.

9. Boehm HP. 2002. Surface oxides on carbon and their analysis: a critical assessment. *Carbon* 40:145-9

10. Gardiner DJ. 1989. *Practical Raman spectroscopy*. Springer-Verlag

11. Ferrari AC, Basko DM. 2013. Raman spectroscopy as a versatile tool for studying the properties of graphene. *Nat. Nanotechnol.* 8:235-46

12. Beams R, Cancado LG, Novotny L. 2015. Raman characterization of defects and dopants in graphene. *AIP Adv.* 27

13. Dufrene YF. 2002. Atomic force microscopy, a powerful tool in microbiology. *J. Bacteriol.* 184:5205-13

14. Girit CO, Meyer JC, Erni R, Rossell MD, Kisielowski C, et al. 2009. Graphene at the Edge: Stability and Dynamics. *Science* 323:1705-8

15. Smith BW, Luzzi DE. 2001. Electron irradiation effects in single wall carbon nanotubes. *J. Appl. Phys* 90:3509-15

16. Williams D.B., C.B. C. 1996. The Transmission Electron Microscope. In *Transmission Electron Microscopy*. Boston, MA: Springer. Number of.

17. Perkampus H. 1992. Evaluation of UV-VIS Spectral Bands. In *UV-VIS Spectroscopy and Its Applications.* Berlin, Heidelberg: Springer. Number of.

18. Apkarian R, Joy D. 2006. *Scanning Microscopy for Nanotechnology*. Springer

19. Goldstein GI, Newbury DE, Echlin P, Joy DC, Fiori C, Lifshin E. 1981. *Scanning electron microscopy and x-ray microanalysis*. New York: Plenum Press

20. Clegg W. 1998. *Crystal Structure Determination (Oxford Chemistry Primer)*. Oxford: Oxford University Press

21. *Condition for the constructive interference of waves on a crystal layer. CC BY-NC-ND 3.0 DE.* https://www.didaktik.physik.uni-muenchen.de/elektronenbahnen/elektronenbeugung/einfuehrung/bragg-bedingung.php

22. Wagoner G. 1964. TURBOSTRATIC GRAPHITE. *Carbon* 1:404-5

23. Brunauer S, Emmett PH, Teller E. 1938. Adsorption of gases in multimolecular layers. *J. Am. Chem. Soc.* 60:309-19

24. Sing KSW. 1998. Adsorption methods for the characterization of porous materials. *Adv. Colloid Interface Sci.* 76:3-11

25. Coats AW, Redfern JP. 1963. THERMOGRAVIMETRIC ANALYSIS. *Analyst* 88:906-24

26. Rubakhin SS, Sweedler JV. 2010. *A Mass Spectrometry Primer for Mass Spectrometry Imaging*. 21-49 pp.

27. Sze A, Erickson D, Ren LQ, Li DQ. 2003. Zeta-potential measurement using the Smoluchowski equation and the slope of the current-time relationship in electroosmotic flow. *J. Colloid Interface Sci.* 261:402-10

28. Mjones, LarryisGood. Zeta Potential for a particle in dispersion medium. CC BY 3.0

29. Hanaor D, Michelazzi M, Leonelli C, Sorrell CC. 2012. The effects of carboxylic acids on the aqueous dispersion and electrophoretic deposition of ZrO2. *J. Eur. Ceram. Soc.* 32:235-44

30. Greenwood R, Kendall K. 1999. Selection of suitable dispersants for aqueous suspensions of zirconia and titania powders using acoustophoresis. *J. Eur. Ceram. Soc.* 19:479-88

Chapter 3: Preparation of Novel Carbon Nanomaterials

3.1 The limitations of GO

As noted earlier in the introduction, there are as many protocols for preparing graphene oxide, GO, (using permanganate or otherwise), as there are structural models. Clearly, therefore, the controversy surrounding the chemical structure of GO cannot be overstated (1; 2). In essence, there are two major issues surrounding GO that need to be addressed. The first is that a full comprehension of the mechanism of GO oxidation and preparation needs to be established amongst the scientific community. The utilisation of drastically different oxidising conditions, as well as different forms of graphite, inevitably leads to GOs of variable degrees of oxidation, structure, chemistry and sizes (3-9). The consequence of which is that almost all GO studies are not directly comparable. Even if the same oxidation protocol is used, differing workup and/or isolation procedures can lead to GOs of variable integrity (3). The second issue which needs to be addressed is the absolute structure of GO, regardless of whether its nature is dynamic or not, its structure needs to be fully appreciated. It is noteworthy that different types of GO will have their uses and niches in different applications, and this should not be discouraged, but a clear understanding of how each one is made and what constitutes each material, in terms of functionality, is paramount.

In the near future, the industrial scale preparation of GO will have to be rationalised. Currently there are no (realistic) protocols employed in the literature (in the author's opinion) than can meet this demand. The bottleneck in the workup is the cause for most concern. Repetitive washing, centrifugation, filtration and/or dialysis are required to purify GO, which can then only be isolated (successfully) *via* lyophilisation or vacuum drying. On an industrial scale, most of these steps would ideally have to be excluded. Another concern for industrial scale GO preparation is the sheer amount of toxic manganese (or other) waste that will have to be disposed of. Indeed, one of the most commonly employed preparation protocols in the literature quotes 6 equiv. of permanganate per mass equiv. of graphite (6).

Another area which is increasing in popularity is nano-graphene oxide (nGO), i.e. GO but with lateral dimensions below 100 nm. The interest in nGO has arisen for its potential application in therapeutics (10), cellular imaging and drug delivery,(11) desalination(12) and lithium ion batteries (13). Just like GO, its shortcomings lie in the preparation procedure and the uncertainty of its chemical nature. In fact, the preparation of nGO is even lengthier than conventional GO since GO is often used a precursor to nGO. The nGO is therefore typically synthesised *via* the ultrasonic breakdown of GO which is then centrifuged and decanted to isolate the nGO material (14). In some cases, a pre-oxidation step of the carbon source is initially required (15). Similarly, since the structure of GO remains elusive, the structure of nGO is also a matter of debate amongst the scientific community.

3.2 Outline of chapter

The exploration of new methodologies and top-down approaches towards the preparation of novel carbon nanomaterials are reported in this chapter. In this regard, the preparation and characterisation of three novel carbon nanomaterials are described and benchmarked against conventional permanganate oxidised GO (PM-GO). These are (1) carboxylated graphene nanoflakes (cx-GNFs), a well-defined and less structurally controversial material compared with PM-GO (2); nGO, a nano graphene-oxide which is prepared *via* an eco-friendly protocol and (3) DC-GO, prepared by dichromate oxidation (of graphite) to structurally compare against PM-GO. A schematic illustrating the preparation of each material is shown on in Fig. 3.1, followed by a proposed structural model. The four materials are characterised alongside each other using various spectroscopic and imaging techniques to justify these models. Lastly, individual sections specific to each material are discussed, highlighting the unique nature of each material as well as a more in depth discussion regarding its preparation.

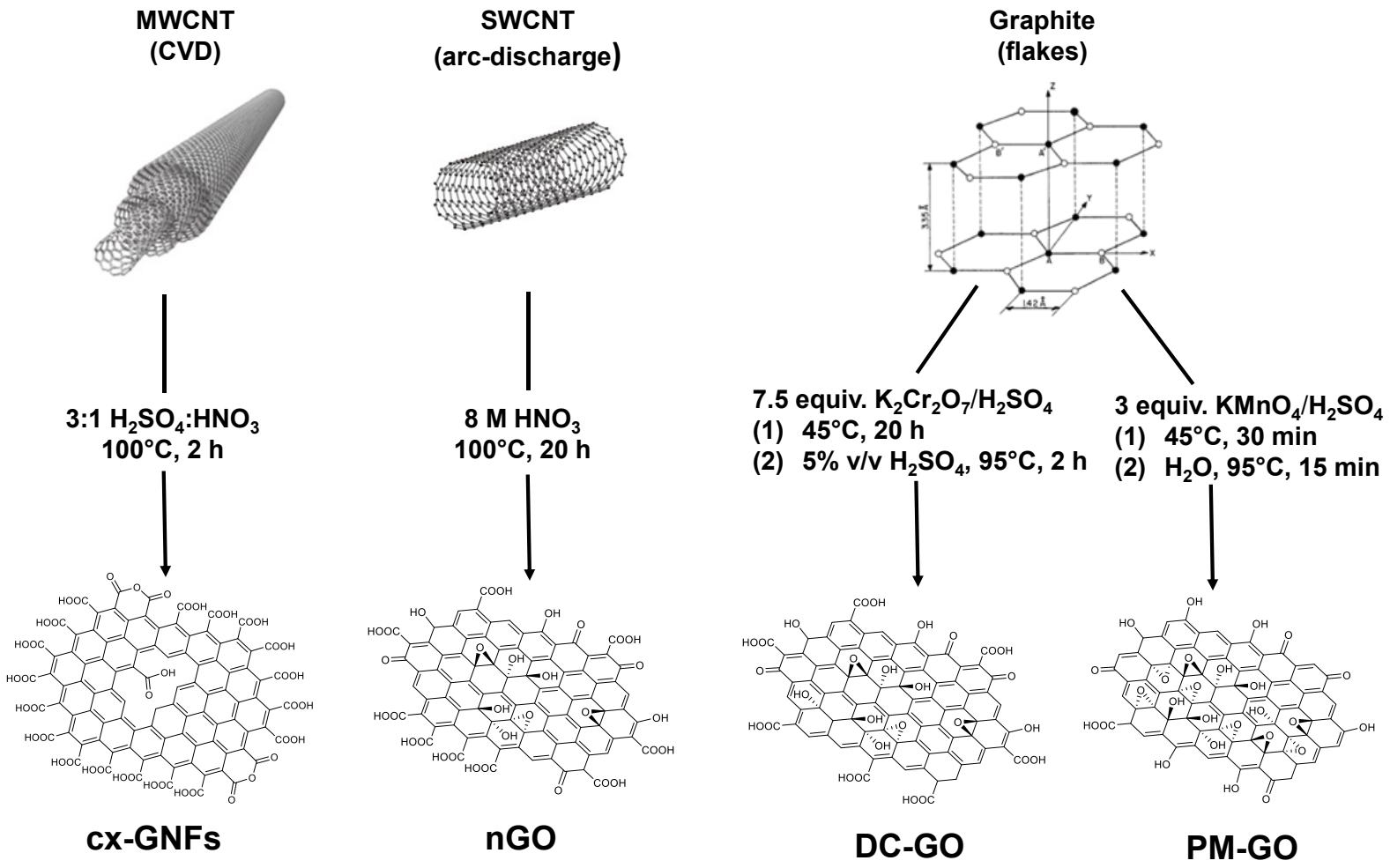

Fig. 3.1 The top-down preparation of carbon nanomaterials and approximate structural models (not to scale), representing the functional groups present. Evidence supporting these structural models will be presented in this chapter.

3.3 Characterisation of novel carbon nanomaterials

A schematic representation showing the top-down preparation of the four carbon materials is shown in Fig. 3.1. The formation of highly carboxylated graphene nanoflakes (cx-GNFs) is the most notable of all the structures. In general, the number of carboxylic acid groups decreases in the order cx-GNFs >> nGO > DC-GO > PM-GO. In the case of the cx-GNFs and the nGO, the intramolecular formation of carboxylic anhydrides is also possible owing to their highly carboxylated nature; this is discussed in detail in Chapter 4. The cx-GNFs are the only material to solely contain unoxidised carbon *i.e.* C(0), and carboxylic acids/anhydrides *i.e.* C(III) species, whilst the other materials display a distribution of carbon in oxidation states between 0 and 3. This makes the cx-GNFs one of the most unique materials in the carbon literature.

3.3.1 Characterisation of carbon materials by XPS and ^{13}C ssNMR spectroscopy

The purity of the four carbon materials is illustrated by the XPS survey spectra in Fig. 3.2 which shows carbon and oxygen as the only elements present; as indicated by the C1s and O1s binding energies (B.E.) at ~285 and ~530 eV respectively, as well as their corresponding Auger peaks at 1224 and 984 eV.

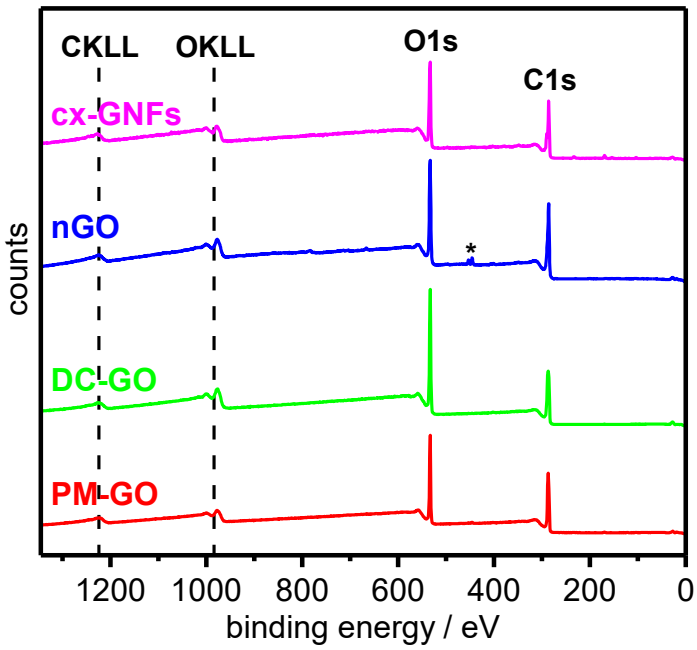

Fig. 3.2 XPS survey spectra of cx-GNFs (magenta), nGO (blue), DC-GO (green) and PM-GO (red). The peak represented by the asterisk is due to the indium substrate.

The high-resolution XPS C1s regions are shown in Fig. 3.3. As expected, the spectrum of the cx-GNFs (magenta) can be deconvolved into two peaks, one corresponding to sp^2 carbon at ~285 eV and the second to C(III) species at ~289 eV, which we attribute to carboxylic acid groups (16-18). By comparison, the other three carbon materials also show these peaks in varying degrees but also clearly exhibit a third peak at ~287 eV which is typically assigned to C(I) species such as alcohols and epoxides (19). The presence of C(II) species such as aldehydes and ketones which appear at ~288 eV are also likely to present on these three carbon materials but not on the cx-GNFs.

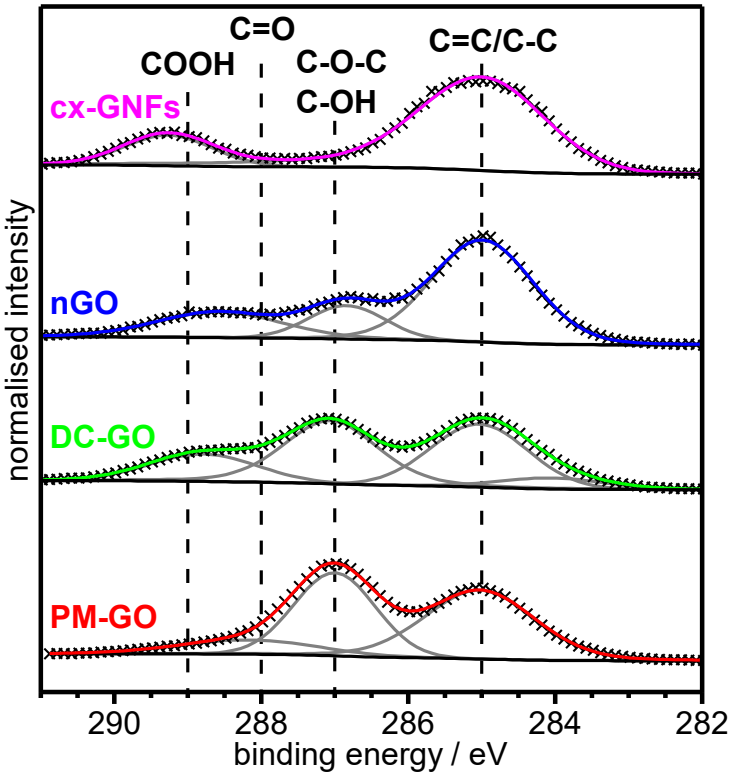

Fig. 3.3 XPS C1s spectra of cx-GNFs (magenta), nGO (blue), DC-GO (green) and PM-GO (red). The crosses represent the experimental data whereas the black, grey and coloured lines are the Shirley background functions, fitted peaks and peak sums, respectively.

It is noteworthy that the interpretation of the XPS C1s region can be subjective, particularly where peak fitting is concerned (20). For instance, C(II) species readily overlap with C(I) and C(III) functionality in the peak fitting process, making it difficult to ascertain their presence with any degree of certainty, let alone concentration. Similarly, carbon bonded to itself in either a sp^2 or sp^3 fashion cannot be distinguished by XPS. In fact, there is increasing evidence to suggest that these assignments are often incorrect in the carbon literature (21). In order to complement XPS, ^{13}C ssNMR spectroscopy was employed to confirm the functional groups present on each carbon material. Fig. 3.4 illustrates the ^{13}C ssNMR spectra of each of the four materials respectively.

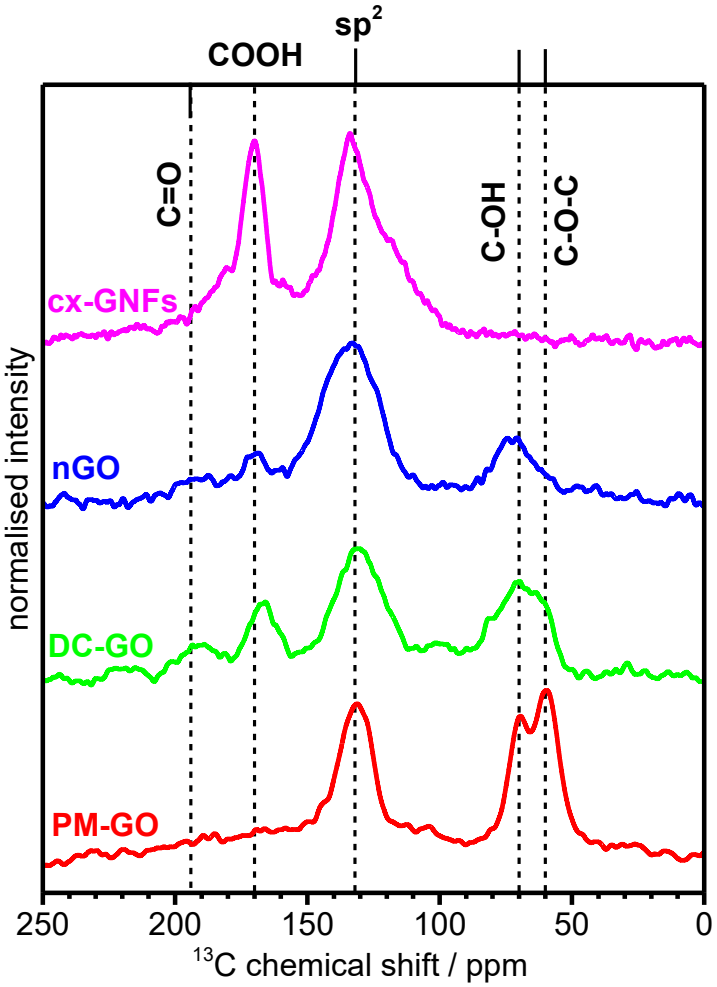

Fig. 3.4 ^{13}C ssNMR spectra of cx-GNFs (magenta), nGO (blue), DC-GO (green) and PM-GO (red).

The ^{13}C ssNMR spectra are in good agreement with the XPS data. The cx-GNFs show two intense peaks at 130 and 170 ppm which can be attributed to unoxidised sp^2 carbon and carboxylic acids respectively (22). The absence of any peak at 60 or 70 ppm is a strong indication that C(I) species (alcohols and epoxides), and hence basal plane functionality, are not present (22). Furthermore, there is no significant feature at 190 ppm suggesting that C(II) species (aldehydes and ketones) are not present in appreciable quantities, if at all. Similarly, the ^{13}C ssNMR spectra of the other three materials agree with the XPS data surprisingly well by the fact that the relative intensities of each feature in ^{13}C ssNMR is reflected in the XPS spectra. Confirmation of C(I) species is certain in these three materials, whilst C(II) and C(III) are not noticeably observed for the PM-GO but apparent in the DC-GO and less significantly in the nGO, as expected. The results align quite nicely with the LK structural model of GO since nGO and DC-GO have significantly smaller flake sizes compared with PM-GO, as will be discussed in section

3.3.3. For instance, the LK model suggests that species such as carboxylic acids and ketones are situated on the flake edge whilst epoxides and hydroxyls are mainly located on the basal plane. Hence the smaller flake size of the nGO and DC-GO would implicate a higher ratio of carboxylic acids/ketones to epoxides/hydroxyls, on account of these two materials having significantly higher edge to basal plane ratios than PM-GO; and this is what is observed.(23) Hence the structural models proposed in Fig. 3.1.

3.3.2 Characterisation of carbon materials by FT-IR and Raman spectroscopy

The IR spectra of the four carbon materials are shown in Fig. 3.5.

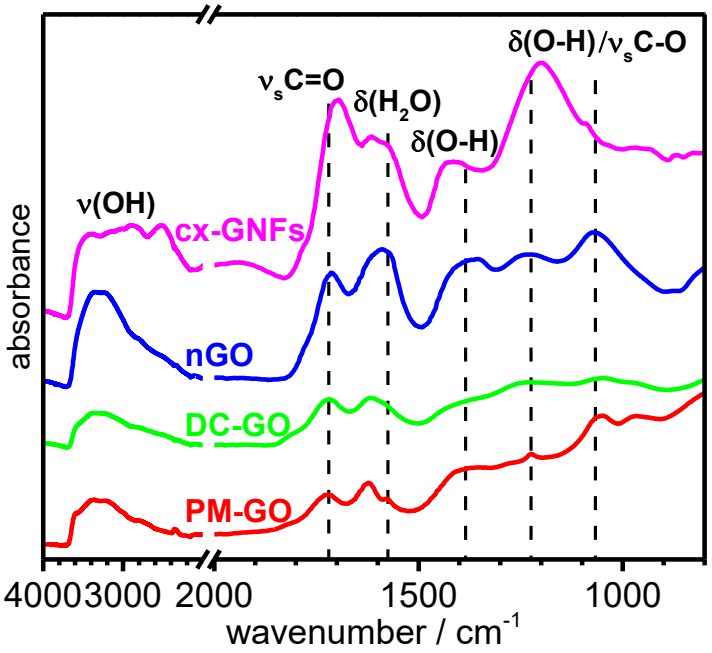

Fig. 3.5 IR spectra of cx-GNFs (magenta), nGO (blue), DC-GO (green) and PM-GO (red).

The highly carboxylated nature of the cx-GNFs is apparent by the very strong and broad O-H stretching frequency between 3600 cm^{-1} and 2500 cm^{-1} (24) in the IR spectrum (magenta) in Fig. 3.5. This is further corroborated by the C=O stretching frequency at ~1700 cm^{-1} (25) as well as the O-H bending and C-O stretching at ~1380 cm^{-1} and ~1200 cm^{-1} respectively (26; 27). The broad peak at ~1590 cm^{-1} will have contributions from O-H bending from water molecules as well as the C=C stretching of the cx-GNFs (26; 27). The other three carbon materials have remarkably similar IR spectra, showing less broad O-H stretching (as a consequence of containing fewer carboxylic acid groups) as well as

an additional feature at ~1050 cm^{-1}, which can be ascribed to C-O stretching *i.e.* from hydroxyls/epoxides (28). The feature at ~1200 cm^{-1} may also contain a contribution from epoxides for these three materials (28).

The Raman spectra of all four carbon materials are illustrated in Fig. 3.6.

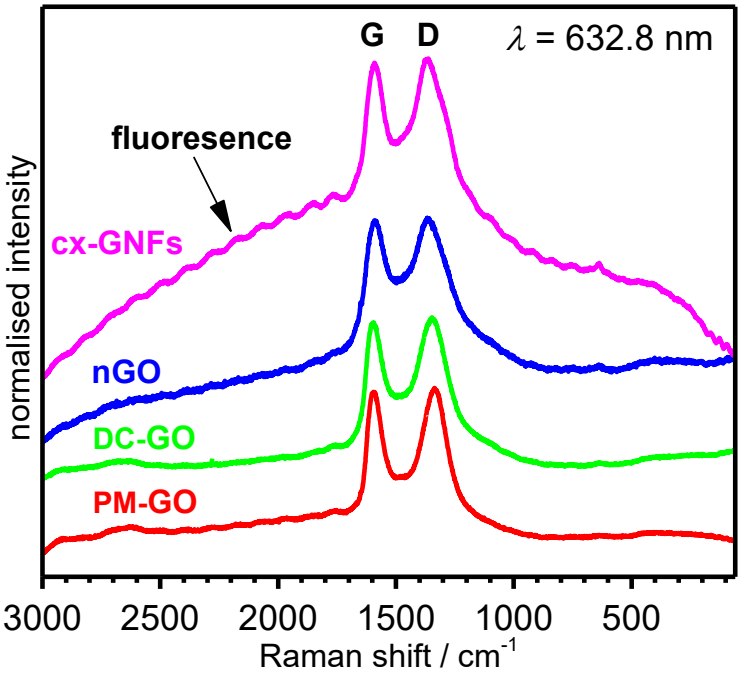

Fig. 3.6 Raman spectra of cx-GNFs (magenta), nGO (blue), DC-GO (green) and PM-GO (red).

All four carbon materials exhibit the characteristic G and D bands associated with oxidised graphenic materials. The G band (~1600 cm^{-1}) is found in all carbon materials and is due to the doubly degenerate in plane stretching mode of sp^2 carbon, corresponding to the E_{2g} irreducible representation (29; 30). The D band (~1350 cm^{-1}) by contrast is not Raman active in the absence of defects (such as oxidised carbon, vacancies, grain boundaries, edges etc.) and is therefore commonly known as the disorder-induced band (30). In the presence of disorder however, momentum conservation is met allowing for the D band to become active (31-33). Unlike the G band, the D band is also dispersive, i.e. varies with laser excitation energy and therefore its peak position is wavelength dependent (29). Another important band that is sometimes observed in carbon materials is the 2D band (~2700 cm^{-1}), which is a second-order Raman process resulting in the in-plane ring breathing of carbon atoms (29). The 2D band belongs to the totally symmetric A'_1 irreducible representation and is the strongest

band observed for defect-free graphene (29). In the case of the carbon materials in Fig. 3.6 it is not appreciably observed. It is noteworthy that the regular wave-like humps seen in the Raman spectra of the cx-GNFs is most likely the result of fluorescence.

3.3.3 Characterisation of carbon materials by AFM and TEM

An AFM image of cx-GNFs spin coated onto a highly oriented pyrolytic graphite (HOPG) substrate, along with the corresponding height and size distributions are shown in Fig. 3.7(a)-(c) respectively.

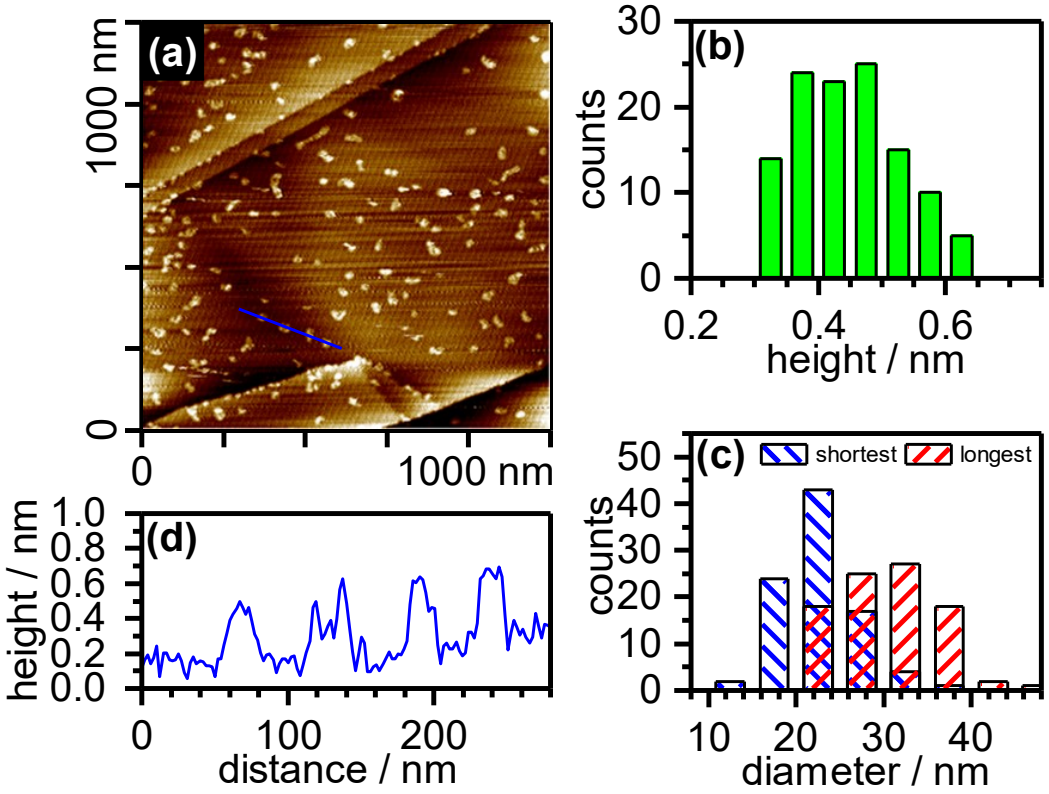

Fig. 3.7 (a) AFM image of cx-GNFs spin coated onto HOPG, (b) height and (c) diameter distribution and (d) line profile of the cx-GNFs taken from the blue line in (a).

Several AFM images of the cx-GNFs such as the one on Fig. 3.7(a) were recorded and the average heights and lengths of the cx-GNFs were determined using line profiles such as the one in Fig. 3.7(d). The average height of the cx-GNFs was determined to be (0.5 ± 0.1) nm, in good agreement with oxidised monolayer graphene (18), see Fig. 3.7(b). This value and associated error was calculated by taking 116 measurements of 91 individual flakes, and represents the mean and 1.s.d. about the mean respectively. The

fact that there are more measurements than flakes are due to some of the flakes having a small step in their height profile, possibly due to adsorbed fragments, and this is therefore also taken into consideration. This is discussed in detail shortly, in the context of nGO. Furthermore, given the roughness of the AFM image, one would expect an error of at least 0.1 nm. Similarly, the average lateral dimensions of the cx-GNFs were measured to be (22 ± 4) nm and (31 ± 5) nm for the shortest (blue) and longest (red) lengths respectively, *c.f.* Fig. 3.7(c). The shortest and longest lengths were considered as a consequence of the asymmetry of the flakes, which naturally resulted in one side being longer than the other. In both cases, the value and reported error reflect the mean and 1.s.d. of the 91 measured individual cx-GNFs. Similar results were also obtained by TEM (see Fig. 3.8), where the shortest and longest lateral lengths of the cx-GNFs were calculated to be (15 ± 4) nm and (23 ± 6) nm respectively. Once again, the value and error represent the mean and 1.s.d. of 18 measured cx-GNFs. Just like AFM, the dimensions of the cx-GNFs measured by TEM were done so using line profiles.

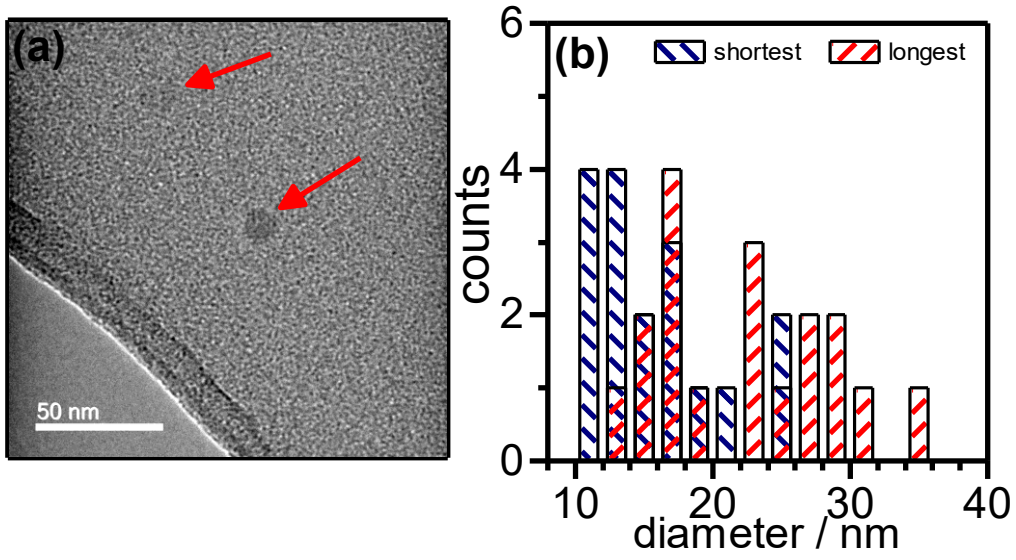

Fig. 3.8 (a) TEM image of two cx-GNFs highlighted by red arrows and (b) diameter distribution of the cx-GNFs as seen in TEM.

Likewise, the AFM image of nGO and its corresponding height and lateral size distribution, and line profile can be seen in Fig. 3.9(a)-(d) respectively. Complementary TEM is also shown in Fig. 3.10.

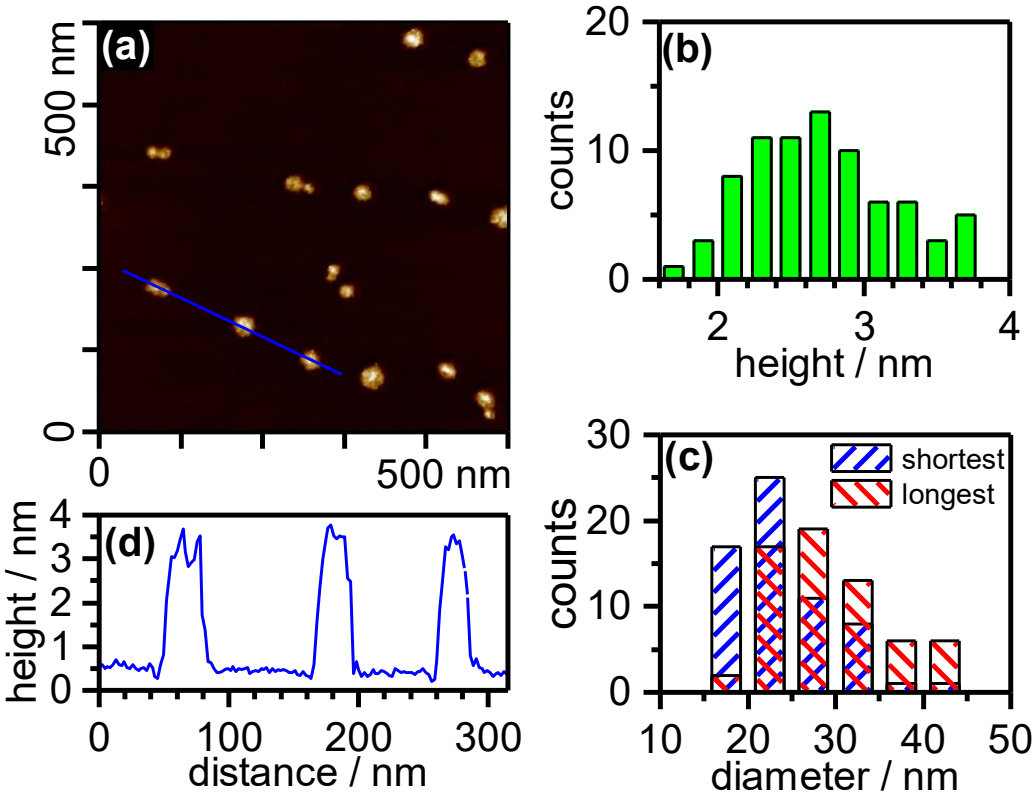

Fig. 3.9 (a) AFM image of nGO spin coated onto HOPG, (b) height and (c) diameter distribution, and (d) line profile of the nGO taken from the blue line in (a). Modified from reference (23) with permission from Elsevier.

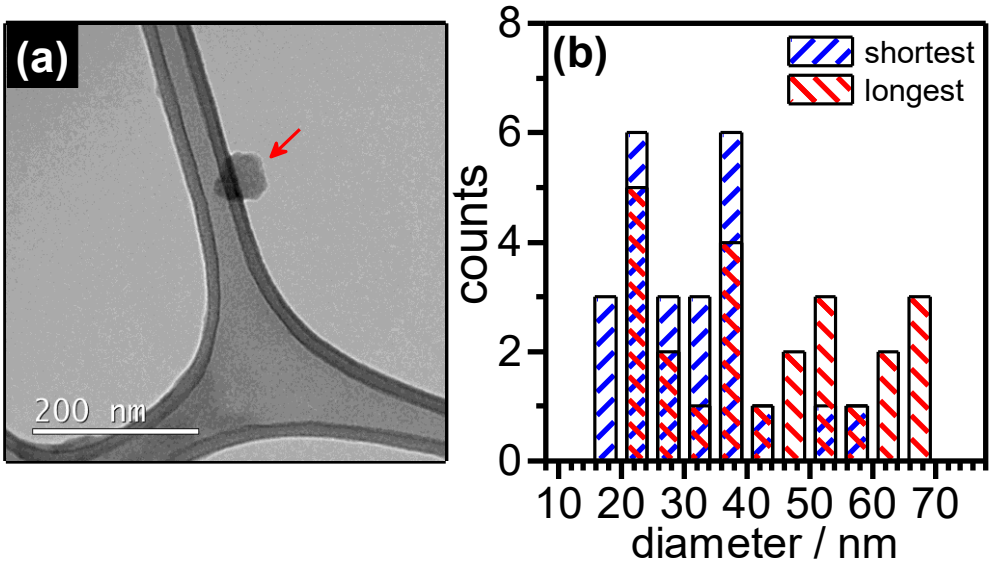

Fig. 3.10 (a) TEM image of an nGO flake highlighted by the red arrow and (b) diameter distribution of the nGO as seen in TEM. Reprinted from ref (23) with permission from Elsevier.

Interestingly, the size distributions of the nGO were found to be very similar to those of the cx-GNFs, (24 ± 6) nm and (29 ± 6) nm for the shortest (blue) and longest (red) lengths respectively, according to the analysis of 63 individual nGO flakes from multiple AFM images, such as the one in Fig. 3.9, which is representative of the sample. Similar results were obtained by TEM analysis, whereby the size distribution of 24 nGO flakes, determined from line profiles of TEM images such as the one in Fig. 3.10(a), resulted in lateral dimensions of (27 ± 9) nm and (40 ± 15) nm for the shortest (blue) and longest (red) lengths respectively. A significant difference between the nGO flakes and the cx-GNFs however, is that the nGO flakes had noticeable dome-like features (see AFM Fig. 3.9 (a)) suggesting that smaller flakes had adsorbed onto the larger nGO flakes. The average height of 78 measurements of 63 nGO flakes was (2.6 ± 0.5) nm, most likely due to these smaller adsorbed fragments. Indeed, the adsorption of smaller graphenic fragments onto a larger nGO flake has also been shown by AFM in other nano-GO literature (11). It should be noted that all values and associated errors determined using AFM/TEM were calculated in the same way as the cx-GNFs.

A representative AFM image of DC-GO can be seen in Fig. 3.11(a). Height analysis of the DC-GO flakes in Fig. 3.11(b) revealed that the flakes were (1.8 ± 0.8) nm high, corresponding to ~1-3 GO layers. In contrast to the cx-GNFs and the nGO, the DC-GO showed significant variation in flake size- (32 ± 15) nm and (47 ± 25) nm for the shortest (blue) and longest (red) lengths respectively, as evidenced by the AFM image in Fig. 3.11(c). The large size distribution is suggestive that larger flakes are not stable and readily break down into smaller fragments. It is noteworthy that all the values were calculated in the same way as previously described for the cx-GNFs and the nGO, using line profiles such as the one in Fig. 3.11(d), except that 133 and 70 measurements were determined for the heights and lengths, respectively.

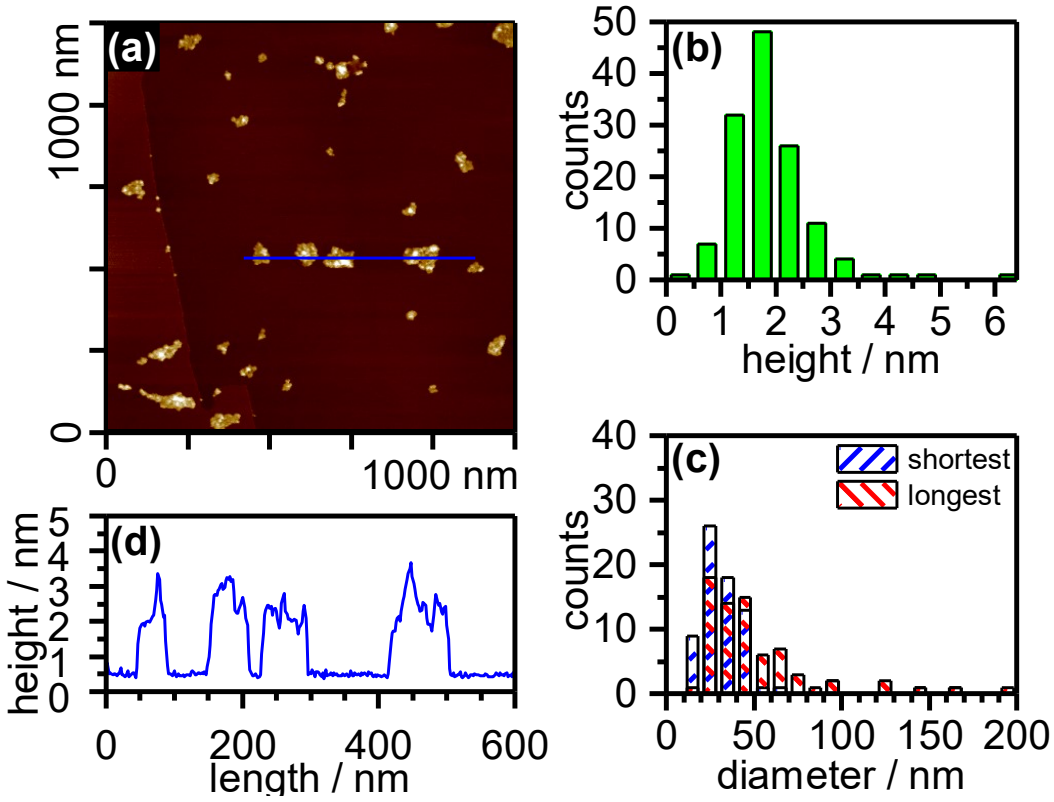

Fig. 3.11 (a) AFM image of DC-GO spin coated onto HOPG, (b) height and (c) diameter distribution, and (d) line profile of the DC-GO flakes taken from the blue line in (a).

An AFM image of PM-GO is shown in Fig. 3.12(a). Height analysis of the PM-GO flakes in Fig. 3.11(b) indicates that the average flake is a single sheet-(0.8 ± 0.2) nm, in good agreement with GO produced *via* Chen *et*. *al*.(34) On the other hand, PM-GO displayed much larger flakes sizes compared to the previous nanomaterials, (220 ± 110) nm and (330 ± 160) nm for the shortest (blue) and longest (red) lengths respectively, according to the size distribution in Fig. 3.12(c). This suggests that the PM-GO flakes are more structurally stable w.r.t DC-GO, given that both are prepared from the same type of graphite. Analysis of both height and size distributions of PM-GO was performed by analysing 73 individual PM-GO flakes, over multiple AFM images using line profiles such as the one in Fig. 3.12(d). Statistics were performed as described previously for the other nanomaterials.

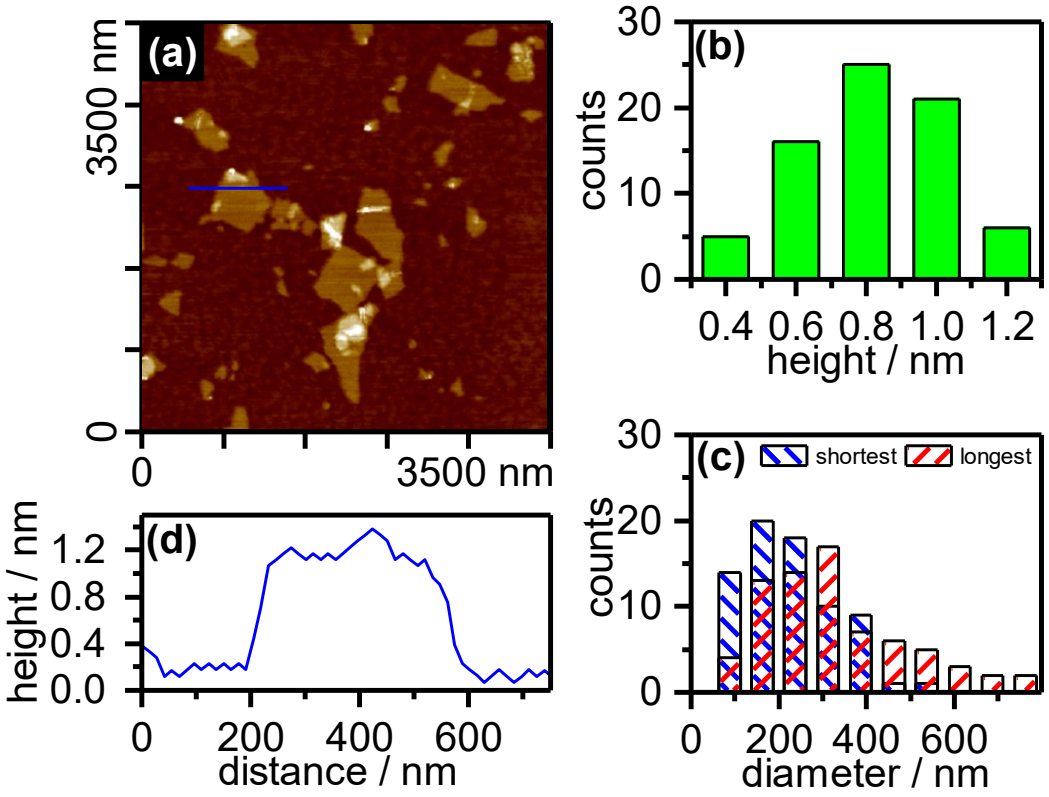

Fig. 3.12 (a) AFM image of PM-GO spin coated onto a mica substrate, (b) height and (c) diameter distribution, and (d) line profile of a PM-GO flake taken from the blue line in (a).

3.4 A closer look at cx-GNFs

In this section the optimised preparation of cx-GNFs is discussed as well as a more detailed outlook on the materials used and the by-products of the reaction mixture. The morphology of the resulting cx-GNFs is also explored.

3.4.1 Preparation of cx-GNFs

A schematic illustration showing the preparation of cx-GNFs is shown in Fig. 3.13.

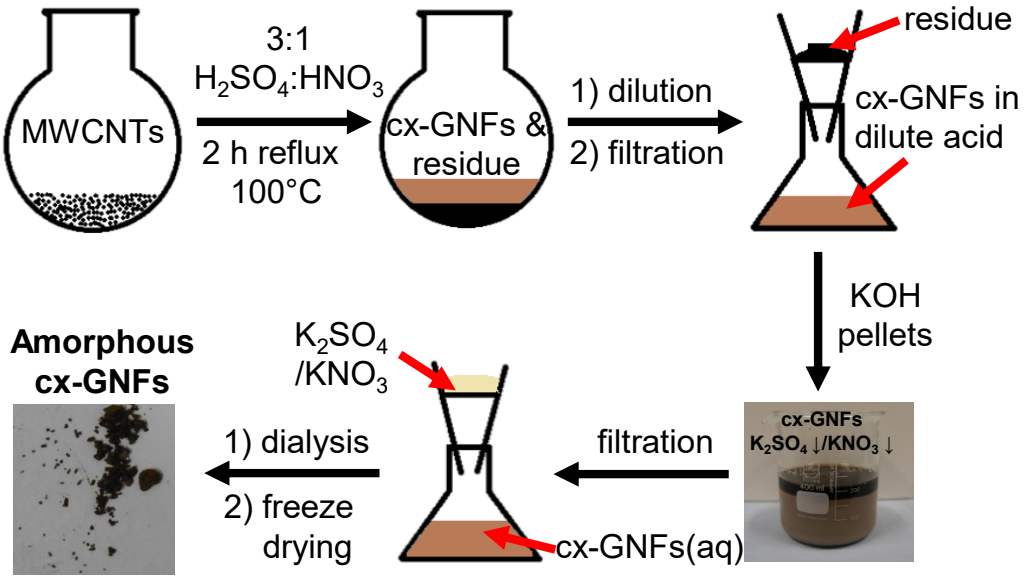

Fig. 3.13 Schematic illustration of the preparation of cx-GNFs.

The precursor to cx-GNFs are MWCNTs. In this work, MWCNTs (CVD) from Bayer Materials Science were used. However, we have shown (Appendix Fig. A3.1) that MWCNTs from alternative sources such as Elicarb CVD MWCNTs (Thomas Swan Ltd.) can also be utilised, obtaining a very similar product (35). These MWCNTs are refluxed in a 3:1 mixture of H_2SO_4 and HNO_3 acid for 2 h at 100°C. Typically, 10 mg of MWCNTs can be processed per mL of acid mixture. It should be noted that the treatment of MWCNTs with this acid mixture is well documented in the literature, resulting in the oxidation of the MWCNTs as well as the introduction of various types of defects.(36-38) However, in this case we are concerned with the over-oxidised and broken down MWCNTs, resulting in the formation of the cx-GNFs.

After the reaction, a brown-black dispersion of cx-GNFs and unreacted MWCNT precipitate (termed residue) is observed which is diluted three-fold with deionised water and filtered to separate the residue from the cx-GNFs (35). The conditions used in the preparation were chosen because after 2 h of acid treatment the optical absorbance of the cx-GNF dispersion began to decrease, as shown in Fig. 3.14, suggesting the breakdown of the material into quantum dots (QD).(39) Similarly, the use of a 3:1 mixture of H_2SO_4 to HNO_3 acid resulted in a higher yield of cx-GNFs compared with a 1:1 mixture. It should be noted that the absorbance of the cx-GNF dispersion will be influenced by the presence of CNTs which will scatter the incoming light and give misleading results. To ensure this was not the case, a 200 nm hydrophilic polycarbonate filter membrane was used to separate the cx-GNFs from the MWCNTs prior to optical absorbance

measurements. Furthermore, the absence of CNTs from the recorded AFM images of the cx-GNFs confirms this to be true.

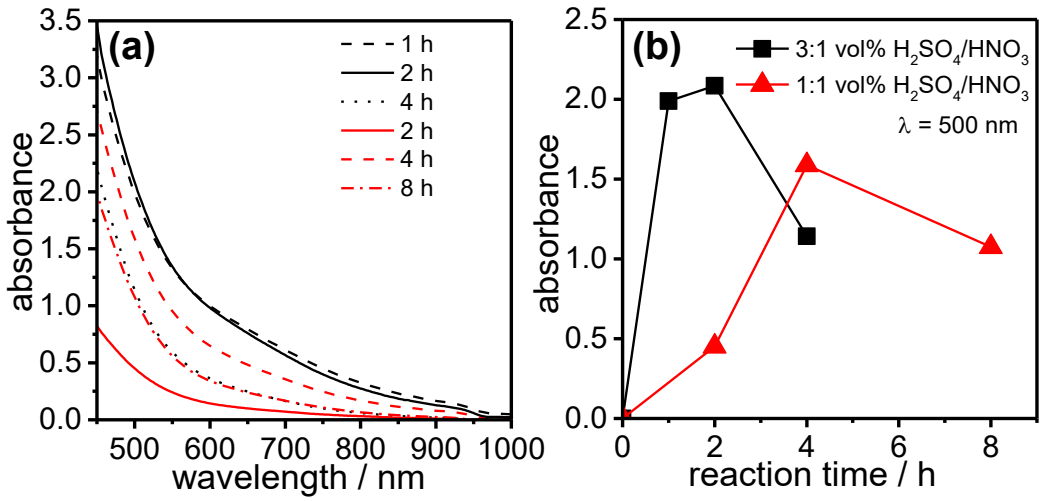

Fig. 3.14 Optical absorbance spectra of the filtered reaction mixtures after oxidation in (i) 3:1 H_2SO_4/HNO_3 after 1 hour (black dashed), 2 hours (black solid) and 4 hours (black dotted) and (ii) 1:1 H_2SO_4:HNO_3 after 2 hours (red solid), 4 hours (red dashed) and 8 hours (red dot-dashed). (b) Absorbance values of the spectra in (a) at 500 nm

After filtration, the cx-GNF dispersion is then neutralised by the slow addition of KOH pellets which results in a super-saturated salt solution, causing the precipitation of K_2SO_4 and some KNO_3. Fascinatingly, the cx-GNFs remain dispersed in solution (*c.f.* photographic image in Fig. 3.13 despite the presence of highly soluble inorganic salts, illustrating just how hydrophilic the material is. In fact, the cx-GNFs have never been known to precipitate out from an aqueous solution, even after a couple of years. The cx-GNFs are then removed from the precipitated salts by filtration once again and the remaining cx-GNF dispersion is dialysed against deionised water to remove the remaining dissolved salts. The cx-GNFs are isolated from solution *via* lyophilisation, yielding an amorphous brown powder in ~16% yield by mass. Further details on the preparation of cx-GNFs can be found in the experimental section chapter 8 section 8.1.

A major advantage of the cx-GNF preparation over conventional PM-GO is the absence of $KMnO_4$ from the reaction mixture, hence removing manganese as a toxic by-product of the synthesis. Furthermore, the formation of cx-GNFs occurs within 2 h which is significantly shorter than most oxidation protocols (5; 6). There is also no need for a second exfoliation step or repeated washing *via* centrifugation/sonication (3; 5; 6).

3.4.2 Comparison of cx-GNFs with the residue and MWCNTs

Comparison of the MWCNT starting material, residue and cx-GNFs by XPS are shown in Fig. 3.15. The increase in oxidised carbon is apparent in both the XPS survey and C1s regions, increasing in the order MWCNTs < residue < cx-GNF. In the MWCNTs, virtually no oxygen is present and the typical asymmetric line shape of sp^2 carbon is observed in the C1s region at ~284.5 eV, see Fig. 3.15. The π-π* feature is also just noticeable above the background at ~291 eV (40). Similarly, the residue also exhibits significant asymmetry in the C1s region (green spectrum), suggesting that the residue consists of mainly CNTs, which have been oxidised but not broken down, as indicated by the feature at ~289 eV which can be attributed to C(III) species such as carboxylic acids (40). Alternatively, it is possible that the CNTs in the residue have remained almost intact and are instead coated by the cx-GNFs, preventing their oxidation (41). This is analogous to the OD seen on oxidised CNTs as previously reported by Salzmann *et. al.*, and discussed earlier in the introduction. The possibility of C(I) and C(II) species on the residue (286-288 eV) can also not be ruled out. The final oxidised product, the cx-GNFs is a highly carboxylated material as described earlier in section 3.3.1.

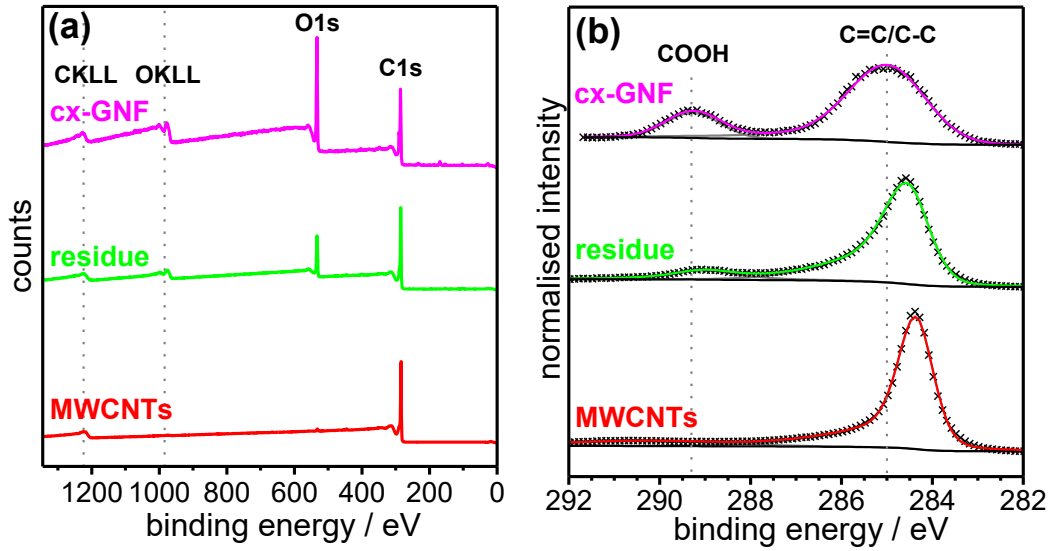

Fig. 3.15 XPS survey and (b) C1s regions of cx-GNFs (magenta), residue (green) and MWCNTs (red).

The difference between the three materials is also highlighted in the Raman spectra in Fig. 3.16. The D/G ratios of the cx-GNFs, residue and MWCNTs were calculated to be ~1, (1.48 ± 0.09) and (1.87 ± 0.07) respectively. The FWHM of the D and G bands in all three carbon materials were determined to be greater than 60 cm^{-1}, and in some cases were close to or exceeded 100 cm^{-1}. The broad FWHM of the materials suggests that

the average separation between two defects (L_D) is ~ 1 nm (42; 43). However, this strictly only holds true for single-layer graphene and caution must be taken when assigning other carbon materials. Nonetheless, this approach has also been successfully applied to rGO (42). Furthermore, the gradual disappearance of the 2D band indicates the loss of graphenic structure as the MWCNTs are oxidised to cx-GNFs (44).

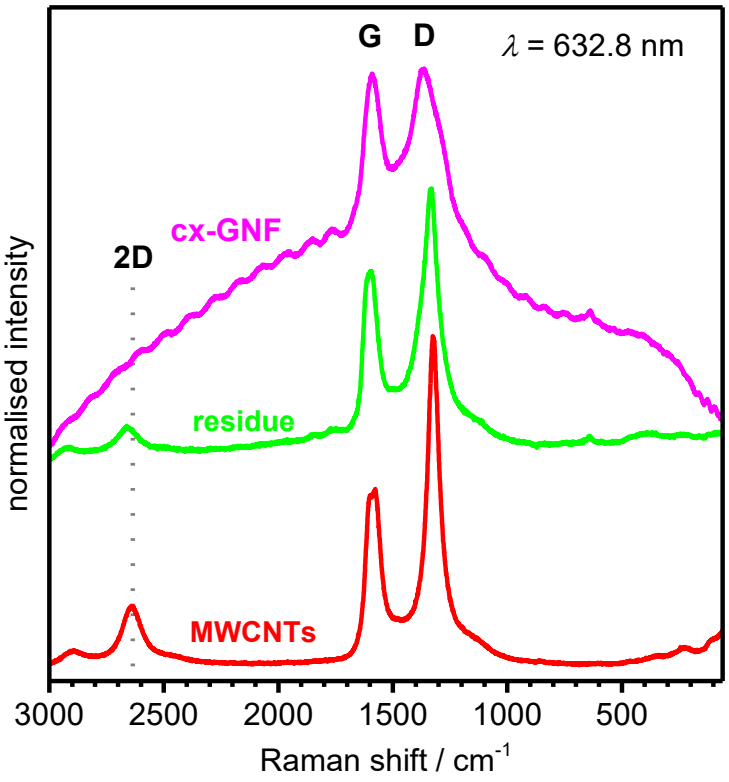

Fig. 3.16 Raman spectra of cx-GNFs (magenta), residue (green) and MWCNTs (red).

3.4.3 Comparison of amorphous (a-GNFs) and turbostratic (t-GNFs) cx-GNFs

An interesting feature of the cx-GNFs is that high surface area amorphous powders (a-GNFs) can be prepared as well as large crystalline-like low surface area turbostratic flakes (t-GNFs). The SEM and photographic images in Fig. 3.17 illustrate the differences between a-GNFs and t-GNFs. In each case, small cx-GNFs of ~30 nm (*c.f.* Fig. 3.7) are the constituents of these bulk materials.

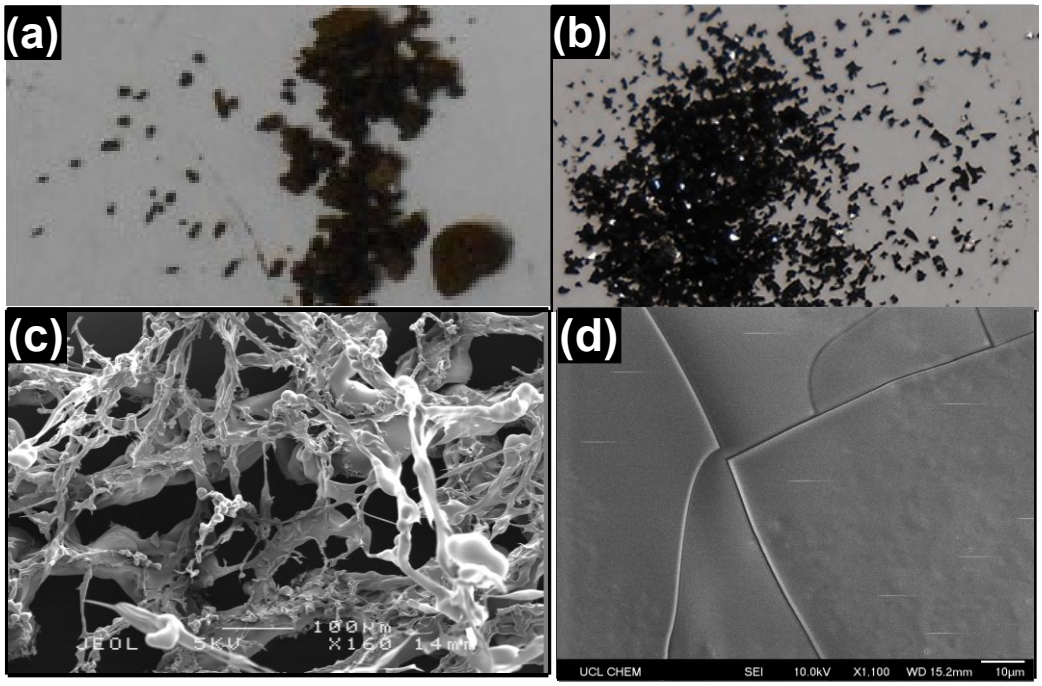

Fig. 3.17 Optical (a) and (b), and SEM (c) and (d) images of a-GNFS and t-GNFs respectively.

.

The cx-GNFs as prepared in Fig. 3.13 are amorphous like the a-GNFs depicted in Fig. 3.17(a/c).The amorphous nature arises as a result of the freeze-drying process which freezes the cx-GNFs in a highly disordered state without the opportunity to re-order. Alternatively, instead of freeze-drying, the aqueous dispersion of cx-GNFs after dialysis can be left to stand in air to slowly allow the water to evaporate. This is analogous to crystallisation where the dissolved species (in this case cx-GNFs) are able to re-order themselves into a thermodynamically stable state, typically forming a crystalline structure. The t-GNFs produced in this way display a turbostratic morphology as depicted in Fig. 3.17(b,d), and evidenced by the XRD pattern (red) in Fig. 3.18(a) and respective *d*-spacing in (b) (45). By contrast, the a-GNF (blue) does not show any features in the XRD pattern.

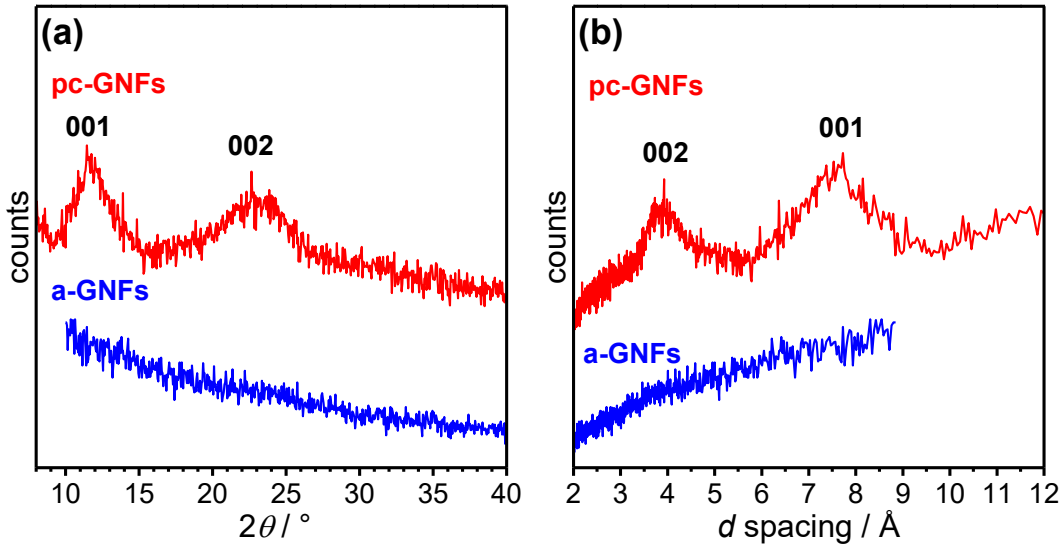

Fig. 3.18 Powder XRD patterns of (a) raw data a-GNFs (blue) and t-GNFs (red) and (b) d-spacing of a-GNFs (blue) and t-GNFs (red) converted from (a).

In turbostratic materials, there is a permanent rotational and translational misalignment between adjacent layers (46). In the case of graphitic-like materials such as the t-GNFs, this means that the 001 reflection is observed as well as the conventional 002 reflection seen in graphite. By comparison with GO, only the 001 reflection is observed due to the extensive oxidation of the graphenic basal plane which results in an increase in *d*-spacing between the adjacent sheets (47).

The t-GNFs in Fig. 3.17(d) were mechanically exfoliated using scotch tape (48) and imaged by AFM-Fig. 3.19(a). The flakes were found to be flat to within 3 nm as indicated by the height profile in Fig. 3.19(c).However, there were very apparent hole-defects in the sample or 'nano-cavities' in the flake (as indicated by the red arrows in Fig. 3.19(a)). It is speculated that at these regions there is an absence of carboxylic acid groups and therefore the 'propagation' process between adjacent hydrogen bonded cx-GNFs ends or 'terminates', thus resulting in these cavities.

The t-GNFs were then carbonised under vacuum to 900°C (now referred to as carb-GNFs), re-exfoliated using scotch tape, and imaged once more with AFM (Fig. 3.19(b)). Interestingly, after carbonisation the roughness of the flake increased substantially, as shown by the height profile in Fig. 3.19(d). The image Ra, image Rq and image Rmax of the carb-GNFs increased to 2.44, 3.09 and 24.3 nm respectively, compared to the image Ra, image Rq and image Rmax of the t-GNFs which were found to be 0.53, 0.82 and

12.8 nm respectively. The 'nano-cavities' observed earlier in the t-GNFs are less apparent and individual flakes (indicated by the red arrows) can now be seen.

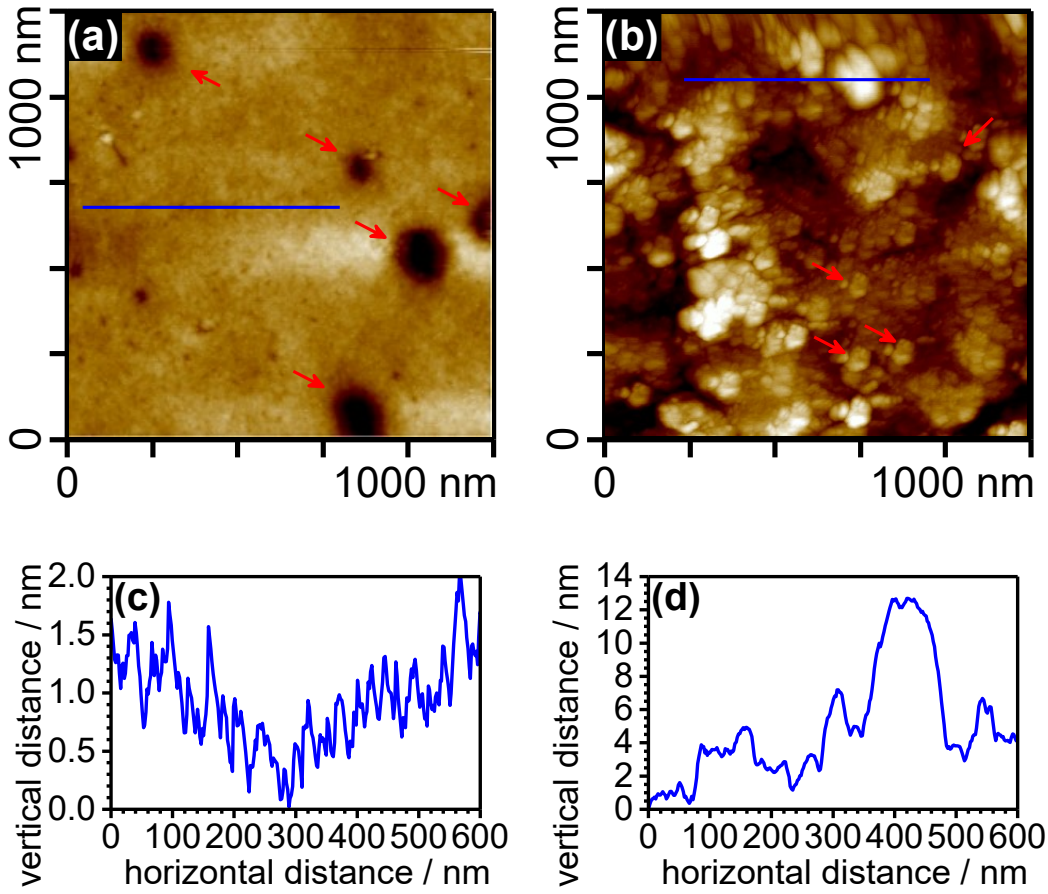

Fig. 3.19 AFM image of the surface of a t-GNFs (a) before and (b) after carbonising and (c)-(d) height profiles of (a) and (b) indicated by the blue lines respectively. Red arrows indicate in (a) holes and (b) individual carb-GNFs respectively.

BET surface area measurements were carried out on the carb-GNFs (see appendix Fig. A3.2) and the surface area was determined to be only 36 m^2/g compared with the theoretical value of 2600 m^2/g for graphene (49). By comparison, the a-GNFs in Fig. 3.17(a) were carbonised and a BET surface area of ~600 m^2/g was determined (appendix Fig. A3.2), illustrating the variation in morphology the cx-GNFs can adopt.

3.5 A closer look at nGO

In this section the eco-friendly preparation of nGO is discussed as well as a closer look at the material itself and reaction by-products.

3.5.1 Preparation of nGO

The preparation of nGO is illustrated in Fig. 3.20.

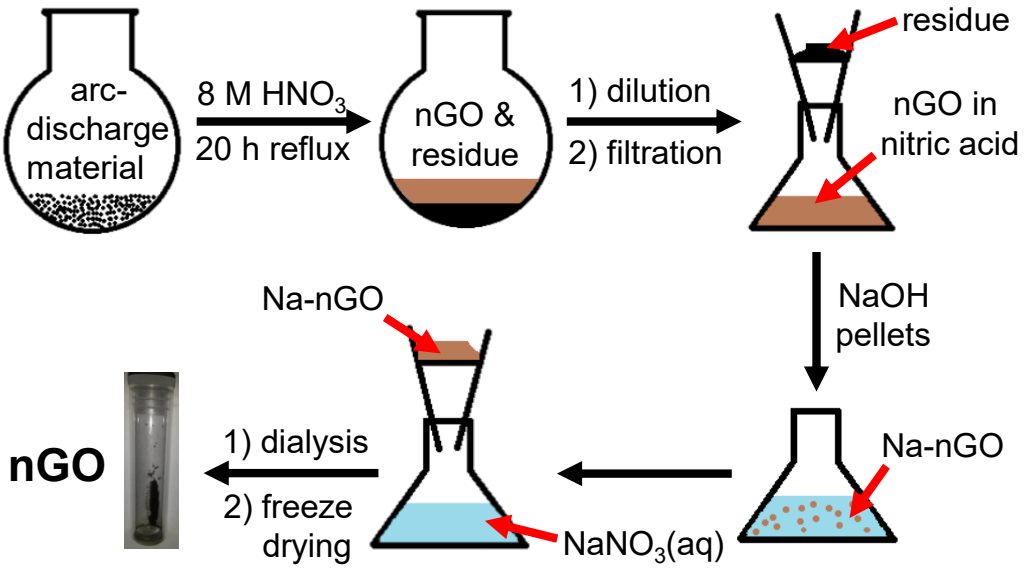

Fig. 3.20 Schematic illustration of the preparation of nGO. Reprinted from ref (23) with permission from Elsevier.

The as produced SWCNTs, as specified by Materials and Electrochemical Research (MER) corporation, from where they were purchased, are derived from an arc-discharge carbon source (ADC) consisting of SWCNTs (12+ w/w), fullerenes (10 w/w), metal catalyst (25 w/w), MWCNTs and other graphitic carbon (10 w/w) and amorphous carbon (43 w/w), is the raw material used in the preparation of nGO. The carbonaceous mixture is initially ultrasonicated in 8 M HNO_3 for 30 min before refluxing at 100°C for 20 h. The preparation can be scaled up proportionately with current GO protocols with 50 mL of 8 M HNO_3 able to process one gram of ADC material. The resulting mixture of dispersed nGO and unreacted black residue is diluted three-fold with deionised water and filtered to separate the nGO from the residue. Neutralisation of the acidic mixture with NaOH results in the precipitation of the sodium salt of the nGO which can be isolated by simple filtration. Removal of the Na^+ from the nGO is readily accomplished by ion exchange or dialysis on re-dispersing the nGO in deionised water. Freeze-drying isolates the nGO

material in the same way as the cx-GNFs in ~21% yield by mass (23). Further details of the experimental procedure can be found in chapter 8 section 8.2.

This unique procedure in preparing nGO has many advantages over conventional nGO synthesis in the literature. For instance, the standard $KMnO_4/H_2SO_4$ oxidation protocol is replaced with 8 M HNO_3 (which actually contains more water than it does acid), and is not only less oxidising/explosive but relatively cleaner (although there is still some way to go before the process itself can be considered environmentally friendly or 'green'). The use of $KMnO_4$ results in a huge amount of manganese waste which has to be reduced to Mn(II), typically with peroxide, before disposal as a hazardous waste substance. By contrast, the only by-products of the nGO synthesis are unreacted carbon (relatively benign) and aqueous sodium nitrate which is significantly less toxic. The metal catalyst is expected to be removed during the filtration and dialysis steps, however the ADC can be readily pre-treated beforehand to remove the metal catalyst entirely. Similarly, many treatment methods for the removal of NO_x fumes are already available on an industrial scale (50). It may even be possible to recycle the NO_x gas back into nitric acid. Nonetheless, the major advantage in the preparation of nGO is that repeated sonication and centrifugation steps are not required to wash and breakdown the material into nano-sized flakes, as is the case when GO is used a precursor.

3.5.2 Comparison of nGO with the residue and ADC

The XPS survey and C1s regions in Fig. 3.21 illustrate the differences between the nGO, the residue and ADC material.

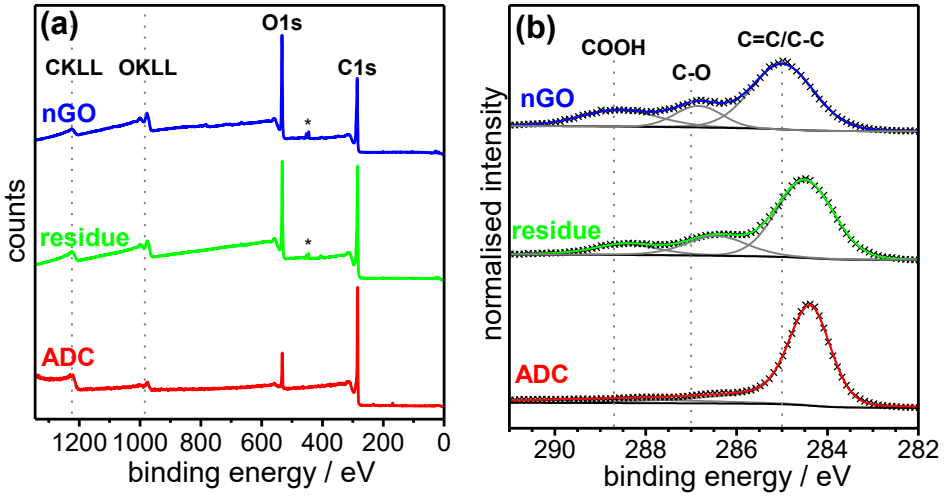

Fig. 3.21(a) XPS survey and (b) C1s regions of nGO (blue), residue (green) and ADC (red).Peaks denoted by the asterisk are due to the indium substrate.

The C/O ratios extracted from the XPS survey spectra of the three materials in Fig. 3.21(a) are shown in Table 3.1. The analysis was carried out by integration of the carbon and oxygen peaks with consideration given to the relative sensitivity factors of carbon and oxygen. For statistics, three samples of nGO were prepared and each sample was measured three times. For the residue, two samples were prepared and each sample was measured twice. The as-received ADC was measured three times. The error was considered by calculating 1.s.d. about the mean of the combined measurements. From the results, it can be seen that the C/O atomic ratio decreases in the order ADC > residue > nGO in line with an increasing degree of oxidation. Just like the residue of the cx-GNFs, the residue of the nGO is likely to be coated with adsorbed nGO flakes (41), resulting in the nGO and residue exhibiting similar XPS C1s spectra as seen in Fig. 3.21(b).

Table 3.1 Quantification of the XPS survey C/O ratio of nGO, residue and ADC.

Carbon material	C/O ratio
nGO	2.2 ± 0.1
residue	3.3 ± 0.6
ADC	17.7 ± 0.8

A similar conclusion can be reached by comparing the IR and Raman spectra of the three materials in Fig. 3.22(a)-(b). In the IR spectra (Fig. 3.22(a)), the relatively weak absorbance of the ADC suggests that little oxygen functionality is present. Likewise, the residue exhibits the same features as the nGO albeit at lower intensities, further suggesting that the residue constitutes adsorbed nGO flakes. From the Raman spectra in Fig. 3.22(b), the presence of radial breathing modes (RBM) below 200 cm^{-1} and the splitting of the G band (~1590 cm^{-1}) into G^+ and G^- components in the ADC spectrum confirm that the starting material is rich in carbon nanotubes (51; 52). The broad and intense D band (~1306 cm^{-1}) in the ADC spectrum gives rise to an I_D/I_G peak intensity ratio of 0.46 ± 0.07 indicating a significant amount of structural defects (51-54). A similar case can be made for the broad 2D peak (~2618 cm^{-1}) which is usually more intense for high-quality SWCNTs (54). After oxidation of the ADC material, the RBM and 2D modes can still be seen in the Raman spectrum of the insoluble residue albeit at lower intensities. The G band splitting is no longer clearly seen, and the D band has grown more intense (I_D/I_G = 0.74 ± 0.02) and is shifted to higher wavenumbers (~1347 cm^{-1}), which further indicates that the residue contains oxidised CNTs. This is confirmed by TEM analysis of the residue shown in Fig. 3.22(c), in which CNTs are clearly seen. Carbon onions in the TEM image are also present (indicated by the red arrows) which arise as result of dissolved metal particles, leaving behind their carbon coated shell. In

the final oxidised product, the nGO, only G and D bands are observed in the Raman spectrum, evidencing the complete breakdown/removal of the CNTs. It should be noted that the calculation of the I_D/I_G ratio is typically determined by calculating the mean and 1.s.d. of three different spots on a sample.

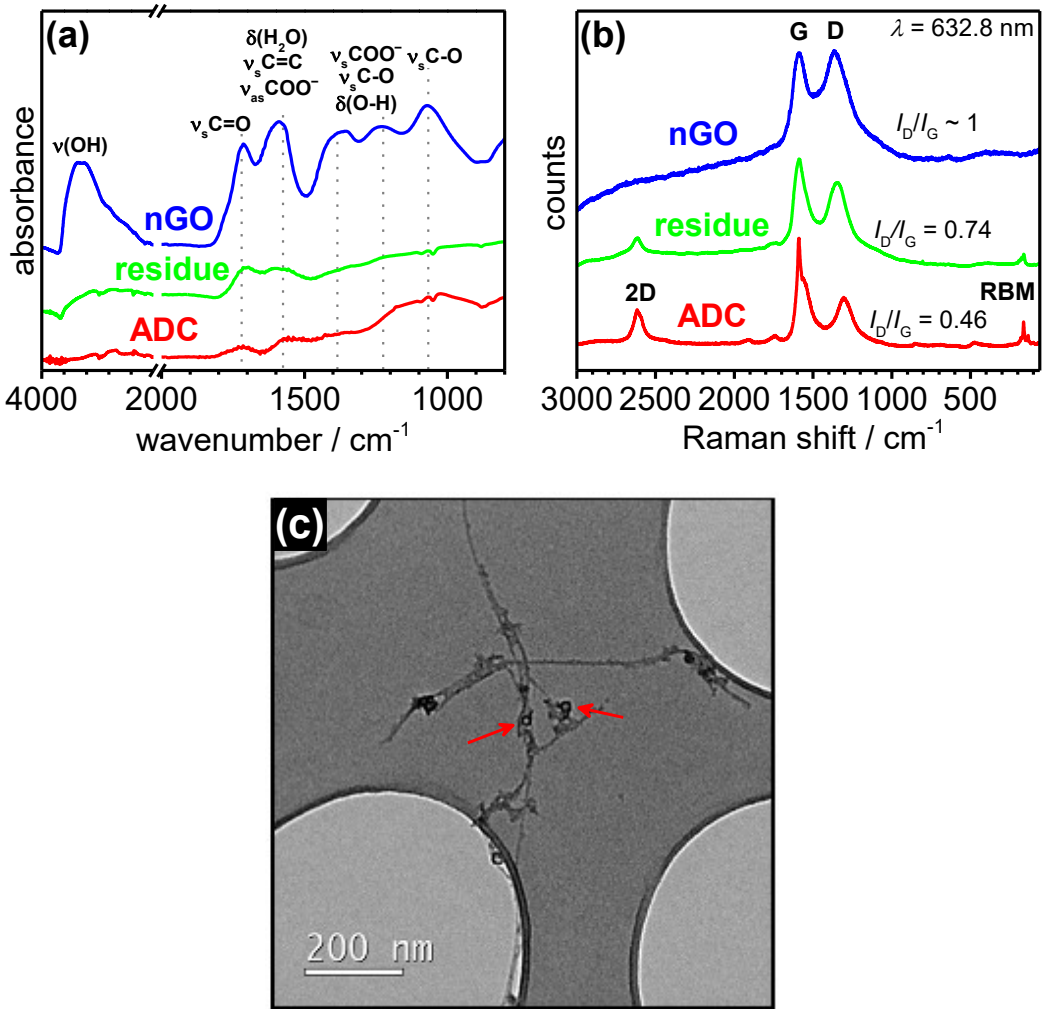

Fig. 3.22(a) FT-IR and (b) Raman spectra of nGO (blue), residue (green) and ADC (red). (c) TEM image of the residue. The red arrows indicate the carbon onions. Reprinted from ref (23) with permission from Elsevier.

3.5.3 The active precursor towards the synthesis of nGO

There are many varieties of carbon present in ADC as described earlier, and it is unclear which (if not more than one) material is the active precursor in synthesis of nGO. Given that the yield of nGO is 21% by mass, the nGO cannot be solely derived from the breakdown of SWCNTs, which only constitutes 12+ w/w of the ADC. Hence it is suspected that amorphous carbon may be the active ingredient given the large weight

percentage (~43%) of this material. MWCNTs and fullerenes are not suspected since MWCNTs are not readily broken down under these conditions (as evidenced by the TEM image of the residue in Fig. 3.22(c)), and fullerenes are too small to form the nGO in the first place. To understand the nature of ADC, TGA was carried out on the material and the results are shown in Fig. 3.23(a). The TGA data shows a sharp mass loss centered at 310°C, which is attributed to the burning of the amorphous carbon. The second mass loss, centered at 365°C, is due to the rest of the carbon material such as the CNTs. The relatively low temperature required to burn off the CNTs illustrates just how defective the material is (55). In order to determine the precursor to nGO, the ADC material was heated in air to 325 °C to burn off all the amorphous carbon before being treated with 8 M HNO_3 in the same way as described earlier in section 3.5.1. The absorbance of the resulting filtrate (containing dispersed nGO) was measured *via* UV-Vis spectroscopy and compared against the filtrate of the 8 M HNO_3 treated ADC which had not undergone heat treatment. The results shown in Fig. 3.23(b) show that the absorbance of the heat treated ADC filtrate (black) was only 28% of the value of the non-heat treated dispersion (blue) at λ = 500 nm. The results therefore strongly indicate that the amorphous carbon plays a significant role in the formation of the nGO. The remaining 28% could be accounted for by the SWCNTs or more thermally stable amorphous carbon.

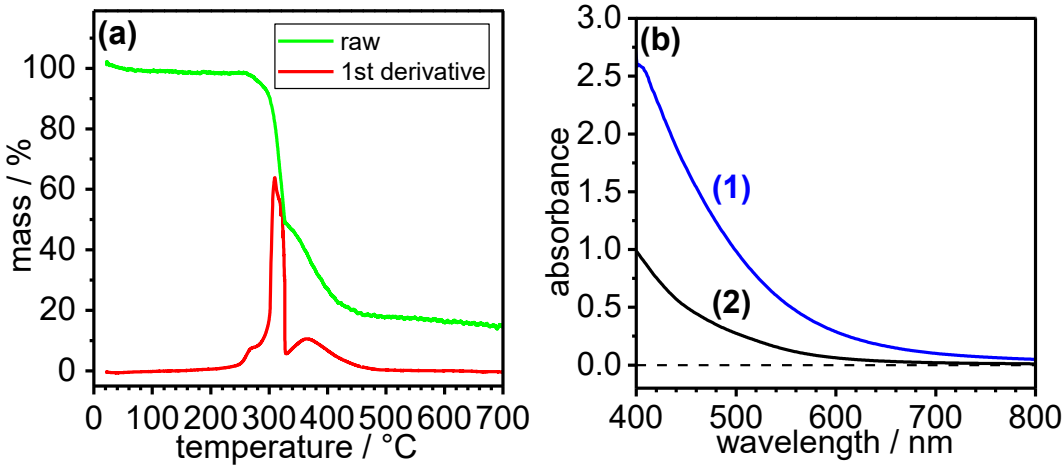

Fig. 3.23 (a) TGA of the as-received ADC material upon heating in air at 3°C min^{-1}. (b) Optical absorbance spectra of the filtrates after the 20 hour reactions with 8 M nitric acid of (1) ADC without heat treatment and (2) the ADC material after heating to 325°C at 3°C min^{-1} in air. Both filtrates were diluted twenty-fold with deionised water before recording the absorbance spectra. The red dashed line illustrates an absorbance value of zero across the wavelength range. Reprinted from reference (23) with permission from Elsevier.

3.5.4 Comparison of amorphous (a-nGO) and turbostratic (t-nGO) nGOs

Similar to the cx-GNFs, the nGO also displays turbostratic like qualities when subjected to the same slow evaporation treatment as outlined earlier in section 3.4.3. By contrast however, the XRD pattern of the t-nGO is incredibly broad and no distinct features can be observed suggesting that the material is highly disordered (*c.f.* appendix Fig. A3.3). Nonetheless, AFM analysis of the roughness of the mechanically exfoliated flakes (Fig. 3.24(a)) showed the t-nGO to be reasonable flat, with the image Ra, image Rq and image Rmax determined to be 0.79, 1.07 and 12.3 nm respectively. Interestingly, after annealing (Fig. 3.24(b)), the roughness only increased slightly, with image Ra, image Rq and image Rmax values of 0.88, 1.13 and 12.8 nm respectively. This was very different compared to the cx-GNFs after annealing which increased surface roughness considerably (*c.f.* Fig. 3.19). However, similar to the cx-GNFs after annealing, the individual nGO flakes (carb-nGOs) can also be seen as indicated by the red arrows in Fig. 3.24(b).

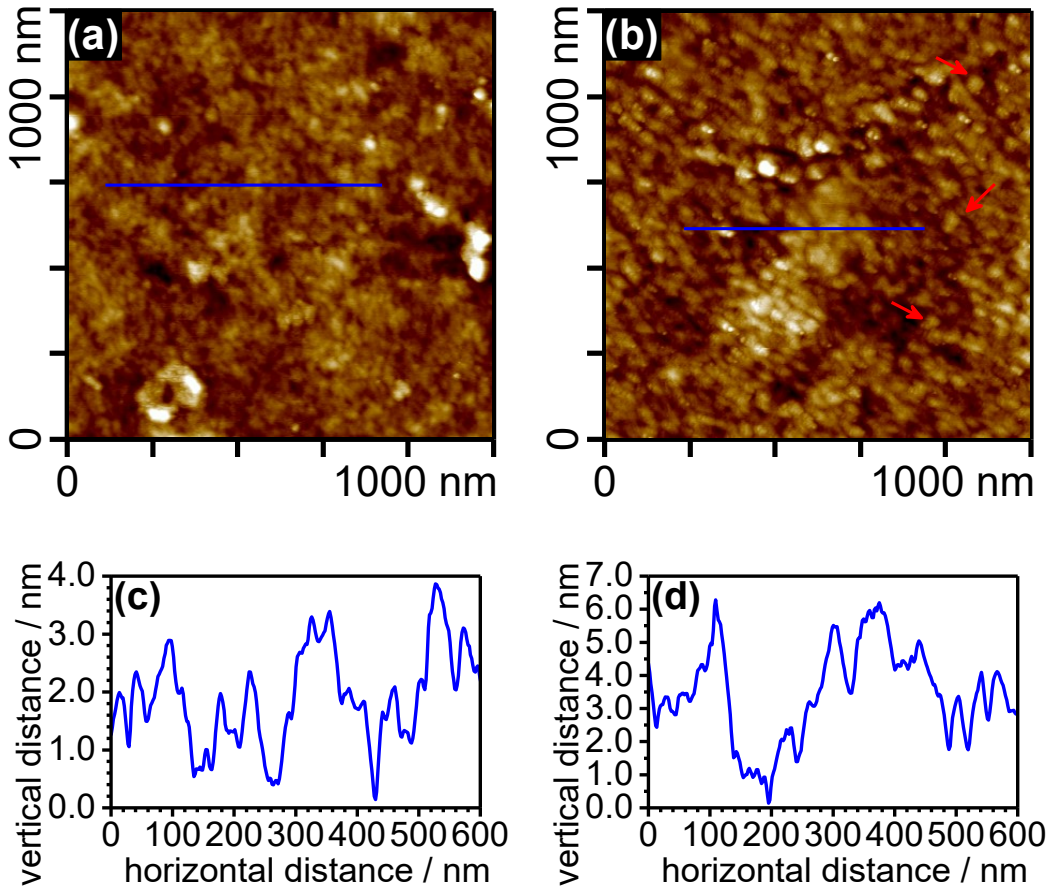

Fig. 3.24 AFM image of the surface of a t-GNFss (a) before and (b) after carbonising and (c)-(d) height profiles of (a) and (b) indicated by the blue lines respectively. Red arrows indicate in (b) individual carb-nGOs respectively.

3.6 A closer look at DC-GO

Chandra *et.al*. first reported the preparation of GO from expandable graphite using dichromate in 2010 (4). In their work, graphite is left stirring in a dichromate/sulfuric acid mixture for 5 d at room temperature before finally being exfoliated with water and subsequent workup procedures. Despite this very interesting route to GO, the chemical nature of the material remains elusive, largely due to the limited characterisation techniques used, in particular the lack of XPS and ^{13}C ssNMR data. In this section, an optimised preparation of DC-GO is reported as well as a discussion on the nature of the material.

3.6.1 Optimised preparation of DC-GO

The optimised preparation of DC-GO is illustrated in Fig. 3.25.

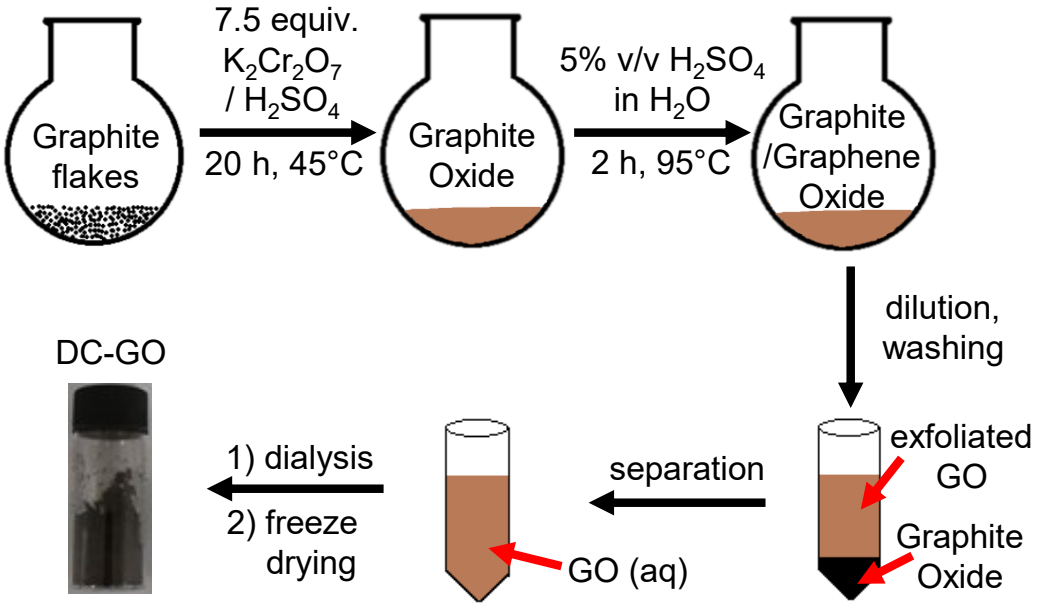

Fig. 3.25 Schematic illustration of the preparation of DC-GO.

In the optimised preparation of DC-GO, graphite flakes are combined with 7.5 mass equiv. of $K_2Cr_2O_7$ in conc. sulfuric acid and heated at 45°C for 20 h with stirring. The increase in temperature from room temperature (as reported by Chandra *et. al*.) to 45°C allowed the reaction time to be significantly reduced from 5 d to 20 h. Furthermore, the use of sodium nitrate originally employed by Chandra *et. al*. was omitted from this

optimised procedure, since it was found to be unnecessary. The subsequent exfoliation step with 5% v/v H_2SO_4 in water was left unchanged, however the workup was slightly improved. Firstly, a few drops of H_2O_2 was added to the mixture before the washing step to ensure that any excess Cr(VI) species was reduced to the significantly less toxic Cr(III). The GO mixture was then centrifuged and washed three times with dilute HCl to remove the Cr(III) before being washed with deionised water, which resulted in a dispersion of GO due to the increase in pH. The dispersed GO was then dialysed against deionised water for further purification and isolated *via* freeze-drying.

To ensure that the DC-GO material produced by the optimised method was the same as that produced by Chandra *et. al.* (and indeed to elucidate the material by Chandra *et. al.*), both materials were fully structurally characterised. DC-GO prepared by the Chandra and optimised procedures are now referred to DC-GO (Chandra) and DC-GO (optimised) respectively (*c.f.* experimental sections in chapter 8 sections 8.3 and 8.4). The XPS and ^{13}C ssNMR of the two materials are shown in Fig. 3.26 and Fig. 3.27 respectively. Similarly, characterisation by FT-IR and Raman spectroscopy as well as AFM are also shown in appendix Figs. A3.4(a) and A3.4(b). It is important to note that the DC-GO characterised at the beginning of this chapter and up until now, refers exclusively to DC-GO (optimised).

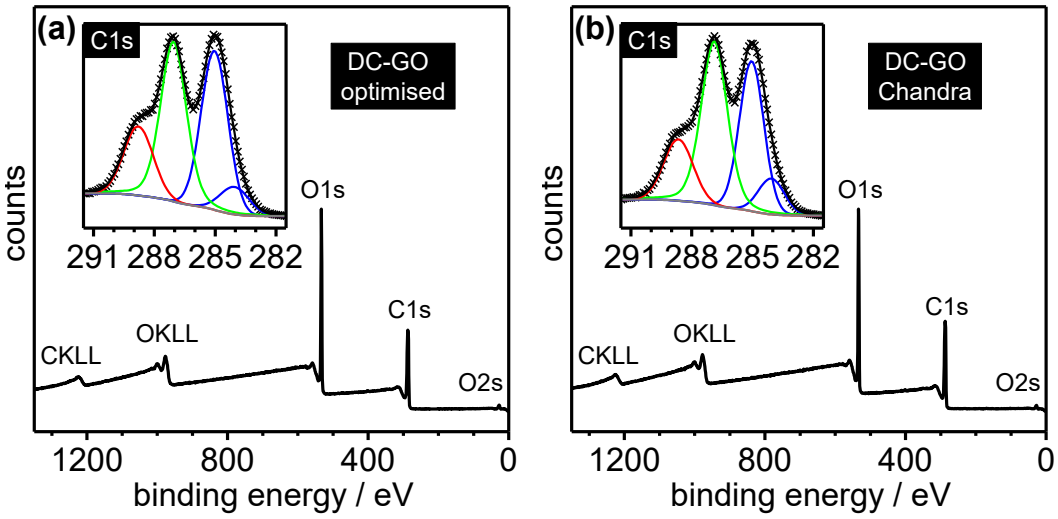

Fig. 3.26 XPS Survey (outset) and C1s regions (inset) of (a) DC-GO (optimised) and (b) DC-GO (Chandra). The crosses represent the experimental data whereas the grey, blue, green, red and black lines are the Shirley background functions, C(0), C(I) and C(III) fitted peaks and peak sum, respectively.

As can be seen in Fig. 3.26, the XPS survey (outset) and C1s regions (inset) of DC-GO (optimised) and DC-GO (Chandra) are very similar. The XPS C1s regions of the two materials were deconvoluted as described earlier in chapter 2 section 2.1, and the results are shown in Table 2.2. For statistics, two separate batches of each material were made, and each batch was measured three times. The data in Table 2.2 therefore represents the average and 1.s.d. of the combined measurements of both batches. As expected, all of the deconvoluted regions are within error of each other.

Table 3.2 Quantification of the deconvoluted XPS C1s regions of DC-GO (optimised) and DC-GO (Chandra).

Carbon Material	C(III) / %	C(I) / %	C(0) / %
DC-GO (optimised)	16.8 ± 0.8	38.9 ± 1.1	44.3 ± 1.6
DC-GO (Chandra)	16.2 ± 0.2	40.8 ± 1.2	43.1 ± 1.3

To further corroborate the XPS data, the ^{13}C ssNMR spectra of both materials were recorded and are shown in Fig. 3.27. Just like XPS, the ^{13}C ssNMR spectra reveal the two materials to be very similar.

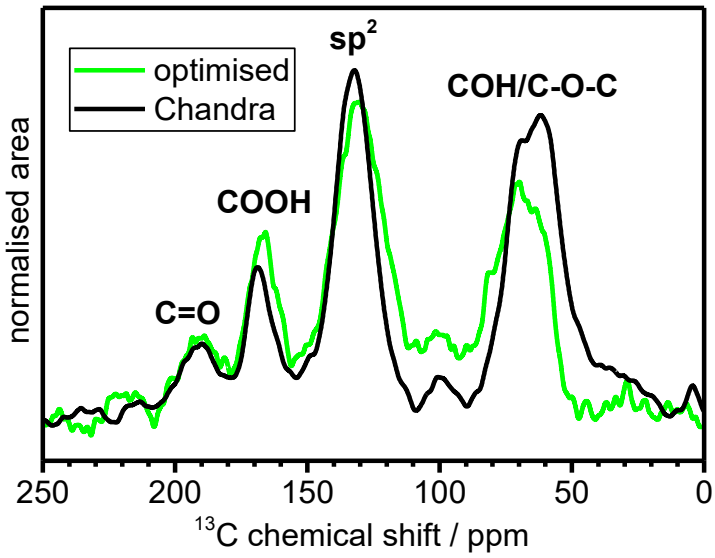

Fig. 3.27 ^{13}C ssNMR spectra of DC-GO (optimised) in green and DC-GO (Chandra) in black.

.

Similarities in the FT-IR and Raman spectra between the two DC-GO materials can also be seen in Fig. A3.4 (appendix). AFM of DC-GO (Chandra) in Fig. A3.5 (appendix) revealed a large distribution of flake sizes, in good agreement with DC-GO (optimised), *c.f.* Fig. 3.11).

In order to determine the optimised conditions required for the preparation of DC-GO (optimised), the temperature, equivalents of $K_2Cr_2O_7$ and reaction time were investigated w.r.t yield and oxidation degree of the material. Initially, the reaction time was decreased from 5 d to 20 h, under the same conditions employed by Chandra *et. al. i.e.* at room temperature (20°C), 75 vol. equiv. of H_2SO_4, 7.5 mass equiv. of $K_2Cr_2O_7$ and 0.75 mass equiv. of $NaNO_3$ per mass equiv. of graphite. However this resulted in a low yielding (18%), slightly less oxidised DC-GO material (appendix Fig. A3.6(a)). On increasing the temperature to 45°C and omitting the $NaNO_3$ from the procedure (in line with current Hummers based oxidation protocols), but retaining the 7.5 equiv. of $K_2Cr_2O_7$, a highly oxidised and high yielding (94%) DC-GO material was produced in only 20 h (*c.f.* appendix Fig. 3.6(b)). This material was found to be similar to the DC-GO prepared by Chandra *et. al.*, and in fact turned out to be the optimised method for preparing DC-GO and is analogous to the material characterised in Fig. 3.26(a), *i.e.* DC-GO (optimised).

To investigate the new procedure more thoroughly, the number of $K_2Cr_2O_7$ equivalents was varied whist keeping the temperature (45°C) and reaction time (20 h) constant. The yield of DC-GO was calculated and its oxidation degree was determined by deconvolving the XPS C1s regions. The results are shown in Fig. 3.28 and the C1s regions in appendix Fig. A3.7 respectively.

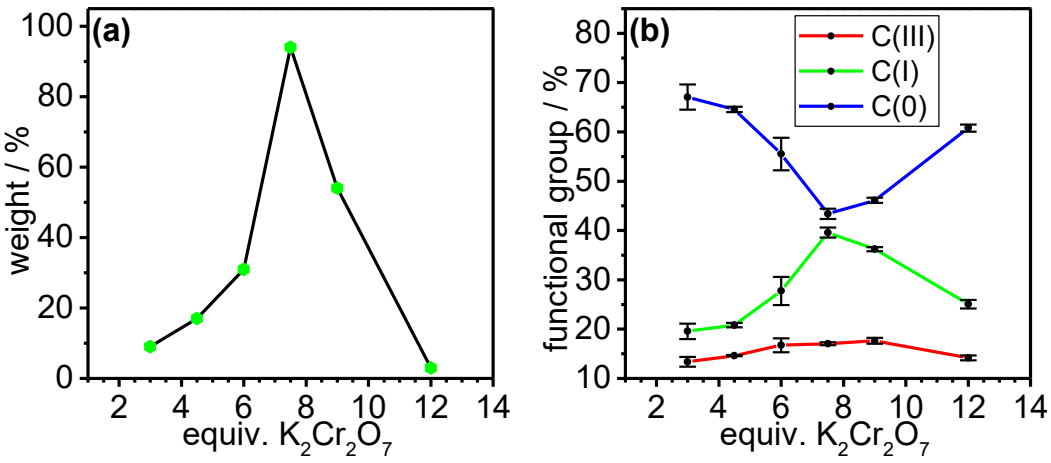

Fig. 3.28 The effect of $K_2Cr_2O_7$ equivalents on the (a) yield and (b) oxidation degree of DC-GO.

In Fig. 3.28 it can be seen that increasing the number $K_2Cr_2O_7$ equivalents from 3 to 7.5 results not only in an increase in yield, but also an increase in oxidation degree. This is evidenced by the increase in C(I) and C(III) species described by the green and red fitted peaks in Fig. 3.28 (b) respectively. Note that since C(II) species overlap between the C(I) and C(III) regions, there will be a C(II) contribution to both the C(I) and C(III) fitted peaks;

but this cannot be accurately quantified. Interestingly, increasing the equivalents further results in a decline in oxidation degree and yield. It is speculated that this may be due to over-oxidation of the material which can result in its decomposition (20). It could also explain why DC-GO exhibits such a large distribution of flake sizes, *i.e*. the fragmentation of larger flakes into smaller ones as a consequence of over-oxidation. It should be noted however, that over-oxidation is not unique to dichromate oxidised GO and can occur under Hummers conditions-see next section on PM-GO. Nonetheless, the results are suggestive that 7.5 equiv. of $K_2Cr_2O_7$ is optimal in achieving highly oxidised GO in high yields.

The preparation of DC-GO was also investigated within a 40 h time period. The optimised 7.5 equivalents of $K_2Cr_2O_7$ was kept constant along with the reaction temperature of 45°C. Once again the yield was calculated and the oxidation degree of each DC-GO sample was determined by deconvolving the XPS C1s region (*c.f*. appendix Fig. A3.8). The results are shown in Fig. 3.29.

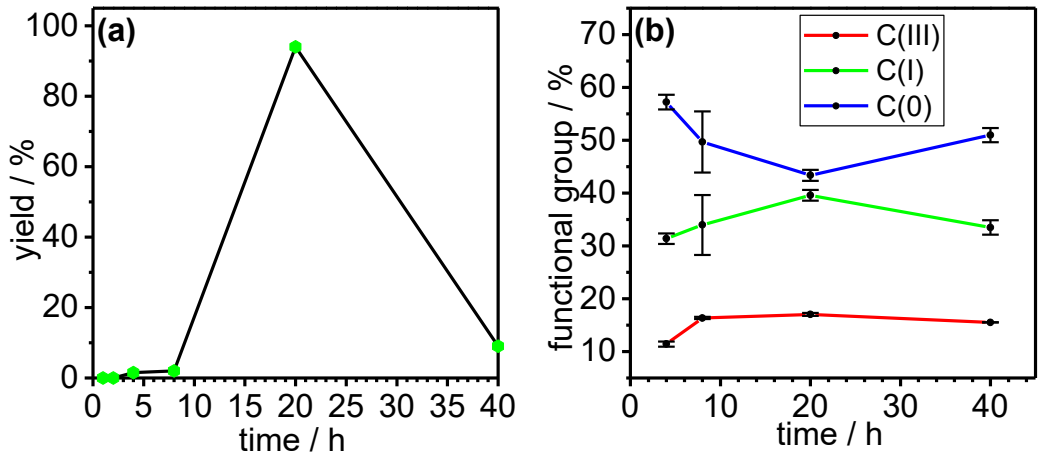

Fig. 3.29 The effect of time on the (a) yield and (b) oxidation degree of DC-GO

It is apparent from Fig. 3.31(a) that a reaction time under 8 h results in little or no yield of DC-GO. Interestingly, the yield rises sharply at 20 h and decreases once again at 40 h. However, it is also clear that oxidation of graphite to DC-GO takes place after only a few hours as evidenced by the reasonably well oxidised DC-GO after 4h (see Fig. 3.29(b)) and appendix Fig. A3.8 (a)). At 8 h the oxidation degree of DC-GO reaches its maximum and remains just as oxidised at 20 h, albeit a much higher yield is obtained at 20 h. At 40 h the DC-GO is less oxidised and the yield has decreased markedly which may be due to over-oxidation, as discussed earlier. Hence the results indicate that DC-

GO is optimally prepared *via* 7.5 equiv. of $K_2Cr_2O_7$ (per mass equiv. of flake graphite) at 45°C for 20 h.

It is noteworthy that there have been attempts to characterise the DC-GO prepared by Chandra *et*. *al*. by other research groups using XPS, but they report a highly reduced material compared with the material reported here (8; 56). We speculate that this is due to the significantly lower equivalents of $K_2Cr_2O_7$ employed and reduced reaction times. In other cases the DC-GO was isolated not through freeze drying, but *via* thermal treatment at 100°C (56), which we show in chapter 4 section 4.6 results in the thermal disproportionation of the material. We therefore conclude that the highly oxidised nature of DC-GO prepared here has not been realised in the literature.

3.7 A closer look at PM-GO

As outlined in the introduction, there are many reported procedures for the preparation of GO using $KMnO_4$ which are based of the original Hummers method (3; 5; 6; 34). The method employed in this work is an eco-friendly modified Hummers method which was reported by Chen *et*. *al*. in 2013 (34). The procedure was specifically chosen for its short and efficient reaction times of 30 and 15 min for the oxidation and exfoliation step respectively, whilst still producing high quality, highly oxidised GO. The procedure also boasts lower equivalents of $KMnO_4$ (3 equiv.) and no $NaNO_3$. Full details of the experimental procedure can be found in chapter 8 section 8.5.

Comparison of PM-GO with DC-GO (optimised) in section 3.3 earlier showed the two materials to be completely different. DC-GO (optimised) for instance displayed a large distribution of flake sizes and was shown to be overall far more oxidised. Nonetheless, the oxidation extent of GO depends on the conditions employed in the synthesis. For illustrative purposes, PM-GO was prepared using the same conditions required to synthesize DC-GO, both *via* our optimised procedure and by Chandra *et*. *al*.'s protocol; the exception of course being that $K_2Cr_2O_7$ was replaced with $KMnO_4$. The PM-GOs prepared in this way are now referred to PM-GO (optimised) and PM-GO (Chandra) respectively (see chapter 8 section 8.6 for full details). Similarly, the original PM-GO prepared using Chen *et*. *al*.'s protocol is now denoted as PM-GO (Chen).

The XPS spectra of PM-GO (optimised) and PM-GO (Chandra) are shown in Fig. 3.30 (b) and (d) respectively. For comparison, the spectra of DC-GO (optimised) and DC-GO (Chandra) are also shown in Fig. 3.30 (a) and (c) respectively.

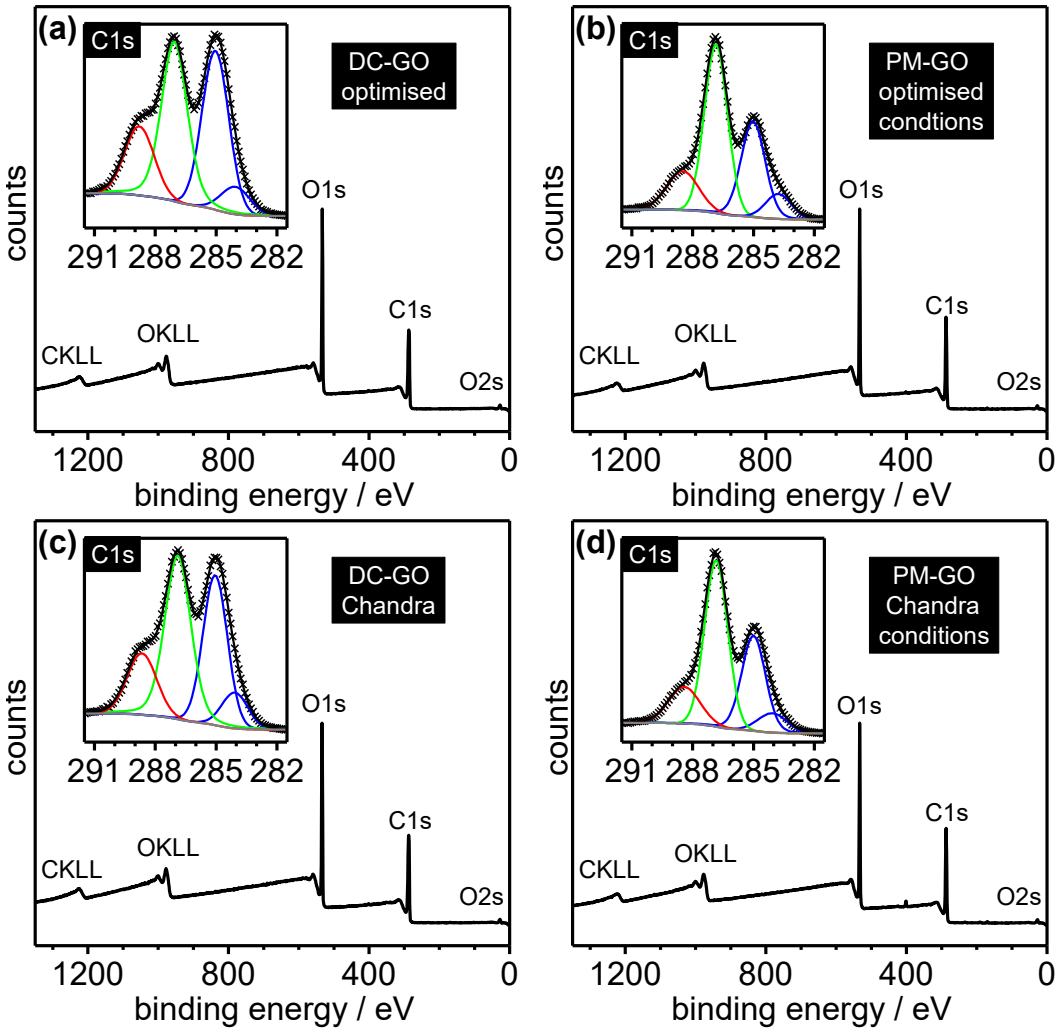

Fig. 3.30 XPS survey (outset) and C1s regions (inset) of DC-GO and PM-GO prepared the optimised DC-GO procedure (a) and (b) and *via* Chandra et. al. procedure (c) and (d) respectively. The crosses represent the experimental data whereas the grey, blue, green, red and black lines are the Shirley background functions, C(0), C(I) and C(III) fitted peaks and peak sum, respectively.

From Fig. 3.30 (b) and (d) it is apparent that PM-GO prepared under these conditions is more oxidised than the PM-GO (Chen), (*c.f.* XPS Fig. 3.3 in section 3.3.1 and Table 3.3 on the next page). The ^{13}C ssNMR spectra (red) in Fig. 3.31 further corroborates the highly oxidised nature of PM-GO prepared in this way. In particular, the intense feature between 60 and 70 ppm (assigned to C(I) species), and the clear formation of carboxylic acids at 170 ppm, mirrors the XPS C1s spectra in Fig. 3.30 (b) and (d). Another intriguing observation is that there is remarkably little difference between PM-GO (Chandra) and

PM-GO (optimised), in the same way as there was little difference between the two DC-GO methodologies.

Direct comparison of the XPS C1s regions of DC-GO and PM-GO (optimised/Chandra) in Fig. 3.30 *via* deconvolution of the fitted peaks (as discussed previously in chapter 2 section 2.1), revealed the DC-GO to be slightly more carboxylated and more graphenic than PM-GO regardless of the procedure (optimised/Chandra *et. al.*) employed. Conversely, PM-GO was shown to contain far more C(I) species. These results are summarised in Table 3.3 and confirmed by ^{13}C ssNMR in Fig. 3.31. The oxidation degree of PM-GO (Chen) is also shown in Table 3.3 for a full comparison. For PM-GO (Chen), the data in Table 3.3 represents the average and 1.s.d. of nine measurements-three separate batches, and each batch measured three times. PM-GO (optimised) and PM-GO (Chandra) statistics represent the average and 1.s.d. of two and three measurements from a single batch respectively. The data for both DC-GO materials are the same as those reported in Table 3.2.

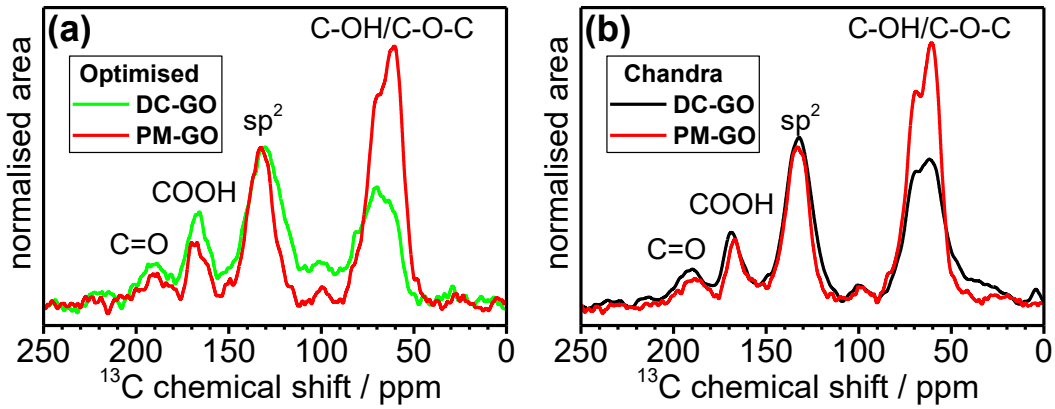

Fig. 3.31 ^{13}C ssNMR of (a) DC-GO (optimised) and PM-GO (optimised) in red and green respectively and (b) DC-GO (Chandra) and PM-GO (Chandra) in back and red respectively.

Table 3.3 Quantification of the XPS C1s deconvolved regions of various carbon materials.

Carbon Material	C(III) / %	C(I) / %	C(0) / %
DC-GO (optimised)	16.8 ± 0.8	38.9 ± 1.1	44.3 ± 1.6
DC-GO (Chandra)	16.2 ± 0.2	40.8 ± 1.2	43.1 ± 1.3
PM-GO (optimised)	15.0 ± 0.3	47.5 ± 0.1	37.5 ± 0.3
PM-GO (Chandra)	15.2 ± 0.4	48.0 ± 0.3	36.8 ± 0.1
PM-GO (Chen)	11.6 ± 1.5	45.2 ± 3.5	43.2 ± 4.9

Given the highly oxidised nature of PM-GO (optimised) and PM-GO (Chandra), it raised the question of whether these materials still showed the same flake size distribution as

PM-GO (Chen), previously illustrated in Fig. 3.12 in section 3.3, or exhibited a distribution of flake sizes similar to DC-GO. Consequently, AFM was performed on PM-GO (optimised) and PM-GO (Chandra) and the images are shown in appendix Fig. A3.9 and A3.10 respectively.

Several high-resolution images, including those in Figs. A3.9 and A3.10, revealed that the conditions utilised in PM-GO (optimised) and PM-GO (Chandra) results in significant flake fragmentation. In fact, when analysing the individual flakes, it became clear that even the smaller flake sizes were often composed of lots of smaller flakes, overlapping with each other. Hence, to accurately determine a size distribution is difficult. Therefore, it can be concluded that these PM-GO conditions results in the over-oxidation and decomposition of the material.

3.8 Conclusions

The preparation and characterisation of three novel carbon nanomaterials (cx-GNFs, nGO and DC-GO (optimised)) are reported and benchmarked against conventional GO (PM-GO). Each are prepared *via* unique methodologies and starting materials, and display remarkably different degrees of oxidation. The cx-GNFs for instance display only carboxylic acids (and some carboxylic anhydrides) as the only oxygen-containing functional group, allowing for facile and non-controversial chemical functionalisation (as will be shown in Ch.5). The nGO is prepared *via* an eco-friendly process which rules out permanganate entirely from the synthesis. The ‘bottle-neck’ workup and purification of conventional nGO preparation in the literature is discarded and replaced with a simple neutralisation and filtration step, yielding only aqueous sodium nitrate and unreacted carbon as the only impurities in the process. DC-GO (optimised/Chandra) is shown for the first time to be a highly oxidised carbon material with more C(III) species than PM-GO, which could constitute an advantage in chemical processing. In essence, it is hoped that the novel carbon materials presented in this chapter will contribute towards the current knowledge and understanding of carbon materials in the literature, in terms of preparation and unique chemical oxidation. In the next chapter, the thermal annealing behaviour of the materials is investigated-another area of great interest and discussion in the carbon literature, owing to the formation of reduced graphene-oxide as an alternative to graphene.

3.9 Chapter 3 References

1. Dimiev AM, Polson TA. 2015. Contesting the two-component structural model of graphene oxide and reexamining the chemistry of graphene oxide in basic media. *Carbon* 93:544-54

2. Rourke JP, Pandey PA, Moore JJ, Bates M, Kinloch IA, et al. 2011. The Real Graphene Oxide Revealed: Stripping the Oxidative Debris from the Graphene-like Sheets. *Angew. Chem. Int. Ed.* 50:3173-7

3. Chen J, Zhang Y, Zhang M, Yao BW, Li YR, et al. 2016. Water-enhanced oxidation of graphite to graphene oxide with controlled species of oxygenated groups. *Chem. Sci.* 7:1874-81

4. Chandra S, Sahu S, Pramanik P. 2010. A novel synthesis of graphene by dichromate oxidation. *Mater. Sci. Eng., B* 167:133-6

5. Dimiev A, Kosynkin DV, Alemany LB, Chaguine P, Tour JM. 2012. Pristine Graphite Oxide. *J. Am. Chem. Soc.* 134:2815-22

6. Marcano DC, Kosynkin DV, Berlin JM, Sinitskii A, Sun Z, et al. 2010. Improved Synthesis of Graphene Oxide. *ACS Nano* 4:4806-14

7. Eigler S, Enzelberger-Heim M, Grimm S, Hofmann P, Kroener W, et al. 2013. Wet Chemical Synthesis of Graphene. *Adv. Mater.* 25:3583-7

8. Muzyka R, Kwoka M, Smedowski L, Diez N, Gryglewicz G. 2017. Oxidation of graphite by different modified Hummers methods. *New Carbon Mater.* 32:15-20

9. Jeong HK, Jin MH, So KP, Lim SC, Lee YH. 2009. Tailoring the characteristics of graphite oxides by different oxidation times. *J. Phys. D: Appl. Phys.* 42

10. Tian B, Wang C, Zhang S, Feng L, Liu Z. 2011. Photothermally Enhanced Photodynamic Therapy Delivered by Nano-Graphene Oxide. *ACS Nano* 5:7000-9

11. Sun X, Liu Z, Welsher K, Robinson JT, Goodwin A, et al. 2008. Nano-Graphene Oxide for Cellular Imaging and Drug Delivery. *Nano Res.* 1:203-12

12. Gahlot S, Sharma PP, Gupta H, Kulshrestha V, Jha PK. 2014. Preparation of graphene oxide nano-composite ion-exchange membranes for desalination application. *RSC Adv.* 4:24662-70

13. Xu Y-T, Guo Y, Li C, Zhou X-Y, Tucker MC, et al. 2015. Graphene oxide nano-sheets wrapped Cu2O microspheres as improved performance anode materials for lithium ion batteries. *Nano Energy* 11:38-47

14. Goncalves G, Vila M, Bdikin I, de Andres A, Emami N, et al. 2014. Breakdown into nanoscale of graphene oxide: Confined hot spot atomic reduction and fragmentation. *Sci Rep* 4

15. Luo J, Cote LJ, Tung VC, Tan ATL, Goins PE, et al. 2010. Graphene Oxide Nanocolloids. *J. Am. Chem. Soc.* 132:17667-9

16. Jung A, Graupner R, Ley L, Hirsch A. 2006. Quantitative determination of oxidative defects on single walled carbon nanotubes. *Phys. Status Solidi B* 243:3217-20

17. Kundu S, Wang Y, Xia W, Muhler M. 2008. Thermal Stability and Reducibility of Oxygen-Containing Functional Groups on Multiwalled Carbon Nanotube Surfaces: A Quantitative High-Resolution XPS and TPD/TPR Study. *J. Phys. Chem. C* 112:16869-78

18. Salzmann CG, Nicolosi V, Green MLH. 2010. Edge-carboxylated graphene nanoflakes from nitric acid oxidised arc-discharge material. *J. Mater. Chem.* 20:314-9

19. Yumitori S. 2000. Correlation of C-1s chemical state intensities with the O-1s intensity in the XPS analysis of anodically oxidized glass-like carbon samples. *J. Mater. Sci.* 35:139-46

20. Eigler S, Dimiev A. 2017. Functionalization and Reduction of Graphene Oxide. In *Graphene Oxide. Fundamental and Applications*. London: Wiley and Sons

21. Fujimoto A, Yamada Y, Koinuma M, Sato S. 2016. Origins of sp(3)C peaks in C-1s X-ray Photoelectron Spectra of Carbon Materials. *Anal. Chem.* 88:6110-4

22. Lerf A, He HY, Forster M, Klinowski J. 1998. Structure of graphite oxide revisited. *J. Phys. Chem. B* 102:4477-82

23. Rosillo-Lopez M, Salzmann CG. 2016. A simple and mild chemical oxidation route to high-purity nano-graphene oxide. *Carbon* 106:56-63

24. Hadzi D, Novak A. 1955. INFRA-RED SPECTRA OF GRAPHITIC OXIDE. *J. Chem. Soc. Faraday Trans.* 51:1614-20

25. Brooks CJ, Eglinton G, Morman JF. 1961. INFRARED SPECTRA OF ARYL CARBOXYLIC ACIDS AND THEIR ESTERS. *J. Am. Chem. Soc.*:106-&

26. Williams D, Fleming I. 2008. *Spectroscopic Methods in Organic Chemistry*. UK: McGraw-Hill Education

27. Dimiev AM, Alemany LB, Tour JM. 2013. Graphene Oxide. Origin of Acidity, Its Instability in Water, and a New Dynamic Structural Model. *ACS Nano* 7:576-88

28. Acik M, Lee G, Mattevi C, Pirkle A, Wallace RM, et al. 2011. The Role of Oxygen during Thermal Reduction of Graphene Oxide Studied by Infrared Absorption Spectroscopy. *J. Phys. Chem. C* 115:19761-81

29. Beams R, Cancado LG, Novotny L. 2015. Raman characterization of defects and dopants in graphene. *AIP Adv.* 27

30. Tuinstra F, Koenig JL. 1970. RAMAN SPECTRUM OF GRAPHITE. *J. Chem. Phys.* 53:1126-&

31. Maultzsch J, Reich S, Thomsen C. 2004. Double-resonant Raman scattering in graphite: Interference effects, selection rules, and phonon dispersion. *Phys. Rev. B* 70

32. Saito R, Jorio A, Souza AG, Dresselhaus G, Dresselhaus MS, Pimenta MA. 2002. Probing phonon dispersion relations of graphite by double resonance Raman scattering. *Phys. Rev. Lett.* 88

33. Pimenta MA, Dresselhaus G, Dresselhaus MS, Cancado LG, Jorio A, Saito R. 2007. Studying disorder in graphite-based systems by Raman spectroscopy. *Phys. Chem. Chem. Phys.* 9:1276-91

34. Chen J, Yao BW, Li C, Shi GQ. 2013. An improved Hummers method for eco-friendly synthesis of graphene oxide. *Carbon* 64:225-9

35. Rosillo-Lopez M, Lee TJ, Bella M, Hart M, Salzmann CG. 2015. Formation and chemistry of carboxylic anhydrides at the graphene edge. *RSC Adv.* 5:104198-202

36. Gomez S, Rendtorff NM, Aglietti EF, Sakka Y, Suarez G. 2016. Surface modification of multiwall carbon nanotubes by sulfonitric treatment. *Appl. Surf. Sci.* 379:264-9

37. Pistone A, Ferlazzo A, Lanza M, Milone C, Iannazzo D, et al. 2012. Morphological Modification of MWCNT Functionalized with HNO3/H2SO4 Mixtures. *J. Nanosci. Nanotechnol.* 12:5054-60

38. Rahmam S, Mohamed NM, Sufian S. 2014. Effect of acid treatment on the multiwalled carbon nanotubes. *MATER. RES. INNOV.* 18:196-9

39. Ye RQ, Xiang CS, Lin J, Peng ZW, Huang KW, et al. 2013. Coal as an abundant source of graphene quantum dots. *Nat. Commun.* 4

40. Datsyuk V, Kalyva M, Papagelis K, Parthenios J, Tasis D, et al. 2008. Chemical oxidation of multiwalled carbon nanotubes. *Carbon* 46:833-40

41. Salzmann CG, Llewellyn SA, Tobias G, Ward MAH, Huh Y, Green MLH. 2007. The role of carboxylated carbonaceous fragments in the functionalization and spectroscopy of a single-walled carbon-nanotube material. *Adv. Mater.* 19:883-+

42. Eigler S, Dotzer C, Hirsch A. 2012. Visualization of defect densities in reduced graphene oxide. *Carbon* 50:3666-73

43. Cancado LG, Jorio A, Ferreira EHM, Stavale F, Achete CA, et al. 2011. Quantifying Defects in Graphene via Raman Spectroscopy at Different Excitation Energies. *Nano Lett.* 11:3190-6

44. Likodimos V, Steriotis TA, Papageorgiou SK, Romanos GE, Marques RRN, et al. 2014. Controlled surface functionalization of multiwall carbon nanotubes by HNO3 hydrothermal oxidation. *Carbon* 69:311-26

45. Li ZQ, Lu CJ, Xia ZP, Zhou Y, Luo Z. 2007. X-ray diffraction patterns of graphite and turbostratic carbon. *Carbon* 45:1686-95

46. Wagoner G. 1964. TURBOSTRATIC GRAPHITE. *Carbon* 1:404-5

47. Mu SJ, Su YC, Xiao LH, Liu SD, Hu T, Tang HB. 2013. X-Ray Diffraction Pattern of Graphite Oxide. *Chin. Phys. Lett.* 30

48. Novoselov KS, Geim AK, Morozov SV, Jiang D, Zhang Y, et al. 2004. Electric field effect in atomically thin carbon films. *Science* 306:666-9

49. Ning GQ, Fan ZJ, Wang G, Gao JS, Qian WZ, Wei F. 2011. Gram-scale synthesis of nanomesh graphene with high surface area and its application in supercapacitor electrodes. *Chem. Commun.* 47:5976-8

50. Jensen AB, Jensen-Holm H, Schröter M. 2000. Catalytic removal of NOx, VOC and dioxin Haldor Topsøe A/S

51. Jorio A, Souza AG, Dresselhaus G, Dresselhaus MS, Swan AK, et al. 2002. G-band resonant Raman study of 62 isolated single-wall carbon nanotubes. *Phys. Rev. B* 65

52. Dresselhaus MS, Dresselhaus G, Jorio A, Souza AG, Saito R. 2002. Raman spectroscopy on isolated single wall carbon nanotubes. *Carbon* 40:2043-61

53. Ferrari AC, Robertson J. 2000. Interpretation of Raman spectra of disordered and amorphous carbon. *Phys. Rev. B* 61:14095-107

54. Puech P, Flahaut E, Bassil A, Juffmann T, Beuneu F, Bacsa WS. 2007. Raman bands of double-wall carbon nanotubes: comparison with single- and triple-wall carbon nanotubes, and influence of annealing and electron irradiation. *J. Raman Spectrosc.* 38:714-20

55. Shi ZJ, Lian YF, Liao FH, Zhou XH, Gu ZN, et al. 2000. Large scale synthesis of single-wall carbon nanotubes by arc-discharge method. *J. Phys. Chem. Solids* 61:1031-6

56. Sitko R, Turek E, Zawisza B, Malicka E, Talik E, et al. 2013. Adsorption of divalent metal ions from aqueous solutions using graphene oxide. *Dalton Trans.* 42:5682-9

Chapter 4: Formation of Carboxylic Anhydrides at the Graphene Edge

4.1 The thermal annealing of GO

In 1965 Boehm and Scholz demonstrated that the thermal decomposition of graphene oxide (GO) varied significantly between samples, particularly if metal salts were present which decreased the thermal stability of GO (1). More recently, it has been demonstrated that GOs contaminated with potassium salts are highly flammable and a serious cause for concern should scaling up production of GO (using $KMnO_4$) reach an industrial level (2).

Despite the variation between different GOs, the thermal annealing of GO under inert conditions can be considered a three-stage process. In the first stage, physisorbed water is removed below 120°C (3-9). This is accompanied by a sharp exfoliation step in the second stage, centered at ~200°C, in which a large volume of gas is produced and constitutes the removal of most of the oxygen containing functional groups (oxo-groups) on GO (3-9). In the third and final stage, the removal of the remaining more thermally stable oxo-groups occurs, followed by the graphitisation of GO to defective graphene/graphite (10; 11). It is noteworthy that the rate at which GO is annealed has a strong influence on the TGA profile. This is clearly illustrated in Fig. 4.1 which compares the annealing of GO at 1°C and 5°C min^{-1} respectively under a nitrogen atmosphere (100 $mL.min^{-1}$). For comparison, the TGA curve of reduced GO (rGO) is also shown. As expected, annealing GO results in a sharp mass loss at ~200°C, however at the faster annealing rate of 5°C min^{-1} the mass loss is far more pronounced, resulting in the loss of all oxygen functionality. Conversely, at 1°C min^{-1} the more thermally stable oxygen functional groups remain after the initial exfoliation step at ~200°C and are gradually removed afterwards. RGO by contrast, exhibits no significant mass loss features as predicted, due to the absence/small quantities of oxygen functionality.

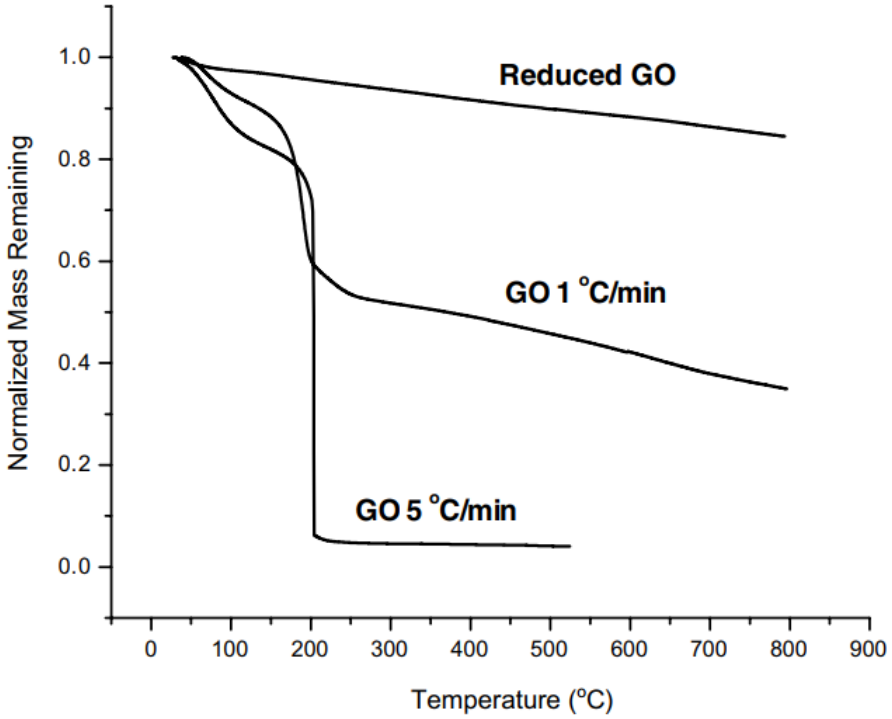

Fig. 4.1 Normalised TGA plots for GO and reduced GO. The downward slopes are due to normal instrument drift. Reprinted from reference [8] with permission from Elsevier.

The rapid exfoliation of GO at ~200°C can occur in an explosive or non-explosive fashion (2; 12). In the former case, the decomposition rate of the oxo-groups (mainly epoxides and hydroxyls) exceeds the diffusion/mass transport rates of the evolved gasses out of GO (2; 12; 13). Once the pressure build-up between the GO layers overcomes the van der Waals forces, rapid exfoliation (explosion) ensues (2; 12; 13). Furthermore, the highly exothermic nature of the thermal decomposition (1.6 $kJ.g^{-1}$) creates a thermal runaway *via* the creation of local hotspots, which further catalyses the explosive decomposition. (2; 12). It is also predicted that the mass and dimensions of GO play a deciding role in whether GO undergoes an explosive or non-explosive annealing behaviour (2). In particular, multilayer structures of GO have been shown to undergo explosive thermal decomposition, in contrast to thin films of GO which are non-explosive (2). The non-explosive thermal annealing behaviour of GO occurs when the diffusion rate of the decomposition gases does not reach the critical pressure required to overcome the van der Waals forces between the GO sheets (2; 13). Furthermore, the heat released from the decomposition dissipates at a faster rate than is required to form local hot spots, so a thermal runaway does not occur (2).

It is important to stress that GO is typically annealed as a powder or as a multi-layered film and therefore does not represent a true monolayer of GO.

The role of water in the thermal annealing of GO has also been the subject of debate in the literature (2; 13). Water is known to be present in GO in large quantities, particularly in between the layers (14-16), and therefore might be expected to play role in the rapid thermal exfoliation of GO. Interestingly however, it has been shown that the absence of interstitial water can still result in the explosive thermal decomposition GO(2). Conversely, Acik *et*. *al*. have utilised FT-IR spectroscopy to show that interstitial water is directly responsible for the formation of hole defects in the GO sheet, which subsequently results in the formation of carbonyl species such as ketones and esters (13). They also demonstrate that in single layer GO films the effect is up to four times less pronounced than in multi-layer GO, due to significantly less water present (13).

In 1934, U. Hofmann *et*. *al*. were the first to propose that GO releases CO and CO_2 gas during its thermal decomposition as opposed to O_2, on the basis that the formation of highly reactive oxygen atoms will react with the GO basal plane (17). Indeed, the formation of CO and CO_2 (and absence of O_2) during the thermal annealing of GO has since been confirmed by other research groups (9; 12; 18; 19). Even so, the exact mechanism, nature and composition of all the species evolved during the thermal annealing of GO remains elusive, despite the fact that GO has been known to be thermally unstable since 1859 (20).

Although TGA and MS have shown H_2O, CO and CO_2 to be the most abundant decomposition products of thermally annealed GO (9; 18; 19; 21), recent gas chromatography-mass spectrometry (GC-MS) investigations into the thermal decomposition of GO have demonstrated the evolution of many other organic species (19). Fig. 4.2 illustrates the various species which have been detected by GC-MS.

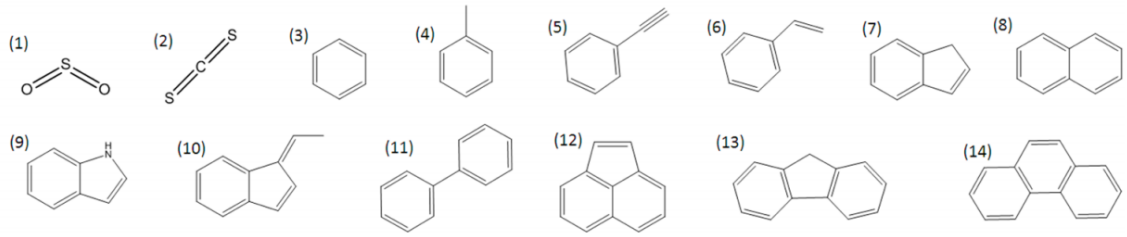

Fig. 4.2 The decomposition products of thermally annealed GO under nitrogen gas elucidated by GC-MS. Adapted from reference [19] with permission from the American Chemical Society.

From Fig. 4.2 it can be seen that a myriad of aromatic hydrocarbons are also produced during the thermal annealing of GO (19). These species are also volatile organic compounds (VOC) and therefore constitute a major health problem in the scaling up of GO as a precursor to graphene (19). The authors note that the large array of VOC produced is suggestive of a radical chain mechanism being a significant decomposition pathway during the annealing of GO. Interestingly, sulfur species such as SO_2 were also observed, indicative of organosulfate groups, whilst the formation of carbon disulphide (CS_2) is further evidence of a radical mechanism involving radical carbon species (19). It is noteworthy that the formation of SO_2 as a thermal decomposition product of GO was first proposed by Boehm and Scholz in 1966 (22). Eigler *et. al*. later demonstrated using TGA-MS that organosulfate groups are cleaved from GO at annealing temperatures between 200 and 300°C, whilst inorganic sulfate is removed at much higher temperatures, typically between 700 and 800°C (9). The TGA-MS data in Fig. 4.3 shows the major gasses evolved during the thermal annealing of GO (9). As expected, physisorbed H_2O (*m*/*z* 18) is initially observed followed by the concerted evolution of H_2O, CO (*m*/*z* 28) and CO_2 (*m*/*z* 44) centered at ~180°C. Above this temperature the decomposition of the more thermally stable oxo-groups occurs, producing a similar gaseous mixture. However, the formation of SO_2 (*m*/*z* 64) is also detected in small quantities at ~250°C corresponding to organosulphate (9). Although the desorption peak for SO_2 appears small in the TGA plot, TGA-IR analysis reveals that up to 15% of the mass loss can be attributed to this species (9). Note that in this instance, the formation of inorganic sulphates are not present.

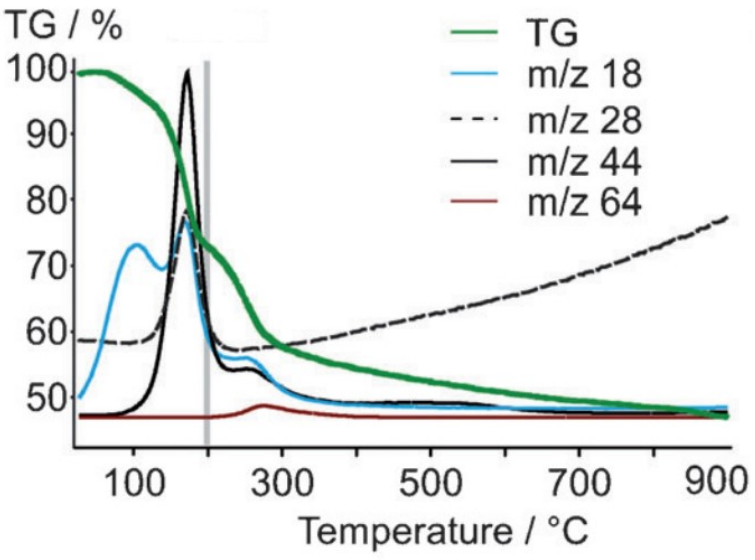

Fig. 4.3 TGA-MS of GO under He gas (80 mL.min^{-1}) at 10°C.min^{-1}; m/z 18, H_2O; m/z 28, CO; m/z 44, CO_2; m/z 64, SO_2. Adapted from reference [9] with permission from Wiley and Sons.

The notion of a radical chain reaction occurring during the thermal annealing of GO has also been suggested by Acik *et*. *al* (23). In this work, it is proposed that H_2O initiates a radical chain reaction which propagates using the existing oxygen functionality present on GO. This in turn generates various oxo-radicals, the nature and composition of which are dependent on the initial ratio of the native oxygen functionality present on GO. Hence the desorption patterns of GO will vary according to this ratio (23).

Undoubtedly, the nature of GO during and after thermal annealing remains controversial (13; 23-26). The concerted evolution of gases in particular makes it difficult to assign evolved gases to a specific functional group. Furthermore, the degree of oxidation on GO will play a deciding role in its decomposition (23; 26). For instance, the conversion of hydroxyl groups into epoxides during longer oxidation times has been demonstrated (26), and therefore the stoichiometry between these two groups will vary significantly. Similarly, the size of the GO flake (as will be demonstrated later in this chapter) can considerably change the annealing behaviour (18; 21). The number of GO layers is also another variable to consider (13). After annealing, the oxo-groups remaining on GO has been suggested to include ethers (23), carbonyls (23) and phenolic groups (24; 25).

The mechanistic details underlying the thermal annealing of GO remains challenging and therefore the application of novel, less structurally controversial carbon nanomaterials are desired. In the next section, the thermal annealing behaviour of such materials are eloquently demonstrated, yielding surprising and opportunistic results.

4.2 Outline of chapter

In this chapter the thermal annealing behaviour of carboxylated graphene nanoflakes (cx-GNFs), nano graphene-oxide (nGO) and dichromate oxidised GO (DC-GO) under vacuum are described and benchmarked against conventional permanganate oxidised GO (PM-GO). The formation of carboxylic anhydrides at the graphene edges of cx-GNFs and nGO is demonstrated experimentally for the first time using FT-IR spectroscopy and *in-situ* mass spectrometry. The mechanism during the thermal annealing of cx-GNFs is fully appreciated and described in detail, as well as the stability of the intermediate products in air and in water.

4.3 The thermal annealing of cx-GNFs

The unique nature of cx-GNFs enables the unambiguous exploration of the chemical properties of COOH groups at the graphene edge. Here we demonstrate that they can transform to the corresponding carboxylic anhydrides with the elimination of water upon heating in vacuum according to the reaction scheme shown in Fig. 4.4(a).

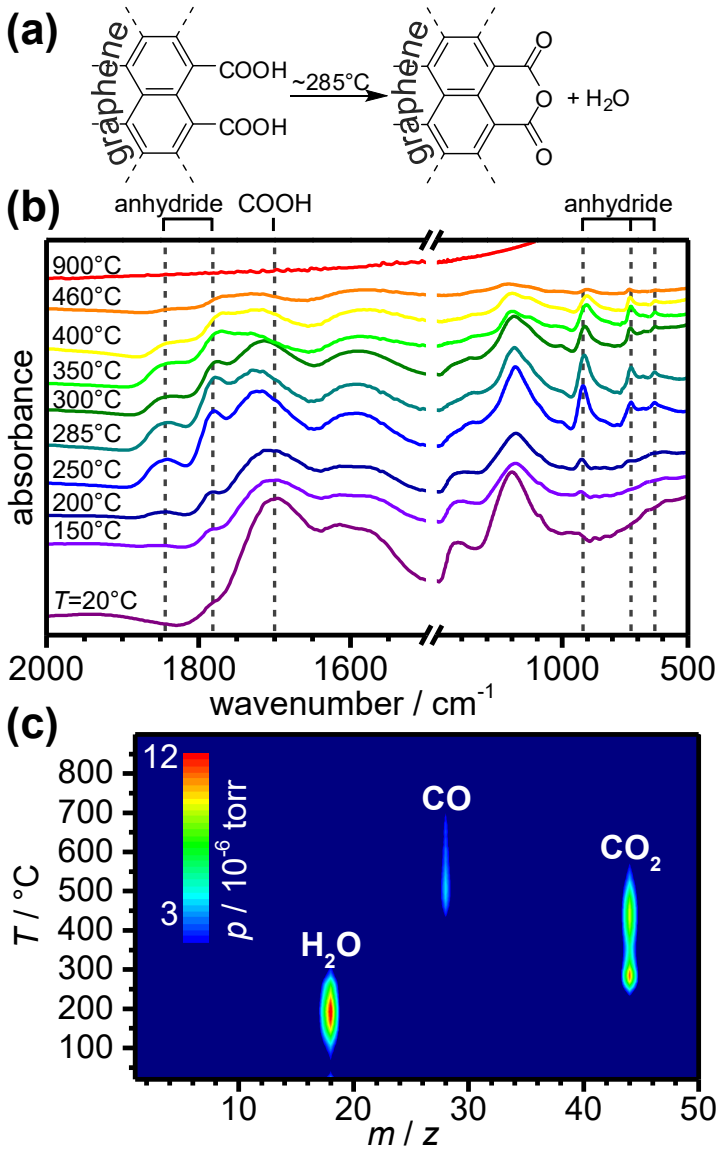

Fig. 4.4 Formation of carboxylic anhydrides upon heating cx-GNFs in high vacuum. (a) Reaction scheme of the anhydride formation. (b) FT-IR spectra of cx-GNFs after heating to the indicated temperatures. (c) In-situ mass spectrometry of desorbing gas species upon heating.

The formation of carboxylic anhydrides is illustrated by the FT-IR spectra in Fig. 4.4(b). The as-made cx-GNFs show an intense peak centered at ~1700 cm^{-1} which is the expected value of the C=O stretching mode of COOH groups (27; 28). Upon heating in vacuum, new C=O stretching peaks emerge at 1781 and 1844 cm^{-1} at the expense of the COOH peak. These two frequencies are indicative for cyclic carboxylic anhydrides and correspond to the asymmetric and symmetric C=O stretching modes, respectively (27; 29-31). Furthermore, the formation of a new peak at ~925 cm^{-1} has also been previously assigned to the C-O-C stretching mode of carboxylic anhydrides (29-31). Interestingly, little is known regarding the less intense bands at ~725 and ~625 cm^{-1} which are also observed during anhydride formation. The conversion of the COOH groups to the anhydride is, however, not fully quantitative which may be due to geometric constraints at the graphene edge such as 'stranded' COOH groups located either between anhydride groups or spatially too distant from other COOH groups so that cyclic anhydrides cannot form. The intensity of the COOH peak decreases markedly above 250°C. However, this does not lead to a further increase of the intensities of the anhydride peaks and is therefore correlated with the thermal decomposition of the 'stranded' COOH groups. The anhydride groups are thermally more stable. However, heating to 460°C leads to almost the complete disappearance of the anhydride C=O stretching peaks as well as the peaks characteristic for anhydrides in the 500 to 1000 cm^{-1} range. At 900°C no appreciable features are observed in the FT-IR spectrum, consistent with the complete removal of polar functional groups.

Close inspection of the FT-IR spectra in Fig. 4.4(b) reveals that the as-made cx-GNF material also displays a weak intensity of the lower wavenumber C=O stretching peak characteristic for anhydrides (1781 cm^{-1}). This suggests that a small fraction of the COOH groups already form anhydrides under ambient conditions before the equilibrium is shifted by heating under vacuum. In chapter 5 we demonstrate how this equilibrium can be exploited to readily chemically functionalise the cx-GNFs.

MS data recorded upon heating cx-GNFs in vacuum corroborate the results from FT-IR spectroscopy (Fig. 4.4(c)). Water is released first upon heating-detailed analysis of the H_2O desorption profile in Fig. 4.5(a) suggests that ~93% of the desorbing water is physisorbed. A second water loss, accounting for the remaining ~7%, is centered at 255°C and is attributed to anhydride formation. (Fig. 4.5(a)). Note that this is in very good agreement with the FT-IR data, placing the anhydride maxima between 250 and 285°C. This is followed by two separate decarboxylation processes centered at about 280 and 440°C, respectively. According to the FT-IR measurements, the first corresponds to the

decarboxylation of the 'stranded' COOH groups and the second to the release of CO_2 due to thermal decomposition of carboxylic anhydrides. Peak fitting of the CO_2 desorption profile shows that about 33% of the CO_2 desorbed is due to stranded COOH groups whilst the remaining 67% is attributed to anhydride decomposition (Fig. 4.5(b)). From this it can be calculated that ~81% of COOH groups on the cx-GNFs can be transformed into carboxylic anhydrides. This value is determined through knowledge of the fact that two carboxylic acids are required to form a single carboxylic anhydride, yet the anhydride itself only undergoes a single decarboxylation step. Hence, from Fig. 4.5(b) the percentage of COOH groups that form anhydrides can be calculated as [(2 x 67.4)/(2 x 67.4) + 32.6] x 100. In the final stage, decarbonylation, the loss of CO, takes place which is consistent with the thermal decomposition pattern of other carboxylic anhydrides (32). Furthermore, analysis of the desorption pattern at *m*/*z* 64 (Fig. 4.5(c)), attributed to SO_2 formation from organosulfate groups, is absent during the annealing of the cx-GNFs. Once again confirming that the cx-GNFs consist solely of COOH groups and a small proportion of the corresponding carboxylic anhydride.

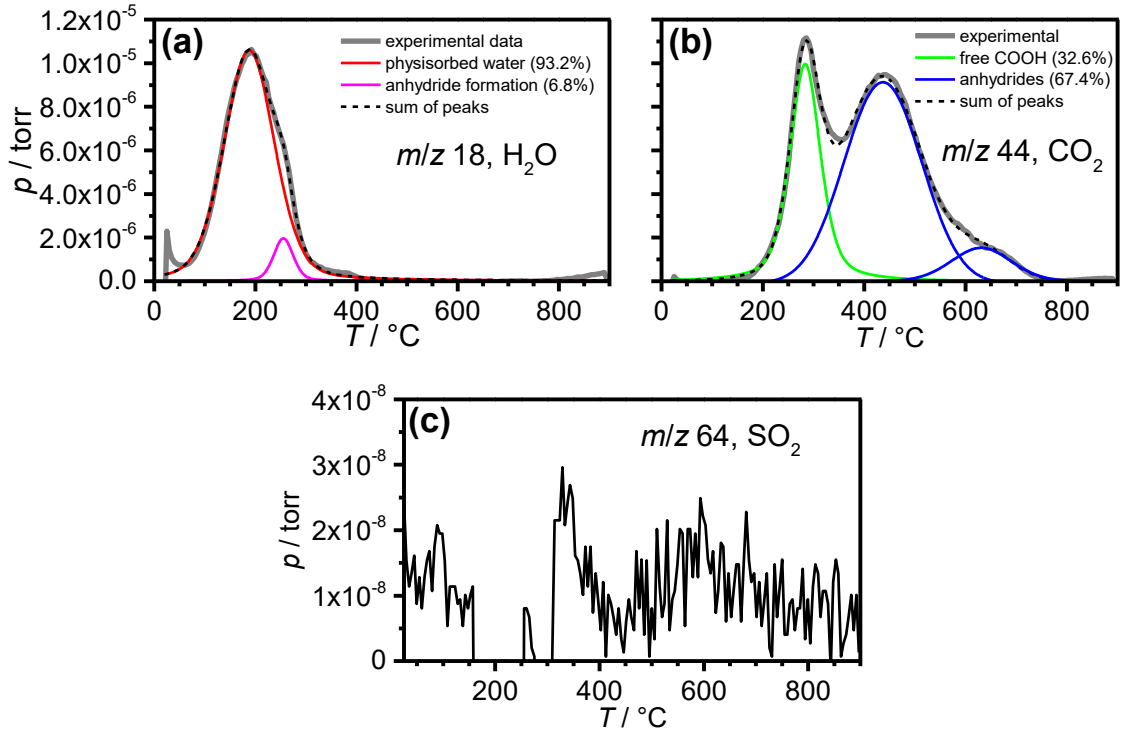

Fig. 4.5 Thermal desorption patterns of cx-GNFs at (a) *m*/*z* 18, H_2O; (b) *m*/*z* 44, CO_2; and (c) *m*/*z* 64, SO_2. The area percentages of the individual components are given in the legend.

In general, the thermal decomposition pattern of cx-GNFs is consistent with what has been observed for aromatic polycarboxylic acids (33). For example, benzene-1,2,3-tricarboxylic acid releases water at 190°C due to anhydride formation followed by decarboxylation of the remaining COOH group at 300°C to give phthalic anhydride. It is noteworthy that the formation and decomposition reactions of carboxylic anhydrides have previously been discussed in the context of chemically functionalised activated carbons (34; 35). However, these investigations were complicated by the chemically diverse nature of activated carbons.

The chemical stability of the anhydride groups (an-GNFs) formed as a result of the thermal desorption of H_2O after heating the cx-GNFs to 285°C was determined by dispersion of an-GNFs in water and exposing an-GNF powder to air. The FT-IR spectra in Fig. 4.6 show that the dispersion in water and exposure to air for 14 days reduced the amount of anhydride groups to the small amount that is present in the as-made material.

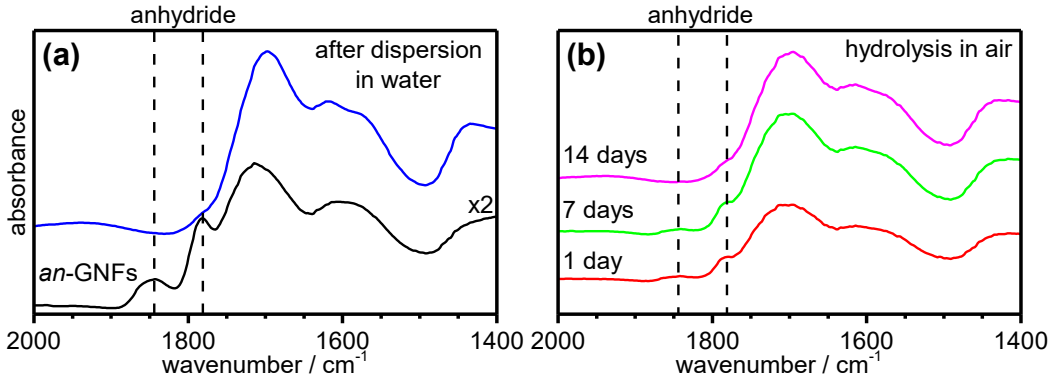

Fig. 4.6 (a) FT-IR spectra of an-GNFs before (black) and after (blue) exposure to liquid water. (b) FT-IR spectra illustrating the hydrolysis of an-GNFs (black) to cx-GNFs upon prolonged exposure to air as indicated by the gradual decrease in the symmetric and asymmetric anhydride stretching modes centered at 1844 cm^{-1} and 1781 cm^{-1} (vertical dashed lines).

For completion, it is also demonstrated that carboxylic anhydride formation can be suppressed. This is achieved with Al^{3+} cations which are known to form some of the strongest complexes with carboxylates (36), and hence should prevent anhydride formation. To do this, a solution of aqueous aluminium chloride (10 mL, 0.1 M) was added to the cx-GNFs (10 mg) and the mixture ultrasonicated for 10 min. After this, the aluminium-chelated GNFs (Al-GNFs) precipitated out of dispersion and were allowed to settle. The mixture was then filtered under reduced pressure through a 0.2 µm track-edged polycarbonate membrane. The Al-GNFs on the membrane were washed with deionised water to remove any excess aluminium chloride before being left to dry on the membrane under reduced pressure. The Al-GNFs were then heated under vacuum to

285°C, in the same way as before with the cx-GNFs, and the *ex-situ* IR was recorded (Fig. 4.7). From the IR spectrum of the Al-GNFs below, it is clear that the formation of carboxylic anhydrides has been suppressed, due to the absence of the anhydride stretching modes at ~1780 and 1840 cm^{-1} respectively. A detailed discussion on the interaction of cx-GNFs with metals is outlined later in Chapter 6.

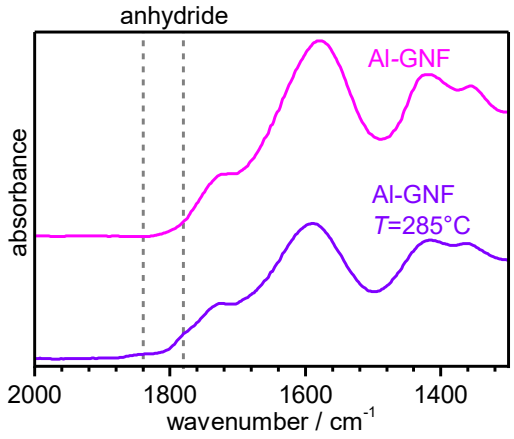

Fig. 4.7 FT-IR spectra of Al-GNFs before and after thermal treatment in vacuum at 285°C.

4.4 The thermal annealing of nGO

The FT-IR spectra and *in-situ* MS pattern representing the thermal annealing behaviour of nGO is shown in Fig. 4.8. Some similarities can clearly be seen between the nGO and the cx-GNF thermal decomposition patterns, whilst some differences are also apparent.

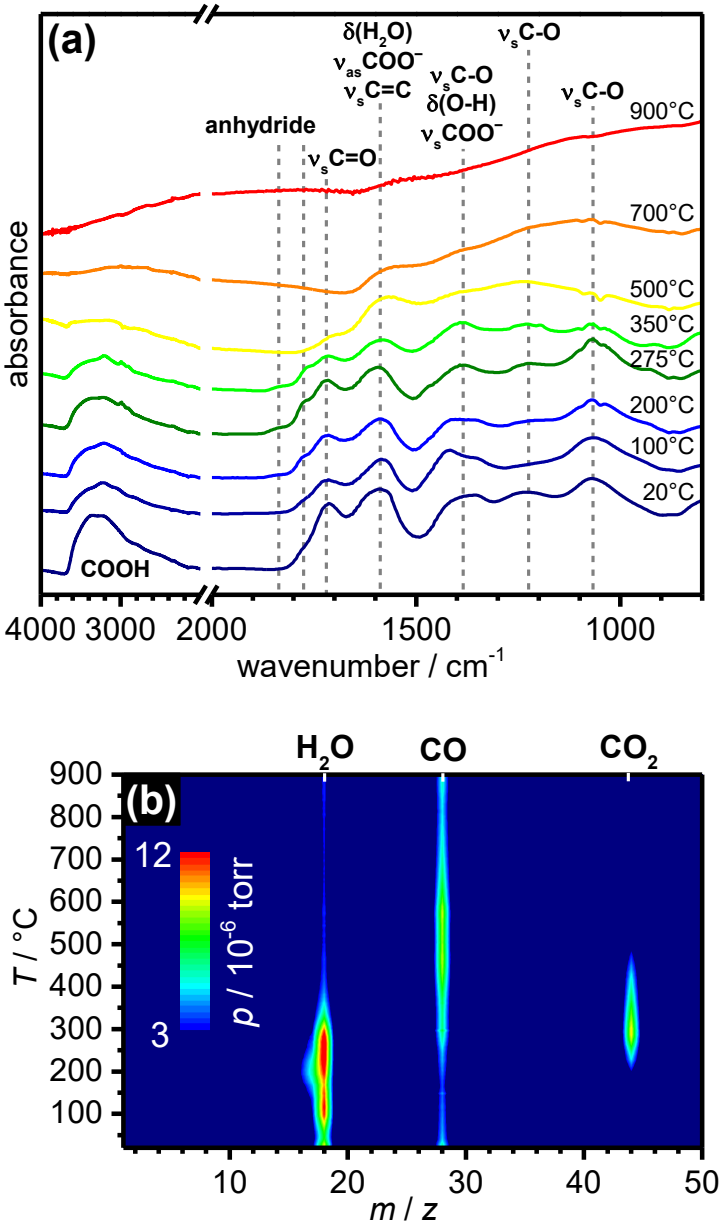

Fig. 4.8 Thermal annealing of nGO under high-vacuum conditions. (a) ATR-IR spectra recorded at room temperature after heating to the indicated temperatures and (b) In situ mass spectrometry pattern.

The FT-IR spectra of the annealed nGO (Fig. 4.8(a)) reveals that cyclic carboxylic anhydrides are also formed during thermal annealing in a similar fashion to the cx-GNFs, albeit to a lesser extent. As expected, the MS pattern in Fig. 4.8(b) confirms that H_2O (*m*/*z* 18) is removed first upon heating and is attributed initially to the removal of physisorbed water and later to anhydride formation, as well the potential decomposition of other oxo-groups such as hydroxyls and epoxides. Similarly, the origin of the CO_2 and CO peaks in the MS pattern above 200°C will have contributions from stranded COOH groups and later on anhydrides, as discussed earlier in the context of cx-GNFs. However, unlike the cx-GNFs, nGO has several other oxygen functionality present such as ketones/aldehydes, epoxides and hydroxyls (as confirmed in the previous chapter). Hence the thermal annealing of nGO is more complicated than the cx-GNFs and thus these species will also contribute towards the detection of CO and CO_2 by MS. Note that since nGO is not prepared in H_2SO_4 media, the formation of organosulfate groups is not possible.

The very fact that nGO can form cyclic anhydrides provides strong evidence for presence of COOH groups in significantly large quantities at the graphene edge, consistent with earlier XPS and ssNMR analysis in chapter 3. It is noted that hydroxyl groups, which may also be present at the graphene edge, could in principle react with carboxylic acids to form lactones and partially contribute towards the lower frequency C=O stretching mode of the anhydride (37). Nonetheless, the presence of the higher frequency C=O mode at ~1840 cm^{-1} certainly confirms the presence of carboxylic anhydrides.

Above 480°C in the MS plot, CO_2 release has declined substantially and is therefore suggestive that all decarboxylation processes have taken place. This is in good agreement with the FT-IR spectrum recorded after heating to 500°C (*cf*. Fig. 4.8(a)) which shows a significant loss of O-H stretching between 3600 $cm^{-1}$and 2500 cm^{-1}, as well as the complete disappearance of the anhydride peaks. Interestingly, the retention of a weak but significant peak at ~1720 cm^{-1}, which later disappears after heating to 700°C, suggests that this carbonyl stretching mode is associated with a functional group which cannot undergo decarboxylation, such as ketones. Furthermore, MS shows a sharp loss of CO between 500 and 700°C, which therefore strongly suggests that the functional groups indicated by the 1720 cm^{-1} peak are ketones and/or aldehydes.

The most intriguing peak in the FT-IR spectrum of thermally annealed nGO is the broad peak centered at ~1587 cm^{-1}, which has been the source of some controversy in the GO literature (38-42). This peak has commonly been assigned to C=C stretching modes as well as the asymmetric stretching mode of carboxylate (38). However, a deuteration

experiment of GO has revealed this peak to shift by ~$2^{1/2}$ wavenumbers to lower frequency which unambiguously means that this peak is associated with the bending mode of water (38). This is understandable for GO which has a relatively low concentration of carboxyl groups and the C=C bonds present are not particularly IR active. Interestingly, heating nGO to 700°C shows that this peak is still present. One can therefore conclude that in case of nGO this peak should mainly be attributed to C=C stretching near the vicinity of polar groups, since water has been removed and COOH groups have decarboxylated at this temperature. This is also consistent with the ssNMR of nGO (chapter 3) which has a larger contribution from sp^2 carbon than GO.

The continuous removal of CO above 700°C in the MS pattern of nGO is consistent with the earlier literature reported by Ganguly *et. al*. (24) and Acik *et. al*. (23) who demonstrate that C-O species such as phenols and ethers are the last to be removed. Indeed, the TGA-MS annealing of GO in Fig. 4.3 illustrates the continual loss of CO even up to 900°C.

4.5 The thermal annealing of PM-GO (Chen), DC-GO (optimised) and PM-GO (optimised)

The MS pattern and corresponding desorption pattern of PM-GO (Chen) during thermal annealing is displayed in Fig. 4.9(a) and (b) respectively.

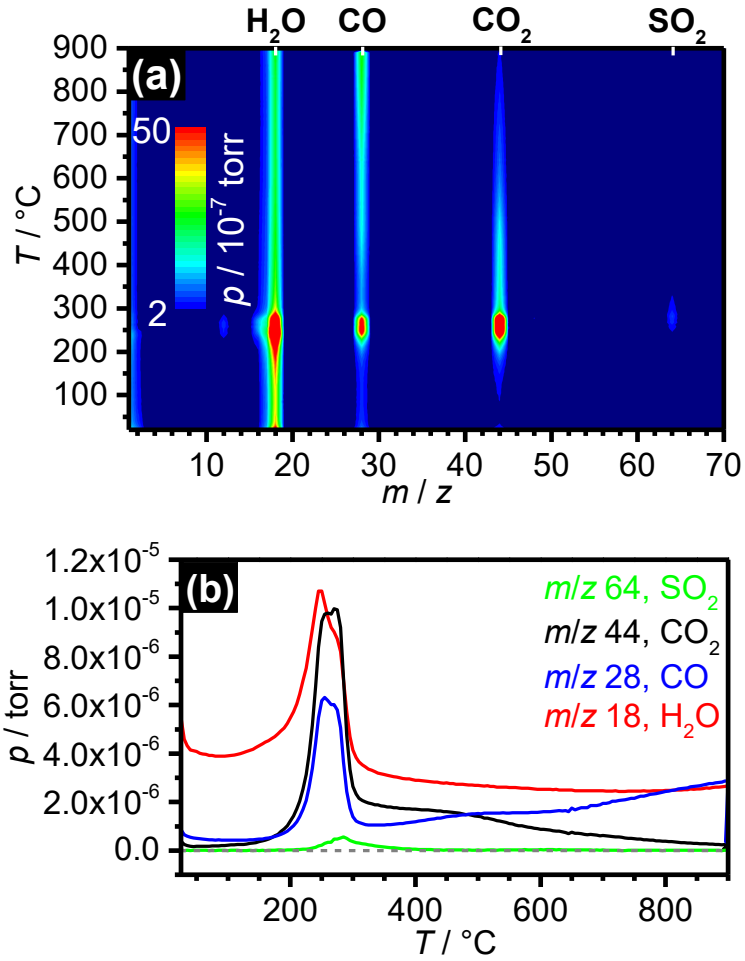

Fig. 4.9 Thermal annealing of PM-GO (Chen) under high-vacuum conditions. (a) *In-situ* MS and (b) corresponding desorption profile showing the major desorbed species. The dashed grey line indicates zero pressure.

From Fig. 4.9 it can be seen that the thermal a of PM-GO (Chen) is in reasonable agreement with the thermal annealing behaviour of GO described by Eigler *et. al* (*c.f.* TGA-MS plot shown earlier in Fig. 4.3). Indeed, H_2O is initially removed, followed by a sharp concerted evolution of gases which can be identified as H_2O, CO and CO_2. Interestingly, however, this simultaneous desorption is observed at ~250°C compared with 180°C in the case of Eigler *et. al*. Furthermore, the formation of SO_2 occurs at the

same time as the main desorption peak in PM-GO (Chen), in contrast to Eigler *et*. *al*. where SO_2 is formed later. The second gaseous desorption, corresponding to the more stable oxo-groups is broader in the case PM-GO (Chen), whilst Eigler *et*. *al*. demonstrate a well-defined mass loss at ~250°C. Remarkably, in both cases the loss of CO continues to increase throughout the thermal treatment, again corroborating the idea that C-O species are the last to be removed (21; 23; 24). The results suggest that whilst the general thermal decomposition pattern of PM-GOs are similar, there are nevertheless differences in functional group composition, flake size etc. that will have an influence on the annealing process. Note that to ensure comparable annealing rates, PM-GO (Chen), and hence all the thermally treated materials reported here, were heated at $10°C.min^{-1}$, in the same way as Eigler *et*. *al*. However, high vacuum conditions were employed as opposed to inert gas which could influence the rate and temperature at which GO decomposes.

The thermal annealing of DC-GO (optimised) is represented by (a) the MS pattern and (b) corresponding desorption pattern in Fig. 4.10 respectively.

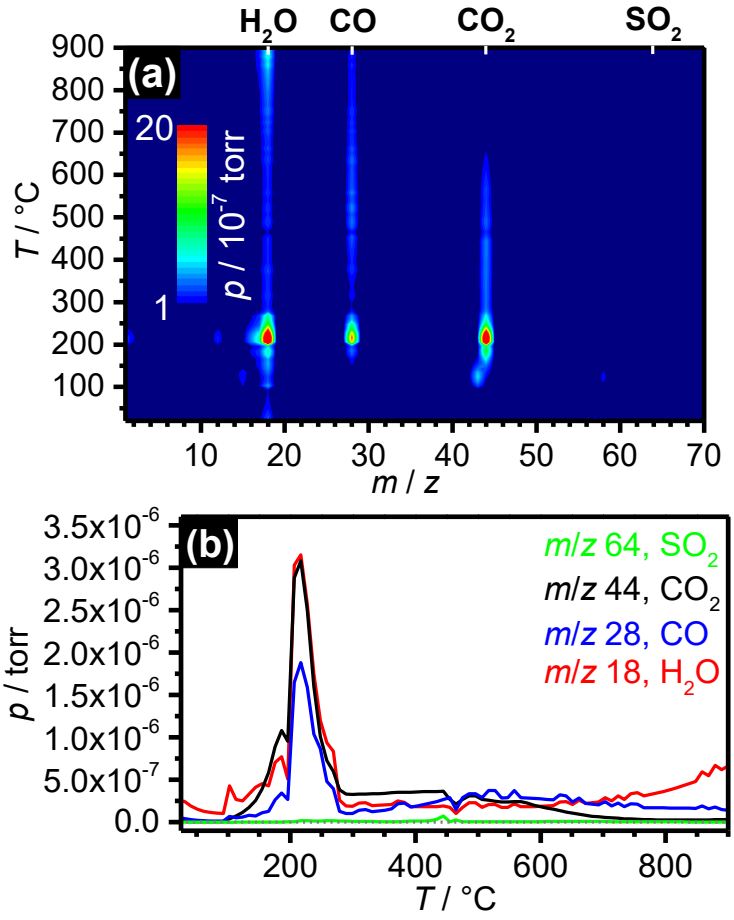

Fig. 4.10 Thermal annealing of DC-GO (optimised) under high-vacuum conditions. (a) *In-situ* MS and (b) corresponding desorption profile showing the major desorbed species.

The thermal annealing pattern of DC-GO (optimised) in Fig. 4.10 shows the characteristic concerted evolution of gases at ~225°C, indicating the material is quite similar to PM-GO (Chen), and GO in general. Intriguingly, the simultaneous desorption of H_2O, CO and CO_2 is not accompanied by SO_2, suggesting that dichromate oxidation does not favour the formation of organosulfate groups. Alternatively, it is also possible that the organosulfate groups are more readily hydrolysed by the lengthier exfoliation step in water. It should also be noted that due to the lower pressures recorded, it is possible that the SO_2 signal cannot be differentiated from the background signal noise. For comparison, the thermal annealing behaviour of PM-GO (optimised) was also performed, and is illustrated in Fig. 4.11 by the (a) MS pattern and (b) desorption profile respectively.

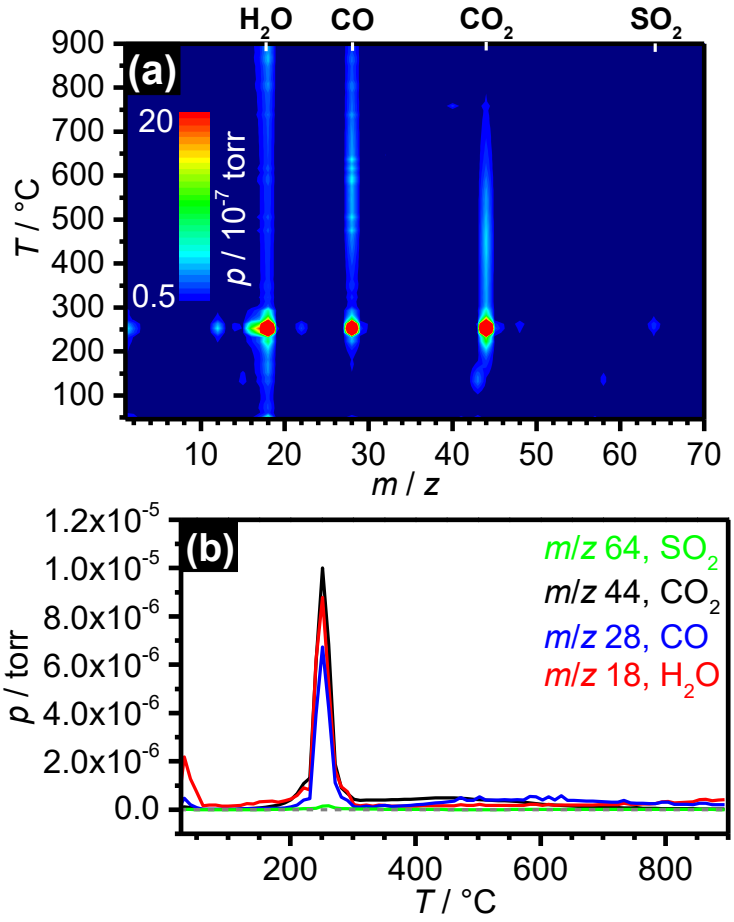

Fig. 4.11 Thermal annealing of PM-GO (optimised) under high-vacuum conditions. (a) *In-situ* MS and (b) corresponding desorption profile showing the major desorbed species.

Similar to DC-GO (optimised), PM-GO (optimised) exhibits a very sharp concerted exfoliation step at ~250°C. A tiny trace of SO_2 can just about be seen above the baseline where the simultaneous evolution of gases is centered. Direct comparison with PM-GO (Chen) in Fig. 4.9 indicates that the preparation of PM-GO (optimised) does not encourage the formation of organosulfate groups. In fact, the thermal annealing of PM-GO (optimised) appears more similar to DC-GO (optimised) than it does PM-GO (Chen), inferring that the methodology of GO preparation is just as important (if not more so) than the nature of the oxidising species.

4.6 Thermal annealing of DC-GO (Chandra) in air

In the last chapter, in section 3.6.1, it was discussed that there had been attempts by other research groups to characterise DC-GO (Chandra) using XPS, which yielded controversial results (43; 44). These materials were found to be significantly reduced compared with the DC-GO (Chandra) reported here. In one case, the material was prepared through identical conditions to ours, yet isolation of the material was achieved through thermal treatment at 100°C (for an unspecified duration), as opposed to lyophilisation (43). Here it is demonstrated that thermal treatment of DC-GO (Chandra) over time results in the annealing of the material, leading to a far more reduced material.

The XPS C1s spectra of the thermally isolated DC-GO (Chandra) in reference (43) is reproduced with permission in Fig. 4.12. A keen eye would soon realise that not only is the material highly reduced in comparison with the material we report, but the assignment of the C=O group is also incorrect. Functional groups such as C=O are well known to be observed in the ~288 eV region (45). The feature which they attribute to C=O at ~285.5 eV is more likely to be due to asymmetry of the main C-C peak, or perhaps even C(I) species such as hydroxyls. The C=O group is therefore unlikely to be present.

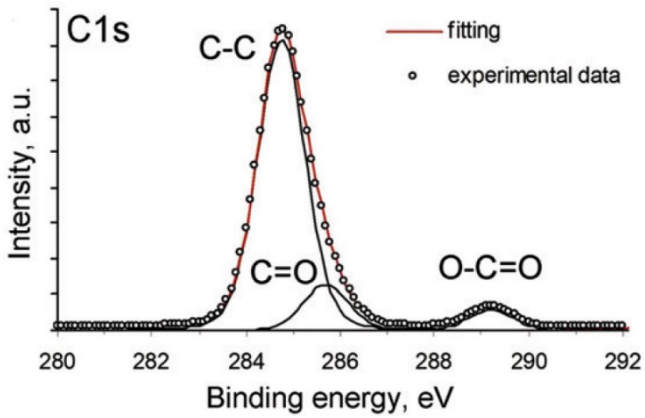

Fig. 4.12 XPS C1s spectrum of DC-GO (Chandra) as reported by Sitko *et. al*. Adapted from reference (43) with permission from The Royal Society of Chemistry.

In order to demonstrate that DC-GO (Chandra) decomposes in air at 100°C, the material was left in an oven at 100°C in air for 16 h, 3 d, and 30 d respectively. Characterisation of the resulting materials by XPS (Fig. 4.13 (b)-(d)) and FT-IR (Fig. 4.14 (b)-(d)) spectroscopy reveal that they are significantly less oxidised compared with the as-made material.

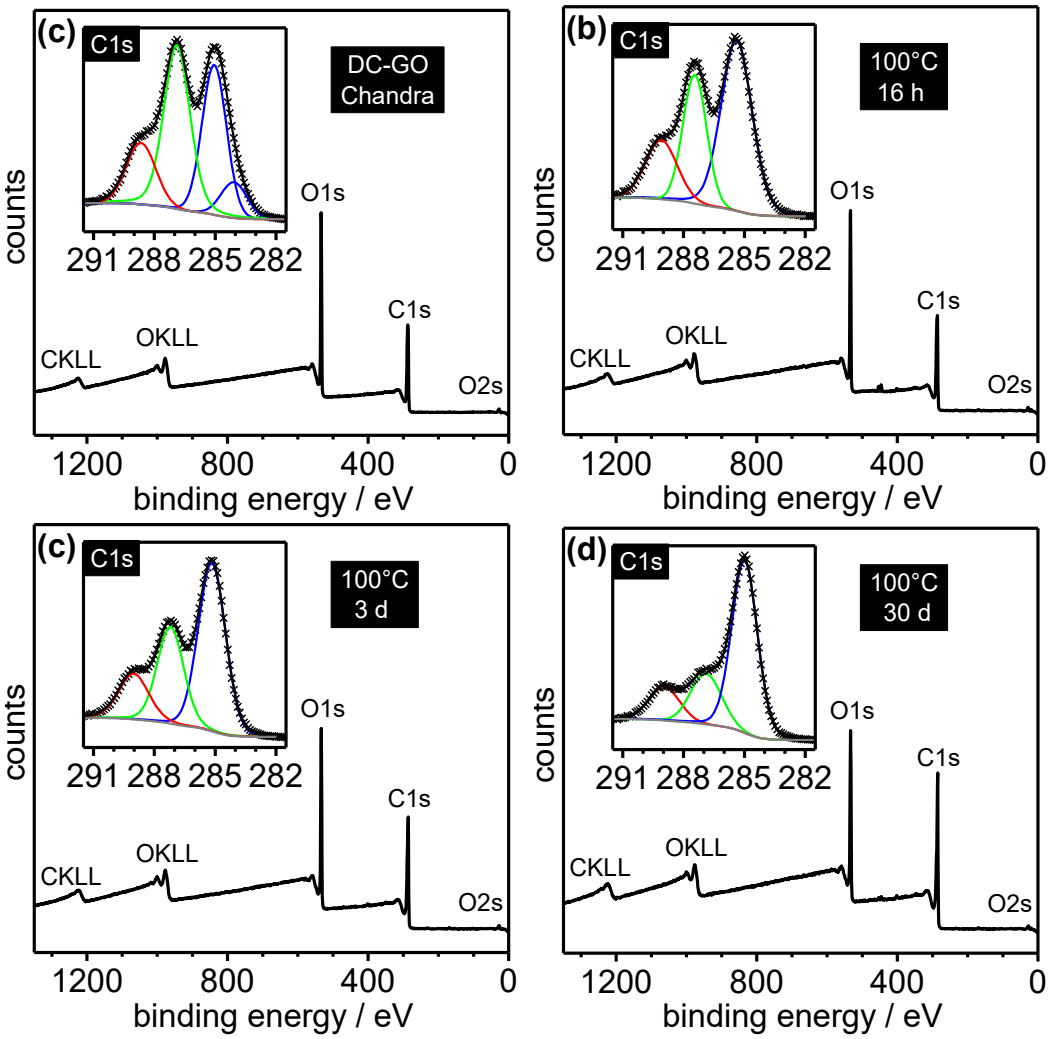

Fig. 4.13 XPS Survey (outset) and C1s regions (inset) of DC-GO (Chandra) after heating at 100°C in air for (a) 0 h, (b) 16 h, (c) 3 d, and (d) 30 d. The crosses represent the experimental data whereas the grey, blue, green, red and black lines are the Shirley background functions, C(0), C(I) and C(III) fitted peaks and peak sum, respectively.

The XPS C1s regions in Fig. 4.13 show a gradual decrease in oxidised carbon species (red and green fitted peaks) with respect to unoxidised carbon (blue) as D-GO (Chandra) is heated for longer times. Quantification of the C1s regions in Fig. 4.13 is shown in Table 4.1 along with the percentage mass loss of the materials after heat treatment in air at 100°C. Interestingly, the C(I) species are removed at a much faster rate than the C(III) functional groups with the C(I)/C(III) ratio decreasing from ~2.6 before heating to ~1.6 after heating for 16 h. The rapid decline in the C(I) functional groups could explain the XPS C1s spectrum reported by Sitko *et. al.* in Fig. 4.12, where no apparent C(I) species are present yet C(III) functionality remains (43). It should be noted that the values

reported for 0 and 3 d in Table 4.1 reflect the mean and error (1.s.d) of three and two measurements, respectively.

Table 4.1 Mass loss and quantification of the functional group changes in the XPS C1s regions of heat-treated DC-GO (Chandra) at various time intervals.

DC-GO (Chandra) 100°C time / *t*	**Mass loss / %**	**C(III) / %**	**C(I) / %**	**C(0) / %**
0	n/a	16.2 ± 0.1	41.9 ± 0.3	41.9 ± 0.3
16 h	16.4	18.3	28.7	53.0
3 d	23.3	16.2 ± 0.6	30.1 ± 0.4	53.7 ± 1.0
30 d	38.6	14.1	21.5	64.4

Similar to the XPS data, the FT-IR spectra of the heat treated DC-GO (Chandra) in Fig. 4.14 reveals that the C=O stretching frequency at ~1720 cm^{-1} remains intense w.r.t the C=C/δ(H_2O) peak at ~1580cm^{-1}, suggesting that C(III) species such as carboxylic acids are fairly stable at 100°C. In particular, there is little difference in the ratio between these peaks at 16 h of heat treatment. However, it should be noted that the intensity of the 1580cm^{-1} peak would be expected to decrease in intensity as a result of the removal of H_2O upon heating. The sharp increase in the peak at ~1200cm^{-1} with increasing heating time is also typically associated with carboxylic acids-*c.f.* cx-GNFs in chapter 3 section 3.3.2.

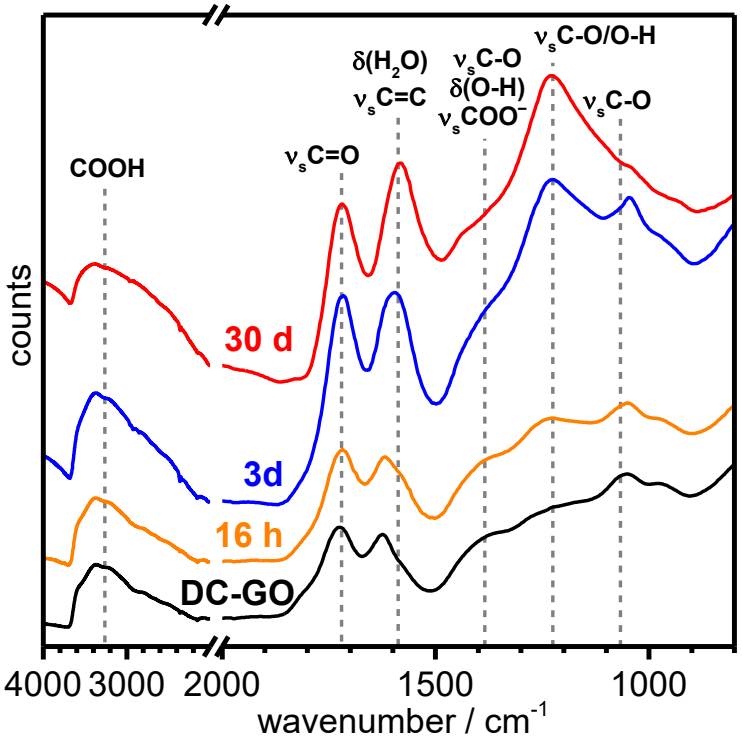

Fig. 4.14 FT-IR spectra of DC-GO (Chandra) after heating at 100°C in air for (a) 0 h (black), (b) 16 h (orange), (c) 3 d (blue), and (d) 30 d (red).

4.7 Conclusions

The formation of carboxylic anhydrides at the graphene edge has been demonstrated experimentally for the first time. Highly carboxylated carbon nanomaterials such as cx-GNFs and nGO have been shown to readily form carboxylic anhydrides upon vacuum annealing. The more thermally stable anhydride groups decompose at significantly higher temperatures than the corresponding acids, giving rise to unique desorption patterns. GO, by contrast undergoes a sharp exfoliation step, resulting in the concerted evolution of gases as the major decomposition pathway. The formation of highly reactive carboxylic anhydrides provides a scope for facile functionalisation with purpose-specific nucleophiles such as amines. In the next chapter, the dynamic equilibrium between the carboxylic acids and anhydrides on cx-GNFs is demonstrated, and fully exploited in the context of chemical functionalisation with well-known amines.

4.8 Chapter 4 References

1. Boehm HP, Scholz W. 1965. Der “Verpuffungspunkt” des Graphitoxids. *Z. Anorg. Allg. Chem.* 335:74-9

2. Qiu Y, Guo F, Hurt R, Kuelaots I. 2014. Explosive thermal reduction of graphene oxide-based materials: Mechanism and safety implications. *Carbon* 72:215-23

3. Hu ZL, Chen YF, Hou QL, Yin RM, Liu FS, Chen H. 2012. Characterization of graphite oxide after heat treatment. *New J. Chem.* 36:1373-7

4. Eigler S, Dimiev A. 2017. Functionalization and Reduction of Graphene Oxide. In *Graphene Oxide. Fundamental and Applications*. London: Wiley and Sons

5. Hassan HMA, Abdelsayed V, Khder A, AbouZeid KM, Terner J, et al. 2009. Microwave synthesis of graphene sheets supporting metal nanocrystals in aqueous and organic media. *J. Mater. Chem.* 19:3832-7

6. Xu XY, Wu T, Xia FL, Li Y, Zhang CC, et al. 2014. Redox reaction between graphene oxide and In powder to prepare In2O3/reduced graphene oxide hybrids for supercapacitors. *J. Power Sources* 266:282-90

7. Wang GX, Yang J, Park J, Gou XL, Wang B, et al. 2008. Facile synthesis and characterization of graphene nanosheets. *J. Phys. Chem. C* 112:8192-5

8. Stankovich S, Dikin DA, Piner RD, Kohlhaas KA, Kleinhammes A, et al. 2007. Synthesis of graphene-based nanosheets via chemical reduction of exfoliated graphite oxide. *Carbon* 45:1558-65

9. Eigler S, Dotzer C, Hof F, Bauer W, Hirsch A. 2013. Sulfur Species in Graphene Oxide. *Chem. A. Eur. J.* 19:9490-6

10. Schniepp HC, Li JL, McAllister MJ, Sai H, Herrera-Alonso M, et al. 2006. Functionalized single graphene sheets derived from splitting graphite oxide. *J. Phys. Chem. B* 110:8535-9

11. Grote F, Gruber C, Borrnert F, Kaiser U, Eigler S. 2017. Thermal Disproportionation of Oxo-Functionalized Graphene. *Angew. Chem. Int. Ed.* 56:9222-5

12. Krishnan D, Kim F, Luo JY, Cruz-Silva R, Cote LJ, et al. 2012. Energetic graphene oxide: Challenges and opportunities. *Nano Today* 7:137-52

13. Acik M, Mattevi C, Gong C, Lee G, Cho K, et al. 2010. The Role of Intercalated Water in Multilayered Graphene Oxide. *ACS Nano* 4:5861-8

14. Dreyer DR, Park S, Bielawski CW, Ruoff RS. 2010. The chemistry of graphene oxide. *Chem. Soc. Rev.* 39:228-40

15. Buchsteiner A, Lerf A, Pieper J. 2006. Water dynamics in graphite oxide investigated with neutron scattering. *J. Phys. Chem. B* 110:22328-38

16. Romanelli G, Liscio A, Senesi R, Zamboni R, Treossi E, et al. 2016. Soft confinement of water in graphene-oxide membranes. *Carbon* 108:199-203

17. Hofmann U, Frenzel A, Csalan E. 1934. Die Konstitution der Graphitsäure und ihre Reaktionen. *Liebigs Ann. Chem* 510:1

18. Rosillo-Lopez M, Lee TJ, Bella M, Hart M, Salzmann CG. 2015. Formation and chemistry of carboxylic anhydrides at the graphene edge. *RSC Adv.* 5:104198-202

19. Sofer Z, Jankovsky O, Simek P, Sedmidubsky D, Sturala J, et al. 2015. Insight into the Mechanism of the Thermal Reduction of Graphite Oxide: Deuterium-Labeled Graphite Oxide Is the Key. *ACS Nano* 9:5478-85

20. Brodie B. 1859. On the Atomic Weight of Graphite. *Philos. Trans. R. Soc. London* 149:249-59

21. Rosillo-Lopez M, Salzmann CG. 2016. A simple and mild chemical oxidation route to high-purity nano-graphene oxide. *Carbon* 106:56-63

22. Boehm HP, Scholz W. 1966. Untersuchungen am Graphitoxyd, IV. Vergleich der Darstellungsverfahren für Graphitoxyd. *Liebigs Ann. Chem.* 691:1-8

23. Acik M, Lee G, Mattevi C, Pirkle A, Wallace RM, et al. 2011. The Role of Oxygen during Thermal Reduction of Graphene Oxide Studied by Infrared Absorption Spectroscopy. *J. Phys. Chem. C* 115:19761-81

24. Ganguly A, Sharma S, Papakonstantinou P, Hamilton J. 2011. Probing the Thermal Deoxygenation of Graphene Oxide Using High-Resolution In Situ X-ray-Based Spectroscopies. *J. Phys. Chem. C* 115:17009-19

25. Lerf A, He HY, Forster M, Klinowski J. 1998. Structure of graphite oxide revisited. *J. Phys. Chem. B* 102:4477-82

26. Jeong HK, Lee YP, Lahaye R, Park MH, An KH, et al. 2008. Evidence of graphitic AB stacking order of graphite oxides. *J. Am. Chem. Soc.* 130:1362-6

27. Boehm HP. 2002. Surface oxides on carbon and their analysis: a critical assessment. *Carbon* 40:145-9

28. Salzmann CG, Nicolosi V, Green MLH. 2010. Edge-carboxylated graphene nanoflakes from nitric acid oxidised arc-discharge material. *J. Mater. Chem.* 20:314-9

29. Meldrum BJ, Rochester CH. 1990. INSITU INFRARED STUDY OF THE MODIFICATION OF THE SURFACE OF ACTIVATED CARBON BY AMMONIA, WATER AND HYDROGEN. *J. Chem. Soc., Faraday Trans.* 86:1881-4

30. Meldrum BJ, Rochester CH. 1990. INSITU INFRARED STUDY OF THE SURFACE OXIDATION OF ACTIVATED CARBON IN OXYGEN AND CARBON-DIOXIDE. *J. Chem. Soc., Faraday Trans.* 86:861-5

31. Yang CQ, Wang XL. 1998. Formation of five-membered cyclic anhydride intermediates by polycarboxylic acids: Thermal analysis and Fourier transform infrared spectroscopy. *J. Appl. Polym. Sci.* 70:2711-8

32. Fields EK, Meyerson S. 1965. BENZYNE BY PYROLYSIS OF PHTHALIC ANHYDRIDE. *Chem. Commun.*:474-&

33. Moldoveanu S. 2010. *Techniques and Instrumentation in Analytical Chemistry*. pp 471-526. Elsevier. 28 pp.

34. Moreno-Castilla C, Carrasco-Marin F, Maldonado-Hodar FJ, Rivera-Utrilla J. 1998. Effects of non-oxidant and oxidant acid treatments on the surface properties of an activated carbon with very low ash content. *Carbon* 36:145-51

35. Figueiredo JL, Pereira MFR, Freitas MMA, Orfao JJM. 1999. Modification of the surface chemistry of activated carbons. *Carbon* 37:1379-89

36. Hunter KA, Liss PS. 1976. MEASUREMENT OF SOLUBILITY PRODUCTS OF VARIOUS METAL-ION CARBOXYLATES. *J. Electroanal. Chem.* 73:347-58

37. Jones RN, Angell CL, Ito T, Smith RJD. 1959. THE CARBONYL STRETCHING BANDS IN THE INFRARED SPECTRA OF UNSATURATED LACTONES. *Can. J. Chem.* 37:2007-22

38. Dimiev AM, Alemany LB, Tour JM. 2013. Graphene Oxide. Origin of Acidity, Its Instability in Water, and a New Dynamic Structural Model. *ACS Nano* 7:576-88

39. Mermoux M, Chabre Y, Rousseau A. 1991. FTIR AND C-13 NMR-STUDY OF GRAPHITE OXIDE. *Carbon* 29:469-74

40. Szabo T, Berkesi O, Forgo P, Josepovits K, Sanakis Y, et al. 2006. Evolution of surface functional groups in a series of progressively oxidized graphite oxides. *Chem. Mater.* 18:2740-9

41. Kovtyukhova NI, Ollivier PJ, Martin BR, Mallouk TE, Chizhik SA, et al. 1999. Layer-by-layer assembly of ultrathin composite films from micron-sized graphite oxide sheets and polycations. *Chem. Mater.* 11:771-8

42. Boehm HP, Heck W, Sappok R, Diehl E. 1964. SURFACE OXIDES OF CARBON. *Angew. Chem. Int. Ed.* 3:669-&

43. Sitko R, Turek E, Zawisza B, Malicka E, Talik E, et al. 2013. Adsorption of divalent metal ions from aqueous solutions using graphene oxide. *Dalton Trans.* 42:5682-9

44. Muzyka R, Kwoka M, Smedowski L, Diez N, Gryglewicz G. 2017. Oxidation of graphite by different modified Hummers methods. *New Carbon Mater.* 32:15-20

45. Yang D, Velamakanni A, Bozoklu G, Park S, Stoller M, et al. 2009. Chemical analysis of graphene oxide films after heat and chemical treatments by X-ray photoelectron and Micro-Raman spectroscopy. *Carbon* 47:145-52

Chapter 5: The Chemistry of Carboxylic Anhydrides at the Graphene Edge

5.1 The covalent functionalisation of GO

The chemical functionalisation of graphene oxide (GO) has widespread use in the literature for photovoltaics (1), optics (2), drug/gene delivery (3; 4), metal sorption (5), sensors (6), Li-ion batteries (7), supercapacitors (8), energy storage (9) and more (10-13). Given the chemically diverse nature of GO, chemical modification may occur *via* basal plane functionalisation (typically through epoxides or hydroxyls) or at the flake edge which harbours a large array of oxygen functionality (oxo-groups), including carboxylic acids and ketones (14; 15). It is noteworthy that in the context of GO, edges are not exclusive to the flake perimeter but also encompass the edges at defect sites. As the GO flake size decreases, the significance of edge functionality will increase, particularly so in the case of nGOs.

The covalent modification of GO is usually achieved through activating GO with more reactive functionality (1-6; 16; 17). although this is not always the case.(18-20). Interestingly, despite hydroxyl and epoxide groups constituting (by far) the majority of the oxo-groups on GO, a lot of emphasis is placed on reactions involving the carboxylic acids (1-6; 16; 17). Typically, the COOH groups on GO are activated using thionyl chloride, (1; 2; 16; 17) oxalyl chloride (21; 22), N-hydroxysuccinimide (NHS) (3; 4; 6) or carbodiimides (5; 17; 23-25) and subsequently treated with the required amine (or other species) to yield the desired modified GO product. Although this type of chemical processing is perfectly reasonable in an organic chemistry context (15), it has a number of insurmountable contradictions w.r.t. GO. Firstly and most obviously, there are not that many COOH groups present on GO (15; 26; 27). An estimate of about 1-2% of COOH groups (of the total carbon content) can be calculated (15; 26; 27) if XPS and ^{13}C-ssNMR are to be taken literally. Consequently, the extent of functionalisation will be limited by this fact, and higher yields are simply impossible. Secondly, epoxides are well known to react directly with amines under mild conditions (14; 28-34). Furthermore, hydroxyls can also potentially react with any of the aforementioned activating reagents (especially thionyl chloride), giving rise to highly reactive functional groups which can then compete with the activated COOH groups (15). It should be noted that hydroxyls and epoxides

constitute approximately half of all the carbon species (including unoxidised carbon) found on GO (15). Finally, modification of the GO sheet is often accompanied by unintentional reduction (17; 20; 35), which is probably due to the harsh conditions employed during the synthesis (36). For instance, the preparation of GO functionalised with amines typically involves a 24 h reflux (or longer) at temperatures of up to 140°C (2; 5; 17; 20). During such a protocol, one cannot expect the stoichiometry of the functional groups on GO to resemble the native structure. Indeed, in the earlier chapter it was demonstrated that GO is not stable to heat treatment in air at 100°C let alone to refluxing in a concoction of chemicals.

Recently, Vacchi *et*. *al*. demonstrated using ^{13}C ssNMR spectroscopy that epoxide groups on GO readily react with amines at room temperature in DMF without the requirement of any activating agents (27). Fig. 5.1 shows how GO was treated with Boc mono-protected triethylene glycol (TEG) diamine as the nucleophile in one of their experiments.

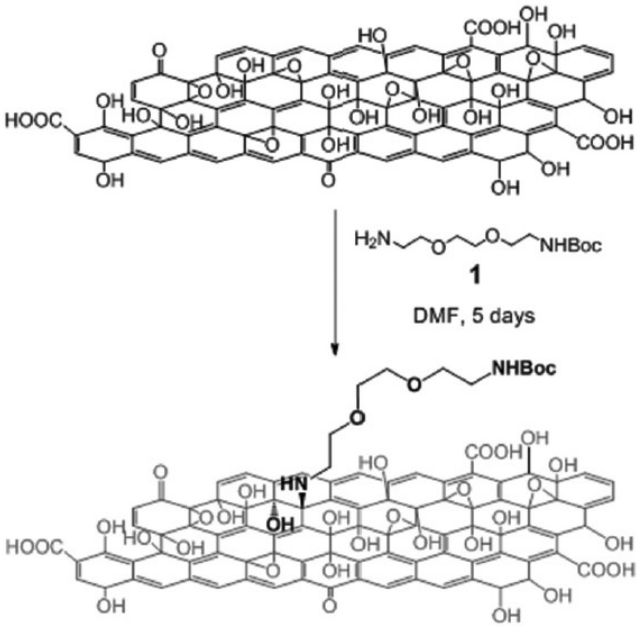

Fig. 5.1 Derivatization of GO via nucleophilic epoxy ring opening by the TEG diamine derivative. For the sake of clarity, only one epoxide group is shown.

The GO was then characterised before (black) and after (red) functionalisation by ^{13}C ssNMR spectroscopy. The results are shown in Fig. 5.2.

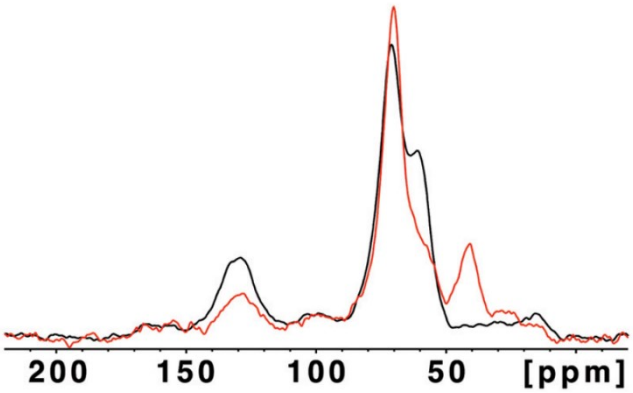

Fig. 5.2 ^{13}C ssNMR of GO before (black) and after (red) functionalisation. Adapted from reference (27) with permission from the Royal Society of Chemistry.

A significant decrease in the intensity of the peak situated at ~60 ppm, attributed to epoxide species, can be seen in the ^{13}C ssNMR spectrum of the functionalised GO (red) w.r.t the unmodified GO (black) in Fig. 5.2. At the same time, an increase in the intensity of the peak at 70 ppm is also observed along with the formation of a new peak at ~40 ppm. This is in good agreement with the opening of the epoxide ring resulting in the formation of new C-N and C-O bonds (both of which appear at ~70 ppm). The presence of methylene groups on the amine are the consequence of the new feature at ~40ppm. The decrease in sp^2 carbon at ~130 ppm in the functionalised GO is also expected since sp^2 C=C bonds are not present in the amine and therefore there will be less overall sp^2 C=C species present in the modified GO. It should be noted that since epoxide/hydroxyl groups are present on both sides of the basal plane of GO, it can result in the steric hindrance of some of these groups towards nucleophilic attack *via* the S_N2 mechanism. Hence the complete conversion of epoxides to C-N/C-O species is unlikely (15).

Vacchi *et. al.* also show that activating the COOH groups with carbodiimides followed by reacting with amines results in the functionalisation of both the activated COOH groups to amides and the epoxide groups to C-N species respectively (27). It was therefore concluded that selective functionalisation of the COOH groups was not possible. Another important observation is that the reduction of GO does not take place after functionalisation, as is often the case (27). This is strong evidence that the reduction of GO is likely to be due to the harsh reaction conditions employed as opposed to the result of chemical modification.

Alternatively, Mungse *et. al.* (37) attempted to selectively functionalise the COOH groups on GO by first reducing GO with hydrazine to remove most of the functionality (in particular epoxides) and then treat the subsequent reduced graphene oxide (rGO) with HNO_3, which is known to introduce COOH into the carbon framework (22). The GO is

then treated with thionyl chloride to activate the COOH groups to the more reactive acid chloride before treatment with octadecylamine (ODA), which yields the corresponding amide (37). A schematic illustrating each of these steps is highlighted in Fig. 5.3.

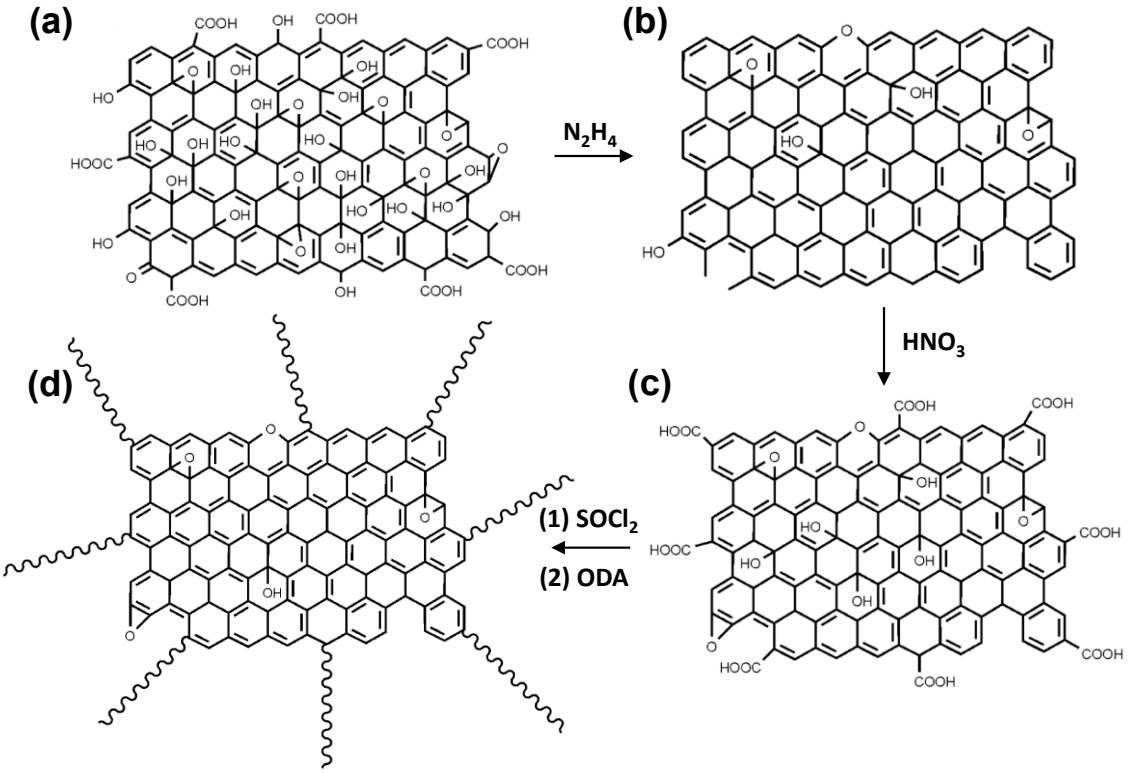

Fig. 5.3 Schematic model of GO before (a) and after (b) reduction with hydrazine, illustrating the distribution of various oxygen functionalities in the basal plane and at edges of sheets, (c) mild oxidation of rGO selectively introduces carboxylic groups at the edges and defects sites of sheets, and (d) ODA-functionalized rGO, prepared by amide linkage on the carboxyl sites of rGO sheets. Adapted from reference (37) with permission from the American Chemical Society.

Although the research conducted by Vacchi and Mungse *et*. *al*. describe a systematic approach to the covalent functionalisation of GO, they (like most other GO functionalisation literature) have one very serious shortcoming. They cannot (conclusively) prove they have covalently modified GO. In the latter case with Mungse *et*. *al*. only XPS and FT-IR data was reported, both of which can be subjective, if analysis of the data is not carefully considered (15; 37). Similarly, even though Vacchi *et*. *al*. utilise ^{13}C ssNMR spectroscopy, it doesn't actually prove that C-N or C(O)N bonds have been formed. In fact, it is entirely possible that in both cases no new covalent bonds have formed and only electrostatic interactions exist. Instead of C-N bonds there can be $C\text{-}O^{-}\ ^{+}NR_3$ interactions instead, similarly amide bonds can be replaced with $C(O)O^{-}\ ^{+}NR_3$ salt

bridges (15). The changes observed in the ^{13}C ssNMR spectrum of Vacchi *et*. *al*. is also consistent with the adsorption of the BOC amine onto the GO sheet. The apparent decrease in the epoxide peak may not have decreased at all, it's just that the C-O and C-N species present on the amine will contribute to the feature at 70 ppm; just like the apparent reduction in the sp^2 C=C peak intensity after chemical modification. To be completely certain of chemical modification, the authors could have also utilised ^{15}N ssNMR spectroscopy which would clearly distinguish between nitrogen present in an amide bond (100-150 ppm) and nitrogen involved in a salt bridge (<100 ppm) (38).

A reasonable undertaking to provide conclusive covalent functionalisation of GO using ^{15}N ssNMR spectroscopy was described by Eigler *et*. *al*.(36) who demonstrated the formation of direct C-N bonds when GO is treated with $^{15}N^{14}N_2$ labelled sodium azide (NaN_3) (36). In this work, N_3^- reacts with epoxide groups forming C-N bonds *via* the S_N2 mechanism as expected. However, given that one of the terminal nitrogen atoms is ^{15}N labelled, one can deduce that the formation of C-^{15}N-^{14}N-^{14}N and C-^{14}N-^{14}N-^{15}N bonds are equally likely and therefore expect the presence of two peaks in the ^{15}N ssNMR spectrum. Indeed, the ^{15}N ssNMR spectra identified two peaks at 91 and 224 ppm which Eigler *et*. *al*. assign to the directly and indirectly ^{15}N labelled C-N_3 bond respectively (36). Interestingly, *ab initio* methods predicted the C-^{15}N-^{14}N-^{14}N peak to appear at 107.4 ppm not the 91 ppm which was experimentally observed.(36) Although the authors state this is in good agreement with their experimental value, it doesn't actually rule out the possibility of salt formation, or even unreacted sodium azide (39). The result is therefore arguably inconclusive.

In summary, the covalent functionalisation of GO has proven to be very challenging, which is largely due to its complex nature. Even with multiple characterisation methods it can be difficult to definitively determine whether a reaction has taken place. One way to remove this controversy is to work with well-defined carbon nanomaterials such as carboxylated graphene nanoflakes (cx-GNFs) whose native structure is well understood.

5.2 Outline of chapter

In this chapter the facile chemical functionalisation of cx-GNFs with amines such as ethylenediamine and cysteamine is demonstrated *via* the dynamic equilibrium that exists between the carboxylic acids and carboxylic anhydrides in aqueous media. Evidence of covalent modification is proposed by consideration of physical properties such as solubility, which are often overlooked in the literature. The functionalised materials are

then shown to interact strongly with gold nanoparticles as well as display a change in zeta potential.

5.3 Direct functionalisation of cx-GNFs with amines

In the previous chapter, it was suggested that carboxylic acids and carboxylic anhydrides on the cx-GNFs exist in a dynamic equilibrium before vacuum annealing. The evidence for this was based on close inspection of the FT-IR spectra of the as-made cx-GNFs as well as the hydrolysed an-GNFs which displayed a weak intensity for the lower wavenumber C=O stretching peak characteristic for carboxylic anhydrides (40). To test whether this hypothesis was correct, the cx-GNFs were treated with either ethylenediamine or cysteamine in aqueous media under ambient conditions (40). Should carboxylic anhydrides exist in equilibrium, the chemical functionalisation of cx-GNFs with amines should take place spontaneously, yielding the corresponding amide plus a free COOH group which could then in principle react with an adjacent COOH group forming another anhydride, leading to a 'cascade of chemical functionalisation' along the carboxylated graphene edge (40).

Hence, in a typical experiment, 20 g of 5 wt % ethylenediamine or cysteamine in deionised water was added to 5 mg of cx-GNFs and the mixtures were allowed to react for one hour at room temperature with occasional swirling. Subsequently, the brown dispersions of eth-GNF or cys-GNF were filtered through a 0.2 μm Whatman polycarbonate membrane to remove any trace of cross-linked flakes. The filtrate was collected, dialysed against deionised water and then freeze dried to yield the functionalised GNF materials.

Fig. 5.4 schematically illustrates the reaction of cx-GNFs with ethylenediamine and cysteamine *via* the formation of the carboxylic anhydride.

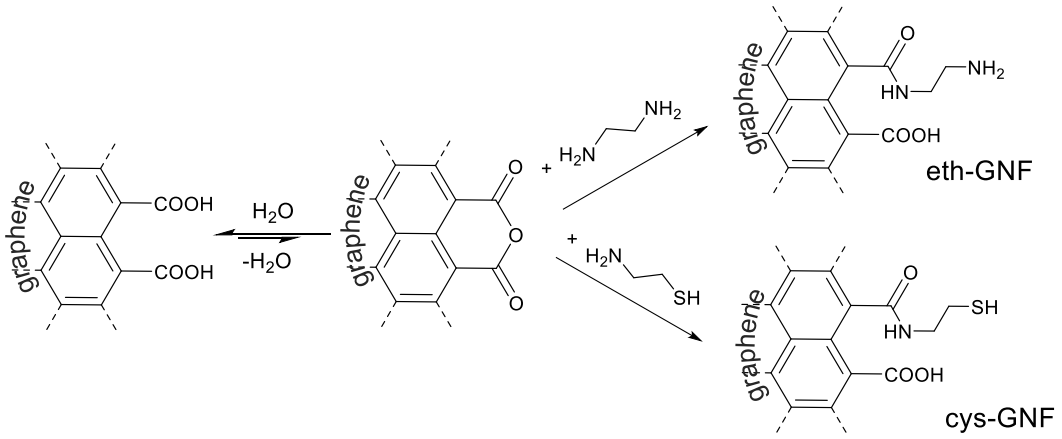

Fig. 5.4 Chemical functionalisation of cx-GNFs with ethylenediamine or cysteamine in aqueous media under ambient conditions *via* the formation of the carboxylic anhydride.

Evidence suggesting the chemical transformation of cx-GNFs into the corresponding amides is illustrated by the XPS and FT-IR data in Fig. 5.5(a)-(d) respectively.

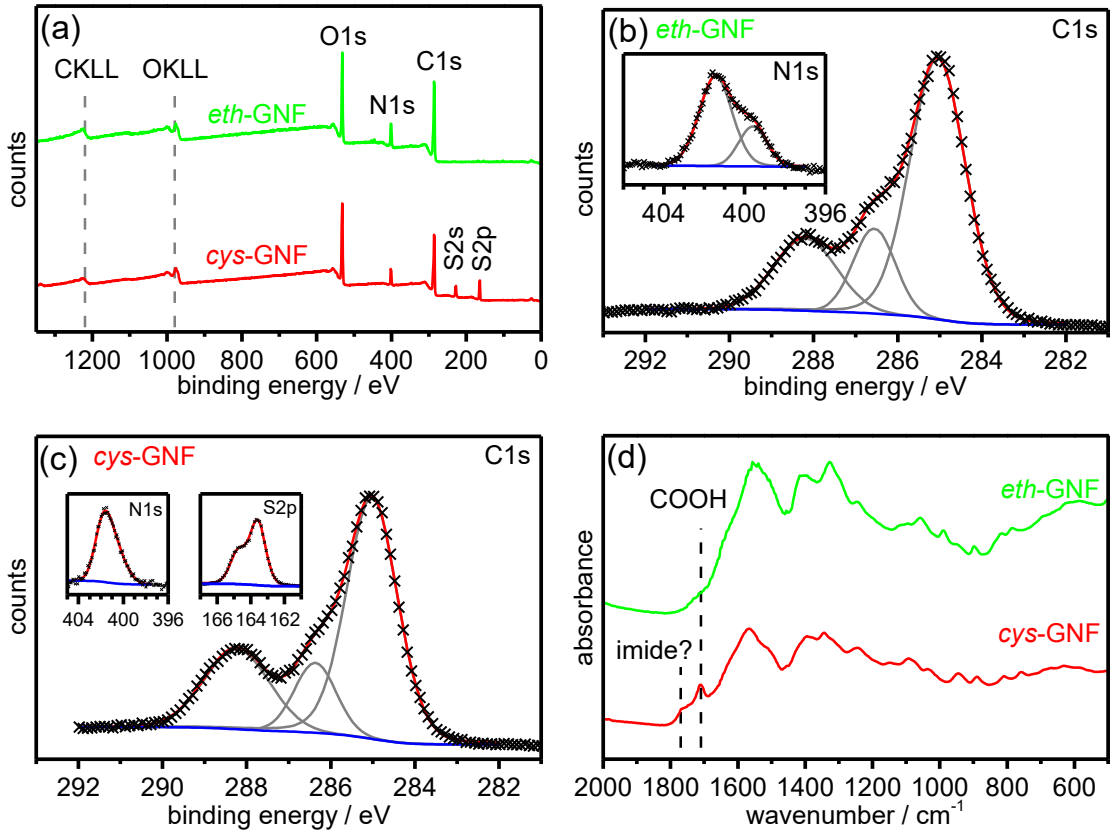

Fig. 5.5 XPS survey spectra of (a) eth-GNFs (green) and cys-GNFs (red). XPS elemental regions of (b) eth-GNFs and (c) cys-GNFs showing C1s regions (outset) and N1s/S2p regions (inset). The crosses represent the experimental data, blue line the background, grey lines the

fitted peaks and the peak sum is shown in red. (d) FT-IR spectra of eth-GNFs (green) and cys-GNFs.

The XPS survey spectra of eth-GNFs in Fig. 5.5(a) confirms the presence of nitrogen species along with carbon and oxygen. A N/C ratio of 0.151 ± 0.007 was determined by measurement of two separate samples which were measured three and two times respectively. The ratio and error reflect the mean and 1.s.d. about the mean respectively. Analysis of the high resolution XPS elemental regions in Fig. 5.5(b) reveals the formation of a third peak in the C1s region at ~286.4 eV which can be attributed to C-N bonds on the ethylenediamine chain (41-43). The shift in the C(III) binding energy from 289.3 eV (in the case of COOH groups on the cx-GNFs) to ~288.2 eV is also consistent with the formation of an amide bond (43). Similarly, the N1s region can be deconvolved into two peaks at ~401.5 and ~399.5 eV corresponding to amide and amine functionality respectively (40). Likewise, the COOH stretching mode in the FT-IR spectrum of eth-GNF (Fig. 5.5(d)) is almost absent and is replaced by a large spectral intensity between 1650 and 1500 cm^{-1}, typical of amide (C=O) stretching and N-H bending modes respectively (44). A similar case can be made for the cys-GNFs, with the exception that sulfur species are also present and thus the N/C ratio is lower (0.09 ± 0.01). Note that this ratio (and associated error) was calculated in the same way as the eth-GNFs, using two samples and measuring them three and two times respectively. The XPS N1s region of cys-GNF can be fitted with a single peak at 401.5 eV corresponding to the amide bond and the terminal thiol group can be attributed to the $S2p_{3/2}$ peak at ~163.5 eV (43; 45). Note that the N/S ratio in the XPS survey spectra is ~1:1 (0.92 ± 0.06) as expected.

In reality, however, a similar situation to GO functionalisation arises. It cannot be conclusively proven that covalent modification has taken place on the eth/cys-GNFs let alone amide functionalisation. In fact, the most suggestive evidence for covalent modification comes from the FT-IR spectra of the cys-GNFs which exhibits a small shoulder at ~1770 cm^{-1} which could be attributed to 5-membered cyclic imides (41; 46). Otherwise, all of the aforementioned XPS and FT-IR data is completely speculative. For instance, the formation of primary ammonium salts are also consistent with the XPS and FT-IR data (47; 48). Other types of covalent modification such as cyclic imides and thioesters are also possible (41; 46; 49-52). Hence the exact nature of eth/cys-GNFs cannot be known for sure. Note, however, that if GO were being considered here, the situation would be even more complicated due to the side reactions which may take place on the basal plane, as discussed earlier.

The dynamic nature of the cx-GNFs is illustrated in Fig. 5.6 and the various scenarios that are possible when cx-GNFs are treated with amines such as ethylenediamine and cysteamine are represented in Fig. 5.7(a) and (b) respectively.

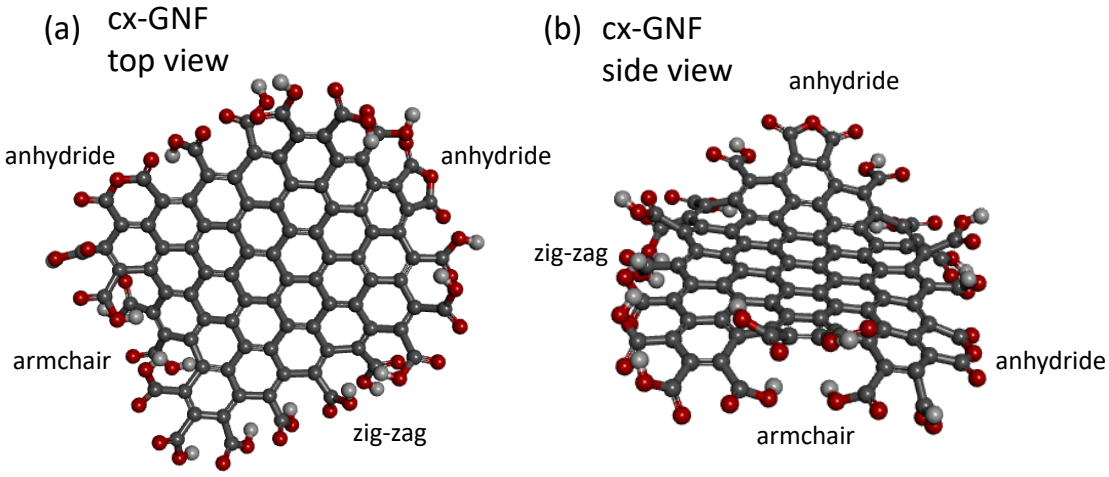

Fig. 5.6 3D geometry optimisation of the cx-GNFs from (a) top view and (b) side view carried out with Discovery Studio visualiser software, using a Dreiding-like forcefield developed by Hahn (53). Carbon, oxygen and hydrogen atoms are shown in black, red and white respectively. Armchair and zig-zag edges, and anhydrides along the flake perimeter are labelled respectively.

It should be noted that the 3D models in Figs. 5.6 and 5.7 are geometry optimisations based on a Dreiding-like forcefield developed by Hahn (53). In this model, the element, bond order, number of bonds and valence are considered, which is based on general force constants and geometry considerations as opposed to individual values. The values used are based on simple hybridisation considerations. In this work, only single molecular structures are considered and therefore van der Waals interactions between adjacent molecules are not taken into consideration.

From Fig. 5.6 it is clear that many permutations of chemical functionality can exist along the flake perimeter. Carboxylic acids can be found at armchair or zig-zag edges and form the corresponding 5- or 6- membered cyclic carboxylic anhydrides respectively. Interestingly, after performing geometry optimisation, the COOH groups at the zig-zag edge (more clearly seen in Fig. 5.6 (a)) are tilted significantly w.r.t to the graphenic basal plane, but are not perpendicular as might be expected for a densely packed structure. Similarly, at alternating armchair edges, COOH groups are directed above and below the basal plane (*c.f.* Fig. 5.6(b)). For simplicity, defects have been excluded from the cx-GNF lattice, yet are expected to exist and also harbour carboxylic acids (and anhydrides). The chemical modification of cx-GNFs with amines can therefore take place *via* anhydrides

or carboxylic acids, as represented in Fig. 5.7. The possibility of physisorption onto to the cx-GNF basal plane can also not be ruled out.

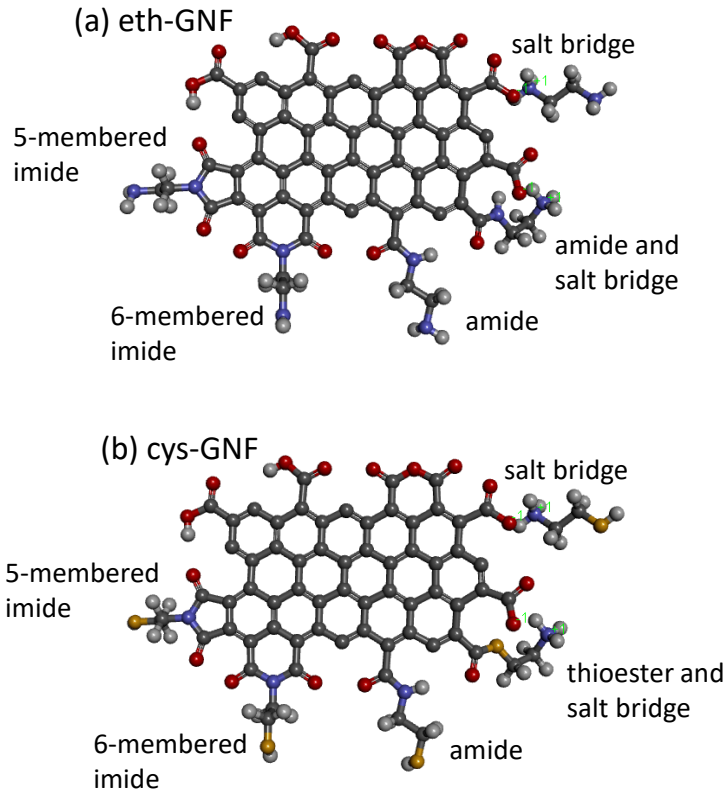

Fig. 5.7 3D geometry optimisations of (a) eth-GNFs and (b) cys-GNFs showing the various possible chemical transformations, carried out with Discovery Studio visualiser software, using a Dreiding-like forcefield developed by Hahn (53). Carbon, oxygen, hydrogen, nitrogen and sulfur atoms are shown in black, red, white, blue and yellow respectively.

In the case of eth-GNFs in Fig. 5.7(a), all of the possible chemical functionalisations depicted are indistinguishable by XPS C1s regions alone (43; 54; 55). The XPS N1s region can differentiate between the different nitrogen species, however the subjective nature of peak fitting and the variation in peak assignments in the literature results in a high degree of uncertainty (15; 41-43; 51; 54; 56). In general, amine groups are typically found <400.0 eV, whilst amides, imides and ammonium-carboxylate salts are observed >400.0 eV (20; 43; 51; 57; 58). Hence, the combined contribution of these last three functional groups results in the observed higher peak area at 401.5 eV in the XPS N1s region of eth-GNF in Fig. 5.5(b) w.r.t the amine group centered at 399.5 eV. Similarly, since the formation of an amide bond over a thioester bond is expected when cysteamine is used (due to the amide being the more thermodynamically favoured product, based on resonance grounds), one can expect very little free amine to be present in the XPS

N1s region of cys-GNF, in good agreement with what is observed (Fig. 5.5(c)). Thioesters, therefore, shown in Fig. 5.7(b) are not probable, and unfortunately cannot be distinguished from thiol groups in the XPS S2p region (49; 50).

The small feature at ~1770 cm^{-1} in the FT-IR spectra of the cys-GNFs, as mentioned earlier, was attributed to 5-membered cyclic imides (note that 6-membered cyclic imides occur at significantly lower frequencies) (52). However, the fact that such a feature is even observed is quite surprising, since in order for an imide to form it would have to proceed *via* the amide which is highly unreactive (41; 59-62). Although imides are prepared by reaction of amines with carboxylic anhydrides (*via* the amide), high temperatures are required and/or an activating species (41; 59-62). The only plausible way under these ambient conditions that an imide could form is if the amide was adjacent to another carboxylic anhydride. Under these circumstances, the terminal amine group (in the case of ethylenediamine) will also be able to compete with the amide for reaction with the carboxylic anhydride. This is less likely to be the case with the terminal thiol (in the case of cysteamine), hence the imide is only observed for the cys-GNFs and not the eth-GNFs.

5.3.1 Confirming covalent functionalisation

Ideally, ^{15}N ssNMR would be useful in distinguishing some of the functional groups present on the eth/cys-GNFs, however the cost and large amount of sample required make this characterisation technique less practical. A simple alternative would be to consider physical properties such as solubility. Whilst this does not confirm specific functionality, it can be used to differentiate whether covalent or non-covalent (salt bridges) are present. For instance, the cx-GNFs are highly soluble in water (> 100 g / L) at room temperature, and do not precipitate out of solution. The eth-GNFs on the other hand are significantly less soluble and the cys-GNFs are only sparingly soluble and precipitate out of solution readily. These results strongly indicate that covalent modification has taken place since salt bridges, in the form of primary ammonium carboxylates, would readily dissolve – perhaps even to a greater extent than the cx-GNFs. Similarly, physisorption of amines onto the cx-GNF basal plane should not alter the solubility since it is the COOH groups that confer the hydrophilicity to the material.

In the case of the eth-GNFs and cys-GNFs, both materials remain soluble in water, albeit to a lesser extent than the cx-GNFs. If, however, amide formation between the cx-GNFs and a bulky amine would result in the precipitation of the GNFs, then this would

unequivocally confirm amide or covalent modification of some sort. A weak linkage such as an electrostatic attraction, would conversely be easy to remove by washing. Hence this section concerns itself with identifying a stable precipitate after the cx-GNFs have been subjected to amine treatment. In this regard, the cx-GNFs were functionalised onto silica gel which had been modified to incorporate amine groups (see Fig. 5.8). Given the very large size of the silica particles (40-63 μm, compared with the cx-GNFs ~30 nm), a covalent bond (such as an amide) between the two materials would render the silica-GNFs (SiO_2-GNFs) completely insoluble in water. Conversely, a salt bridge would result in a brown-black dispersion of the cx-GNFs, as the salt dissociates resulting in the dissolution of the GNFs. It should also be noted that physisorption of the cx-GNFs onto the silica gel is possible, although they too should be able to be washed away readily with deionised water. However, significant physisorption is not expected in the first place since both the cx-GNFs and the silica gel are negatively charged owing to the dissociation of acidic oxygen functional groups.

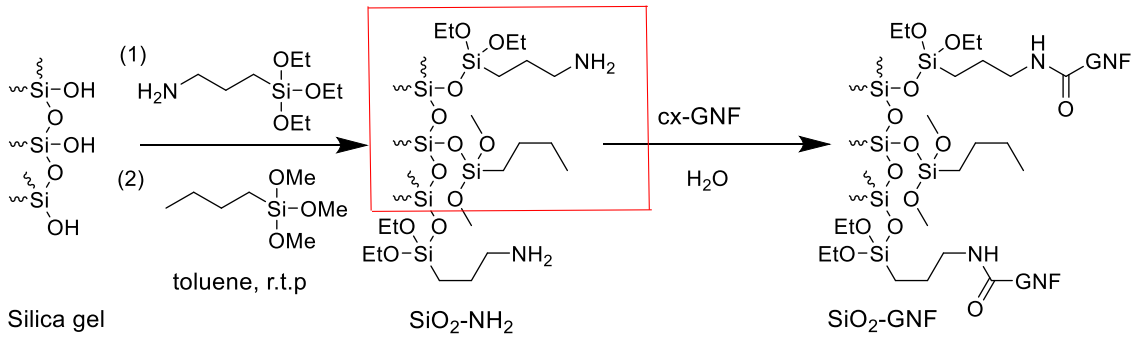

Fig. 5.8 Modification of silica gel with amine groups (SiO_2-NH_2) followed by reaction with cx-GNFs to yield SiO_2-GNFs. The repeated functionalisation unit is shown by the red box.

Modification of silica gel to introduce amine functionality is shown in Fig. 5.8, and is well documented in the literature (63-68). However, the newly introduced amine group is known to participate in salt bridges with unreacted silanol groups, rendering the amine unreactive (69-72). Kamisetty and co-workers (73) overcame this problem by treating the amine functionalised silica once again with an alkylsilane, which reacted with the remaining silanol groups (in theory) and hence acted as a capping agent (*c.f.* reaction (2) in Fig. 5.8) (73).

The capped and amine treated silica (SiO_2-NH_2) was then added to a dispersion of cx-GNFs in deionised water. The almost-immediate brown precipitate formed was filtered and washed with copious volumes of deionised water and dried in air. The filtrate after

washing was found to be completely colourless, indicating the absence of cx-GNFs (see chapter 8 section 8.1.7 for full details). The SiO_2-GNF precipitate was re-immersed in water once again and left overnight to ensure no dissolution of the GNFs occurred-and none was observed. As a control experiment, unmodified silica-gel was combined with cx-GNFs in deionised water and allowed to stand overnight. A dark-brown dispersion was initially observed before filtration suggesting that no reaction between the cx-GNFs and the silica gel had occurred. After filtration, only a white precipitate was collected on the filter membrane whilst the filtrate was dark brown. Hence no modification (or precipitation) occurs between the cx-GNFs and the unmodified silica gel, which conclusively confirms that covalent modification must have taken place between the amine functionalised silica (SiO_2-NH_2) and the cx-GNFs.

The SEM and photographic images in Fig. 5.9 before and after grafting the cx-GNFs onto the silica gel show the changes in morphology that accompany the transformation.

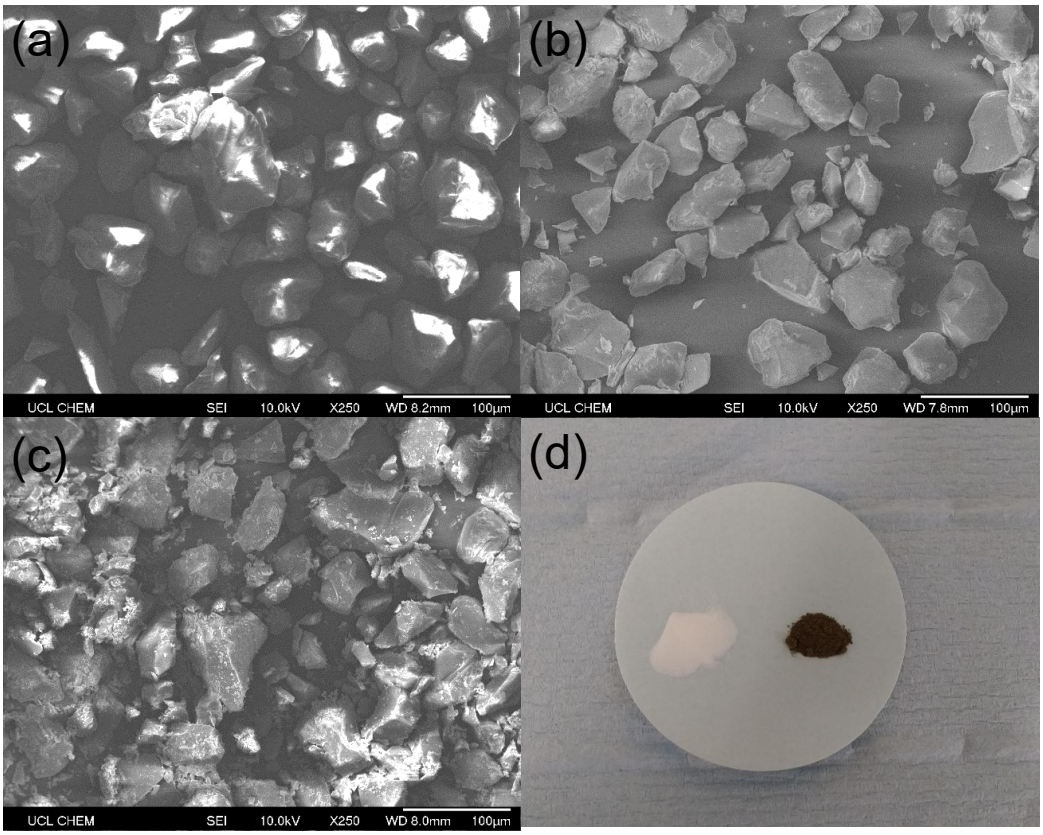

Fig. 5.9 SEM images of (a) silica gel, (b) SiO_2-NH_2 and (c) SiO_2-GNF. (d) Photographic image showing SiO_2-NH_2 (left) and SiO_2-GNF (right).

Little difference can be seen between the silica gel (Fig. 5.9(a)) and SiO_2-NH_2 (Fig. 5.9(b)), however a significant change in the surface morphology of the SiO_2-GNF (Fig.

5.9(c)) is apparent. The previously clean and well-defined surface of the silica particles has been replaced with a rough coating. This is even more evident from the photographic image in (Fig. 5.9(d)). On the left is a fine white power of SiO_2-NH_2, whilst on the right is a brown powder of SiO_2-GNF retrieved after copious washing with deionised water. The two materials lack any resemblance to each other.

The XPS, FT-IR and TGA data in Fig. 5.10 before and after modification of the silica gel and subsequent functionalisation with the cx-GNFs, indicates that the covalent grafting of the cx-GNFs onto the silica gel was successful.

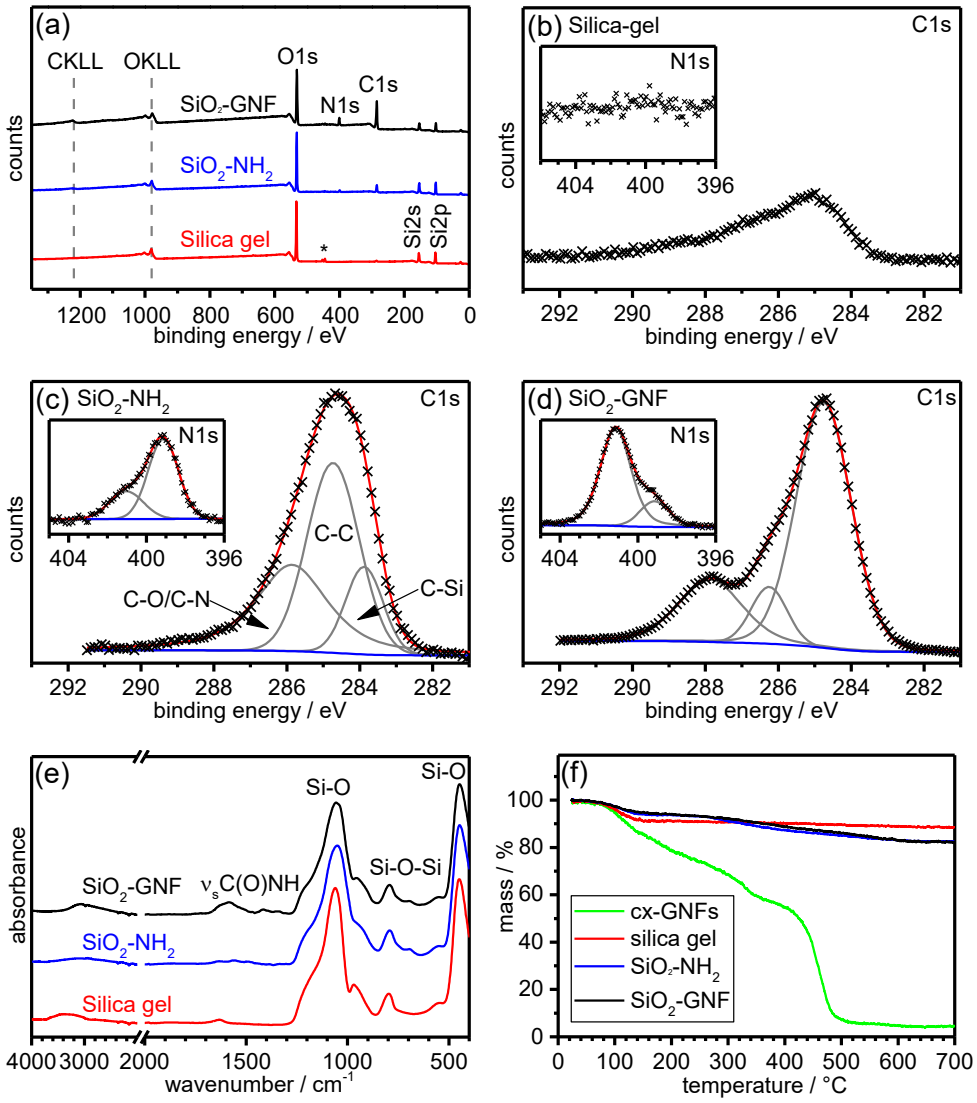

Fig. 5.10 XPS survey spectra of (a) SiO_2-GNFs (black), SiO_2-NH_2 (blue) and silica gel (red). XPS elemental regions of (b) silica gel, (c) SiO_2-NH_2 and (d) SiO_2-GNF, showing C1s regions (outset) and N1s regions (inset). The crosses represent the experimental data, blue line the background, grey lines the fitted peaks and the peak sum is shown in red. (e) FT-IR spectra of silica gel (red), SiO_2-NH_2 (blue) and SiO_2-GNFs (black). (f) TGA of silica gel (red), SiO_2-NH_2 (blue), SiO_2-GNFs (black) and cx-GNFs (green).

The XPS spectra of silica gel in Fig. 5.10 (a) confirmed the presence of silicon and oxygen in a 1:2 ratio as expected. A small amount of adventitious carbon was also present as indicated in Fig. 5.10(b). After modification of the silica gel (Fig. 5.10 (a) and (c)), significant amounts of carbon (18.6 ± 0.3) at. % and an appreciable amount of nitrogen (2.9 ± 0.3) at. % can now be seen. However, due to the surface sensitivity of XPS, these values are exaggerated. Note that these values were determined *via* the averaging and 1.s.d. of three measurements from a large scale preparation. Although this experiment has been repeated successfully on smaller scales, an excess of silica gel was used and therefore the samples obtained would not reflect a 'maximum loading capacity', i.e. the minimum amount of silica gel required to precipitate out the cx-GNFs. The C1s region has been fitted to represent the functionality indicated by the red box in Fig. 5.8 which can be considered a 'repeat' unit (74; 75). The N1s region shows the presence of free amine (399.1 eV) and ammonium salt (401.0 eV). Once the SiO_2-NH_2 is grafted onto the cx-GNFs (Fig. 5.10(a) and (d)) the carbon and nitrogen content increases significantly to (44.5 ± 1.5) at. % and (5.8 ± 0.4) at. % respectively. The GNFs will naturally increase the carbon content, yet the nitrogen content should actually decrease (NB: 44.5 at. % carbon is also far too high!). The enhancement therefore points towards a surface coating of the silica particles by the GNFs. More interestingly, the ratio of the N1s peaks at ~399 and 401 eV are reversed. However, given the insolubility of the GNFs in water after forming the SiO_2-GNF composite, the peak at ~401 eV will have contributions from covalent functionality such as the amide bond.

In good agreement with the XPS data, the FT-IR data in Fig. 5.10(e) before and after chemical modification, show characteristic vibrations for silica at 470, 800 and 950-1250 cm^{-1} corresponding to the Si-O (rocking), Si-O-Si (symmetric stretching) and Si-O (asymmetric stretching) respectively (76). The additional two peaks observed in the silica gel at ~3500 (broad) and ~1630 cm^{-1} can be attributed to O-H stretching and bending modes from water respectively (76). After modification of the silica gel, the SiO_2-NH_2 shows a shift in these two bands to ~3100 and (1600 and 1500) cm^{-1} respectively which can be reassigned to N-H (from NH_2 and NH_3^+) stretching and bending modes respectively (44). Final grafting of the SiO_2-NH_2 onto the cx-GNFs, producing SiO_2-GNFs, results in the formation of *i.e*. an amide bond, indicated by the increased intensity of the broad peak at ~1600 cm^{-1} (44).

Lastly, the TGA data in Fig. 5.10(f) indicate an overall mass loss of ~6 wt% in the SiO_2-NH_2 material relative to the unfunctionalised silica gel, again confirming the modification of the silica particles. Surprisingly, the overall mass loss of the SiO_2-GNFs is similar to

the SiO_2-NH_2, when one would expect an even greater mass loss in the SiO_2-GNFs due to the presence of the cx-GNFs. By considering how much of the SiO_2-NH_2 was added to the cx-GNFs, it was calculated that the cx-GNFs constitute ~5.9 wt% of the total weight of the SiO_2-GNFs, suggesting that the difference should be seen in the TGA pattern. The fact that no additional mass loss was observed could be explained by the aqueous washing step which could have hydrolysed some of the Si-O-C bonds, thus reducing the organic content of the SiO_2-GNFs.

5.3.2 Direct functionalisation of cx-GNFs with ethylenediamine in DMF

The formation of carboxylic anhydrides is unfavourable under aqueous conditions due to the large concentration of water molecules which shifts the equilibrium strongly in favour of the carboxylic acids. An alternative approach would be to perform the reactions in a different solvent, such as DMF, which should potentially result in an initially higher concentration of carboxylic anhydrides. Ethylenediamine was treated with cx-GNFs under identical conditions as before when the eth-GNFs were prepared, except that DMF was used as the solvent instead of water (now referred to as eth-GNF(DMF)). Interestingly, the XPS survey spectra of eth-GNF(DMF) in Fig. 5.11(a) show that the N/C ratio is actually slightly lower when the reaction is performed in DMF (0.137 ± 0.002) than in water (0.151 ± 0.007). Note that two samples of eth-GNF(DMF) were measured, and the ratio and error reflect the mean and 1.s.d. respectively. The results suggest that the reaction between amines and cx-GNFs occurs very quickly and therefore the equilibrium shifts back in favour of the carboxylic anhydrides as they are consumed during the reaction. The exact reason why the yield of amidation is slightly lower in DMF than in water is unclear. However, comparison of the N1s regions of the eth-GNFs(DMF) in Fig. 5.11(b) with the eth-GNFs earlier in Fig. 5.4(b), clearly demonstrates a different preference in the nitrogen bonding environment/type between the two. Note that the C1s region of eth-GNFs(DMF) in Fig. 5.11(b) does not support the presence of DMF in the sample since it is very similar to the C1s spectrum of eth-GNFs. The two methyl groups of DMF, for instance, would contribute strongly to the C(I) peak at ~286.5 eV. Similarly, there is little difference between the two IR spectra. The difference is therefore likely to be due to the solvation behaviour (and overall dispersion properties) of ethylenediamine and cx-GNFs in water and DMF.

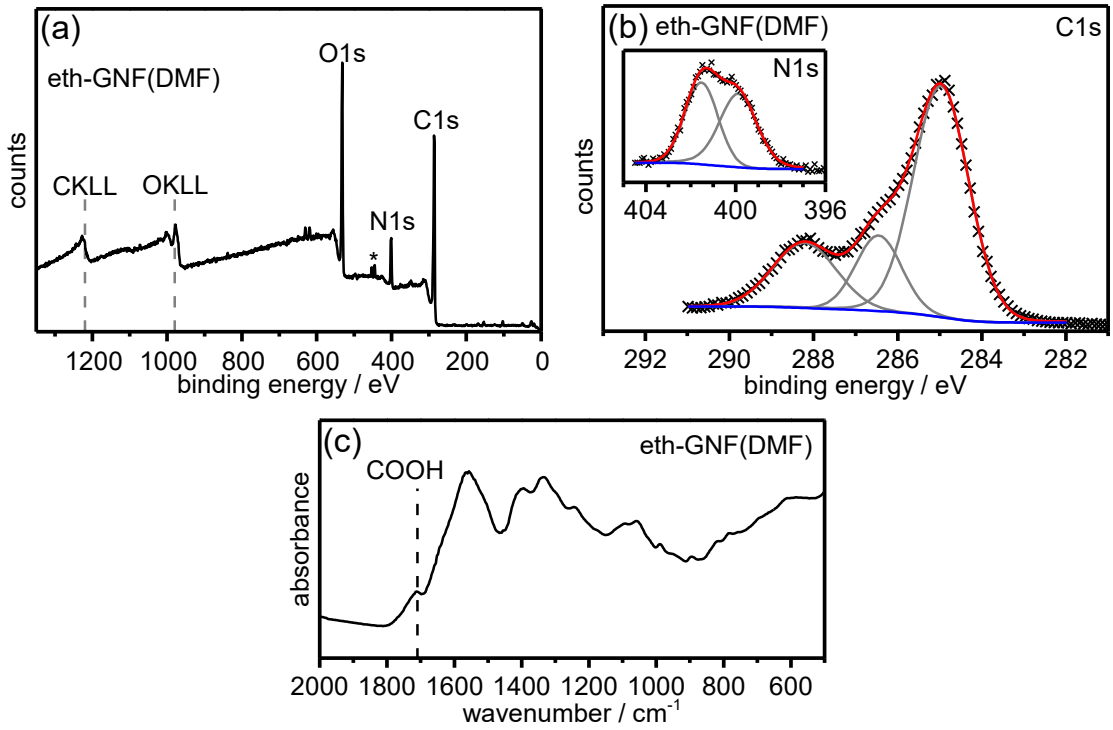

Fig. 5.11 XPS survey spectra (a), elemental regions showing C1s regions (outset) and N1s regions (inset) (b). The crosses represent the experimental data, blue line the background, grey lines the fitted peaks and the peak sum is shown in red. (c) FT-IR spectra of eth-GNFs(DMF).

5.4 What can we do with cys-GNFs and eth-GNFs?

The cys-GNFs prepared earlier were spin coated onto a HOPG substrate along with Au nanoparticles. In a typical experiment, one drop Au nanoparticles (3-7 nm core size, 7-20 nm hydrodynamic diameter, absorption maximum 510-525 nm, OD1, reactant free) dispersed in 0.1 mM phosphate buffered saline solution purchased from Aldrich (752568), was spin coated at 2000 rpm for 2 min onto a freshly cleaved HOPG substrate. The cys-GNFs (one drop, ~0.1 mg mL^{-1}) were then spin coated onto the same substrate in the same way as before.

It is well-known that thiol groups coordinate strongly to gold (77-79), and therefore coordination of the cys-GNFs with the Au particles would suggest the availability of terminal thiol groups at the flake edge (*c.f.* Fig. 5.12). Indeed, the AFM images of the Au treated cys-GNFs (Au-cys-GNFs) in Fig. 5.13 confirms coordination of the Au nanoparticles along the external flake perimeter of the cys-GNFs. In every case, Au nanoparticles were found to be attached to the cys-GNFs and none were observed isolated by themselves. Using multiple AFM images such as the ones in Fig. 5.13, it was

found that 43 of the 46 Au nanoparticles attached to the cys-GNFs were at the external flake perimeter. The remaining three Au nanoparticles were observed at the centre of the flakes. By contrast, when the cx-GNFs were treated with the Au nanoparticles as a control experiment, none of the Au nanoparticles were seen at the external flake perimeter, but they were observed to be attached at the centre of the cx-GNFs. In this way, 14 Au nanoparticles out of 14 were found at the cx-GNF flake centre. The presence of Au nanoparticles at the flake centre could be due to defects in the flake harbouring reactive functionality, or perhaps due to electrostatic interactions between the Au metal the graphenic π system in a cation-π type fashion. This concept is explored in detail in the next chapter.

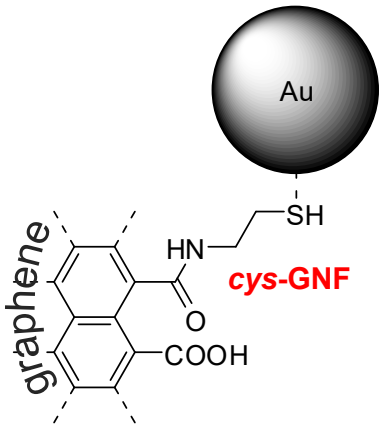

Fig. 5.12 Schematic showing the coordination of gold nanoparticles to cys-GNFs.

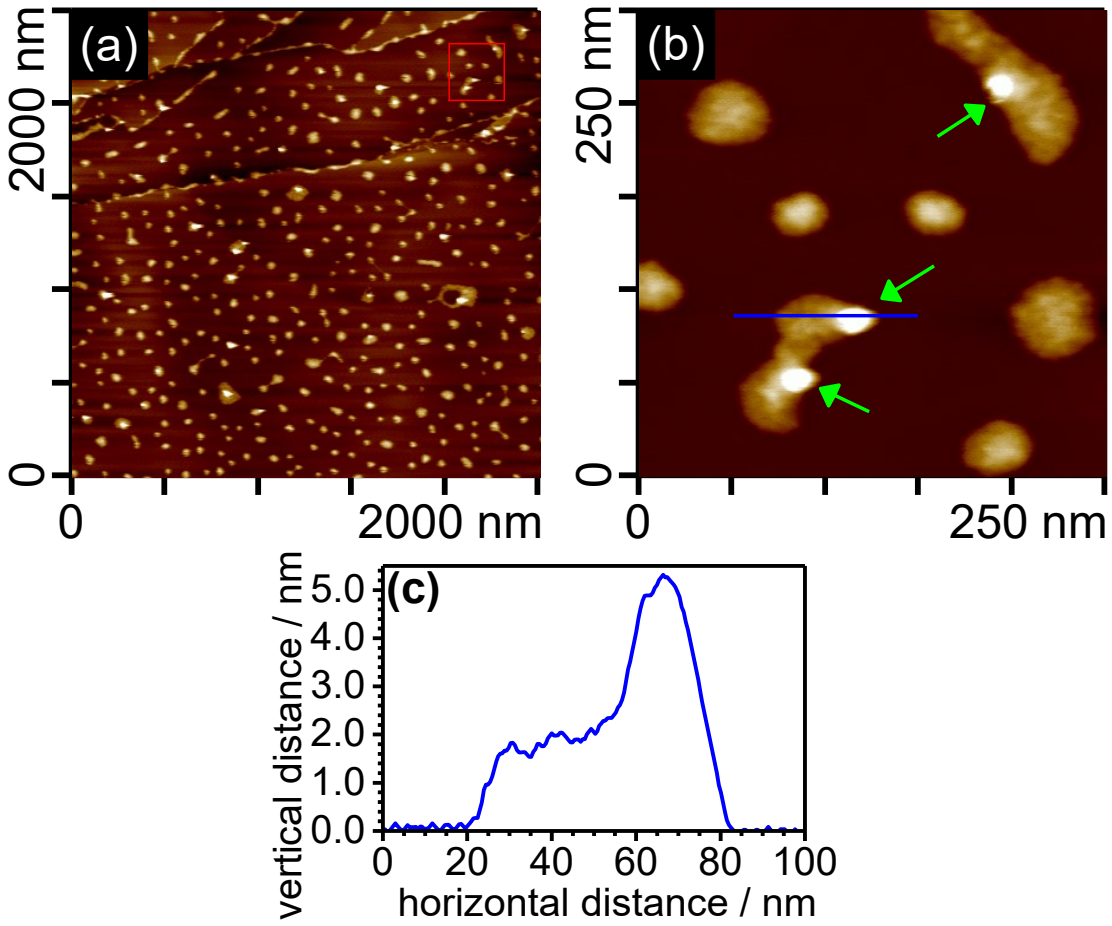

Fig. 5.13(a) AFM image of cys-GNFs spin coated with Au nanoparticles (3-7 nm), (b) zoomed in image of (a) as indicated by the red box. The green arrows point to the Au particles attached to the flake perimeter of the cys-GNFs. (c) line profile of (b) indicated by the blue line.

Interestingly, the height profiles of the Au-cys-GNFs such as the one in Fig. 5.13(c), indicate that grafting cysteamine onto the cx-GNFs results in the vertical height of the cys-GNFs increasing significantly from ~0.45 nm (*c.f.* chapter 3 section 3.3.3) to ~2 nm. Alternatively, given the lower dispersibility of the cys-GNFs, it is possible that stacking may occur resulting in few-layered cys-GNFs.

Given the basic nature of amines, it is expected that the terminal amine groups on the eth-GNFs will have significantly less negative zeta potential compared with the native cx-GNFs (Fig. 5.14). As expected, the zeta potential measurements shown in Fig. 5.14 illustrate that the as-made cx-GNFs display an average zeta potential of about -45 mV due to negatively charged carboxylates which are in equilibrium with the carboxylic acids.

The eth-GNFs, on the other hand, display an average zeta potential of -32 mV as positively charged NH_3^+ groups are introduced. The values are also in good agreement with the aqueous dispersibility of the two materials, with the cx-GNFs exhibiting excellent solubility and the eth-GNFs demonstrating less pronounced dispersion properties. It should be noted, however, that zeta potential assumes spherical particles in solution and not two dimensional structures – hence caution should be undertaken when comparing the zeta potential of 2D structures.

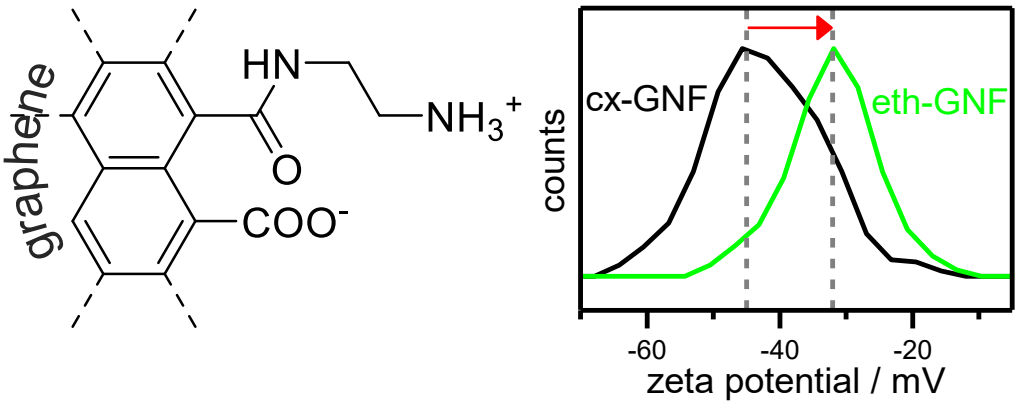

Fig. 5.14 eth-GNFs (left) showing the basic and acidic nature of the amine and carboxyl group respectively. Zeta potential distribution (right) of cx-GNFs (black) and eth-GNFs (green). The red arrows indicated the shift in zeta potential.

5.5 Conclusions

The covalent modification of cx-GNFs with amines has been demonstrated *via* the dynamic equilibrium which exists between the carboxylic acids and anhydrides on the cx-GNFs. The resulting functionalised materials have been shown to exhibit a high affinity for gold nanoparticles as well as reduce the native negative zeta potential of the GNFs. In the next chapter, emphasis will be placed on the chemistry of carboxylic acids groups (as opposed to the anhydride). In particular, their ability to coordinate strongly to a wide range of heavy metals is investigated thoroughly.

5.6 Chapter 5 References

1. Yu DS, Yang Y, Durstock M, Baek JB, Dai LM. 2010. Soluble P3HT-Grafted Graphene for Efficient Bilayer-Heterojunction Photovoltaic Devices. *ACS Nano* 4:5633-40

2. Xu Y, Liu Z, Zhang X, Wang Y, Tian J, et al. 2009. A Graphene Hybrid Material Covalently Functionalized with Porphyrin: Synthesis and Optical Limiting Property. *Adv. Mater.* 21:1275-9

3. Bao HQ, Pan YZ, Ping Y, Sahoo NG, Wu TF, et al. 2011. Chitosan-Functionalized Graphene Oxide as a Nanocarrier for Drug and Gene Delivery. *Small* 7:1569-78

4. Wu HX, Shi HL, Wang YP, Jia XQ, Tang CZ, et al. 2014. Hyaluronic acid conjugated graphene oxide for targeted drug delivery. *Carbon* 69:379-89

5. Qin H, Gong T, Cho Y, Lee C, Kim T. 2014. A conductive copolymer of graphene oxide/poly(1-(3-aminopropyl)pyrrole) and the adsorption of metal ions. *Polym. Chem.* 5:4466-73

6. Wang ZJ, Zhou XZ, Zhang J, Boey F, Zhang H. 2009. Direct Electrochemical Reduction of Single-Layer Graphene Oxide and Subsequent Functionalization with Glucose Oxidase. *J. Phys. Chem. C* 113:14071-5

7. Mai YJ, Zhang D, Qiao YQ, Gu CD, Wang XL, Tu JP. 2012. MnO/reduced graphene oxide sheet hybrid as an anode for Li-ion batteries with enhanced lithium storage performance. *J. Power Sources* 216:201-7

8. Chen S, Zhu JW, Wu XD, Han QF, Wang X. 2010. Graphene Oxide-MnO2 Nanocomposites for Supercapacitors. *ACS Nano* 4:2822-30

9. Wu ZS, Zhou GM, Yin LC, Ren W, Li F, Cheng HM. 2012. Graphene/metal oxide composite electrode materials for energy storage. *Nano Energy* 1:107-31

10. Becerril HA, Mao J, Liu Z, Stoltenberg RM, Bao Z, Chen Y. 2008. Evaluation of solution-processed reduced graphene oxide films as transparent conductors. *ACS Nano* 2:463-70

11. Ji LW, Rao MM, Zheng HM, Zhang L, Li YC, et al. 2011. Graphene Oxide as a Sulfur Immobilizer in High Performance Lithium/Sulfur Cells. *J. Am. Chem. Soc.* 133:18522-5

12. Wang Y, Li ZH, Hu DH, Lin CT, Li JH, Lin YH. 2010. Aptamer/Graphene Oxide Nanocomplex for in Situ Molecular Probing in Living Cells. *J. Am. Chem. Soc.* 132:9274-6

13. Zhang W, Guo ZY, Huang DQ, Liu ZM, Guo X, Zhong HQ. 2011. Synergistic effect of chemo-photothermal therapy using PEGylated graphene oxide. *Biomaterials* 32:8555-61

14. Lerf A, He HY, Forster M, Klinowski J. 1998. Structure of graphite oxide revisited. *J. Phys. Chem. B* 102:4477-82

15. Eigler S, Dimiev A. 2017. Functionalization and Reduction of Graphene Oxide. In *Graphene Oxide. Fundamental and Applications*. London: Wiley and Sons

16. Zhang XY, Huang Y, Wang Y, Ma YF, Liu ZF, Chen YS. 2009. Synthesis and characterization of a graphene-C-60 hybrid material. *Carbon* 47:334-7

17. Wang J, Geng HZ, Luo ZJ, Zhang ST, Zhang JQ, et al. 2015. Preparation, characterization, and chemical-induced hydrophobicity of thermostable amine-modified graphene oxide. *RSC Adv.* 5:105393-9

18. Pu LY, Ma YJ, Zhang W, Hu HL, Zhou Y, et al. 2013. Simple method for the fluorinated functionalization of graphene oxide. *RSC Adv.* 3:3881-4

19. Acocella MR, D'Urso L, Maggio M, Avolio R, Errico ME, Guerra G. 2017. Green and Facile Esterification Procedure Leading to Crystalline-Functionalized Graphite Oxide. *Langmuir* 33:6819-25

20. Kim NH, Kuila T, Lee JH. 2013. Simultaneous reduction, functionalization and stitching of graphene oxide with ethylenediamine for composites application. *J. Mater. Chem. A* 1:1349-58

21. Sekiya R, Uemura Y, Murakami H, Haino T. 2014. White-Light-Emitting Edge-Functionalized Graphene Quantum Dots. *Angew. Chem. Int. Ed.* 53:5619-23

22. Salzmann CG, Nicolosi V, Green MLH. 2010. Edge-carboxylated graphene nanoflakes from nitric acid oxidised arc-discharge material. *J. Mater. Chem.* 20:314-9

23. Quintana M, Montellano A, Castillo AEdR, Van Tendeloo G, Bittencourt C, Prato M. 2011. Selective organic functionalization of graphene bulk or graphene edges. *Chem. Commun.* 47:9330-2

24. Quintana M, Vazquez E, Prato M. 2013. Organic Functionalization of Graphene in Dispersions. *Acc. Chem. Res.* 46:138-48

25. Lee JU, Lee W, Yoon SS, Kim J, Byun JH. 2014. Site-selective immobilization of gold nanoparticles on graphene sheets and its electrochemical properties. *Appl. Surf. Sci.* 315:73-80

26. Marcano DC, Kosynkin DV, Berlin JM, Sinitskii A, Sun Z, et al. 2010. Improved Synthesis of Graphene Oxide. *ACS Nano* 4:4806-14

27. Vacchi IA, Spinato C, Raya J, Bianco A, Menard-Moyon C. 2016. Chemical reactivity of graphene oxide towards amines elucidated by solid-state NMR. *Nanoscale* 8:13714-21

28. Azizi N, Saidi MR. 2005. Highly chemoselective addition of amines to epoxides in water. *Org. Lett.* 7:3649-51

29. Bonollo S, Lanari D, Vaccaro L. 2011. Ring-Opening of Epoxides in Water. *Eur. J. Org. Chem.*:2587-98

30. Bonollo S, Lanari D, Marrocchi A, Vaccaro L. 2011. Stereoselective Ring-Opening Reactions of Epoxides in Water. *Curr. Org. Synth.* 8:319-29

31. Bourlinos AB, Gournis D, Petridis D, Szabo T, Szeri A, Dekany I. 2003. Graphite oxide: Chemical reduction to graphite and surface modification with primary aliphatic amines and amino acids. *Langmuir* 19:6050-5

32. Yang HF, Shan CS, Li FH, Han DX, Zhang QX, Niu L. 2009. Covalent functionalization of polydisperse chemically-converted graphene sheets with amine-terminated ionic liquid. *Chem. Commun.*:3880-2

33. Wang S, Chia PJ, Chua LL, Zhao LH, Png RQ, et al. 2008. Band-like transport in surface-functionalized highly solution-processable graphene nanosheets. *Adv. Mater.* 20:3440-+

34. Mei QS, Zhang K, Guan GJ, Liu BH, Wang SH, Zhang ZP. 2010. Highly efficient photoluminescent graphene oxide with tunable surface properties. *Chem. Commun.* 46:7319-21

35. Zhao QS, Zhu YZ, Sun Z, Li Y, Zhang GL, et al. 2015. Combining palladium complex and organic amine on graphene oxide for promoted Tsuji-Trost allylation. *J. Mater. Chem. A* 3:2609-16

36. Eigler S, Hu YC, Ishii Y, Hirsch A. 2013. Controlled functionalization of graphene oxide with sodium azide. *Nanoscale* 5:12136-9

37. Mungse HP, Khatri OP. 2014. Chemically Functionalized Reduced Graphene Oxide as a Novel Material for Reduction of Friction and Wear. *J. Phys. Chem. C* 118:14394-402

38. 2012. Bruker Almanac Analytical Tables and Product Overview p126.

39. *Hebrew University NMR lab, Fig. 8* http://chem.ch.huji.ac.il/nmr/techniques/1d/row2/n.html#n15

40. Rosillo-Lopez M, Lee TJ, Bella M, Hart M, Salzmann CG. 2015. Formation and chemistry of carboxylic anhydrides at the graphene edge. *RSC Adv.* 5:104198-202

41. Mishra AK, Chattopadhyay DK, Sreedhar B, Raju K. 2006. FT-IR and XPS studies of polyurethane-urea-imide coatings. *Prog. Org. Coat.* 55:231-43

42. Quintana M, Spyrou K, Grzelczak M, Browne WR, Rudolf P, Prato M. 2010. Functionalization of Graphene via 1,3-Dipolar Cycloaddition. *ACS Nano* 4:3527-33

43. Tawil N, Sacher E, Boulais E, Mandeville R, Meunier M. 2013. X-ray Photoelectron Spectroscopic and Transmission Electron Microscopic Characterizations of Bacteriophage-Nanoparticle Complexes for Pathogen Detection. *J. Phys. Chem. C* 117:20656-65

44. Seol YG, Trung TQ, Yoon OJ, Sohn IY, Lee NE. 2012. Nanocomposites of reduced graphene oxide nanosheets and conducting polymer for stretchable transparent conducting electrodes. *J. Mater. Chem.* 22:23759-66

45. Castner DG, Hinds K, Grainger DW. 1996. X-ray photoelectron spectroscopy sulfur 2p study of organic thiol and disulfide binding interactions with gold surfaces. *Langmuir* 12:5083-6

46. Kinyanjui JM, Hatchett DW, Castruita G, Ranasinghe AD, Weinhardt L, et al. 2011. Synthesis and characterization of conductive polyimide/carbon composites with Pt surface deposits. *SYNTHETIC MET.* 161:2368-77

47. Fuchs P, Steinhauser J, Avancini E, Romanyuk YE, Tiwari AN. 2016. Evolution of carbon impurities in solution-grown and sputtered Al:ZnO thin films exposed to UV light and damp heat degradation. *RSC Adv.* 6:53768-76

48. Prisle NL, Ottosson N, Ohrwall G, Soderstrom J, Dal Maso M, Bjorneholm O. 2012. Surface/bulk partitioning and acid/base speciation of aqueous decanoate: direct observations and atmospheric implications. *Atmos. Chem. Phys.* 12:12227-42

49. Machida S, Urano TI, Sano K, Kawata Y, Sunohara K, et al. 1995. Chiral director field in the nematic liquid crystal phase induced by a poly(gamma-benzyl glutamate) chemical reaction alignment film. *Langmuir* 11:4838-43

50. Okamoto M, Ishikawa K, Tanji N, Aoyagi S. 2012. Investigation of the damage on the outermost hair surface using ToF-SIMS and XPS. *Surf. Interface Anal.* 44:736-9

51. Jansen RJJ, Vanbekkum H. 1995. XPS OF NITROGEN-CONTAINING FUNCTIONAL-GROUPS ON ACTIVATED CARBON. *Carbon* 33:1021-7

52. Nyquist RA, Fiedler SL. 1995. INFRARED STUDY OF 5-MEMBERED AND 6-MEMBERED TYPE CYCLIC IMIDES. *Vib. Spectrosc.* 8:365-86

53. Hahn M. 1995. RECEPTOR SURFACE MODELS .1. DEFINITION AND CONSTRUCTION. *J. Med. Chem.* 38:2080-90

54. Ahmed MH, Byrne JA, McLaughlin J, Ahmed W. 2013. Study of Human Serum Albumin Adsorption and Conformational Change on DLC and Silicon Doped DLC Using XPS and FTIR Spectroscopy. *J. Biomater. Nanobiotechnol.* 4:194-203

55. Pan N, Ding LL, Wang R, b YJ, Xia C. 2017. A Schiff base/quaternary ammonium salt bifunctional graphene oxide as an efficient adsorbent for removal of Th(IV)/U(VI). *J. Colloid Interface Sci.* 508:303-12

56. Zorn G, Liu LH, Arnadottir L, Wang H, Gamble LJ, et al. 2014. X-ray Photoelectron Spectroscopy Investigation of the Nitrogen Species in Photoactive Perfluorophenylazide-Modified Surfaces. *J. Phys. Chem. C* 118:376-83

57. Compton OC, Dikin DA, Putz KW, Brinson LC, Nguyen ST. 2010. Electrically Conductive "Alkylated" Graphene Paper via Chemical Reduction of Amine-Functionalized Graphene Oxide Paper. *Adv. Mater.* 22:892-+

58. Graf N, Yegen E, Gross T, Lippitz A, Weigel W, et al. 2009. XPS and NEXAFS studies of aliphatic and aromatic amine species on functionalized surfaces. *Surface Science* 603:2849-60

59. Garad DN, Tanpure SD, Mhaske SB. 2015. Radical-mediated dehydrative preparation of cyclic imides using (NH4)(2)S2O8-DMSO: application to the synthesis of vernakalant. *Beilstein J. Org. Chem.* 11:1008-16

60. Ali MA, Moromi SK, Touchy AS, Shimizu K. 2016. Direct Synthesis of Cyclic Imides from Carboxylic Anhydrides and Amines by Nb2O5 as a Water-Tolerant Lewis Acid Catalyst. *Chemcatchem* 8:891-4

61. Benjamin E, Hijji Y. 2008. The synthesis of unsubstituted cyclic Imides using hydroxylamine under microwave irradiation. *Molecules* 13:157-69

62. Nicolaou KC, Mathison CJN. 2005. Synthesis of imides, N-acyl vinylogous carbamates and ureas, and nitriles by oxidation of amides and amines with Dess-Martin Periodinane. *Angew. Chem. Int. Ed.* 44:5992-7

63. Kinkel JN, Anspach B, Unger KK, Wieser R, Brunner G. 1984. SEPARATION OF PLASMA-MEMBRANE PROTEINS OF CULTURED HUMAN-FIBROBLASTS BY AFFINITY-CHROMATOGRAPHY ON BONDED MICROPARTICULATE SILICAS. *J. Chromatogr.* 297:167-77

64. Wonnacott DM, Patton EV. 1987. HYDROLYTIC STABILITY OF AMINOPROPYL STATIONARY PHASES USED IN THE SIZE-EXCLUSION CHROMATOGRAPHY OF CATIONIC POLYMERS. *J. Chromatogr.* 389:103-13

65. Leyden DE, Luttrell GH. 1975. PRECONCENTRATION OF TRACE-METALS USING CHELATING GROUPS IMMOBILIZED VIA SILYLATION. *Anal. Chem.* 47:1612-7

66. Chiang CH, Ishida H, Koenig JL. 1980. THE STRUCTURE OF GAMMA-AMINOPROPYLTRIETHOXYSILANE ON GLASS SURFACES. *J. Colloid Interface Sci.* 74:396-404

67. Oh SJ, Cho SJ, Kim CO, Park JW. 2002. Characteristics of DNA microarrays fabricated on various aminosilane layers. *Langmuir* 18:1764-9

68. Chrisey LA, Lee GU, Oferrall CE. 1996. Covalent attachment of synthetic DNA to self-assembled monolayer films. *Nucl. Acids Res.* 24:3031-9

69. Kohler J, Chase DB, Farlee RD, Vega AJ, Kirkland JJ. 1986. COMPREHENSIVE CHARACTERIZATION OF SOME SILICA-BASED STATIONARY PHASES FOR HIGH-PERFORMANCE LIQUID-CHROMATOGRAPHY. *J. Chromatogr.* 352:275-305

70. Rochester CH, Yong GH. 1980. INFRARED STUDY OF THE ADSORPTION OF AMINES ON SILICA IMMERSED IN CARBON-TETRACHLORIDE. *J. Chem. Soc. Faraday Trans. I* 76:1158-65

71. Bartell FE, Dobay DG. 1950. THE ADSORPTION OF ALIPHATIC AMINE VAPORS BY SILICA GEL. *J. Am. Chem. Soc.* 72:4388-93

72. Child MJ, Heywood MJ, Yong GH, Rochester CH. 1982. BRONSTED ACIDITY OF SILANOL GROUPS ON SILICA IMMERSED IN CARBON-TETRACHLORIDE. *J. Chem. Soc. Faraday Trans. I* 78:2005-10

73. Kamisetty NK, Pack SP, Nonogawa M, Devarayapalli KC, Kodaki T, Makino K. 2006. Development of an efficient amine-functionalized glass platform by additional silanization treatment with alkylsilane. *Anal. Bioanal. Chem.* 386:1649-55

74. Li KY, Kuan CF, Kuan HC, Chen CH, Shen MY, et al. 2014. Preparation and properties of novel epoxy/graphene oxide nanosheets (GON) composites functionalized with flame retardant containing phosphorus and silicon. *Mater. Chem. Phys.* 146:354-62

75. Liu HB, Hamers RJ. 1998. An X-ray photoelectron spectroscopy study of the bonding of unsaturated organic molecules to the Si(001) surface. *Surf. Sci.* 416:354-62

76. Manna J, Roy B, Sharma P. 2015. Efficient hydrogen generation from sodium borohydride hydrolysis using silica sulfuric acid catalyst. *J. Power Sources* 275:727-33

77. Liu JW. 2012. Adsorption of DNA onto gold nanoparticles and graphene oxide: surface science and applications. *Phys. Chem. Chem. Phys.* 14:10485-96

78. Chuang MK, Lin SW, Chen FC, Chu CW, Hsu CS. 2014. Gold nanoparticle-decorated graphene oxides for plasmonic-enhanced polymer photovoltaic devices. *Nanoscale* 6:1573-9

79. Wang J, Shi AQ, Fang X, Han XW, Zhang YZ. 2015. An ultrasensitive supersandwich electrochemical DNA biosensor based on gold nanoparticles decorated reduced graphene oxide. *Anal. Biochem.* 469:71-5

Chapter 6: Highly efficient heavy-metal extraction from water with cx-GNFs and nGO

6.1 The removal of heavy metals from water using carbon nanomaterials

Exposure to heavy metals causes a wide range of adverse health effects in humans.(1) Lead poisoning, for example, can lead to kidney(2) and bone damage,(1) malfunction of the nervous system,(3) psychosis,(1) infertility,(4) anaemia(5) and cancer.(6; 7) Children in particular are susceptible to the effects of heavy-metal poisoning due to their under-developed blood-brain barrier.(1) Yet, the global exposure levels of humans to heavy metals are on the rise. This is due, for example, to cadmium-based products such as nickel-cadmium batteries, airborne inorganic lead resulting from mines, smelters, battery plants and the glass industry, and contaminated wastewaters from a wide range of chemical processes in industry.(1; 8-10) The contamination of soil and water streams ultimately leads to the incorporation of heavy metals into the human food chain.(1) The efficient removal of heavy metals from drinking water, industrial wastewater and the environment at large is therefore of paramount importance.

Carbon materials have been at the vanguard of aqueous heavy-metal extraction over the last few years.(11-38) This surge in interest arose after the isolation of graphene(39) and its use in metal-extraction processes.(11; 12) More recently, graphene oxide (GO) has been advocated as an alternative to graphene(40-42) as a result of its hydrophilic nature, tuneable pore sizes as well as a stronger chelation ability towards metals due to the oxo-functional groups. Considerable efforts have gone into chemically modifying GO to further enhance its metal extraction capability (*c.f.* Fig. 6.1), including the preparation of hybrid materials with ethylenediamine tetraacetic acid (EDTA),(13; 14) cyclodextrin,(15) polypyrrole,(16) polyethylenimine,(17; 18) silica(19) and many more.(20-23) Lately, some of these functionalised/doped GO materials have been utilised in capacitive deionisation and achieved very good performances with respect to metal extractions.(29-33) Unfortunately, the chemical functionalisation of GO is a

lengthy and expensive step. It is therefore desirable to optimise and further investigate the metal-extraction properties of as-made carbon nanomaterials in order to provide low-cost adsorbents.

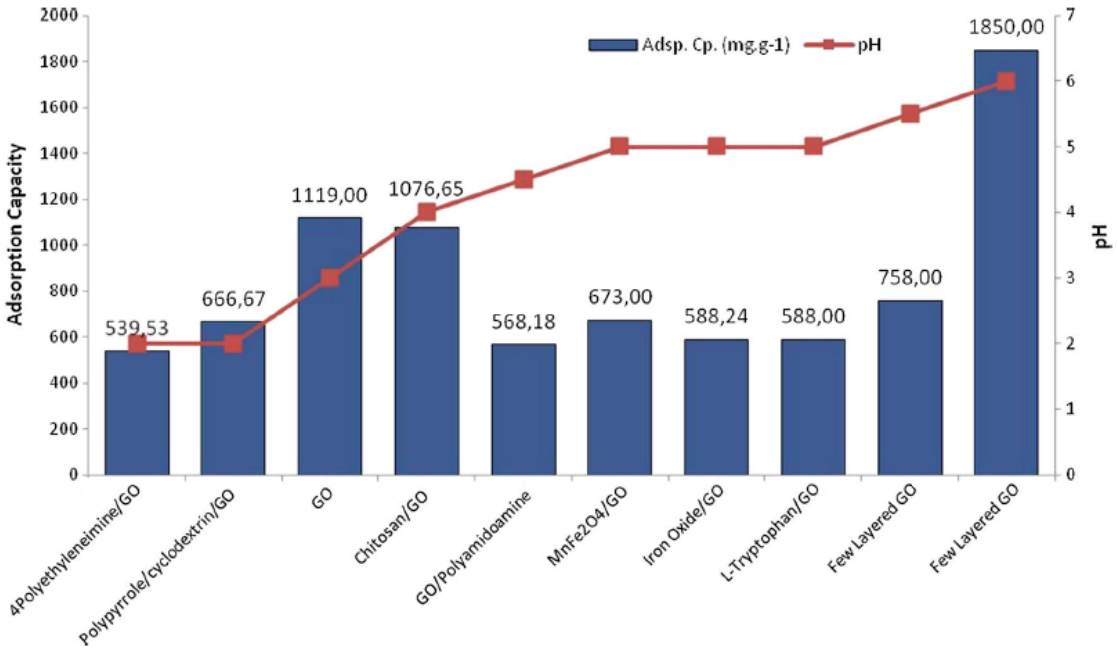

Fig. 6.1 GO-based adsorbents with high capacity and their corresponding pH levels. Adapted from ref [23] with permission of Springer.*(23; 25; 34; 35; 38; 43-48)*

In fact, very little research has so far been conducted using nano-graphene oxides such as carboxylated graphene nanoflakes (cx-GNFs) and nano-graphene oxide (nGO), in heavy metal extraction. This is surprising because the chemical structure of GO, as described earlier in chapter 1 by the Lerf-Klinowski model,(49) suggests that carboxylic acid groups which should be most effective in chelating metals, are located on the edges of GO. Smaller GO sheets with large edge-to-basal-plane ratios should therefore have more carboxylic acid groups per unit mass and hence be well-suited for metal-extraction processes.

6.2 Outline of chapter

In this chapter, the heavy-metal sorption capacity of cx-GNFs and nGO are investigated and benchmarked against conventional permanganate oxidised GO (PM-GO). The PM-GO used here is the same as the PM-GO (Chen) previously described in chapter 3 section 3.3. The heavy-metal cations under investigation are: Fe^{2+}, Cu^{2+}, Fe^{3+}, Cd^{2+} and Pb^{2+}. The chemical mechanisms of heavy-metal binding onto the carbon materials are investigated as well as the recyclability of the cx-GNFs towards the loading and unloading of Pb^{2+} cations. The selectivity of the cx-GNFs towards Pb^{2+} cation extraction in the presence of large quantities of other cations typically present in drinking or industrial waste water such as magnesium and calcium will be investigated.

6.3 Heavy-metal extraction from water with cx-GNFs, nGO and PM-GO

In a typical set of experiments, 10 mg of cx-GNFs, nGO or PM-GO (Chen) were combined with 10 mL of 0.1 M solutions of metal chloride or nitrate salts ($FeCl_2 \cdot 4\ H_2O$, $FeCl_3 \cdot 6\ H_2O$, $CuCl_2 \cdot 2\ H_2O$, $Cd(NO_3)_2 \cdot 4\ H_2O$ and $Pb(NO_3)_2$). The mixtures were then sonicated for 3 x 10 minutes allowing the precipitate to settle out each time for 10 minutes before re-sonicating, resulting in a 60 min total reaction time. This was followed by filtration through a 200 nm polycarbonate membrane and washing with 3 x 10 mL of deionised water to remove any excess metal salt. The material on the membrane was collected and allowed to dry in a vacuum desiccator overnight.

In order to quantify the relative adsorption capacities of cx-GNFs, nGO and PM-GO towards heavy metals, the metal/carbon (M/C) ratio of each metal-carbon composite, denoted as $M^{2+/3+}$@cx-GNFs, $M^{2+/3+}$@nGO or $M^{2+/3+}$@PM-GO respectively or collectively as $M^{2+/3+}$@carbon, was determined from the XPS survey spectra. Fig. 6.2(a) shows the survey spectra of cx-GNFs, nGO and GO after exposure to Pb^{2+} solutions which are hence referred to as Pb^{2+}@cx-GNFs, Pb^{2+}@nGO and Pb^{2+}@PM-GO respectively or collectively as Pb^{2+}@carbon. In the case of Pb^{2+}@carbon, the Pb4f peak was used for the quantification of Pb^{2+}. The XPS survey spectra of the other $M^{2+/3+}$@carbon samples can also be found in Appendix Fig. A6.1. The analysis of multiple M/C survey spectra are represented by the bar graph in Fig. 6.2(b). Each bar

represents the average and 1.s.d. of at least two samples, with each sample measured three times (i.e. three spots in XPS).

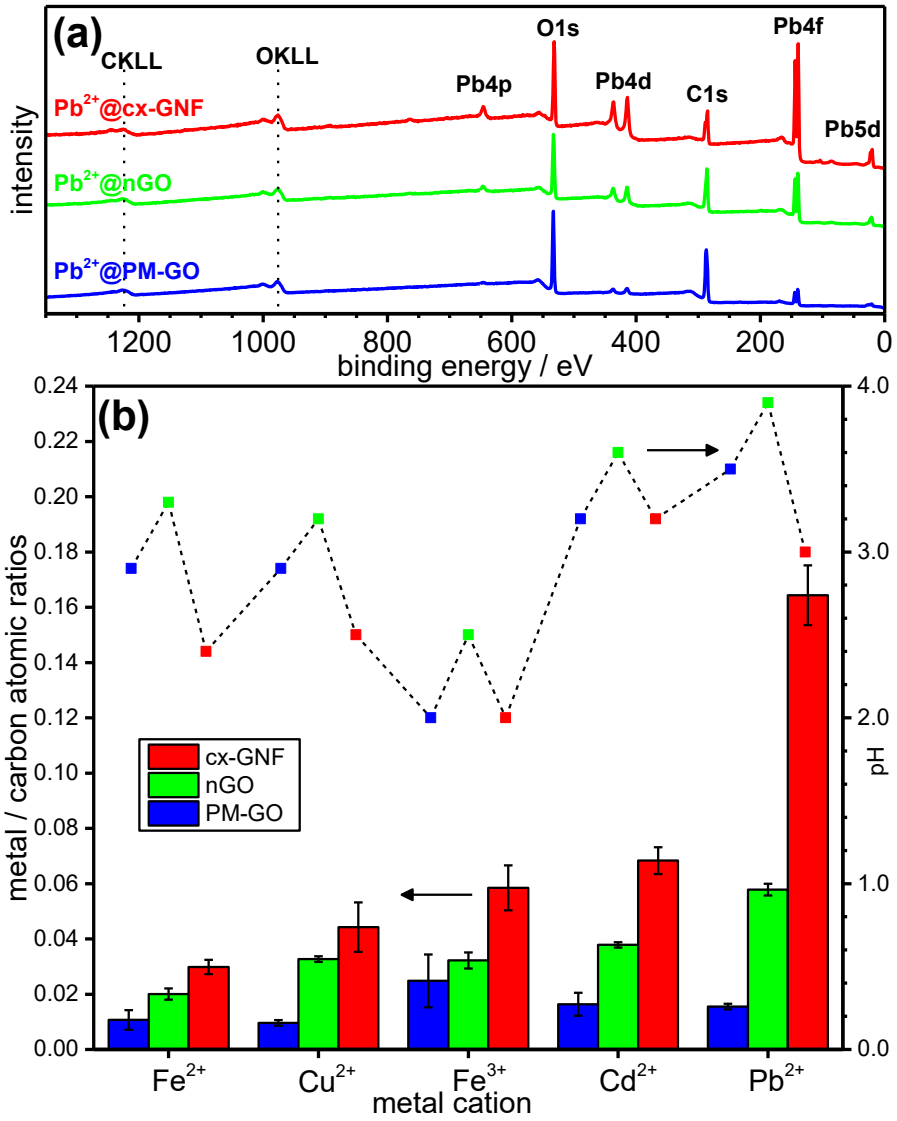

Fig. 6.2(a) XPS survey spectra of Pb^{2+}@cx-GNFs (red), Pb^{2+}@nGO (green) and Pb^{2+}@PM-GO (blue). (b) Bar graph of atomic metal/carbon ratios of cx-GNFs (red), nGO (green) and PM-GO (blue) treated with Fe^{2+}, Cu^{2+}, Fe^{3+}, Cd^{2+} or Pb^{2+} solutions, respectively. The line graph corresponds to the pH of each of the mixtures prior to filtration (10 mg of graphenic material in 10 mL of 0.1 M solutions of the respective metal salts).

It should be noted that while XPS is not a bulk technique, it still has a significant penetration depth of a few nm, which corresponds to tens of layers of atoms. Hence, it is expected that the M/C ratios collected from the XPS survey spectra will be

representative of the samples. However, it should be noted that the M/C ratios between samples will be considered on a relative basis, and not an absolute basis.

A kinetic study of the Pb^{2+} adsorption onto the various carbon materials was also carried out by combining 30 mg of cx-GNFs, nGO or PM-GO (Chen) with 30 mL of 0.1 M $Pb(NO_3)_2$. The mixtures were continuously sonicated to ensure homogeneity. At defined time intervals, 4 mL of this dispersion was filtered through a 200 nm polycarbonate membrane, washed and dried. The Pb/C ratio of each Pb^{2+}@carbon sample was then determined by the XPS survey spectra as described previously. The data reveals that the adsorption equilibria are reached very quickly for nGO and GO (Fig. A6.2). This suggests that the uptake of heavy-metals is not being limited in any way by inaccessible surface area on the nGO and GO. The cx-GNFs show a slight gradual increase in the Pb^{2+} uptake over a time period of 100 minutes. This could be due to the initial formation of dicarboxylate-lead complexes with COOH groups from different flakes which are successively replaced by monocarboxylate complexes as the sonication time progresses.

The fast equilibration of the Pb^{2+} adsorption onto nGO and GO illustrates that their poorer performance with respect to binding Pb^{2+} is not due to kinetic factors but to the intrinsically different interaction properties of the carbon materials with the heavy metals. Furthermore, the exfoliation process of the carbon materials upon sonication, which could potentially limit the accessible surface area, does not appear to be a limiting factor for the heavy metal extraction using nGO and GO.

The ability of a carbon material to extract metal cations from solution is dependent upon a range of parameters including the ionic strength and pH of the mixture. In order to ensure comparable ionic strengths throughout the various adsorption experiments, 10 mg of each carbon material was treated with 10 mL of a 0.1 M solutions of the metal salts which means that the cations are in a large excess. Consequently, the ionic strength of a mixture of cx-GNFs, nGO or GO with a particular metal cation, is approximately constant. Likewise, increasing the pH of a mixture is expected to lead to an increase in metal chelation. This arises as a result of a decrease in H^+ ions in solution which in turn reduces the competition between the metal cations and H^+ ions for the chelating ligand; which in the case of cx-GNFs, nGO and GO, are the oxo-functional groups. Furthermore, increasing the pH to basic conditions would lead to precipitation of metal hydroxide species (34; 50) and therefore give misleading results.

The pH of the $M^{2+/3+}$@carbon mixtures was measured prior to filtration and the results are shown in Fig. 6.2(b). It can be seen that for a particular metal ion, the pH of the $M^{2+/3+}$@cx-GNFs ≤ $M^{2+/3+}$@GO < $M^{2+/3+}$@nGO indicating that the cx-GNFs are at a disadvantage for metal sorption with respect to GO and nGO for the reasons discussed earlier. The lower pH of the cx-GNFs is expected given the highly carboxylated nature of the material and the fact that carboxylic acids are much stronger acids than alcohols and the other functional groups found at high concentrations on GO. Indeed, 1 mg mL^{-1} aqueous dispersions of cx-GNFs, nGO and GO gave pH values of 2.5, 3.3 and 3.0 respectively. Interestingly, the pH of GO is slightly lower than nGO despite nGO containing more carboxylic acid groups. However, GO has many more acidic hydroxyl groups on its basal plane, and given that its structural instability in water generates even more acidic functional groups,(51) this result is not necessarily surprising.

Despite the lower pH of the cx-GNFs, they clearly outperform the other two carbon materials at extracting metals as evidenced by the M/C ratios obtained from the XPS survey spectra shown in Fig. 6.2(b). For example, the cx-GNFs can bind about 10 times more Pb^{2+} than GO. This is partially due to the number of carboxylic acid groups per unit mass of each material. For instance, the cx-GNFs consist of (17 ± 3) at. % COOH groups according to the integrated C(III) XPS C1s region at approx. 289.0 eV, compared to (15 ± 2) and (10 ± 2) at. % for nGO and GO respectively. However, it should be noted that this value is exaggerated for nGO and GO which will have significant contributions from C(II) species such as ketones, as demonstrated previously by ^{13}C-NMR studies in chapter 3 section 3.3.1. Carboxylic acids are bidentate and generally stronger metal chelators compared to monodentate alcohols and epoxides. Indeed, it has been proposed by other authors that COOH groups are the most efficient functional group on graphenic materials at removing Pb^{2+} cations.(11) However, this alone cannot rationalise the significantly enhanced adsorption capacity of the cx-GNFs. Clearly, other sorption mechanisms are taking place, as will be discussed in the next section.

It is important to stress that despite nGO achieving better extraction results compared to GO, the pH of the $M^{2+/3+}$@nGO mixtures were on average 0.4 units more basic than for $M^{2+/3+}$@GO, allowing the nGO flakes to better coordinate to metals. Hence, the actual ability of nGO to remove heavy metals compared to GO may not be as pronounced as shown in Fig. 6.2(b) if the extractions were carried out at the same pH. It is noteworthy that buffer solutions were deliberately not used for these experiments, instead the natural pH of the $M^{2+/3+}$@carbon mixtures was relied upon. This removes any doubt with respect

to the effect ionic strength and foreign species might have in influencing the metal-sorption capability of the carbon materials.

6.4 Binding mechanism of heavy-metals onto cx-GNFs

The area-normalised XPS C1s spectra of the $M^{2+/3+}$@cx-GNFs are shown in Fig. 6.3. The most immediate observation is the additional peak at ~286.7 eV which is present in all the $M^{2+/3+}$@cx-GNFs but absent for the pure cx-GNFs. Furthermore, the areas of the C(III) peaks at ~288.5 eV are larger and shifted towards lower binding energies for the $M^{2+/3+}$@cx-GNFs. The newly formed peaks at 286.7 eV suggest non-covalent cation-π interactions between the metal cations and the graphenic basal plane of the cx-GNFs.(52-54) This can be rationalised by considering the electrostatic attraction between the positively charged metal cations and the graphenic π-electrons which creates a local deshielding effect along the graphenic basal plane where the metal cations have adsorbed. This in turn confers a δ^+ charge on the carbon atoms resulting in an increase in the binding energy of its core electrons. Hence, the observed decrease in the relative C1s C-C/C=C peak intensity with respect to the C(III) peak. This effect is most noticeable for the Pb^{2+}@cx-GNFs sample which has the highest M/C ratio of all the $M^{2+/3+}$@cx-GNFs (Fig. 6.2(b))), suggesting that Pb-π interactions are the most favourable out of all the heavy metals under these conditions, perhaps because Pb^{2+} has the lowest solvation enthalpy.(55) Alternatively, the results can also be interpreted as a covalent Lewis acid-base interaction whereby the $M^{2+/3+}$ cations and carbon π electrons act as the electron receptor and donor respectively.(11; 25) It is noteworthy that the pure cx-GNFs were ultrasonicated in the same way as the $M^{2+/3+}$@cx-GNFs to ensure this feature was not the result of mechanical agitation.

These changes in the XPS C1s region before and after heavy-metal loading onto the cx-GNFs are not unique to heavy metals. Indeed, it was found that alkali (Na^+) and alkaline earth metals (Mg^{2+} and Ca^{2+}) as well as rare-earth metals (Y^{3+}) and group 3 elements such as Al^{3+} all exhibited similar enhancements on loading onto the cx-GNFs (*c.f.* Appendix Fig. A6.3). Note that since these are not redox-active elements, one can conclude the enhancements seen in the XPS C1s region are not due to redox processes.

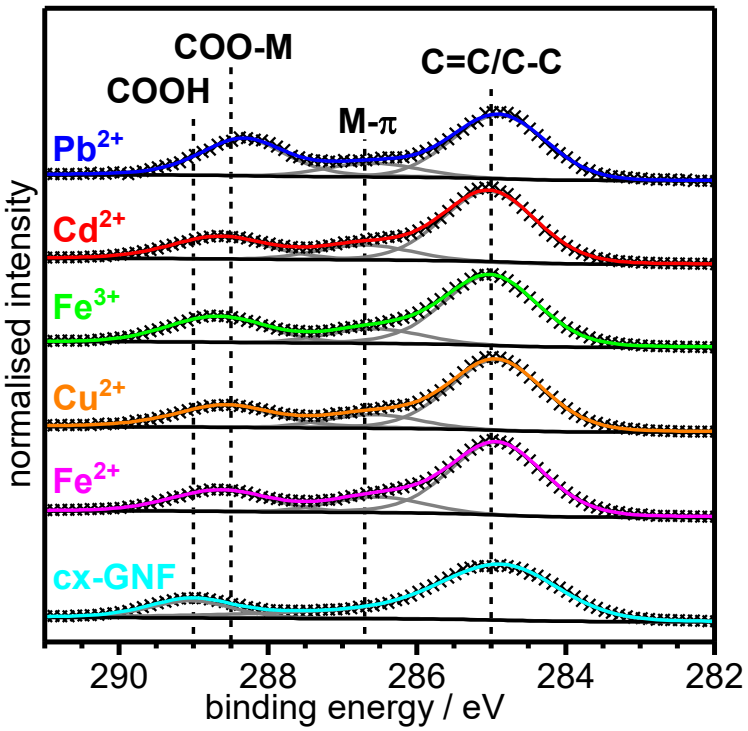

Fig. 6.3 Area-normalised XPS C1s spectra of cx-GNFs (cyan), Fe^{2+}@cx-GNFs (magenta), Cu^{2+}@cx-GNFs (orange), Fe^{3+}@cx-GNFs (green), Cd^{2+}@cx-GNFs (red) and Pb^{2+}@cx-GNFs (blue). The crosses are the experimental data, grey lines are the fitted peaks, black line is the Shirley background function and the coloured lines are the peak sums respectively.

To further prove that the trends observed in the XPS C1s spectra are due to metal interactions with the graphenic basal plane (be they electrostatic, covalent or a mixture of both in nature; and now collectively referred to as M-π), solid state ^{13}C-NMR spectra of the cx-GNFs were collected before and after exposure to a Pb^{2+} solution (Fig. 6.4). The ^{13}C-NMR spectra of the cx-GNFs and Pb^{2+}@cx-GNFs both exhibit two peaks, one associated with COOH groups (~170 ppm) and another for sp^2 graphenic carbon (~130 ppm).(49) A distinct shift to higher ppm (downfield shift) is observed for both peaks in the spectrum of Pb^{2+}@cxGNFs, indicating more deshielded environments. The downfield shift observed for the sp^2 carbon from 134 to 137 ppm is in good agreement with M-π interactions which induce a deshielding effect on the aromatic rings as described earlier.(53) However, the downfield shift of the COOH group from 170 to 176 ppm is most likely the result of chelation between the Pb^{2+} ions and the carboxyl groups on the cx-GNFs.(56; 57) It is noteworthy that the absence of C(I) species such as epoxides and alcohols between 60 and 70 ppm in the Pb^{2+}@cx-GNFs spectrum proves that the newly formed peaks at 286.7 eV in the XPS C1s regions of the $M^{2+/3+}$@cx-GNFs are due to M-π interactions and not to the formation of alcohol or epoxide groups. Interestingly, the M-

π interactions were not observed in the XPS C1s spectra of $M^{2+/3+}$@GO but were noticeable to a small extent for the $M^{2+/3+}$@nGO materials (Fig. A6.4). This could be because the cx-GNFs and nGO nanomaterials have more intact aromatic sp^2 basal planes compared to GO, as evidenced by the higher intensity of the sp^2 C=C peak in the solid state ^{13}C-NMR spectra (*c.f.* chapter 3 section 3.3.1).

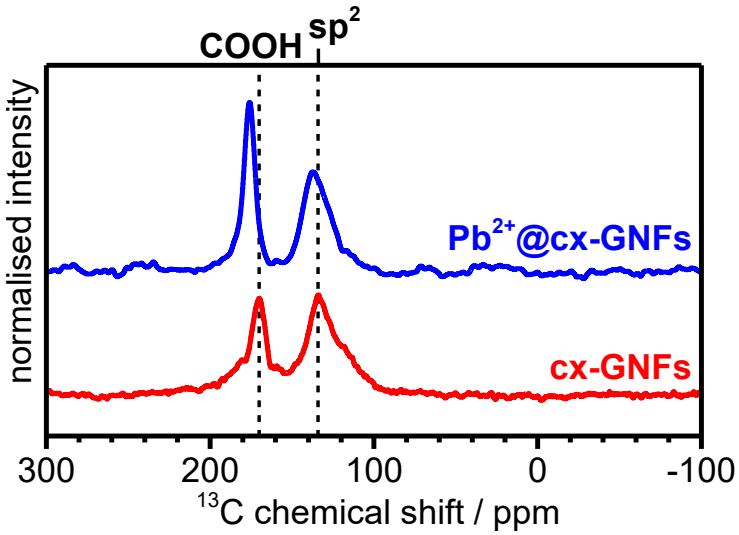

Fig. 6.4 ^{13}C-NMR spectra of cx-GNFs (red) and Pb^{2+}@cx-GNFs (blue). Vertical dashed lines denote peak positions of functional groups.

Further evidence for metal chelation between the heavy-metal cations and the carboxylic acid groups of the cx-GNFs is provided by the significant shift to lower binding energy of the XPS C1s C(III) peak from ~289 eV to 288.5 eV (Fig. 6.3), consistent with the weakening of the C=O bond in COOH to form an extended electron delocalised system in the metal carboxylate.(58) This is further emphasised by the bathochromic shift in the C=O stretching frequency from about 1715 cm^{-1} of the COOH groups in the cx-GNFs to 1558 cm^{-1} of the metal carboxylates in the $M^{2+/3+}$@cx-GNFs (Fig. 6.5). Interestingly, the effect is also most pronounced for Pb^{2+}@cx-GNFs, suggesting that Pb^{2+} ions interact most strongly with the cx-GNFs both *via* M-π interactions as well as the metal-carboxylate chelation. Consequently, these two effects taken together explain the exceptionally high performance of the cx-GNFs for extraction of Pb^{2+} compared with the other carbon materials as shown in Fig. 6.2(b). It is noteworthy that the IR spectra of both the $M^{2+/3+}$@nGO as well as $M^{2+/3+}$@GO also show the same

bathochromic shift (Appendix Fig. A6.5) indicating that metal complexation has taken place, albeit to lesser extents.

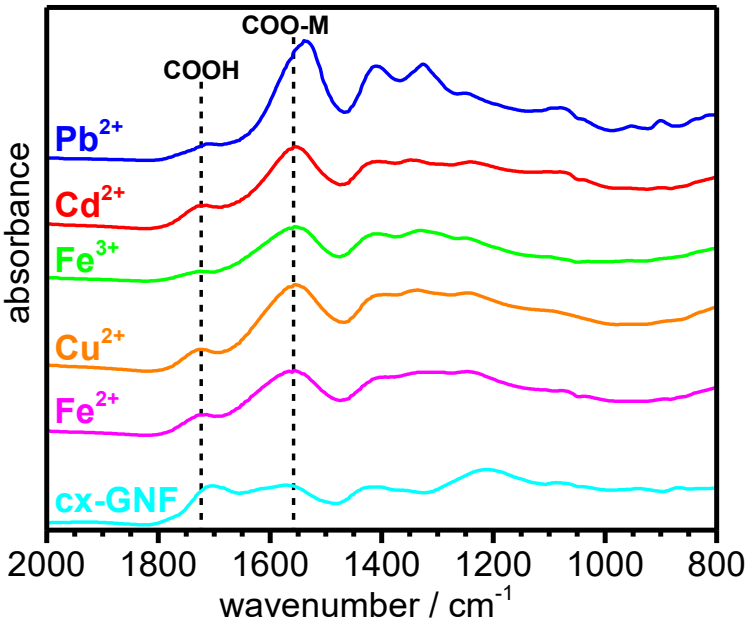

Fig. 6.5 ATR-IR spectra of cx-GNFs (cyan), Fe^{2+}@cx-GNFs (magenta), Cu^{2+}@cx-GNFs (orange), Fe^{3+}@cx-GNFs (green), Cd^{2+}@cx-GNFs (red) and Pb^{2+}@cx-GNFs (blue).

The combination of strong M-π interactions and chelation of carboxylic acids to metals explains why the cx-GNFs are able to adsorb metals more strongly than nGO and PM-GO.

6.5 Adsorption capacity of Pb^{2+} cations on cx-GNFs, nGO and GO using optical absorbance spectroscopy

In order to directly quantify, and thus compare, the adsorption capacities of the Pb^{2+}@carbons with other adsorbents, the three carbon materials were treated with an excess of Pb^{2+} cations. However, 5 mM concentrations of $Pb(NO_3)_2$ were used instead of the 0.1 M concentrations utilised in the metal-sorption experiments in section 6.3 (Fig. 6.2(b)). This was because the 0.1 M $Pb(NO_3)_2$ was in a large excess and greatly exceeded the loading capacity of the graphenic materials. To ensure equilibrium had been reached at this 5 mM $Pb(NO_3)_2$ concentration, the Pb/C ratio of the Pb^{2+}@carbons was determined from the XPS survey spectra in (Appendix Fig. A6.6) and found to be in agreement with the Pb/C ratios in Fig. 6.2(b), when 0.1 M $Pb(NO_3)_2$ was used.

In a typical experiment, 10 mg of cx-GNFs, nGO or GO were combined with 10 mL of 5 mM $Pb(NO_3)_2$ solutions. The mixtures were then ultrasonicated, filtered and washed in the way as described earlier in section 6.3. The colourless filtrates as well as 10 mL of a 5 mM Pb^{2+} solution (as a control) were topped up to 250 mL with deionised water. 4 mL of these solutions were acidified with 1 mL of 5 mM HCl, combined with a large excess solution of 2,5-dimercapto-1,3,4-thiadiazole dipotassium salt (DMTD-K^+)(59) and topped up to 10 mL. The yellow solutions were then transferred into quartz cuvettes of 1 cm path length, and optical absorbance spectra were recorded between 300 and 500 nm. Finally, the Pb^{2+} sorption capacities of the carbon materials were calculated from the difference in the optical absorbances at 400 nm between the initial 5 mM solution and the solutions after the Pb^{2+} extraction.

It should be noted that 2,5-dimercapto-1,3,4-thiadiazole dipotassium salt (DMTD-K^+),(59) depicted in Fig. 6.6(a) is a well-known chelating agent for Pb^{2+} cations. Chelation of DMTD-K^+ with Pb^{2+} cations occurs in 2:1 ratio and results in the formation of a yellow solution, whose concentration can be determined accurately using a calibration plot (*c.f.* Appendix Fig. A6.7(a)).(59) In this case absorbance values were taken at λ = 400 nm (Appendix Fig. A6.7(b)). Example optical absorbance spectra of the remaining (unreacted) Pb^{2+} cations after treatment of 5 mM $Pb(NO_3)_2$ with the cx-GNFs, nGO and GO can be found in Fig. 6.6(b). It is noteworthy that Pb^{2+} was chosen over the other heavy-metals for adsorption measurements since the adsorption of Pb^{2+} cations on the carbon materials demonstrated the greatest variability, as evidenced by Fig.6.2(b).

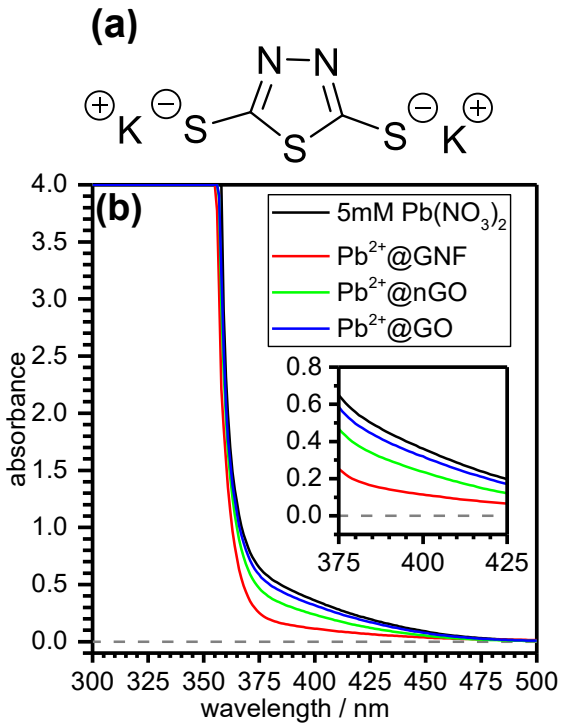

Fig. 6.6(a) The chemical structure of DMTD-K^+ and (b) optical absorbance spectra in the λ = 500-300 nm range (outset) and zoomed in region at λ = 400 nm (inset) of the remaining (unreacted) Pb^{2+} cations after treatment of 5 mM $Pb(NO_3)_2$ with the cx-GNFs, nGO and GO.

The calculated adsorption values of the Pb^{2+}@carbon derived from the optical absorbance spectra (such as those illustrated in Fig. 6.6(b)) are shown in Table 6.1. For each carbon material, the data in Table 6.1 represents the average and error (1.s.d.) of three samples, each measured three times. The results demonstrate that the adsorption capacity of the cx-GNFs towards Pb^{2+} ions are approximately six times that of conventional GO. Note that under the same pH conditions, it is likely that this value is even higher.

Table 6.1 Average sorption capacities of Pb^{2+} cations on cx-GNFs, nGO and GO

Carbon material	Adsorption capacity / $mg.g^{-1}$	Conditions
cx-GNFs	659 ± 6	pH 2.2, *T* 293 K
nGO	336 ± 6	pH 3.3, *T* 293 K
GO	102 ± 76	pH 3.1, *T* 293 K

In comparison with other functionalised graphenic materials, according to recent reviews,(23; 26) the cx-GNFs are one of the best materials to date at extracting Pb^{2+} cations from aqueous solutions (see Table 6.2). For clarity, the table has been modified to include the cx-GNFs in the appropriate rankings (top 5). It is noteworthy that an attempt was made to determine the sorption capacity of activated charcoal (AC), towards Pb^{2+} cations, but it was found to be negligible in comparison with the graphenic materials (even when treated with 0.1 M $Pb(NO_3)_2$). Indeed, the Pb/C ratio of Pb^{2+}@AC was determined to be one order of magnitude below GO and therefore two orders of magnitude lower than the Pb^{2+}@GNF (*c.f.* Appendix Fig. A6.8). This is in good agreement with Yang *et. al.* who demonstrated the adsorption capacity of Cu^{2+} cations on GO is about ten times higher than activated charcoal.(60) Furthermore, the cx-GNFs outweigh other common sorbents such as zeolites and biomass-derived sorbents by an order of magnitude.(23; 61)

Table 6.2 Adsorption capacities of the top ten GO-based adsorbents at extracting Pb^{2+} cations. Table adapted from [ref. 23] with permission from Springer.

Adsorbent	**Max. adsorption capacity / mg.g^{-1}**	**pH**
FGO1	1850.00 (333 K)	6.0
GO	1119.00 ± 41 (298 K)	5.0
FGO2	758.00 (333 K)	5.5-7.5
MnFe2O4/GO	673.00	5.0
cx-GNFs	**659 ± 6 (293 K)**	**2.2**
Iron Oxide/GO	588.24 (303 K)	5.0
EDTA/MGO	508.40 (298 K)	4.2
GO/PAMAMs	568.18 (298 K)	4.5
EDTA/GO	479.00 ± 0.82 (298 K)	6.8
Chitosan/GO	461.30 (318 K)	6.0
Chitosan/GO-SH	447.00 (293 K)	5.0

From Table 6.2 it can be seen that all of the Pb^{2+} cations were extracted at pH ≥ 4.2. This is because a sharp increase in Pb^{2+} adsorption on GO is observed on increasing

the pH from 2 to 4. (23; 27; 34; 35) Above pH 4.2, the adsorption capacity does not change as significantly with pH. Hence above pH 4.2, a true maximum adsorption capacity can be obtained.(23; 27; 34; 35) It should be noted, however, that these are generalisations and do not always hold true.(25) Under these circumstances, the cx-GNFs are expected to exhibit a very high (maximum) adsorption capacity at optimum pH. The true relevance of a maximum adsorption capacity at an ideal pH in the application of heavy-metal treatment is unclear. Whilst the presence of heavy-metals in water streams is expected to lower the pH of the water streams below neutral conditions, the metal-extraction process is likely to involve the metals being passed through large columns of adsorbents where the local pH is more likely to reflect the natural pH of the adsorbent. Hence, investigating the adsorbents at their natural pH in aqueous solution (as described in this work) may be more industrially relevant. The alternative would be to ensure that the adsorbent always operates at optimum pH by constantly flushing the column with an appropriate buffer solution, which is costly and time consuming.

Other factors influencing the adsorption capacity of heavy-metals on GO include ionic strength and temperature.(11; 25; 36-38; 62) In the case of the former, inorganic anions have only a small influence on the adsorption capacity as they interact with the solvated metal cations through outer-sphere complex formation.(25; 36; 37) However, the effect of cations on the adsorption capacity is more significant as they may compete directly for the adsorbent (i.e. the oxo-groups on GO), through the formation of inner-sphere interactions.(25; 36; 37) Temperature, by contrast, has a huge effect on adsorption capacity as is evidenced by the 'number 1' spot in Table 6.2 taken by few-layered graphene oxide (FGO). The impressive adsorption capacity of 1850 $mg.g^{-1}$ was carried out at 333 K (60°C) by Zhao and co-workers.(25) Indeed, Zhao *et. al*. demonstrated that the capacity FGO towards Pb^{2+} cations increases from 842 $mg.g^{-1}$ to 1850 $mg.g^{-1}$ on increasing the temperature from 273 K to 333 K, an increase of 120 %. Similarly, Jia *et. al*. obtained adsorption capacities of 344 and 758 $mg.g^{-1}$ when Pb^{2+} cations were treated with FGO at 273 K and 333 K respectively.(38) Note that to ensure the adsorption capacities we report in Table 6.1 were carried out at 293 K, the quartz cuvettes containing the Pb^{2+} cations were placed in a device which allowed for external water cooling/heating.

The adsorption of Pb^{2+} cations on GO is clearly an endothermic process.(11; 25; 38) The endothermicity can be rationalised by considering the strongly solvated Pb^{2+} cations which require more energy to dehydrate than is gained by chelation/adsorption on GO.(25) Hence the endothermicity of dehydration outweighs the exothermicity of

adsorption.(25) Increasing the temperature allows the dehydration of Pb^{2+} cations to occur more readily and thus adsorption on GO becomes more likely.(25) The overall Gibbs free energy change (ΔG^0) is negative implying that the entropy change on adsorbing Pb^{2+} cations onto GO is positive and outweighs the endothermicity of the process.(25) The entropy gain most likely reflects the removal of the hydration shell surrounding the Pb^{2+} cations on adsorbing onto GO.(25) The increase in entropy as a result of dehydration therefore outweighs the decrease in entropy due to adsorption.

The sorption mechanism of Pb^{2+} cations on GO has been shown to be pH dependent, suggesting outer-sphere adsorption at low pH and inner-sphere complexation at high pH.(11; 25; 34; 62) Interestingly, Zhao *et*. *al*. demonstrated that at pH values below 10, adsorption of Pb^{2+} cations on GO results in a decrease in pH due to inner-sphere coordination.(25) The inner-sphere coordination can be treated as an ion exchange mechanism where H^+ ions are replaced with Pb^{2+} cations.(25) The liberated H^+ ions hence contribute towards the global decrease in pH.(25) Above pH 10, the authors note, no appreciable change in pH is detected.(25)

Conversely, Huang and co-workers revealed that the adsorption of Pb^{2+} cations on GO with lower oxidation degrees resulted in a significant rise in pH when experiments were conducted between pH 3 and 5.(11) In fact, in one case, the pH of a GO dispersion increased from 4.00 to 6.11 on addition of sub milli-molar concentrations of Pb^{2+} cations.(11) Interestingly, at pH 2 no observable change in pH was detected after the addition of Pb^{2+} cations, yet significant decreases in pH were noted under basic conditions.(11) Huang *et*. *al*. propose that the results are consistent with Pb^{2+} cations and the π electron system of GO behaving as Lewis acids and donors respectively, in the same way as described earlier between the cx-GNFs and the metal cations.(11) Between pH 3 and 5 the Pb^{2+} cations adsorb strongly onto the graphenic basal plane which is accompanied by the simultaneous adsorption of H^+ ions, resulting in the observed increase in pH.(11) At low pH it is expected that the GO sheet has a less negative surface potential, disfavouring the adsorption of Pb^{2+} cations, and hence little change is observed in pH.(11) At higher pH (>7.6), the decrease in pH when the Pb^{2+} cations are adsorbed can be explained by an increased competition in inner-sphere chemistry which liberates H^+ ions, as discussed earlier, which outweighs the adsorption of the ions on the graphenic basal plane.(11) That is to say, that under basic conditions a significant number of acidic functional groups (carboxyls, hydroxyls *etc*.), will be deprotonated and thus negatively charged. Hence these species will form strong complexes with the Pb^{2+} cations.

Recently, Showalter *et. al*. demonstrated using X-ray absorption fine structure (XAFS) that the sorption of Pb^{2+} cations on GO is predominantly outer-sphere at low pH whilst mainly inner-sphere at high pH.(62) The exact cut-off between the two remains unclear.(62)

In this work, the adsorption of Pb^{2+} cations on cx-GNFs, nGO and GO resulted in an increase in pH of 0.4-0.5 units when 0.1 M $Pb(NO_3)_2$ was used. However, in this case the increase in pH is most likely the result of combining the 0.1 M $Pb(NO_3)_2$ solution, which is pH 4.3, with the carbon materials respectively. Hence the pH of 1 $mg.mL^{-1}$ dispersions of cx-GNFs, nGO and GO increase from 2.5, 3.0 and 3.3 to 3.0, 3.5 and 3.9 respectively.

However, when the adsorption measurements were carried out using 5 mM $Pb(NO_3)_2$, little change in the pH of nGO and GO was detected before and after the addition of Pb^{2+} cations. This suggests that inner-sphere coordination by the oxo-groups is almost perfectly counter-balanced by the adsorption of Pb^{2+} and H^+ on the basal planes. This can be rationalised by considering that whilst nGO has more COOH groups than GO, and should therefore have a greater degree of inner-sphere coordination, nGO also has a more intact sp^2 carbon framework which would encourage Pb^{2+} and H^+ ion adsorption on the basal plane. Evidence for both of these assumptions is suggested by XPS and FT-IR spectra in Appendix Figs. A6.4 and A6.5 respectively which indicate enhanced M-π and COO-M coordination respectively for nGO w.r.t GO (note that these spectra were collected when the materials were treated with 0.1 M $Pb(NO_3)_2$, and are consequently not a direct comparison). Furthermore, consideration is not being taken towards the interaction of Pb^{2+} cations with the other oxo-groups on GO which would alter the scenario. In reality, therefore, the situation is more complex. With regards to the cx-GNFs, the pH decreases slightly from 2.5 to 2.2 when 5mM $Pb(NO_3)_2$ was added. This is not unexpected since Huang *et. al* also observed no increase in pH at this pH due to the less negative surface potential of the graphenic sheet as described earlier. The slight decrease in pH is therefore the result of inner-sphere metal-carboxylate complexes. Since the chelation ability of COOH groups towards Pb^{2+} cations will be low at this pH, due to competition with H^+ ions, only a small decline in pH is expected. Lastly, since buffer solutions were used in the literature studies, it is unclear to what extent these buffers could have altered the sorption mechanism(s).

Comparison of the Pb^{2+}@carbon adsorption capacities (determined from optical absorbance spectra) in Table 6.1 with the Pb/C ratios from XPS in Fig. 6.2(b), and appendix Figs. A6.2 and A6.6 respectively, suggests that XPS is reliable at a semi-

quantitative level. From Table 6.1, the cx-GNFs were found to adsorb approximately twice as many Pb^{2+} cations than nGO; according to XPS, the cx-GNFs should adsorb ~2.5 times more. Similarly, the adsorption capacity of nGO in Table 6.1 was determined to be on average at least 3 times that of GO, in reasonable agreement with the aforementioned XPS data. However the cx-GNF capacity is ~6.5 times that of GO which is not as high as suggested by the XPS spectra, which implied up to an order of magnitude in difference. Having said this, the error in the adsorption capacity of GO using optical absorbance spectroscopy was exceptionally high which could be attributed to the large variation in the morphology of GO. Indeed, there exists a significant discrepancy between reported adsorption capacities within the GO literature, with values differing by up to an order of magnitude under similar conditions.(23) Furthermore, different characterisation methods are used to determine adsorption capacities, such as optical absorbance spectroscopy, flame atomic absorbance spectrometry (FAAS) and inductively coupled mass spectrometry (ICP-MS). Furthermore, for a given published set of data, only one technique is typically employed to determine the adsorption capacity.

6.6 Reversibility and selectivity of Pb^{2+} cations adsorbed on cx-GNFs

The XPS spectra in Fig. 6.7 illustrate the reversible loading and unloading of Pb^{2+} cations onto the cx-GNFs. Initially, the cx-GNFs (Fig. 6.7(a)) were treated with 0.1 M $Pb(NO_3)_2$ in the same way as described earlier (section 6.3), yielding the corresponding Pb^{2+}@cx-GNF material (Fig. 6.7(b)). The Pb^{2+} cations were then removed by treatment with formic acid (Fig. 6.7(c)), leaving behind only a small trace of Pb^{2+} cations. A small quantity of calcium (3%) was also detected in the XPS survey spectrum which was most likely the result of the gradual uptake of Ca^{2+} cation traces in the deionised water during the multiple dialysis steps to remove the Pb^{2+} cations (see chapter 8 section 8.2.16). It is noteworthy that after the unloading of Pb^{2+} cations from the Pb^{2+}@cx-GNFs there is clear reversibility in the XPS C1s region back to the original cx-GNFs in terms of the relative peak intensities. Finally, after removal of the Pb^{2+} cations, the cx-GNFs were re-treated with 0.1 M $Pb(NO_3)_2$ solution as before which again yielded Pb^{2+}@cx-GNF without any change in the loading efficiency as indicated by the Pb/C ratio (Fig. 6.7(d)). As expected due to the reversible behaviour, the final XPS C1s region was similar compared to the spectrum of the Pb^{2+}@cx-GNF upon first loading of the cx-GNF with Pb^{2+} cations.

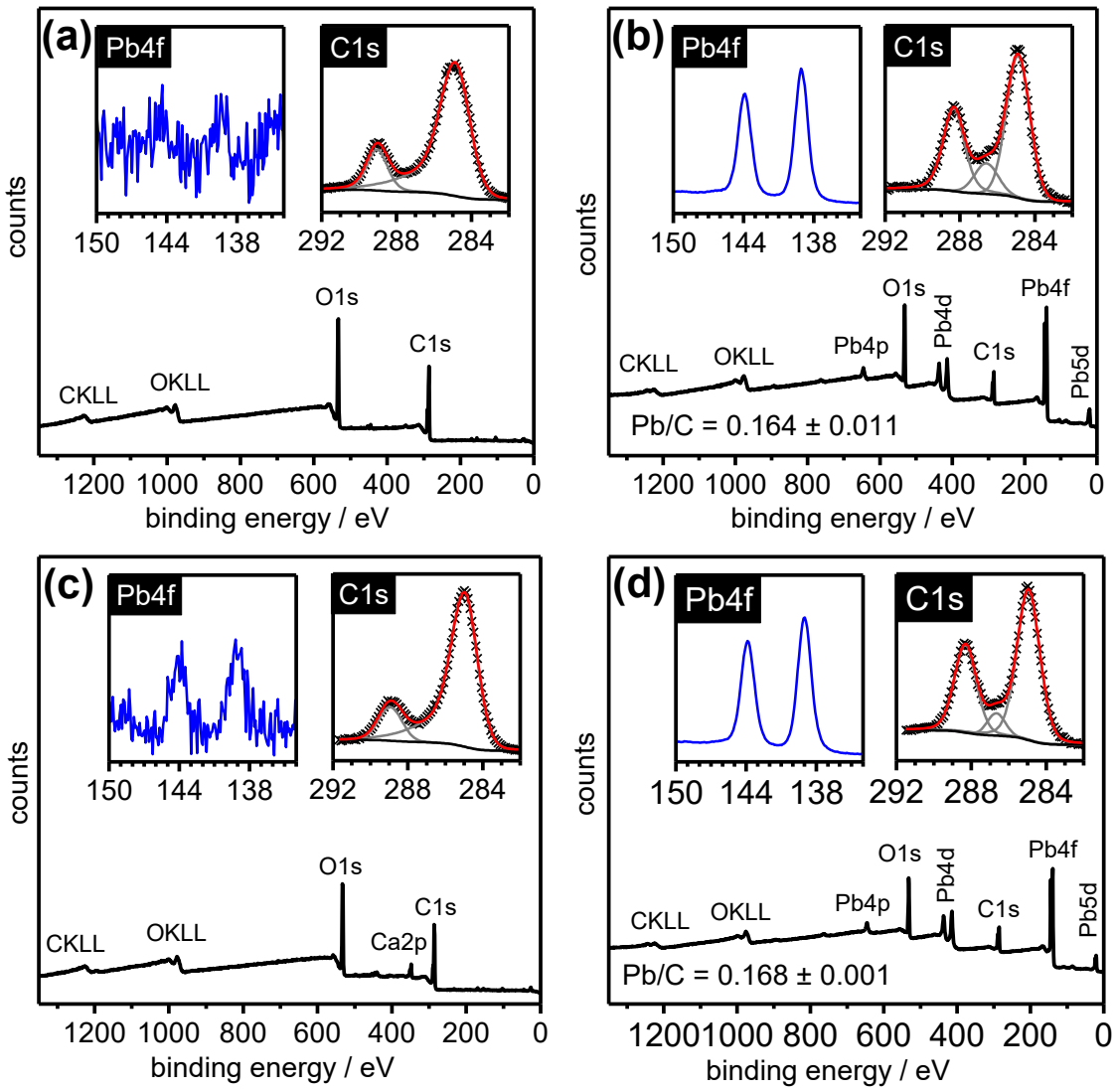

Fig. 6.7 Reversible loading of Pb^{2+} cations onto cx-GNFs. XPS survey spectra (outset), Pb4f regions (inset, left) and C1s regions (inset, right) of (a) cx-GNFs before Pb^{2+} cation addition, (b) after Pb^{2+} cation addition, (c) treatment of (b) with formic acid to remove Pb^{2+} cations and (d) after reloading with Pb^{2+} cations.

To assess the selectivity of the cx-GNFs towards Pb^{2+} cation extraction in the presence of other cations, the cx-GNFs were treated with mixtures containing lead cations as well as calcium or magnesium cations. In a typical experiment, 5 mL of a 2 M $Ca(NO_3)_2$ or $Mg(NO_3)_2$ solution was combined with 5 mL of either a 0.2 M or 0.02 M $Pb(NO_3)_2$ solution to give 10 or 100 molar excesses of Ca^{2+} or Mg^{2+} cations. The solutions were then combined with 10 mg of cx-GNFs and the precipitated GNFs were collected as described in section 6.3 earlier.

Calcium and magnesium were chosen because these cations are the most common divalent metal cations found in drinking or industrial waste waters. The Mg^{2+} or Ca^{2+} cations were either in a 10 or 100 molar excess compared to the lead ions. In the presence of 10 mole equivalents of Ca^{2+} or Mg^{2+} cations per equivalent of Pb^{2+}, only Pb^{2+} cations were removed from solution (Fig. 6.8(a) and (c)) and in the same quantities as reported before in Fig. 6.2(b) where no other cations were present. When 100 mole equivalents were employed, there was still a significant selectivity towards the Pb^{2+} cations as shown in Fig. 6.8(b) and (d). Indeed, an average Pb^{2+}/Mg^{2+} ratio of 6.5 and Pb^{2+}/Ca^{2+} ratio of 2.0 was determined from the XPS survey spectra.

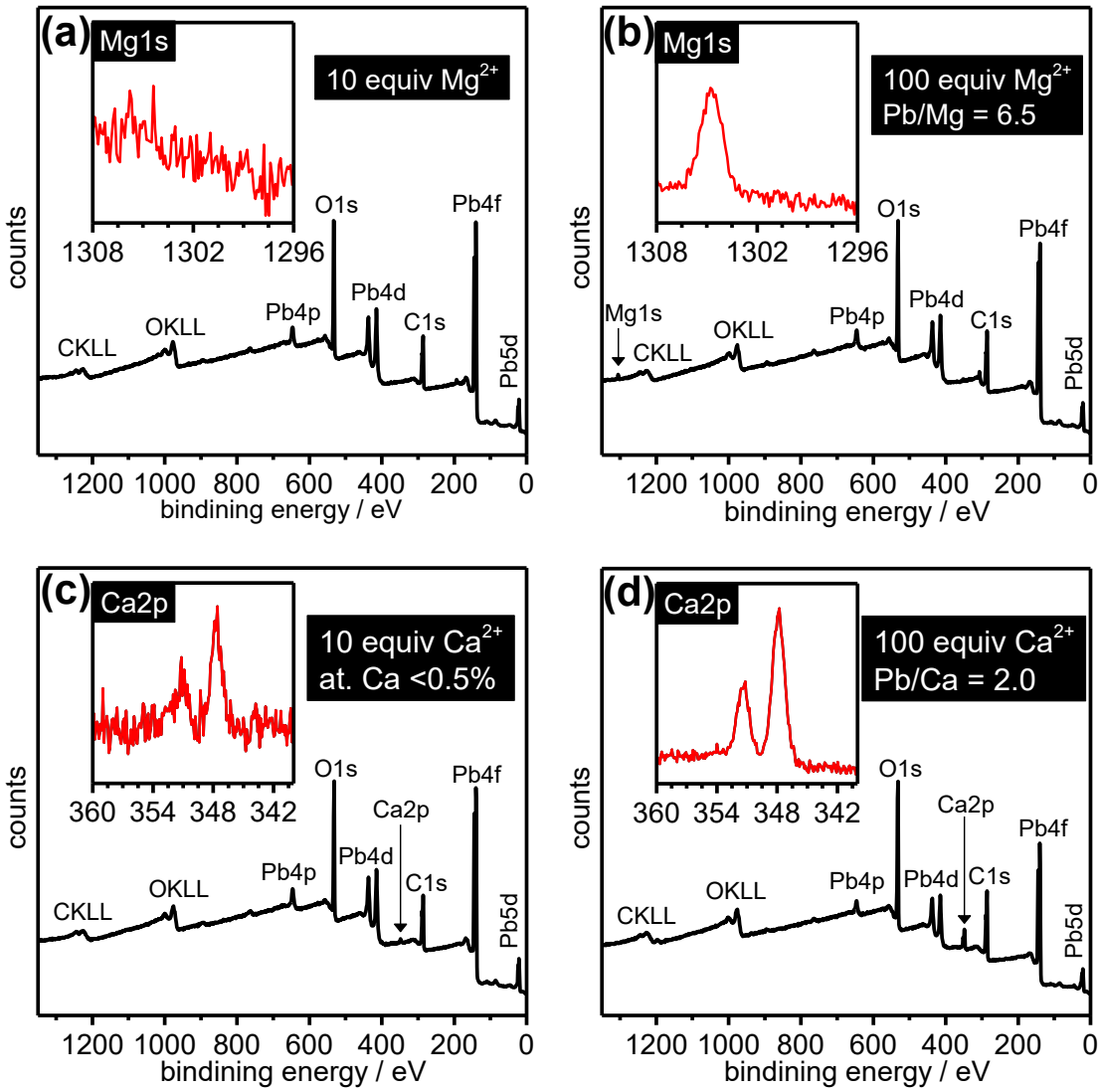

Fig. 6.8 XPS survey spectra (outset) and Mg1s or Ca2p regions (inset) of cx-GNFs treated with a mixture of Pb^{2+} cations and 10 equiv. Mg^{2+} cations (a) or Ca^{2+} cations (b) or 100 equiv. Mg^{2+} cations (c) or Ca^{2+} cations (d).

For clarity, the Pb/C ratios of the selectivity measurements are shown in the bar graph in Fig. 6.9. Each bar represents the mean and 1.s.d error of three samples, each sample being measured three times. The red bar represents the Pb^{2+}@GNF in Fig. 6.2(b) in the absence of any other metal cations.

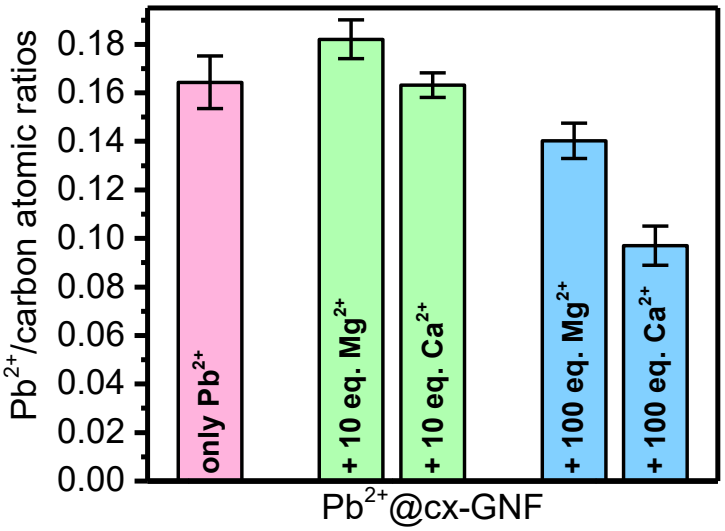

Fig. 6.9 Pb/C atomic ratios determined from XPS survey spectra of cx-GNFs treated with Pb^{2+} cations only (red), Pb^{2+} cations with 10 equivalents Ca^{2+} or Mg^{2+} cations (green), and Pb^{2+} cations with 100 equivalents Ca^{2+} or Mg^{2+} cations (blue).

Interestingly, the results suggest that the affinity of the cx-GNFs towards Ca^{2+} cations is much greater than Mg^{2+} cations. This could be due to Mg^{2+} cations forming strong and stable solvation spheres in water, hence a lot of energy is required for their dehydration.(63) Conversely, calcium has been shown to adopt various hydration spheres, which could aid the sorption process.(63) Nonetheless, the cx-GNFs clearly demonstrate a strong selectivity towards Pb^{2+} cations in the presence of up to 100 equivalents of Mg^{2+} or Ca^{2+} cations. Furthermore, the Pb^{2+}@GNF can be readily recycled with formic acid to yield the cx-GNFs once again which can then be reloaded with Pb^{2+} cations without any loss in efficiency.

The exact reason why the cx-GNFs display such a remarkable and unique selectivity for Pb^{2+} cations over other metal cations is unclear. It is likely that the relatively weak solvation sphere of Pb^{2+} plays a crucial role. Moreover, the relatively diffuse nature of the Pb^{2+} cation compared with other smaller metal cations, would be more preferable in the context of M-π interactions, where the electron π is very diffuse.

6.7 Conclusions

Cx-GNFs and nGO are highly efficient materials for the extraction of a wide range of heavy metals and outperform conventional GO by up to six times. In fact, they can easily compete with carbon nanomaterials which have been chemically functionalised for the purpose of heavy metal extraction.(23; 26) Furthermore, they outweigh other common sorbents such as zeolites and biomass-derived sorbents by an order of magnitude (23; 61). In the case of cx-GNFs, a remarkable affinity for Pb^{2+} cations even in the presence of large excesses of Mg^{2+} and Ca^{2+} cations has been demonstrated. Detailed insights into the chemical binding mechanisms of the heavy metal cations onto the cx-GNFs were gained, highlighting the formation of metal carboxylates as well as M-π interactions as the two dominating modes for metal-carbon interactions. The high efficiency of the cx-GNFs for heavy-metal extraction can therefore be attributed to the large number of carboxylic acid groups but also the intact graphenic areas on the basal plane. The loading and unloading of Pb^{2+} cations onto the cx-GNFs was found to be completely reversible allowing for the cx-GNFs to be readily recycled. Consequently, out of all the investigated as-made graphene materials, the cx-GNFs are most suited for future applications in heavy-metal extraction processes.

6.8 Chapter 6 References

1. Jarup L. 2003. Hazards of heavy metal contamination. *Br. Med. Bull.* 68:167-82

2. Mortada WI, Sobh MA, El-Defrawy MM, Farahat SE. 2001. Study of lead exposure from automobile exhaust as a risk for nephrotoxicity among traffic policemen. *Am. J. Nephrol.* 21:274-9

3. Lidsky TI, Schneider JS. 2003. Lead neurotoxicity in children: basic mechanisms and clinical correlates. *Brain* 126:5-19

4. Apostoli P, Bellini A, Porru S, Bisanti L. 2000. The effect of lead on male fertility: A time to pregnancy (TTP) study. *Am. J. Ind. Med.* 38:310-5

5. Schwartz J, Landrigan PJ, Baker EL, Orenstein WA, Vonlindern IH. 1990. LEAD-INDUCED ANEMIA - DOSE-RESPONSE RELATIONSHIPS AND EVIDENCE FOR A THRESHOLD. *Am. J. Public Health* 80:165-8

6. Steenland K, Boffetta P. 2000. Lead and cancer in humans: Where are we now? *Am. J. Ind. Med.* 38:295-9

7. Silbergeld EK, Waalkes M, Rice JM. 2000. Lead as a carcinogen: Experimental evidence and mechanisms of action. *Am. J. Ind. Med.* 38:316-23

8. Barakat MA. 2011. New trends in removing heavy metals from industrial wastewater. *Arab. J. Chem.* 4:361-77

9. Hua M, Zhang S, Pan B, Zhang W, Lv L, Zhang Q. 2012. Heavy metal removal from water/wastewater by nanosized metal oxides: A review. *J. Hazard. Mater.* 211:317-31

10. Hsu L-C, Huang C-Y, Chuang Y-H, Chen H-W, Chan Y-T, et al. 2016. Accumulation of heavy metals and trace elements in fluvial sediments received effluents from traditional and semiconductor industries. *Sci. Rep.* 6:34250

11. Huang ZH, Zheng XY, Lv W, Wang M, Yang QH, Kang FY. 2011. Adsorption of Lead(II) Ions from Aqueous Solution on Low-Temperature Exfoliated Graphene Nanosheets. *Langmuir* 27:7558-62

12. Deng XJ, Lu LL, Li HW, Luo F. 2010. The adsorption properties of Pb(II) and Cd(II) on functionalized graphene prepared by electrolysis method. *J. Hazard. Mater.* 183:923-30

13. Cui LM, Wang YG, Gao L, Hu LH, Yan LG, et al. 2015. EDTA functionalized magnetic graphene oxide for removal of Pb(II), Hg(II) and Cu(II) in water treatment: Adsorption mechanism and separation property. *Chem. Eng. J.* 281:1-10

14. Madadrang CJ, Kim HY, Gao GH, Wang N, Zhu J, et al. 2012. Adsorption Behavior of EDTA-Graphene Oxide for Pb (II) Removal. *ACS Appl. Mater. Interfaces* 4:1186-93

15. Fan LL, Luo CN, Sun M, Qiu HM. 2012. Synthesis of graphene oxide decorated with magnetic cyclodextrin for fast chromium removal. *J. Mater. Chem.* 22:24577-83

16. Li SK, Lu XF, Xue YP, Lei JY, Zheng T, Wang C. 2012. Fabrication of Polypyrrole/Graphene Oxide Composite Nanosheets and Their Applications for Cr(VI) Removal in Aqueous Solution. *Plos One* 7

17. Sui N, Wang LN, Wu XH, Li XH, Sui J, et al. 2015. Polyethylenimine modified magnetic graphene oxide nanocomposites for Cu2+ removal. *RSC Adv.* 5:746-52

18. Liu Y, Xu L, Liu JS, Liu XY, Chen CH, et al. 2016. Graphene oxides cross-linked with hyperbranched polyethylenimines: Preparation, characterization and their potential as recyclable and highly efficient adsorption materials for lead(II) ions. *Chem. Eng. J.* 285:698-708

19. Sitko R, Zawisza B, Talik E, Janik P, Osoba G, et al. 2014. Spherical silica particles decorated with graphene oxide nanosheets as a new sorbent in inorganic trace analysis. *Anal. Chim. Acta* 834:22-9

20. Zhou GY, Liu CB, Tang YH, Luo SL, Zeng ZB, et al. 2015. Sponge-like polysiloxane-graphene oxide gel as a highly efficient and renewable adsorbent for lead and cadmium metals removal from wastewater. *Chem. Eng. J.* 280:275-82

21. Hou WJ, Zhang YM, Liu T, Lu HW, He L. 2015. Graphene oxide coated quartz sand as a high performance adsorption material in the application of water treatment. *RSC Adv.* 5:8037-43

22. Hu XJ, Liu YG, Wang H, Chen AW, Zeng GM, et al. 2013. Removal of Cu(II) ions from aqueous solution using sulfonated magnetic graphene oxide composite. *Sep. Purif. Technol.* 108:189-95

23. Duru I, Ege D, Kamali AR. 2016. Graphene oxides for removal of heavy and precious metals from wastewater. *J. Mater. Sci.* 51:6097-116

24. Alagappan PN, Heimann J, Morrow L, Andreoli E, Barron AR. 2017. Easily Regenerated Readily Deployable Absorbent for Heavy Metal Removal from Contaminated Water. *Sci. Rep.* 7:6682

25. Zhao GX, Ren XM, Gao X, Tan XL, Li JX, et al. 2011. Removal of Pb(II) ions from aqueous solutions on few-layered graphene oxide nanosheets. *Dalton Trans.* 40:10945-52

26. Wang S, Li X, Liu Y, Zhang C, Tan X, et al. 2017. Nitrogen-containing amino compounds functionalized graphene oxide: Synthesis, characterization and application for the removal of pollutants from wastewater: A review. *J. Hazard. Mater.* 342:177-91

27. Sitko R, Janik P, Zawisza B, Talik E, Margui E, Queralt I. 2015. Green Approach for Ultratrace Determination of Divalent Metal Ions and Arsenic Species Using Total-Reflection X-ray Fluorescence Spectrometry and Mercapto-Modified Graphene Oxide Nanosheets as a Novel Adsorbent. *Anal. Chem.* 87:3535-42

28. Wang L, Yu F, Ma J. 2017. Design and Construction of Graphene-Based Electrode Materials for Capacitive Deionization. *Acta Physico-Chimica Sinica* 33:1338-53

29. Liu PY, Yan TT, Shi LY, Park HS, Chen XC, et al. 2017. Graphene-based materials for capacitive deionization. *J. Mater. Chem. A* 5:13907-43

30. Wang M, Xu XT, Tang J, Hou SJ, Hossain MSA, et al. 2017. High performance capacitive deionization electrodes based on ultrathin nitrogen-doped carbon/graphene nano-sandwiches. *Chem. Commun.* 53:10784-7

31. Liu LJ, Guo XR, Tallon R, Huang XK, Chen JH. 2017. Highly porous N-doped graphene nanosheets for rapid removal of heavy metals from water by capacitive deionization. *Chem. Commun.* 53:881-4

32. Chen MM, Wei D, Chu W, Wang T, Tong DG. 2017. One-pot synthesis of O-doped BN nanosheets as a capacitive deionization electrode for efficient removal of heavy metal ions from water. *J. Mater. Chem. A* 5:17029-39

33. Liu PY, Yan TT, Zhang JP, Shi LY, Zhang DS. 2017. Separation and recovery of heavy metal ions and salt ions from wastewater by 3D graphene-based asymmetric electrodes via capacitive deionization. *J. Mater. Chem. A* 5:14748-57

34. Sitko R, Turek E, Zawisza B, Malicka E, Talik E, et al. 2013. Adsorption of divalent metal ions from aqueous solutions using graphene oxide. *Dalton Trans.* 42:5682-9

35. Tan MT, Liu X, Li W, Li HX. 2015. Enhancing Sorption Capacities for Copper(II) and Lead(II) under Weakly Acidic Conditions by L-Tryptophan-Functionalized Graphene Oxide. *J. Chem. Eng. Data* 60:1469-75

36. Upadhyay RK, Soin N, Roy SS. 2014. Role of graphene/metal oxide composites as photocatalysts, adsorbents and disinfectants in water treatment: a review. *RSC Adv.* 4:3823-51

37. Liu MC, Chen CL, Hu J, Wu XL, Wang XK. 2011. Synthesis of Magnetite/Graphene Oxide Composite and Application for Cobalt(II) Removal. *J. Phys. Chem. C* 115:25234-40

38. Jia WB, Lu SS. 2014. Few-layered graphene oxides as superior adsorbents for the removal of Pb(II) ions from aqueous solutions. *Korean J. Chem. Eng.* 31:1265-70

39. Novoselov KS, Geim AK, Morozov SV, Jiang D, Zhang Y, et al. 2004. Electric field effect in atomically thin carbon films. *Science* 306:666-9

40. Chang H, Wu H. 2013. Graphene-based nanocomposites: preparation, functionalization, and energy and environmental applications. *Energy Environ. Sci.* 6:3483-507

41. Zhao G, Wen T, Chen C, Wang X. 2012. Synthesis of graphene-based nanomaterials and their application in energy-related and environmental-related areas. *RSC Adv.* 2:9286-303

42. Zhao G, Li J, Ren X, Chen C, Wang X. 2011. Few-Layered Graphene Oxide Nanosheets As Superior Sorbents for Heavy Metal Ion Pollution Management. *Energy Environ. Sci.* 45:10454-62

43. Liu L, Li C, Bao CL, Jia Q, Xiao PF, et al. 2012. Preparation and characterization of chitosan/graphene oxide composites for the adsorption of Au(III) and Pd(II). *Talanta* 93:350-7

44. Chen JH, Xing HT, Guo HX, Weng W, Hu SR, et al. 2014. Investigation on the adsorption properties of Cr(VI) ions on a novel graphene oxide (GO) based composite adsorbent. *J. Mater. Chem. A* 2:12561-70

45. Chauke VP, Maity A, Chetty A. 2015. High-performance towards removal of toxic hexavalent chromium from aqueous solution using graphene oxide-alpha cyclodextrin-polypyrrole nanocomposites. *J. Mol. Liq.* 211:71-7

46. Zhang F, Wang B, He SF, Man RL. 2014. Preparation of Graphene-Oxide/Polyamidoamine Dendrimers and Their Adsorption Properties toward Some Heavy Metal Ions. *J. Chem. Eng. Data* 59:1719-26

47. Kumar S, Nair RR, Pillai PB, Gupta SN, Iyengar MAR, Sood AK. 2014. Graphene Oxide-MnFe2O4 Magnetic Nanohybrids for Efficient Removal of Lead and Arsenic from Water. *ACS Appl. Mater. Interfaces* 6:17426-36

48. Yang X, Chen CL, Li JX, Zhao GX, Ren XM, Wang XK. 2012. Graphene oxide-iron oxide and reduced graphene oxide-iron oxide hybrid materials for the removal of organic and inorganic pollutants. *RSC Adv.* 2:8821-6

49. Lerf A, He HY, Forster M, Klinowski J. 1998. Structure of graphite oxide revisited. *J. Phys. Chem. B* 102:4477-82

50. Zhao GX, Li JX, Ren XM, Chen CL, Wang XK. 2011. Few-Layered Graphene Oxide Nanosheets As Superior Sorbents for Heavy Metal Ion Pollution Management. *Environ. Sci. Technol.* 45:10454-62

51. Dimiev AM, Alemany LB, Tour JM. 2013. Graphene Oxide. Origin of Acidity, Its Instability in Water, and a New Dynamic Structural Model. *ACS Nano* 7:576-88

52. Dougherty DA. 1996. Cation-pi interactions in chemistry and biology: A new view of benzene, Phe, Tyr, and Trp. *Science* 271:163-8

53. Jeong SY, Kim SH, Han JT, Jeong HJ, Lee GW. 2012. Highly Concentrated and Conductive Reduced Graphene Oxide Nanosheets by Monovalent Cation-pi Interaction: Toward Printed Electronics. *Adv. Funct. Mater.* 22:3307-14

54. Machida M, Mochimaru T, Tatsumoto H. 2006. Lead(II) adsorption onto the graphene layer of carbonaceous materials in aqueous solution. *Carbon* 44:2681-8

55. Burgess J. 1978. *Metal ions in solution*. pp 182-183. Chinchester, England: Ellis Horwood

56. Pesek JJ, Schneider JF. 1988. THE DETECTION OF MERCURY, LEAD, AND METHYLMERCURY BINDING-SITES ON LYSOZYME BY C-13 NMR CHEMICAL-SHIFTS OF THE CARBOXYLATE GROUPS. *J. Inorg. Biochem.* 32:233-8

57. Sisombath NS, Jalilehvand F, Schell AC, Wu Q. 2014. Lead(II) Binding to the Chelating Agent D-Penicillamine in Aqueous Solution. *Inorg. Chem.* 53:12459-68

58. Park S, Lee K-S, Bozoklu G, Cai W, Nguyen ST, Ruoff RS. 2008. Graphene oxide papers modified by divalent ions - Enhancing mechanical properties via chemical cross-linking. *ACS Nano* 2:572-8

59. Ahmed MJ, Mamun MA. 2001. Spectrophotometric determination of lead in industrial, environmental, biological and soil samples using 2,5-dimercapto-1,3,4-thiadiazole. *Talanta* 55:43-54

60. Yang ST, Chang YL, Wang HF, Liu GB, Chen S, et al. 2010. Folding/aggregation of graphene oxide and its application in Cu2+ removal. *J. Colloid Interface Sci.* 351:122-7

61. De Gisi S, Lofrano G, Grassi M, Notarnicola M. 2016. Characteristics and adsorption capacities of low-cost sorbents for wastewater treatment: A review. *Sustain. Mater. Technol.* 9:10-40

62. Showalter AR, Duster TA, Szymanowski JES, Na CZ, Fein JB, et al. 2016. Sorption mechanisms of metals to graphene oxide. *Proc. 16th International*

Conference on X-ray Absorption Fine Structure (XAFS), *Karlsruhe Inst Technol, Karlsruhe, GERMANY*, *2015*, 712:

63. Ikeda T, Boero M, Terakura K. 2007. Hydration properties of magnesium and calcium ions from constrained first principles molecular dynamics. *J. Chem. Phys.* 127

Chapter 7: Final Conclusions and Outlook

The primary aim of this thesis was to prepare novel carbon nanomaterials, characterise their structures, to understand their chemistry and to explore their use in a wide range of applications. These materials were designed as an alternative to conventional graphene oxide prepared *via* permanganate oxidation (PM-GO). PM-GO, despite being a promising and widely used material has many short comings, most notably the controversy surrounding its structure (1-4) and the non-eco-friendly way in which it is produced (5-8). To address these issues, three novel nanomaterials were prepared. These included highly carboxylated graphene nanoflakes (cx-GNFs), which are structurally well defined-constituting only of unoxidised sp^2 carbon and carboxylic acid groups. Nano-graphene oxide (nGO) - prepared using an eco-friendly route which replaces the conventional oxidation protocol of potassium permanganate in sulfuric acid with 8 M nitric acid, significantly reducing the oxidation strength of the mixture. The 'bottle-neck' purification process of typical GO processing which involves repetitive centrifugation and ultrasonication was replaced with a simple filtration step and ion-exchange/dialysis. The third and final material, which is GO prepared *via* dichromate oxidation, DC-GO, was structurally characterised and optimised for the first time. The alternative ratio of functional groups present on this material compared with PM-GO can provide for alternative chemical functionalisation protocols, *i.e*. to take advantage of the increased number of carboxylic acid groups.

The thermal annealing behaviour of the materials established that the cx-GNFs, and to a lesser extent the nGO, undergo unique decomposition pathways compared to PM-GO and DC-GO. In particular, the formation of carboxylic anhydrides at the graphene edges of these two materials was demonstrated experimentally for the first time. In fact, it was demonstrated that 81% of the carboxylic acid groups on the cx-GNFs are able to convert to carboxylic anhydrides. It was further shown that these carboxyl groups on the cx-GNFs exist in a dynamic equilibrium with the carboxylic anhydrides in water, allowing for facile room temperature chemical functionalisation with amines (not that the cx-GNFs are highly soluble in water, ~100 mg mL^{-1}). The fact that the cx-GNFs consist only of carboxyl (and a small number of anhydride) groups as the only oxygen-functionalities, allowed for simpler interpretation of the reaction products compared with PM-GO.

Finally, the cx-GNFs and the nGO were benchmarked against PM-GO in their ability to extract heavy-metal cations from water. Both materials were found to be exceptional at

extracting heavy-metals, and the cx-GNFs were shown to outperform some of the best purpose-built GO-hybrid materials reported in the literature at extracting Pb^{2+} cations from solution. Indeed the cx-GNFs were found to outperform PM-GO by up to six times, despite being at a pH disadvantage. The mode of metal-binding onto the cx-GNFs was also investigated - the formation of strong metal-carboxylate complexes as well as cation-pi (M-π) interactions were responsible for the strong binding affinity of the cx-GNFs towards metal cations. In general, the assignment of the new features in the XPS C1s regions of the $M^{2+/3+}$@GNFs as M-π interactions, contributed significantly towards the interpretation of XPS spectra of metal-carbon composites.

The unique nature of the cx-GNFs means they have been involved in a number of collaborations with other research groups. These include DNA sensors (9), ice-nucleation (10) and electrochemistry (11; 12). Ongoing collaborative research involves E-Coli sensors, metal-sensors and carbon frameworks. The potential impact of the cx-GNFs can therefore not be understated. A future outlook would be to look towards applying the cx-GNFs in the context of devices for heavy metal extraction, as well as to explore additional applications the cx-GNFs could be used for. The idea would be to find the most cost-effective and useful application.

In essence, the work presented in this thesis is not just about reporting the preparation and chemistry of new carbon materials, but also to contribute towards the current understanding of carbon materials in the literature in general. Carbon materials are expected to play a huge role in the future in regards to applications, yet their full potential is not realised. It is not in the interests of scientists to ‘stick with’ conventional materials and to not explore the new possibilities that new materials have to offer. Hence, this thesis encourages the exploration of carbon, new strategies and insights into its fundamental nature.

7.1 Chapter 7 References

1. Dimiev AM, Polson TA. 2015. Contesting the two-component structural model of graphene oxide and reexamining the chemistry of graphene oxide in basic media. *Carbon* 93:544-54

2. Rourke JP, Pandey PA, Moore JJ, Bates M, Kinloch IA, et al. 2011. The Real Graphene Oxide Revealed: Stripping the Oxidative Debris from the Graphene-like Sheets. *Angew. Chem. Int. Ed.* 50:3173-7

3. Rourke JP, Wilson NR. 2016. Letter to the Editor: A defence of the two-component model of graphene oxide. *Carbon* 96:339-41

4. Dimiev AM, Alemany LB, Tour JM. 2013. Graphene Oxide. Origin of Acidity, Its Instability in Water, and a New Dynamic Structural Model. *ACS Nano* 7:576-88

5. Lowe SE, Zhong YL. 2017. Challenges of Industrial-Scale Graphne Oxide Production. In *Graphene Oxide: Fundamentals and Applications*, ed. A Dimiev, S Eigler. London: Wiley and Sons. Number of.

6. Chen J, Yao BW, Li C, Shi GQ. 2013. An improved Hummers method for eco-friendly synthesis of graphene oxide. *Carbon* 64:225-9

7. Marcano DC, Kosynkin DV, Berlin JM, Sinitskii A, Sun Z, et al. 2010. Improved Synthesis of Graphene Oxide. *ACS Nano* 4:4806-14

8. Rosillo-Lopez M, Salzmann CG. 2016. A simple and mild chemical oxidation route to high-purity nano-graphene oxide. *Carbon* 106:56-63

9. Crick CR, Sze JYY, Rosillo-Lopez M, Salzmann CG, Edel JB. 2015. Selectively Sized Graphene-Based Nanopores for in Situ Single Molecule Sensing. *ACS Appl. Mater. Interfaces* 7:18188-94

10. Whale TF, Rosillo-Lopez M, Murray BJ, Salzmann CG. 2015. Ice Nucleation Properties of Oxidized Carbon Nanomaterials. *J. Phys. Chem. Lett.* 6:3012-6

11. Lounasvuori MM, Rosillo-Lopez M, Salzmann CG, Caruana DJ, Holt KB. 2015. The influence of acidic edge groups on the electrochemical performance of graphene nanoflakes. *J. Electroanal. Chem.* 753:28-34

12. Lounasvuori MM, Rosillo-Lopez M, Salzmann CG, Caruana DJ, Holt KB. 2014. Electrochemical characterisation of graphene nanoflakes with functionalised edges. *Faraday Discuss.* 172:293-310

Chapter 8: Additional experimental details

In this chapter the details of experimental data collection are described as well as the experimental methodologies. All experimental data collection was carried out at University College London (UCL).

8.1 Synthesis

8.1.1 Preparation of cx-GNFs

1.00 g of MWCNTs (3 to 15 walls, 5-20 nm outer diameter and 2-6 nm inner diameter and 1 to 10 μm in length; purchased from Bayer Materials Science or Elicarb (Thomas Swan Ltd)) were ultrasonicated in a 100 mL mixture of 3:1 vol% conc. H_2SO_4 acid (95-97% w/w) and conc. nitric acid (70% w/w) for 30 minutes. The reaction mixture was heated for 2 h at 100°C, cooled to room temperature and diluted three-fold with deionised water. The black dispersion was filtered through a 200 nm track-etched polycarbonate membrane and the black residue on the membrane was collected and washed with deionized water and vacuum dried. The black filtrate was neutralised with KOH and the white salt precipitate (consisting mainly of K_2SO_4) was removed by filtration. The black filtrate was re-acidified with dilute formic acid and then dialysed against high-purity Milli-Q water using a SpectraPor 3 regenerated cellulose dialysis membrane (Spectrum laboratories, MWCO 3.5 kDa). Once the conductivity of the surrounding water was <5 $\mu S.cm^{-1}$ the dispersion was passed over a cation exchange resin (Amberlite IR120, Sigma-Aldrich), if necessary, and freeze dried to give 160 mg of brown-black cx-GNFs.

8.1.2 Preparation of nGO

Arc-discharge (ADC) material consisting of single-wall carbon nanotubes (SWCNT) (diameter: 0.7- 1.2 nm, length: 10-50 μm), multi-wall carbon nanotubes (MWCNT) (diameter: 8-20 nm, length: 2-20 μm) and graphitic carbon was purchased from the Materials and Electrochemical Research (MER) Corporation (MRSW grade). 420 mg of this material was ultrasonicated in 21 mL of 1:1 distilled water/conc. HNO_3 acid for 30 min and then refluxed in air for 20 h, generating brown NO_x fumes. The resulting dispersion was diluted three fold with distilled water and then filtered under vacuum through a 0.2 μm track-etched Whatman polycarbonate membrane. The black residue

on the membrane was washed with deionised water and dried in air whilst the brown-black filtrate was neutralized by carefully adding NaOH pellets. On neutralization, precipitation of Na-nGO occurred. The mixture was then filtered under vacuum in the same way as before and the resulting filtrate (containing $NaNO_3$) was discarded. The Na-nGO left on the membrane was re-dispersed in ~0.1 M HNO_3 acid and dialyzed against distilled water via a regenerated cellulose dialysis membrane from Spectrum Laboratories, MWCO 3.5 kDa, flat width 45 mm. The dialysis was considered complete when the conductivity of the surrounding water was <5 μS cm^{-1}. The purified dispersion was then freeze dried to obtain 90 mg (21 % yield by mass) of brown-black nGO material.

8.1.3 Preparation of DC-GO (Chandra)(1)

Graphite flakes (2.5 g, 1 equiv.) and $NaNO_3$ (1.875 g, 0.75 equiv) were combined with H_2SO_4 (187.5 mL, 95-97% w/w) and left stirring for 15 min in an ice bath. $K_2Cr_2O_7$ (18.8 g, 7.5 equiv) was added slowly to the mixture over a period of 2 h. The mixture was then left stirring at room temperature (20°C) for 5 d. The dark green viscous mixture was transferred to an ice bath and aqueous H_2SO_4 (375 mL, 5% v/v) was added slowly over a period of 1 h. The mixture was then heated at 95°C for 2 h and left to cool back down to room temperature and diluted a further two-fold with deionised water. The mixture was centrifuged at 5000 r.p.m for 20 min and the dark blue-green solution containing the reduced Cr(III) species was decanted away. The remaining brown-black solid was collected and washed a further three times with aqueous HCl (5% v/v), discarding the clear supernatant each time. The brown-black solid was then re-dispersed in deionised water via ultrasonication for 20 min and centrifuged at 5000 r.p.m for 40 min. The dark brown supernatant containing the DC-GO was collected and the remaining solid was re-dipsersed/ultrasonicated in deionised water and centrifuged as before a further two times (or until the supernatant was colourless), collecting and combining the supernatants at the end of each cycle. The dispersed DC-GO was concentrated *in vacuo* at 50°C and dialysed against a Spectra/Por 3 regenerated cellulose dialysis membrane (MWCO 3.5 kDa) and freeze dried to obtain the desired DC-GO (~1 g yield by mass).

8.1.4 Preparation of DC-GO (optimised)

Graphite flakes (2.5 g, 1 equiv.) were combined with H_2SO_4 (187.5 mL, 95-97% w/w) and left stirring for 15 min in an ice bath. $K_2Cr_2O_7$ (18.8 g, 7.5 equiv) was added slowly to the mixture over a period of 2 h. The mixture was then left stirring at 45°C for 20 h. The dark

green viscous mixture was transferred to an ice bath and aqueous H_2SO_4 (375 mL, 5% v/v) was added slowly over a period of 1 h. The mixture was then heated at 95°C for 2h and left to cool back down to room temperature and diluted a further two-fold with deionised water, and a few drops of H_2O_2 (30% w/w) were added. The mixture was centrifuged at 5000 r.p.m for 20 min and the dark blue-green solution containing the reduced Cr(III) species was decanted away. The remaining brown-black solid was collected and washed a further three times with aqueous HCl (5% v/v), discarding the clear supernatant each time. The brown-black solid was then re-dispersed in deionised water via ultrasonication for 20 min and centrifuged at 5000 r.p.m for 40 min. The dark brown supernatant containing the DC-GO was collected and the remaining solid was re-dipsersed/ultrasonicated in deionised water and centrifuged as before a further two times (or until the supernatant was colourless), collecting and combining the supernatants at the end of each cycle. The dispersed DC-GO was concentrated in vacuo at 50°C and dialysed against a Spectra/Por 3 regenerated cellulose dialysis membrane (MWCO 3.5 kDa) and freeze dried to obtain the desired DC-GO (94% yield by mass).

8.1.5 Preparation of PM-GO (Chen)(2)

Graphite flakes (500 mg, 100 mesh, Sigma Aldrich) was combined with concentrated sulfuric acid (12.5 mL, 97% w/w) at 0°C with stirring. Potassium permanganate (1.50 g) was added slowly to the reaction mixture and the mixture was heated at 40°C for 30 min. Deionised water (25 mL) was added carefully to the mixture and the mixture was heated once more at 95°C for 15 min with stirring. The resulting brown mixture was then diluted by addition of deionised water (85 mL) followed by dropwise addition of hydrogen peroxide (5 ml, 30% v/v) to reduce any excess permanganate. The resulting yellow-green mixture was filtered through a 200 nm polycarbonate membrane, washed with aqueous HCl (75 mL, 10% v/v) and allowed to dry. The dry powder was re-dispersed in deionised water (100 mL) and dialysed against deionised water using a SpectraPor 3 regenerated cellulose dialysis membrane (Spectrum Laboratories, MWCO 3.5 kDa). The GO was then exfoliated by ultrasonication for 90 minutes, and the dispersion was centrifuged at 3000 rpm for 40 min. The supernatant was collected and ultrasonicated once more for 30 min, filtered through compacted glass wool, and passed over a cation exchange resin (Amberlite IR120, Sigma-Aldrich). The dispersion was concentrated and freeze dried to obtain a light brown solid (500 mg).

8.1.6 Preparation of PM-GO (Chandra) and PM-GO (optimised)

PM-GO (Chandra) and PM-GO (optimised) were prepared according to experimental sections 8.2.4 and 8.2.5 of this chapter respectively, with the exception that $K_2Cr_2O_7$ was replaced with $KMnO_4$.

8.1.7 Preparation of SiO_2-GNFs

SiO_2-NH_2 was initially prepared by combining silica gel (1.00 g, 40-63 μm) with 3-aminopropyltriethoxysilane (2 v/v in toluene, 250 mL) and stirred at room temperature for 1 h. The resulting amine functionalised silica gel was then filtered on a 0.2 μm Whatman Teflon membrane and washed three times, first with toluene, then a 1:1 toluene-methanol mixture, and finally methanol. Once dry, the material was treated with the capping agent (n-butyltrimethoxysilane, 2 v/v in toluene) in the same way as just described, and washed in the same way. The dry SiO_2-NH_2 was found to weigh 1.25 g after the amidation and capping, suggesting successful grafting. The SiO_2-NH_2 was then added slowly to a ~0.5 $mg.mL^{-1}$ brown dispersion of cx-GNFs (25.4 mg/50 mL) with occasional swirling, resulting in the formation of a brown precipitate (SiO_2-GNFs). The SiO_2-NH_2 was added until the dispersion of cx-GNFs just turned colourless, indicating maximum loading capacity of the cx-GNFs. 403 mg of SiO_2-NH_2 was required to completely precipitate 25.4 mg of cx-GNFs, suggesting a loading capacity/stoichiometry of ~15.9 mg of SiO_2-NH_2 per mg of cx-GNFs. The SiO_2-GNFs were then filtered on a 0.2 μm Whatman polycarbonate membrane and washed with copious volumes of deionised water. The SiO_2-GNFs were then dried in a vacuum desiccator.

8.1.8 Reversibility of cx-GNFs towards Pb^{2+} cations

75 mg of Pb^{2+}-loaded cx-GNFs (Pb^{2+}@cx-GNF) were sonicated in 10 mL of formic acid for <1 min. The dark brown dispersion was diluted with deionised water until pH 2 and then dialysed against deionised water *via* a SpectraPor 3 regenerated cellulose dialysis membrane (Spectrum laboratories, MWCO 3.5 kDa). Once the conductivity of the surrounding water was below 5 $\mu S.cm^{-1}$ the dispersion was passed over an ion exchange resin (Amberlite IR120, Sigma-Aldrich). The dispersion was dialysed once more, concentrated *in vacuo* and freeze dried to regenerate the cx-GNFs. The cx-GNFs were then treated again with a 0.1 M Pb^{2+} solution in the same way.

8.2 Chapter 8 References

1. Chandra S, Sahu S, Pramanik P. 2010. A novel synthesis of graphene by dichromate oxidation. *Mater. Sci. Eng., B* 167:133-6

2. Chen J, Yao BW, Li C, Shi GQ. 2013. An improved Hummers method for eco-friendly synthesis of graphene oxide. *Carbon* 64:225-9

Appendix chapter 3 additional figures

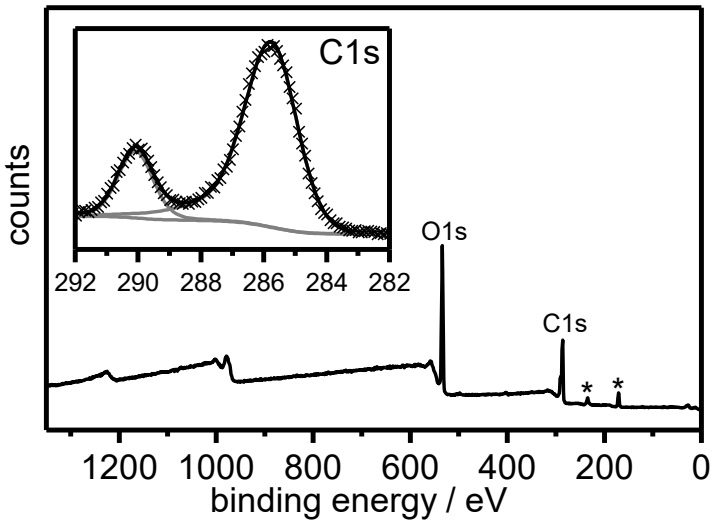

Fig. A3.1 cx-GNFs derived from Elicarb CVD MWCNTs (Thomas Swan Ltd.) under the same conditions as employed using Bayer MWCTNs.

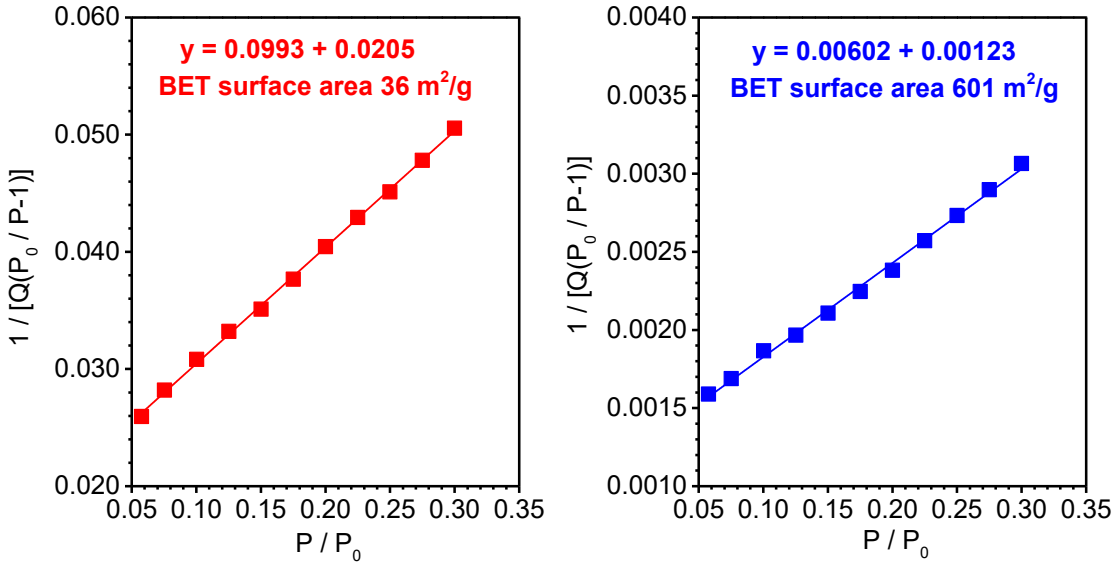

Fig. A3.2 BET surface area plot of t-GNFs (red) and a-GNFs (blue).

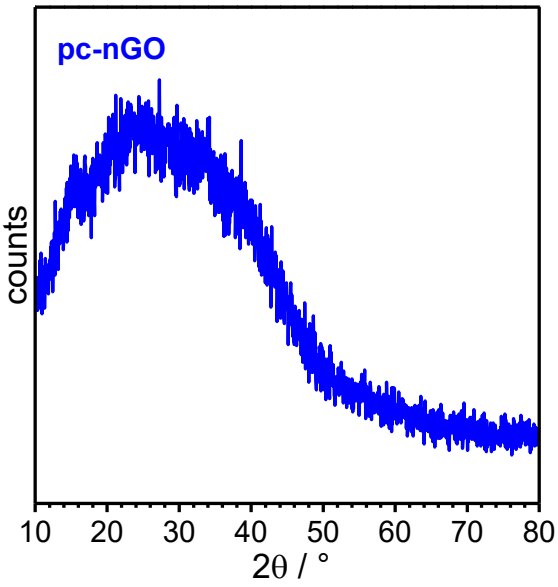

Fig. A3.3 Powder XRD pattern of pc-nGO

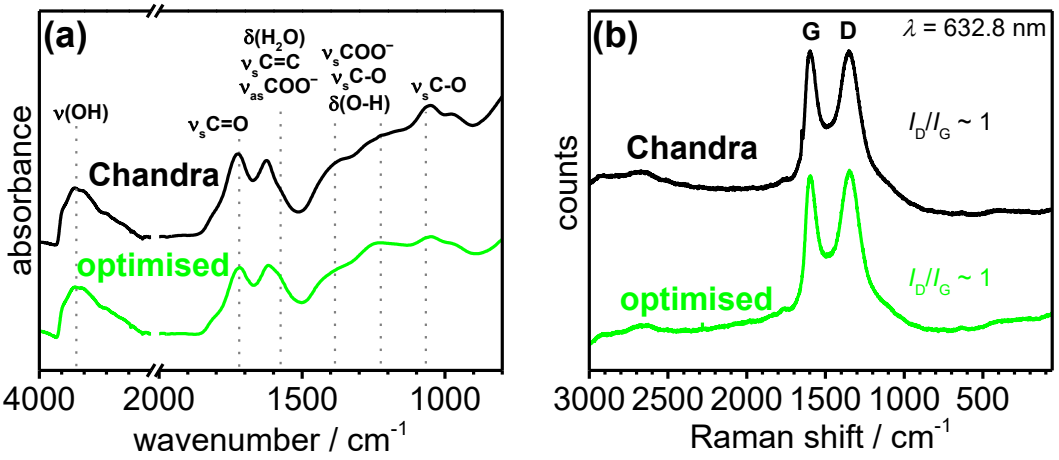

Fig. A3.4 (a) FT-IR and (b) Raman spectra of DC-GO (optimised) in green and DC-GO (Chandra) in black.

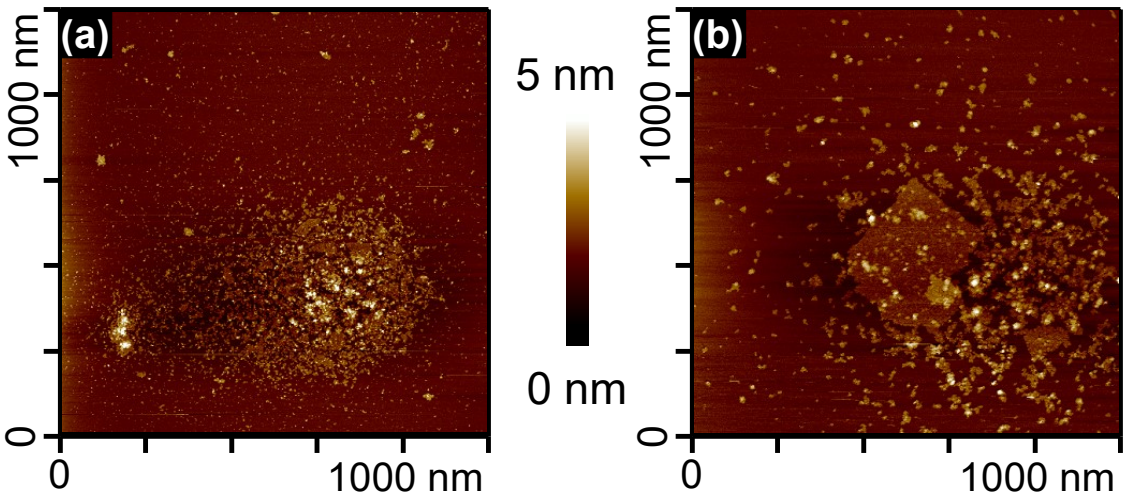

Fig. A3.5 AFM images of DC-GO (Chandra)

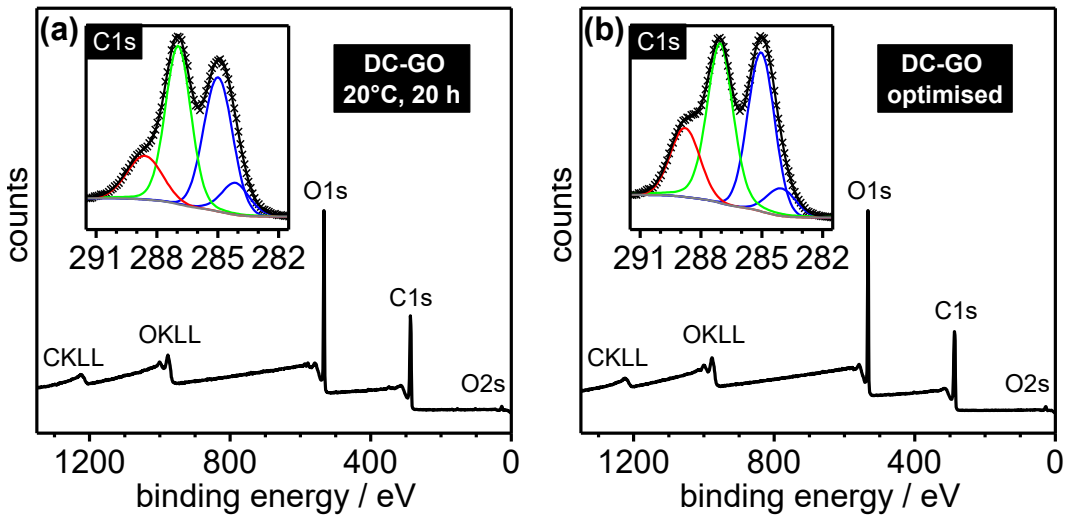

Fig. A3.6 XPS survey (outset) and C1s region (inset) of (a) less oxidised DC-GO prior to optimisation and (b) after optimisation, *i.e.* DC-GO (optimised). The crosses represent the experimental data whereas the grey, blue, green, red and black lines are the Shirley background functions, C(0), C(I) and C(III) fitted peaks and peak sum, respectively.

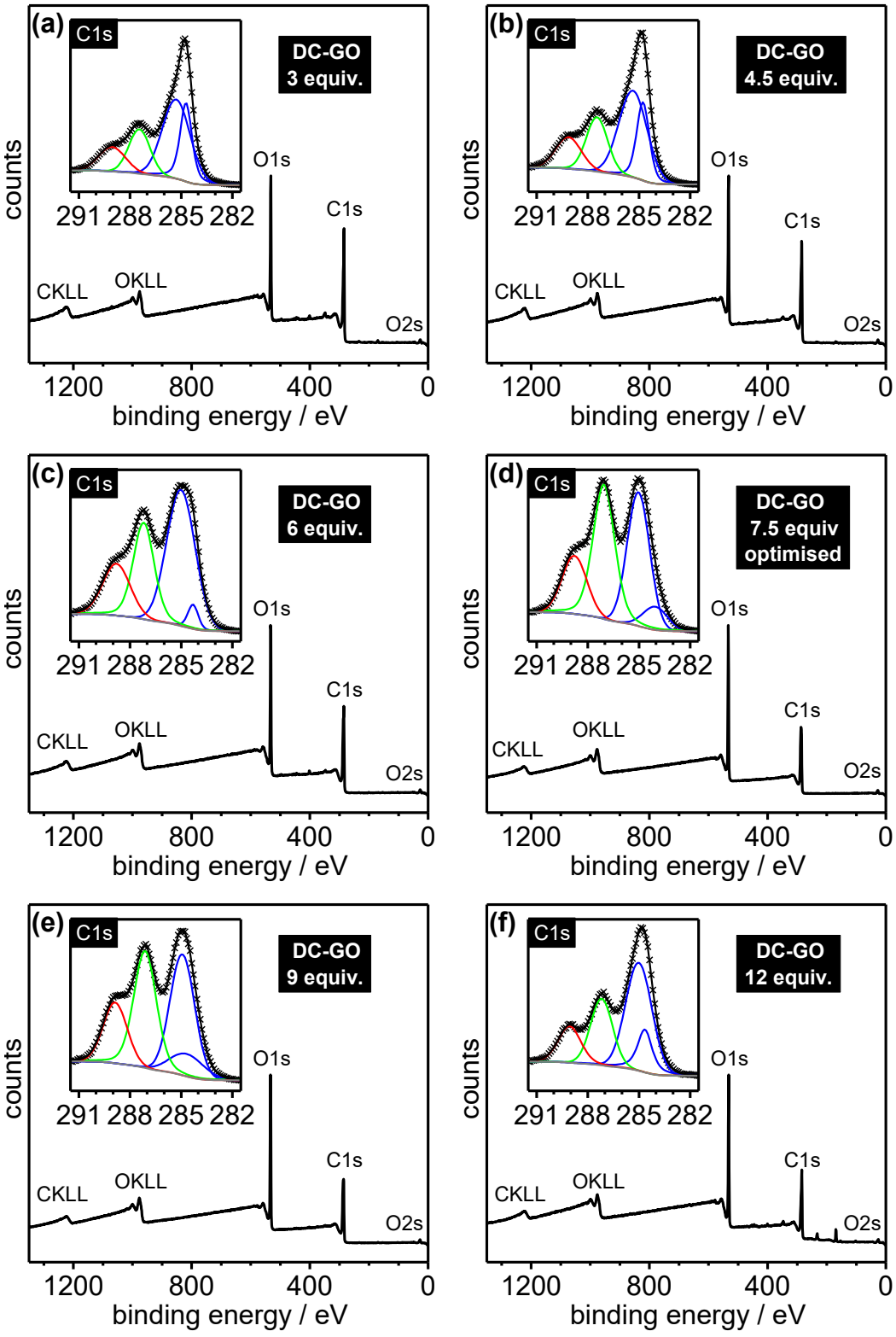

Fig. A3.7 Optimisation of the DC-GO protocol. XPS survey (outset) and C1s region (inset) of DC-GO prepared with (a) 3, (b) 4.5, (c) 6, (d) 7.5, (e) 9 and (f) 12 equivalents of $K_2Cr_2O_7$ per equivalent of graphite. Temperature and time were kept constant at 45°C and 20 h respectively. The crosses represent the experimental data whereas the grey, blue, green, red and black lines are the Shirley background functions, C(0), C(I) and C(III) fitted peaks and peak sum, respectively.

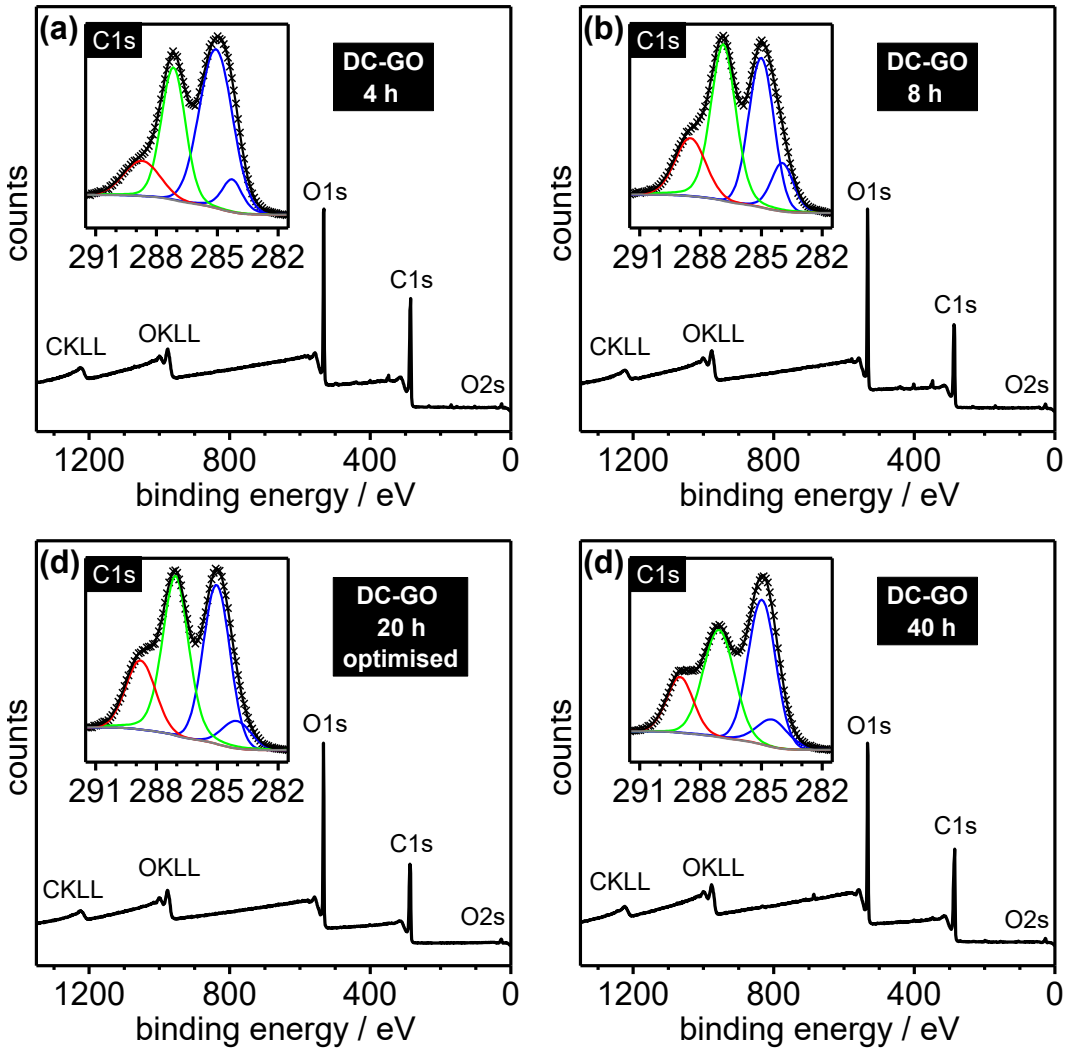

Fig. A3.8 Optimisation of the DC-GO protocol. XPS survey (outset) and C1s region (inset) of DC-GO oxidised for (a) 4 h, (b) 8 h, (c) 20 h and (d) 40 h respectively. Temperature and the number of equivalents of $K_2Cr_2O_7$ used were kept constant at 45°C and 7.5 respectively. The crosses represent the experimental data whereas the grey, blue, green, red and black lines are the Shirley background functions, C(0), C(I) and C(III) fitted peaks and peak sum, respectively.

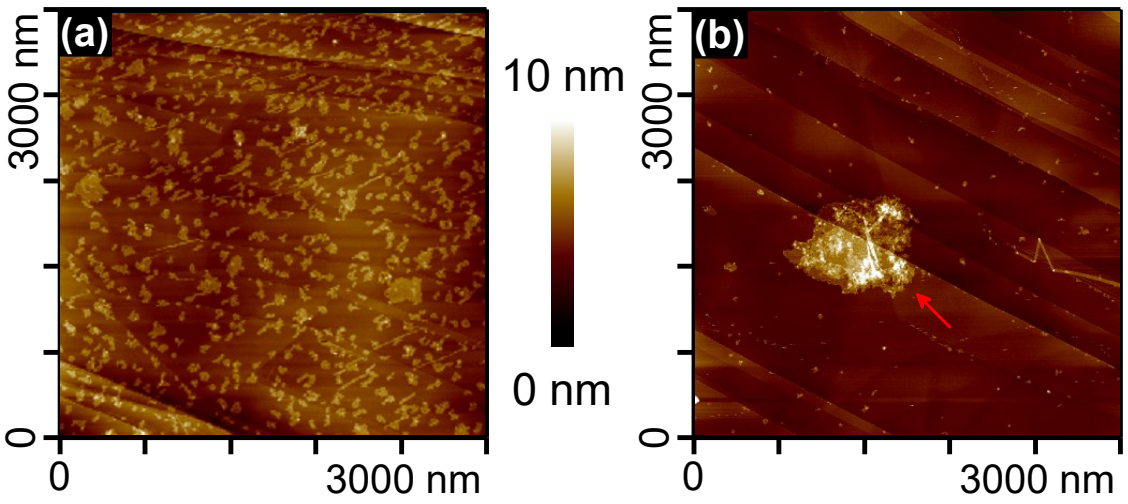

Fig. A3.9 AFM images of PM-GO (optimised).

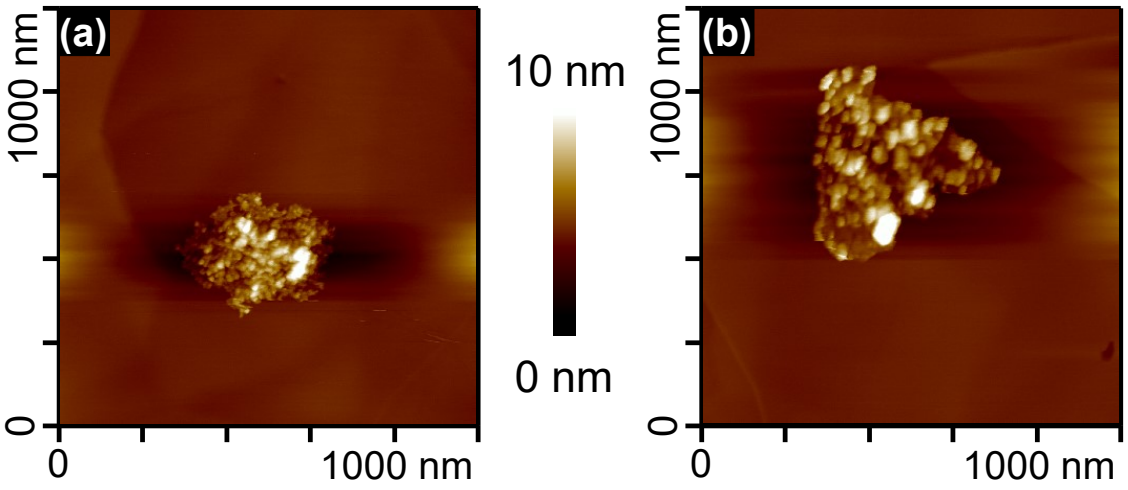

Fig. A3.10 AFM images of PM-GO (Chandra).

Appendix Chapter 6 Figures

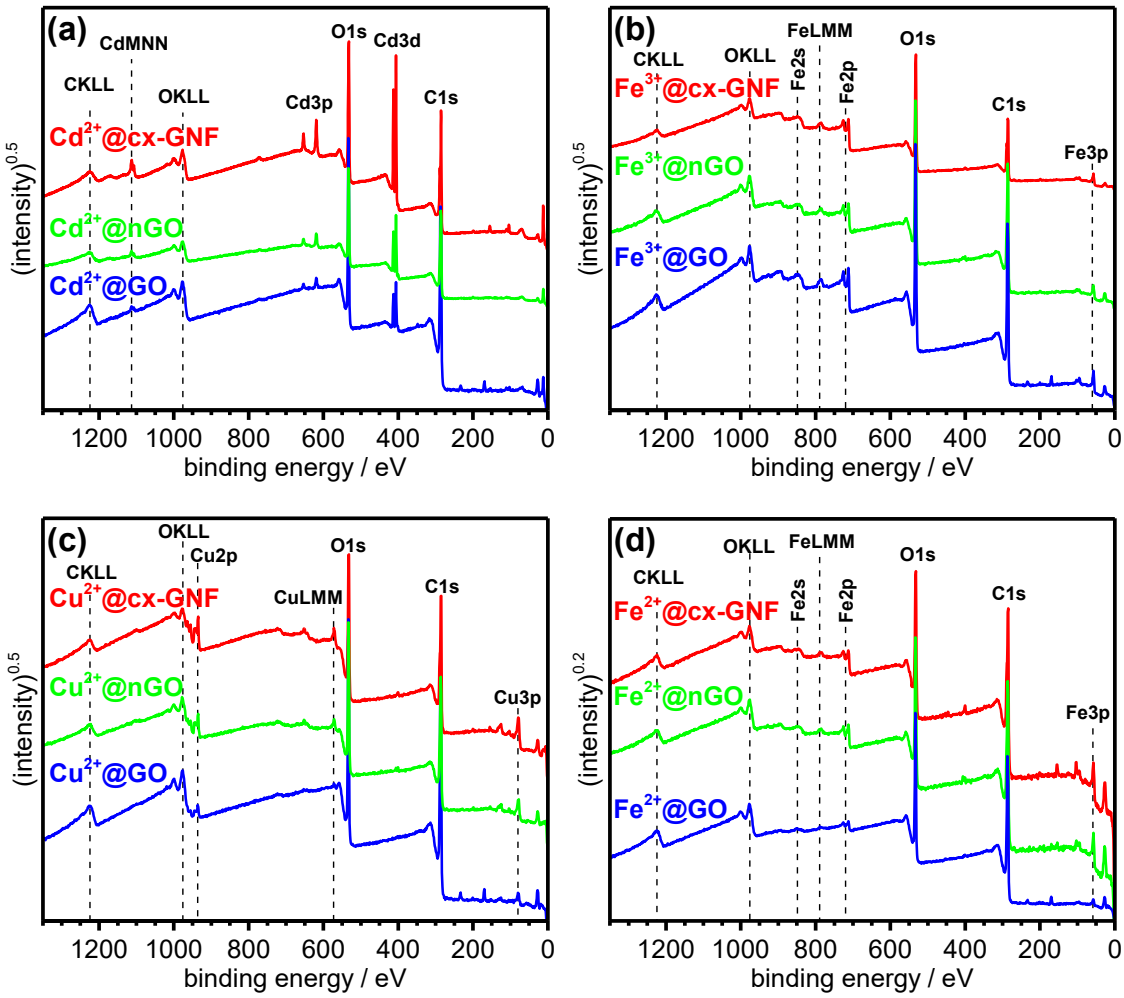

Fig. A6.1 The XPS survey spectra of $M^{2+/3+}$@cx-GNF (red), $M^{2+/3+}$@nGO (green) and $M^{2+/3+}$@GO (blue) treated with Cd^{2+}, Fe^{3+}, Cu^{2+} and Fe^{2+} cations are shown in (a)-(d) respectively. Black dashed lines indicate the major peaks in the spectra.

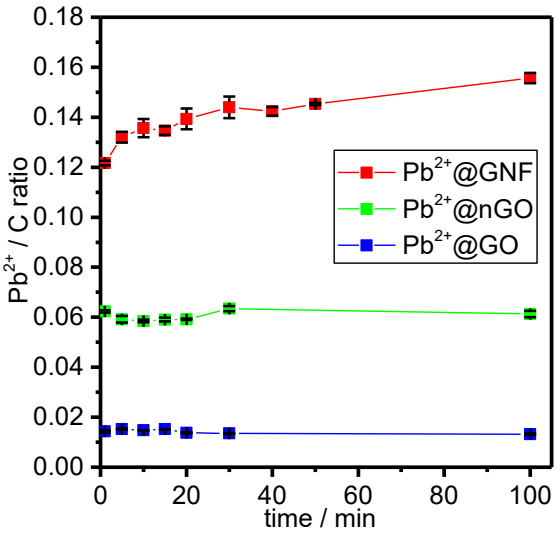

Fig. A6.2 The influence of contact time between Pb^{2+} cations and cx-GNF (red), nGO (green) and GO (blue) on the Pb/C ratio calculated from the XPS survey spectra. [Conditions: 10 mg of each carbon material was treated with 10 mL of 0.1 M $Pb(NO_3)_2$, in the same way as carried out in Fig. 2(b)].

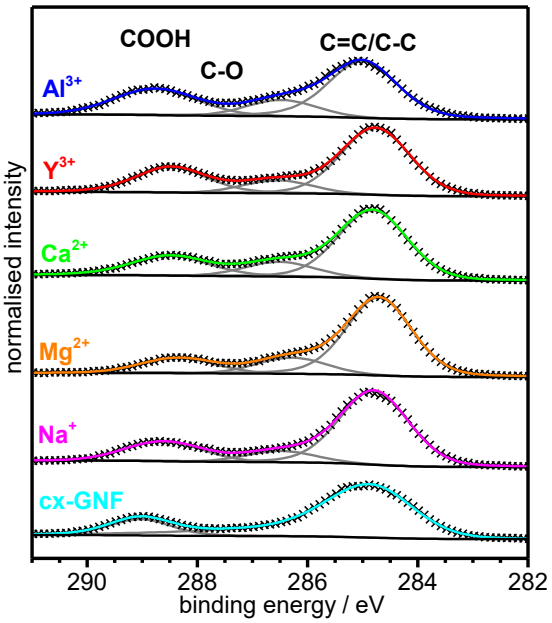

Fig. A6.3 Area-normalised XPS C1s spectra of cx-GNFs (cyan), Fe^{2+}@cx-GNFs (magenta), Cu^{2+}@cx-GNFs (orange), Fe^{3+}@cx-GNFs (green), Cd^{2+}@cx-GNFs (red) and Pb^{2+}@cx-GNFs (blue). The crosses are the experimental data, grey lines are the fitted peaks, black line is the Shirley background function and the coloured lines are the peaks sums respectively.

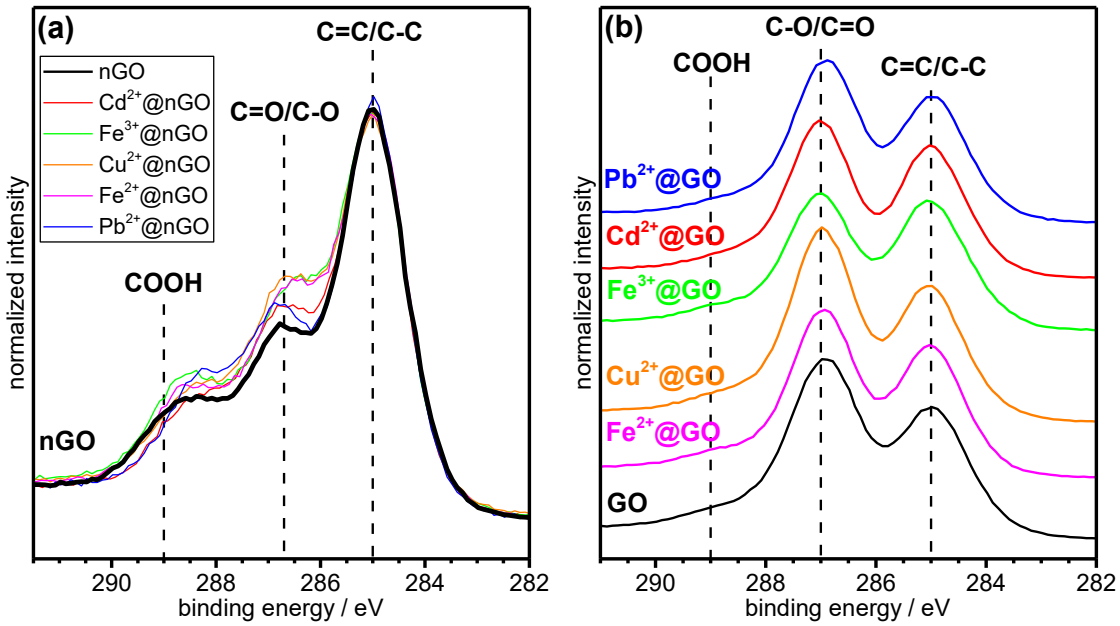

Fig. A6.4 XPS C1s spectra of (a) nGO and (b) GO treated with Fe^{2+} cations (magenta), Cu^{2+} cations (orange), Fe^{3+} cations (green), Cd^{2+} cations (red), Pb^{2+} cations (blue) and controls (black).

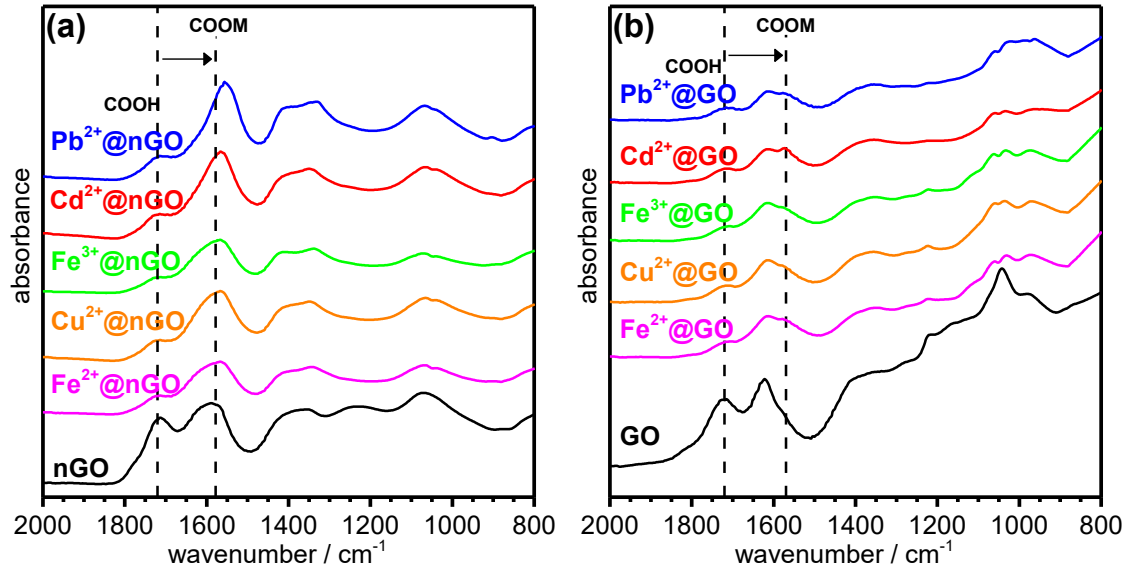

Fig. A6.5 ATR-IR spectra of (a) nGO and (b) GO treated with Fe^{2+} cations (pink), Cu^{2+} cations (orange), Fe^{3+} cations (green), Cd^{2+} cations (red), Pb^{2+} cations (blue) and controls (black).

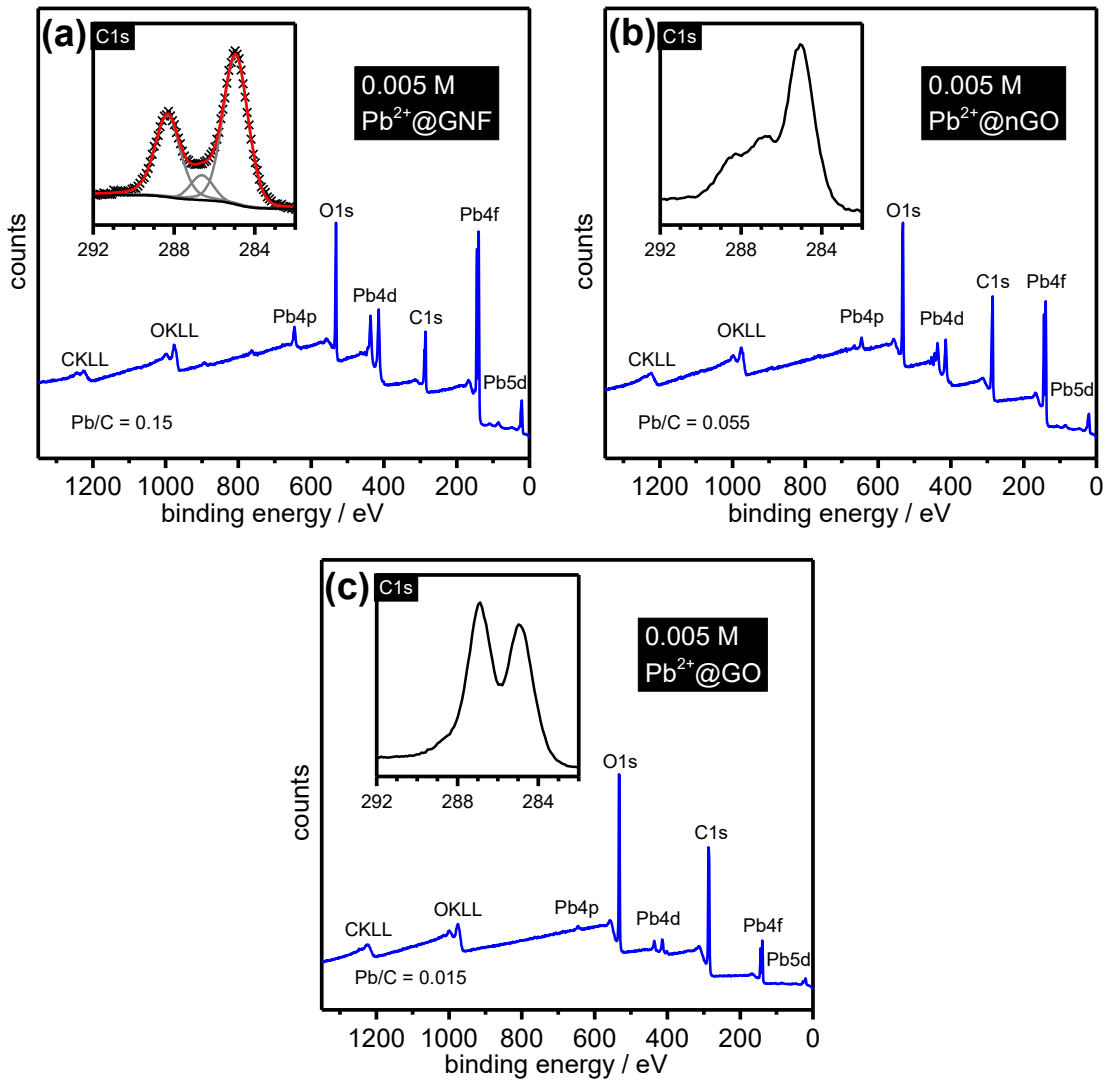

Fig. A6.6 XPS survey spectra (outset) and C1s region (inset) of Pb^{2+}@carbon treated with 0.005 M $Pb(NO_3)_2$.

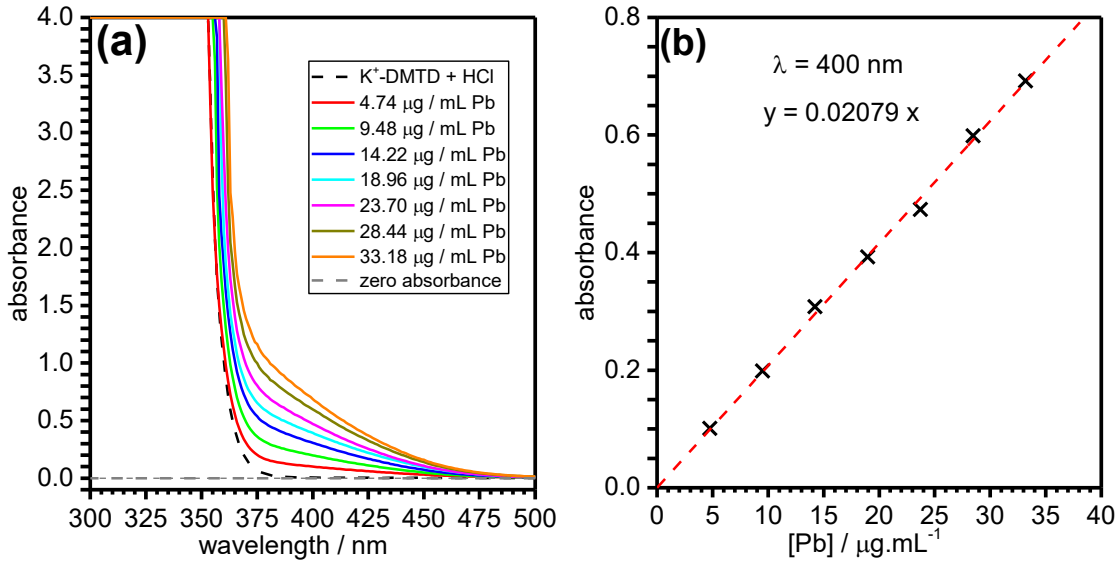

Fig. A6.7(a) Optical absorbance spectra of the Pb-DMTD complex in 0.005 M aqueous HCl in the 5-35 µg.mL^{-1} concentration range. (b) Calibration plot of the absorbance values at λ = 400 nm from (a).

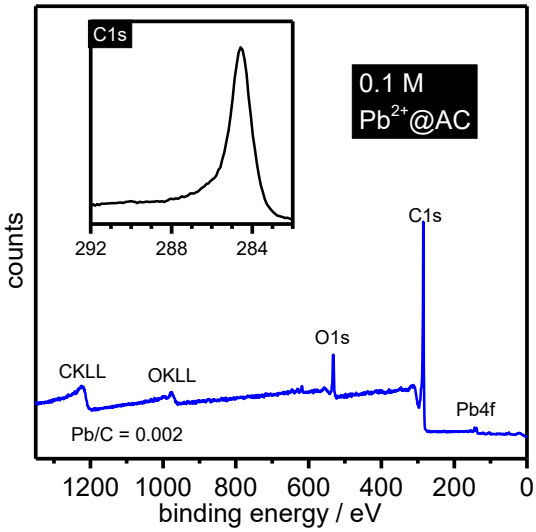

Fig. A6.8 XPS survey spectra (outset) and C1s region (inset) of Pb^{2+}@AC treated with 0.1 M $Pb(NO_3)_2$.